Seismic behaviour of structures with basements in liquefiable soil

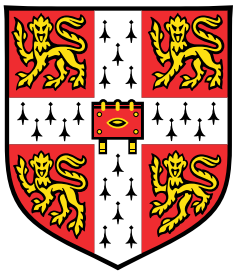

Fiona Elizabeth Hughes

Department of Engineering
University of Cambridge

This dissertation is submitted for the degree of
Doctor of Philosophy

Queens' College July 2019

Declaration

I hereby declare that except where specific reference is made to the work of others, the contents of this dissertation are original and have not been submitted in whole or in part for consideration for any other degree or qualification in this, or any other, university. This dissertation is my own work and contains nothing which is the outcome of work done in collaboration with others, except as specified in the text and Acknowledgements. This dissertation contains fewer than 65,000 words including appendices, footnotes, tables and equations, but excluding the bibliography, and has fewer than 150 figures.

Fiona Elizabeth Hughes
July 2019

Seismic behaviour of structures with basements in liquefiable soil

Fiona Elizabeth Hughes

Earthquake induced liquefaction can cause significant damage in the built environment. Structures on shallow foundations can suffer large settlement and rotation, and light underground structures can uplift. The performance of structures with basements, which intuitively combines these two problems, is not understood.

In this thesis, the seismic behaviour of structures with basements in liquefiable soil has been investigated. A series of highly instrumented dynamic centrifuge tests showed that the presence of a basement can reduce the liquefaction induced settlement of a structure whilst maintaining the natural isolation provided by liquefied soil. The generation of positive excess pore pressures during shaking increased the buoyancy force provided by the basement. When the ratio of uplift to total weight during liquefaction was controlled, this buoyancy reduced settlement compared to structures with shallow foundations without basements.

The centrifuge test data showed that structures with basements were susceptible to suffer a large accumulation of rotation during earthquake induced liquefaction. Compared to structures without basements, resistance to rotation provided by the soil decreased because the buoyancy provided by the basement reduced the vertical effective stresses below the structure. Rotation was exacerbated by an increase in the moment loading imposed by the structure due to the presence of the basement. An increase in the plan area of the basement was found to reduce residual rotation.

A mechanical model for displacement and rotation in liquefiable soil was developed using data from the centrifuge test series. It was based on a traditional mass-spring-damper model, with the addition of slider elements to incorporate accumulation of displacement and rotation. The model was able to replicate the centrifuge test results when liquefaction occurred. Parametric studies using the model found that residual rotation was highly sensitive to the basement width and height of the centre of gravity of the structure.

In summary, liquefaction induced settlement and rotation, and seismic demand of a structure can be minimised by including a basement and controlling the basement geometry, mass distribution, and total weight of the structure. The increase in usable space that a basement provides in a building is anticipated to make this mitigation method an attractive option compared to conventional alternatives such as soil improvement.

Acknowledgements

Firstly, I would like to thank my supervisor, Professor Gopal Madabhushi, for his support, guidance, and enthusiasm during the course of this research. I would like to thank my advisor, Dr Stuart Haigh, for his technical advice and support. I am also grateful to Professor Malcolm Bolton and Professor Giulia Viggiani for engaging discussions on my research work.

I have been fortunate to work alongside many talented researchers at the Schofield Centre. I am indebted to them for their help, suggestions and encouragement. In particular, I would like to thank Abdul Zeybek, Alessandro Fusco, Chang Ye Gue, Jad Boksmati, Jefferey Lau, Njemile Faustin, Orestis Adamidis, Peter Kirkwood, Samy Garcia Torres, Srikanth Madabhushi, Stefan Ritter, Stephan Van Eeden, and Talia da Silva. I am also grateful to all of the technicians at the Schofield Centre for their assistance and advice.

I am thankful for the opportunities I have had during my PhD. My colleagues on the Earthquake Engineering Field Investigation Team (EEFIT) reconnaissance mission to Ecuador in 2016, the inaugural Society for Earthquake and Civil Engineering Dynamics (SECED) Young Members committee, and the Cambridge University Geotechnical Society committee greatly enriched my PhD experience. I am thankful to Queens' College for the opportunity to teach first year undergraduate engineering students and the guidance they provided.

This work was made possible by the generous funding from the Engineering and Physical Sciences Research Council (EPSRC), the University of Cambridge School of Technology, and Queens' College. In addition, I am indebted to Queens' College for the support provided throughout my studies in Cambridge, particularly Dr Andrew Gee and Dr James Kelly.

I am extremely fortunate to have unwavering support from my family: my parents, Madalyn and Geoff, and my sister, Heather. I am grateful for their understanding, advice and encouragement. My final thanks go to Simon - thank you your continuous support and encouragement, and for making life more fun.

List of publications

Journal articles

Hughes, F. E. and Madabhushi, S. P. G. (2019), 'Liquefaction Induced Displacement and Rotation of Structures with Wide Basements', *Soil Dynamics and Earthquake Engineering* **120**, 75–84.

Chian, S. C., Wilkinson, S. M., Whittle, J. K., Mulyani, R., Alarcon, J. E., Pomonis, A., Saito, K., Fraser, S., Goda, K., Macabuag, J., Offord, M., Hunt-Raby, A. C., Sammonds, P., Franco, G., Stone, H., Ahmed, B., **Hughes, F. E.**, Jirouskova, N. K., Kaminski, S. and Lopez, J. (2019), 'Lessons Learnt From the 2009 Padang Indonesia , 2011 Tohoku Japan and 2016 Muisne Ecuador Earthquakes', *Frontiers in Built Environment* **5**:73.

Hughes, F. E. and Madabhushi, S. P. G. (2020), 'Behavior of Structures with Basements Located in Liquefiable Soils', *Journal of Geotechnical and Geoenvironmental Engineering* **146**(7), 04020051.

Conference papers

Franco, G., Stone, H., Ahmed, B., Chian, S. C., **Hughes, F. E.**, Jirouskova, N., Kaminski, S., Lopez, J., Van Drunen, N. G. and Querembas, M. (2017), The April 16 2016 M_W 7.8 Muisne Earthquake in Ecuador - Preliminary Observation from the EEFIT Reconnaissance Mission of May 24 - June 7, *in* '16th World Conference on Earthquake Engineering', Santiago, Chile.

Hughes, F. E. and Madabhushi, S. P. G. (2017), Control of liquefaction induced settlement of buildings using basement structures, *in* 'Proceedings of the 3rd International Conference on Performance-based Design in Earthquake Geotechnical Engineering', Vancouver, Canada.

Hughes, F. E. and Madabhushi, S. P. G. (2018), Dynamic Response of a Structure with a Basement Sited on Liquefiable Soil, *in* '16th European Conference on Earthquake Engineering', Thessaloniki, Greece.

Hughes, F. E. and Madabhushi, S. P. G. (2018), The importance of vertical accelerations in liquefied soils, *in* '9th International Conference on Physical Modelling in Geotechnics', London, United Kingdom, pp. 967–973.

Hughes, F. E. and Madabhushi, S. P. G. (2019), Co-seismic rotation and displacement of a structure with a basement sited in liquefiable soil, *in* '7th International Conference on Earthquake Geotechnical Engineering', Rome, Italy, pp. 2898–2905.

Technical report

Franco, G., Stone, H., Ahmed, B., Chian, S. C., **Hughes, F. E.**, Jirouskova, N., Kaminski, S., Lopez, J., Van Drunen, N. G., Molina Hutt, C. and Querembas, M. (2018), The Muisne, Ecuador Earthquake of 16 April 2016. A field report by EEFIT, Technical report, The Institution of Structural Engineers. URL: *https://www.istructe.org/resources/report/eefit-mission-muisne-ecuador- earthquake/*

Table of contents

List of figures

List of tables

Nomenclature

Roman Symbols

A	Cross sectional area
a	Acceleration
A_γ	Shear strain amplitude
B	Width of basement
b	Width of superstructure
B_c	Cone diameter
c	Damping constant
d_{50}	Mean particle diameter
D	Depth of basement
d	Height of horizontal spring and dashpot above bottom of basement
e	Void ratio
F	Force
f	Frequency
G	Shear modulus
g	Earth's gravitational field
G_s	Specific gravity
H	Depth of the soil stratum

h	Height of superstructure
I_o	Moment of inertia
I_a	Arias intensity
I_C	Relative crushability
I_D	Relative density
i	Hydraulic gradient
I_R	Relative density index
K_0	Lateral earth pressure coefficient at rest
k	Spring stiffness
K_P	Passive earth pressure coefficient
L	Length of basement
m	Mass
N	Gravity scaling factor
p	Mean stress
q_b	Bearing pressure
q_{c1N}	Normalised cone resistance
q_c	Cone resistance
Q	Slider threshold
q	Axial-deviatoric stress
R_0	Pore pressure reduction constant
r_d	Stress reduction coefficient
R	Pore pressure reduction factor
r_u	Excess pore pressure ratio
T_n	Natural period

u	Pore pressure
v_s	Shear wave velocity
V_{ult}	Degraded central vertical load capacity
V	Volume
W	Weight

Greek Symbols

γ'_s	Buoyant unit weight of soil
γ	Shear strain
γ_w	Unit weight of water
γ_s	Saturated unit weight of soil
ν	Poisson's ratio
ϕ	Friction angle
ϕ_{crit}	Critical state friction angle
ψ	Dilatancy angle
ψ_c	State parameter
σ	Normal stress
τ	Shear stress
θ	Rotation
ζ	Damping ratio

Superscripts

$'$	Effective

Subscripts

0	Initial
a	Atmospheric

B	Basement
b	Below basement
s	Side of basement
CoG	Centre of gravity
dy	Dynamic
ex	Excess
h	Hydrostatic
L	Liquefaction
max	Maximum
n	Natural
S	Superstructure
st	Static
U	Uplift
v	Vertical

Other Symbols

U/W	Ratio of the uplift to total weight when the surrounding soil liquefies

Acronyms / Abbreviations

BPT	Becker penetration test
CPT	Cone penetration test
CRR	Cyclic resistance ratio
CSR	Cyclic shear stress ratio
DRILS	Displacement and Rotation In Liquefiable Soil
FFT	Fast Fourier transform
HDPE	High-density polyethylene

LVDT Linear variable displacement transducer

MEMS Microelectromechanical system accelerometer

OCR Overconsolidation ratio

PIV Particle image velocimetry

PMMA Polymethyl methacrylate

PPT Pore pressure transducer

PTFE Polytetrafluoroethylene

SAM Stored angular momentum

SDOF Single degree of freedom

SOF State of practice

SPT Standard penetration test

SSI Soil-structure interaction

Chapter 1

Introduction

1.1 Background

Earthquakes are a commonly occurring, catastrophic natural phenomenon. Large magnitude events can cause massive damage to infrastructure and enormous loss of life. Recent examples of cataclysmic earthquakes include the 2010 Haiti earthquake, the 2011 Tōhoku earthquake in Japan, and the 2015 Gorkha earthquake in Nepal. These are the three deadliest earthquakes of the last decade, with death tolls of approximately 316,000, 15,700 and 9,000 respectively (Guilbert 2017). Improvements to design, construction, and mitigation practices are required to reduce the number of casualties, fatalities, and the financial impact of earthquakes. Advances in geotechnical earthquake engineering are required for this purpose.

Within the field of geotechnical earthquake engineering, earthquake induced liquefaction is one of the most destructive phenomena. The term liquefaction is used to describe the reduction in strength and stiffness of loose, saturated, sandy soils subjected to cyclic loading such as earthquake shaking. The very large stiffness and strength degradation renders liquefied soil an extremely problematic soil state. Soils particularly susceptible to liquefaction include sediments deposited in the past few thousand years, river channel and flood plain alluvium, and poorly compacted fills, which are commonplace around the world. Specifically, a number of mega cities in seismically active areas are located on soil susceptible to liquefaction, for example Delhi and Jakarta. Liquefaction is therefore a widespread, worldwide problem.

Earthquake induced liquefaction has caused significant damage in historic and recent earthquakes, particularly in the built environment. It can cause structures on shallow foundations to suffer large settlement and rotation (Cubrinovski et al. 2011, Bertalot et al. 2013, Bray & Dashti 2014), and light underground structures to uplift (Towhata 2008, Bhattacharya et al. 2011, Chian & Tokimatsu 2011, Tokimatsu et al. 2012). Despite significant research into liquefaction induced damage to buildings and infrastructure, damage of this nature is

continuing to occur. The recent disastrous seismic events in Japan in 2011, as a consequence of the Tōhoku earthquake (Bhattacharya et al. 2011), and in New Zealand in 2010-2011, as a consequence of the series of earthquakes in Christchurch (Cubrinovski et al. 2011), show that even countries with advanced seismic building codes are not well protected against liquefaction. There remains a need to better understand the phenomenon of liquefaction, with a view to mitigating damage to infrastructure.

Very little is known regarding the seismic behaviour of structures partially buried in liquefiable soil, which is the case for many modern buildings with basements. This is surprising for two reasons. Firstly, there is an increasing tendency for buildings to have basements. Urban centres are becoming densely populated and land prices are rising, making it desirable to use underground space for parking and storage. Secondly, it is intuitive that partially buried structures combine the propensity of structures with shallow foundations to settle and light subsurface structures to float. They may therefore perform advantageously during earthquake induced liquefaction by reducing the total vertical displacement of a structure.

1.2 Case study: the 16th April 2016 Muisne, Ecuador earthquake

On April the 16^{th} 2016, an M_w = 7.8 earthquake with an epicentre 29 km south-southeast of Muisne in northern Ecuador, caused an estimated 673 fatalities, 6,300 severe injuries and damage throughout the Manabí region. A seven person team was deployed by the Earthquake Engineering Field Investigation Team (EEFIT) with the objective of surveying the damage and recording observations that would help the scientific and professional community understand the event and its consequences. Participation in this reconnaissance mission provided an invaluable opportunity during the first year of this research project to observe earthquake damage, learn more about disciplines related to earthquake engineering, and to begin to appreciate the difficulties of disaster response and emergency relief. Some of the results presented in this chapter have been reported previously (Hughes & Madabhushi 2017, Franco et al. 2017, 2018).

Geotechnical failures were widespread during the Muisne earthquake. Damage was worsened by the river levels and water table being abnormally high at the time of the mainshock, which occurred towards the end of the annual rainy season, which had possibly been intensified by the 2015-2016 El Niño phenomenon. Examples of different types of geotechnical failures observed in the Manabí region are shown in the photographs in

Figure 1.1. Differential settlement of a structure with a shallow foundation caused cracking of concrete beams and connections, as shown in Figure 1.1(a). Heave of floor slabs was observed in the same structure, which is consistent with bearing capacity failure (Figure 1.1(b)). Large landslides also occurred on coastal cliffs and in hilly inland regions. Figure 1.1(c) is an aerial view showing scars of a large landslide which occurred below the crest of a ridge and destroyed 4 buildings. Liquefaction induced lateral spreading was observed at numerous locations, and was exacerbated by rivers being in spate at the time of the earthquake. An example is shown in Figure 1.1(d).

An observation of particular interest to this research project was the damage to a shrimp farm on the sea front in Pedernales, 36 km south-southwest of the epicentre, which is understood to have been caused by earthquake induced liquefaction, as shown in the photographs

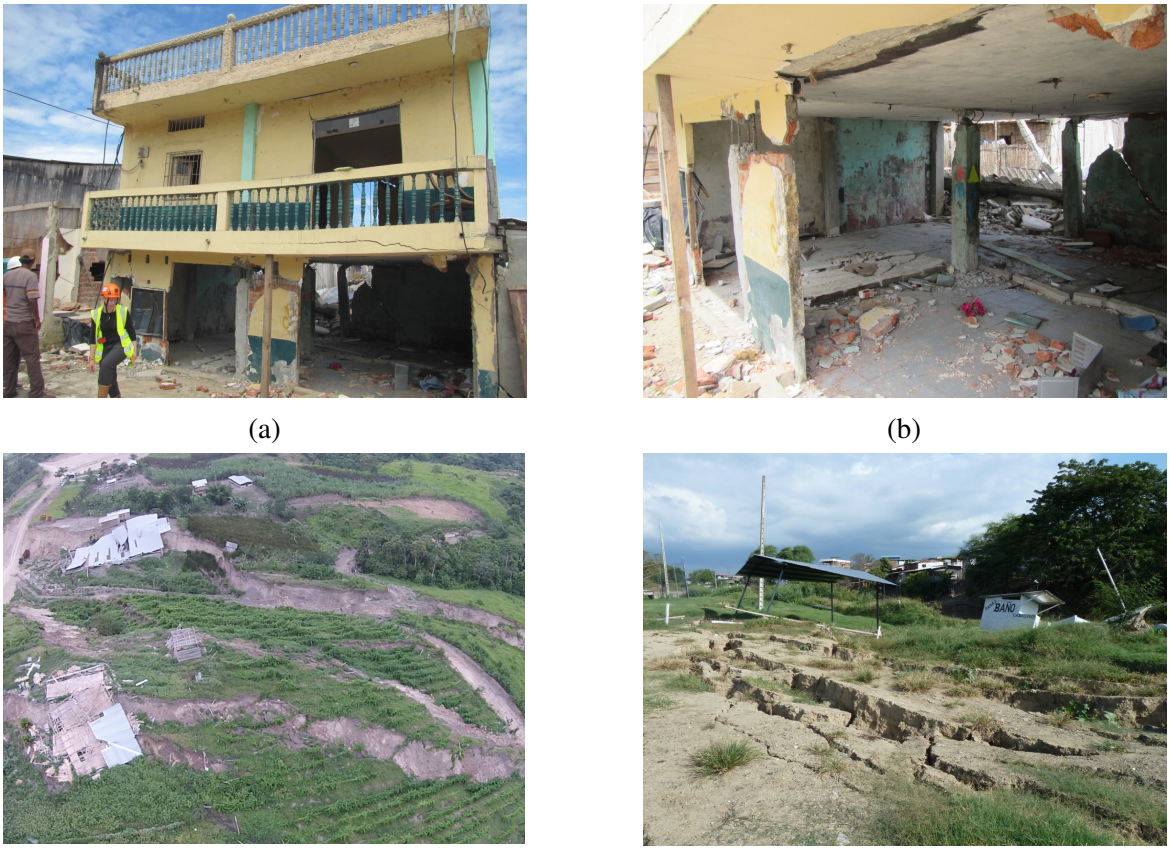

(a) (b)

(c) (d)

Fig. 1.1 Geotechnical failures in the April 16^{th} 2016 M_w = 7.8 Muisne, Ecuador earthquake. (a) Differential settlement of a structure with a shallow foundation, resulting in cracking of concrete beams and connections, (b) Heave of floor slabs in the same structure, consistent with bearing capacity failure, (c) Aerial photograph of large landslide, showing scars and destroyed buildings, (d) Liquefaction induced lateral spreading of a riverbank.

in Figure 1.2. A structure with underground storage tanks, which were empty at the time of the earthquake, experienced relative uplift compared to the structures adjacent to it, which did not have underground storage tanks. Relative uplifts of 120 mm and 210 mm were measured compared to the adjacent structures, as shown in Figures 1.2(b,c,d). Absolute settlements are not known due to the surrounding ground having settled. The structure with subsurface storage tanks can be likened to a one storey building with a one storey basement. This implies that it is possible to reduce liquefaction induced structure settlement using basement storeys. Whilst it is not possible to infer the effects of a basement on taller or heavier structures, the behaviour of this shrimp farm suggests that it is an avenue worthwhile investigating.

(a)

(b)

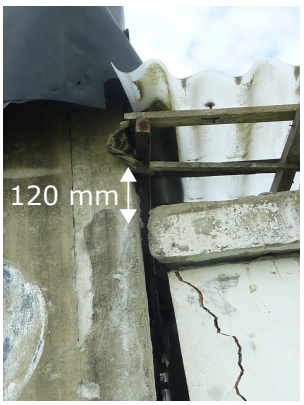

(c)

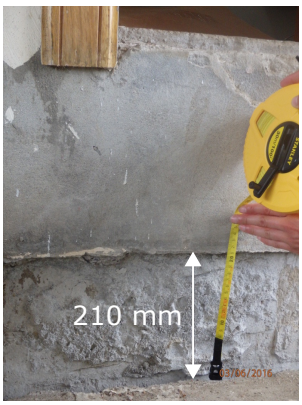

(d)

Fig. 1.2 Evidence of relative uplift of a partially buried, buoyant structure, (a) Aerial photograph of position of shrimp farm on the sea front in Pedernales, taken with a drone. Red rectangle identifies the structure with underground storage tanks, (b) Evidence of relative uplift highlighted in red rectangle, (c) Differential settlement of 120 mm relative to the adjacent structure facing the shoreline which is identified in (a) by the blue dot, (d) Differential settlement of 210 mm relative to the adjacent structure shown in (b) and identified in (a) by the yellow dot.

1.3 Research aims

The overarching aim for this research project is to ascertain the seismic behaviour of structures with basements in liquefiable soil. Specifically, the behaviour of these structures during earthquake induced liquefaction will be investigated. Intuitively, these partially buried structures combine the propensity of structures with shallow foundations to settle and light buried structures to float. It is hypothesised that they may therefore perform advantageously during earthquake induced liquefaction by reducing the total vertical displacement of a structure.

The dynamic response and stability of structures with basements in liquefiable soils will be assessed. An emphasis will be placed on soil-structure interaction. The dependence of their performance on base shaking amplitude, structure weight, and basement geometry will be investigated, which is informative for practical design. In addition, the behaviour of liquefied soil surrounding a partially buried, buoyant structure will be investigated.

1.4 Thesis layout

The subsequent chapters in this thesis are as follows:

- **Chapter 2**
  A critical review of the literature is presented in this chapter. The historical development of the understanding of liquefaction is reviewed, methods to assess liquefaction susceptibility are discussed, and the current understanding of liquefaction induced damage to buildings and infrastructure is assessed.

- **Chapter 3**
  In this chapter, the principles of centrifuge modelling are explained. Subsequently, the facilities used at the Schofield Centre at the University of Cambridge to perform the dynamic centrifuge tests discussed in this thesis are presented.

- **Chapter 4**
  The focus of this chapter is on the influence of a shallow, narrow basement on the seismic behaviour of a structure located on liquefiable soil. Emphasis is placed on the performance of these structures when rigid extenders are attached to the basement.

- **Chapter 5**
  The seismic behaviour of structures with wide basements is examined in this chapter. The effect of changes in mass eccentricity and the ratio of uplift to total weight are

investigated. The resultant vertical force and moment imposed by these structures on the surrounding soil are considered.

- **Chapter 6**
  This chapter presents the findings from using a miniature cone penetration test (CPT) device in-flight in the centrifuge tests. Emphasis is placed on the change in cone resistance between CPTs conducted before and after a sequence of earthquakes.

- **Chapter 7**
  In this chapter, a mechanical model is developed to model the displacement and rotation of a structure with a basement during earthquake induced liquefaction. It is first used to enable further insight to be obtained on the behaviour of the structures observed in the centrifuge tests. A parametric study is subsequently conducted to apply the findings from the centrifuge tests to a wider number of structure properties and input motions, intermediate to those used in the centrifuge test series.

- **Chapter 8**
  The main conclusions of the thesis are outlined in the final chapter. Recommendations for both practical design and future research directions are proposed.

Chapter 2

Literature review

Soil liquefaction is a highly destructive consequence of large earthquake events. Unprecedented damage to modern buildings and infrastructure during the 1964 Niigata earthquake brought earthquake induced liquefaction to the forefront of priorities for the engineering community (Ohsaki 1966, Ishihara 1993). Preceding this earthquake, research into the phenomenon of liquefaction was in its infancy. Following the Niigata earthquake, research in this field accelerated dramatically. However, liquefaction induced damage continues to cause significant destruction during large earthquake events around the world. This suggests that the current design and implementation of mitigation methods is inadequate. Furthermore, it raises the question of whether the fundamental understanding of the phenomenon of soil liquefaction is correct.

In this chapter the historical development of the understanding of liquefaction is reviewed, methods to assess liquefaction susceptibility are discussed, and the current understanding of liquefaction induced damage to buildings and infrastructure is assessed.

2.1 Liquefaction

Liquefaction is the term used to describe the reduction in strength and stiffness of saturated, sandy soils when the vertical effective stress approaches zero due to the generation of positive excess pore pressure.

2.1.1 Liquefaction of earth dams

Initial interest in the phenomena of soil liquefaction stemmed from the desire to understand the catastrophic failure of a number of earth dams. Specifically, the first use of the term soil liquefaction in geotechnical engineering was to describe the failure of the Calaveras

Dam in California (Hazen 1920). It was proposed that an increase in pressure of pore fluid in a saturated granular material reduces interparticle pressure between soil grains, which decreases the frictional resistance of the material (Hazen 1920). Research over the past 100 years has consolidated this theory.

The failure of earth dams incentivised the need for a framework to determine the stability, and therefore safety, of this type of structure. To this purpose, the concept of a critical void ratio was proposed (Casagrande 1936). Data obtained from drained direct shear and consolidated drained triaxial tests were used to determine the critical void ratio of a cohesionless soil, which equated to the state of continuous deformation at constant resistance and constant volume. The line joining these ratios at difference effective stresses was defined as the critical void ratio line. Casagrande (1936) hypothesised that cohesionless sands which plot above the critical void ratio line in their in situ state would be susceptible to liquefaction under undrained conditions. In this case, the increase in pore pressure reduces the interparticle friction and impairs the stability of the mass. Casagrande proposed that dense sands which plot below the critical state line would be safe against liquefaction due to a decrease in pore pressure temporarily increasing the stability of the mass. However, this hypothesis was proven incorrect by the Fort Peck Dam slide in 1938, where a sand which plotted below the critical void ratio line failed with a very large strength loss (Casagrande 1971).

2.1.2 Liquefaction as an undrained event

Research in the field of soil liquefaction gained momentum following the Niigata 1964 earthquake. The focus shifted from dam failure to earthquake induced liquefaction. A significant amount of this early research was based on the assumption that earthquake loading, consisting of cyclic loading of approximately 1-5 Hz, is sufficiently rapid to prevent flow of water within the pore space of soil (Seed & Lee 1966, Ishihara et al. 1975, Luong & Sidaner 1981). This classifies earthquake induced liquefaction as an undrained event.

Undrained element tests formed the basis of the early understanding of earthquake induced liquefaction. Undrained cyclic triaxial test data showed that danger of liquefaction of saturated sand, in a contractive (loose) state, in undrained conditions increased with a change in the following factors: an increase in void ratio, a decrease in confining pressure, an increase in magnitude of cyclic stress or strain, and an increase in number of cycles of applied shear stress (Seed & Lee 1966). These data also showed that positive excess pore pressures could be generated in dense sand samples lying below the critical void ratio line. However, unlike loose sands, these samples did not undergo sudden failure. The term "cyclic mobility" was used to describe the progressive softening of a portion of a specimen subjected to cyclic loading, but which was sufficiently dense to remain safe against liquefaction failure

(Casagrande 1971). Further undrained triaxial test results were used to develop this definition, and the term cyclic mobility was subsequently used to describe the gradually increasing cyclic strains that can occur in loose or dense sand and don't entail a loss in shear strength (Castro 1975). This behaviour was separated from liquefaction, which was defined as a loss in shear strength and failure only when a driving force applying shear stress becomes greater than the undrained shear strength of the soil (Castro 1975). Figure 2.1 shows the difference in stress path and stress-strain curve for loose and dense sand obtained from cyclic torsion shear tests (Ishihara 1985).

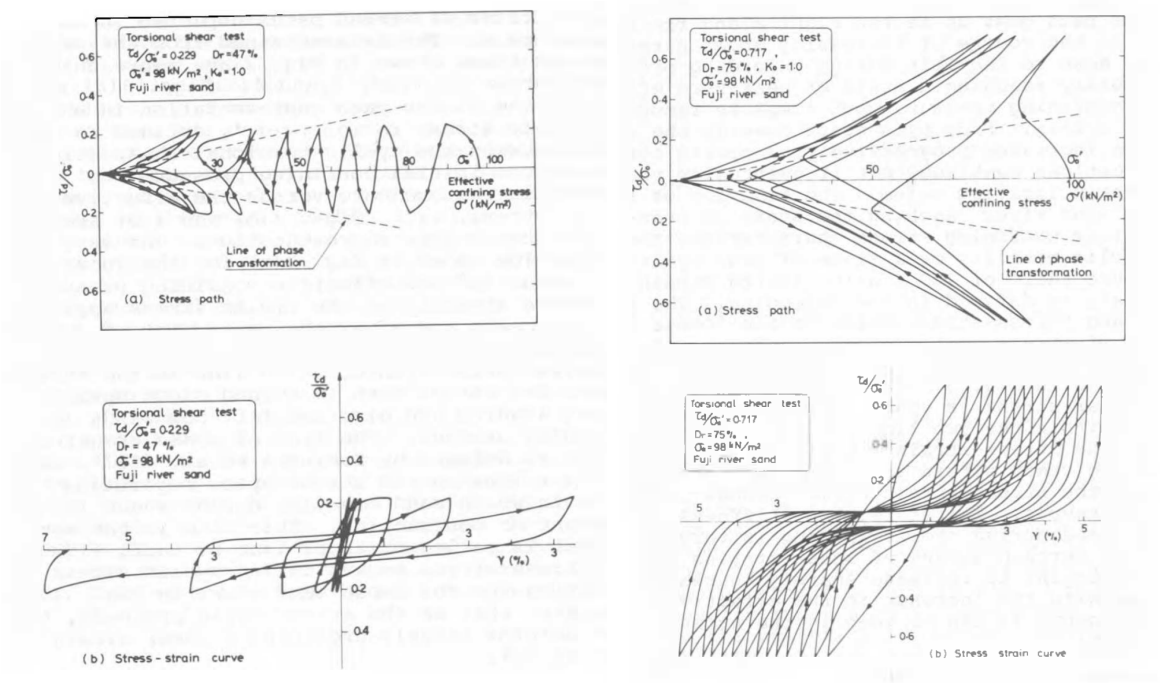

(a) (b)

Fig. 2.1 Stress path and stress-strain curve obtained from cyclic torsion shear tests for (a) Loose sand, (b) Dense sand (Ishihara 1985).

To further advance the development of methods to determine if a soil was at danger of liquefying was the need to understand the mechanisms through which liquefaction is initiated. Undrained cyclic triaxial test data were used to develop frameworks to understand the behaviour of saturated sandy soils which were cyclically loaded in undrained conditions (Ishihara et al. 1975, Luong & Sidaner 1981). These initial data and frameworks were limited to cases where no static shear stresses were present. Lines were proposed to separate contractive and dilative behaviour in $p' - q$ space, which have a shallower gradient than the failure line.

Ishihara et al. (1975) called this line the phase transformation line, and stated that liquefaction was initiated when the stress path reached this line (Figure 2.2). They noted that there is considerable difficulty when trying to follow the stress path after liquefaction. Following an independent series of tests, Luong & Sidaner (1981) called this line the characteristic state line, and found it to have a shallower gradient in extension than compression. In compression, the region above the characteristic state line was defined as the surcharacteristic zone, where dilatant behaviour was exhibited, and the region below the characteristic state line was the subcharacteristic zone, where contractive behaviour was exhibited. Liquefaction of sand was said to only occur under alternating cyclic loading which reaches the characteristic threshold on both sides of zero deviatoric stress (Luong & Sidaner 1981).

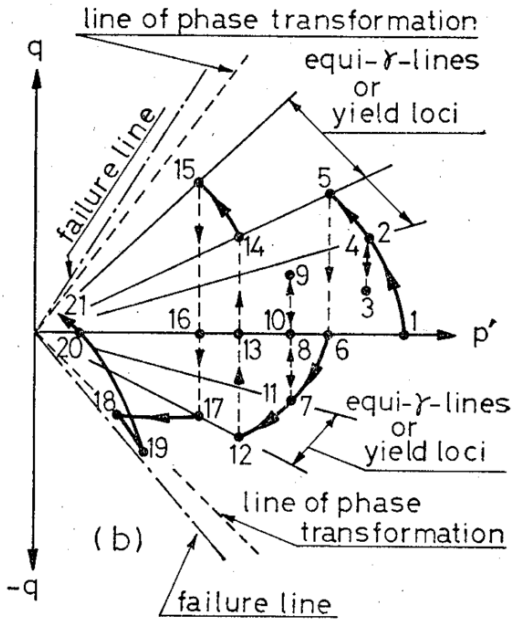

Fig. 2.2 Stress path trace of saturated Niigata sand subject to cyclic stresses of irregular amplitude in undrained conditions, from undrained triaxial tests (Ishihara et al. 1975). Numbers identify sequential points along the stress path.

The initial confining pressure and static shear stress govern the proximity of a soil element from these state lines in $p' - q$ space, and therefore dictate how much loading is required for them to be reached. Undrained element testing has been used extensively to understand the influence of these parameters on the cyclic resistance of sands. An increase in initial static shear stress was found to both decrease liquefaction resistance (Castro 1975) and increase it (Vaid & Chern 1983). These contradictory results were subsequently explained to be a consequence of the effect of static shear stress being strongly dependent on both

the initial confining stress and soil density (Vaid & Finn 1979, Vaid & Chern 1983, Vaid et al. 1985). In a loose sand, additional initial shear stress lowers resistance to liquefaction as it moves an element closer to the failure envelope. However, if the initial shear stress is greater than the cyclic shear stress applied, then no stress reversal will take place, increasing resistance to liquefaction. Furthermore, soil relative density determines the mechanism of strain development - strain softening in looser, contractive sand, and cyclic mobility in denser sand. The interdependency of these variables means that the threshold between these two mechanisms depends on confining stress and static shear.

2.1.3 Liquefaction as a partially drained event

An increasingly large body of evidence suggests that liquefaction is a partially drained event. The partially drained nature of liquefaction can be described using the critical state framework (Schofield 1981, Muhunthan & Schofield 2000), as it takes into account volume change during loading. In the same fashion as the frameworks developed by Ishihara et al. (1975) and Luong & Sidaner (1981), the critical state framework defines a line in $p' - q$ space which separates contractive (loose or "wet") and dilative (dense or "dry") granular materials. The line separating these two regions is the critical state line. It defines the critical state of a material, which is reached when the mean effective stress, p', and the axial-deviator stress, q, satisfy Equations 2.1 and 2.2 (Schofield & Wroth 1968):

$$q = Mp' \tag{2.1}$$

$$v = \Gamma - \lambda ln p' \tag{2.2}$$

where v is the specific volume, M is the critical state frictional constant, Γ is the ordinate of the critical state line, and λ is the gradient of the compression line. At critical state a material yields at constant volume, hence behaving as a frictional fluid rather than a yielding solid (Schofield & Wroth 1968).

Within the critical state framework, Been & Jefferies (1985) defined the state parameter, ψ_c, as a measure of the deviation of the current void ratio of the soil, e, from the void ratio at critical state at the current mean stress, e_c:

$$\psi_c = e - e_c \tag{2.3}$$

The state parameter is positive for soil elements on the loose side of critical state, and negative for those on the dense side, and therefore is a normalising index for soil behaviour

irrespective of stress level or material type (Been & Jefferies 1985). At critical state, the state parameter is zero.

When a soil element on the loose or "wet" side of the critical state line is subject to cyclic shear stresses it has a tendency to contract (Schofield & Wroth 1968). If drainage is restricted, but not necessarily completely prevented, this tendency to contract causes pore water pressure to rise. This causes a reduction in effective stress which continues until the fracture surface is reached, as shown in Figure 2.3. At this point the frictional contacts between the soil grains are completely lost and the soil has met the proposed criteria for liquefaction (Hazen 1920). The pore pressure gradients and resulting transmission of pore fluid determines the ensuing behaviour of the soil. Hydraulic fracture, piping, channelling, boiling, fissuring, and fluidisation can occur (Schofield 1981).

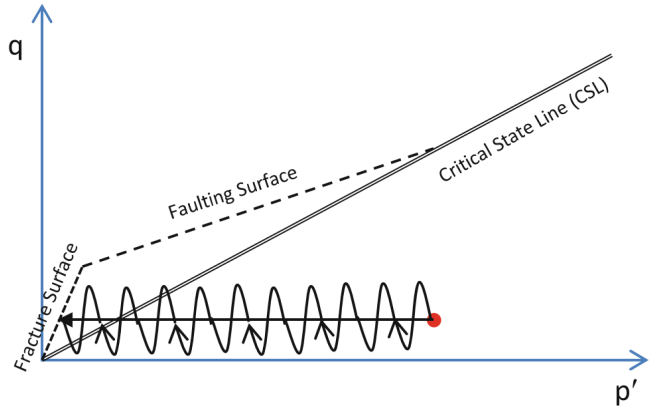

Fig. 2.3 Critical State framework for soil liquefaction, after Muhunthan & Schofield (2000) (Madabhushi & Haigh 2012).

Fissures and fractures occurring in the soil body as the effective stress approaches zero will increase the permeability of the soil by providing channels which allow fluid migration. A dramatic increase in permeability of saturated sand when the effective stress drops below 0.1 kPa has been observed in laboratory tests (Haigh et al. 2011). However, in these tests the near zero effective stress state was reached by fluidisation of a sand column using a large upward hydraulic gradient, not by cyclic shearing of the soil. There may, therefore, be dynamic effects which are present in earthquake induced liquefaction that this laboratory test does not replicate.

Observations from dynamic centrifuge tests imply that liquefaction is a partially drained event. Novel tests conducted by Adamidis & Madabhushi (2018*b*) restricted drainage during liquefaction for a section of loose sand in a level bed by enclosing it within a chamber. It was found that restricting drainage out of the enclosed chamber did not replicate the behaviour

outside in the remainder of the soil body. In addition, restricting drainage out did not result in an undrained response within the chamber, as localised fluid flow and void redistribution occurred as a consequence of bringing the boundaries enclosing the volume of soil closer together (Adamidis & Madabhushi 2018*b*).

Co-seismic liquefaction induced settlement corroborates the theory that liquefaction is a partially drained event. Results from an extensive number of dynamic centrifuge tests have observed liquefaction induced structure and free-field settlements to occur in the co-seismic period (Liu & Dobry 1997, Sasaki & Tamura 2004, Coelho et al. 2007, Dashti et al. 2010*a*, Mitrani & Madabhushi 2010, Chian 2012, Zeybek & Madabhushi 2016, Adamidis & Madabhushi 2018*a*). For this to be possible, drainage must occur in the co-seismic period to enable volumetric strains to be accumulated. For a period after shaking ceases but before excess pore pressures dissipate, soil remains in a near zero effective stress state. However, the rate of settlement is greatest in the co-seismic period and reduces to a much smaller value in the post-seismic period. This suggests that a near zero effective stress state is not a sufficient condition for rapid liquefaction induced settlements to occur. These data are particularly powerful as centrifuge modelling does not require prior assumptions about the drainage conditions.

Unfortunately, it is difficult to validate these observations using field measurements. This is primarily due to the spatial and temporal variability in earthquake occurrence, and also the lack of instrumented sites. The sparse co-seismic data available from borehole arrays consists of acceleration and pore pressure time histories, and is not accompanied by concurrent displacement measurements (Zeghal & Elgamal 1994, Yang & Sato 2000).

2.1.4 Definition of liquefaction

The proportion of an applied stress, σ, carried by the structure of soil particles, σ', can be calculated using Terzaghi's effective stress principle (Terzaghi 1943):

$$\sigma = \sigma' + u \tag{2.4}$$

where u is the pore pressure. This principle is reliant on the soil body being in equilibrium.

When loose, saturated, sandy soils are subjected to cyclic loading, the tendency to contract when sheared results in the generation of positive excess pore pressure (Hazen 1920). If this pore pressure cannot be dissipated at the rate which it is generated, a reduction in effective stress, σ', will ensue, which can result in a near-zero effective stress state (Seed & Lee 1966). Liquefaction has been defined as having occurred when the positive excess pore pressure, $u_{ex}(t)$, generated at a location becomes equal to the value of the vertical effective stress

before shaking began, σ'_{v0} (Seed & Lee 1966). This is commonly communicated using an excess pore pressure ratio, $r_u(t)$, defined as the ratio of the generated excess pore pressure divided by the initial vertical effective stress immediately before shaking commenced:

$$r_u(t) = \frac{u_{ex}(t)}{\sigma'_{v0}} \tag{2.5}$$

This ratio becomes equal to one when liquefaction occurs. The reduction in vertical effective stress associated with liquefaction results in a very large stiffness and strength degradation, rendering it an extremely problematic soil state.

For level, open ground the above definition for liquefaction is easy to apply. The total vertical stress can be readily calculated and the effective stress is only affected by a change in excess pore pressure. However, below a building foundation or surrounding a buried structure this definition of liquefaction is inadequate (Madabhushi & Haigh 2012). Redistribution of total stress in the soil can occur due to either co-seismic movement of the structure or due to changes in stiffness of the soil (Coelho et al. 2007). This is in addition to changes in effective stress due to generation of excess pore pressure. It is potentially erroneous to use the definition of liquefaction detailed in Equation 2.5 as the positive excess pore pressure being equal to the initial vertical effective stress does not necessarily equate to the current vertical effective stress becoming equal to zero. Madabhushi & Haigh (2012) argue that the definition for liquefaction should refer to the current effective stress, since this is what determines the mechanical behaviour of the soil. Unfortunately, soil-structure interaction makes it problematic to calculate the instantaneous effective stress. In practice, it is difficult to separate the change in vertical effective stress due to excess pore pressure generation from that due to the change in total stress. However, this can be achieved using finite element analysis.

2.1.5 Evaluation of susceptibility to liquefaction

It is desirable to assess the potential for earthquake induced liquefaction at a given site. The most commonly used methods are based on the semi-empirical "simplified procedure" established by Seed & Idriss (1971). Here the cyclic shear stress ratio (CSR) induced by an earthquake is compared to the capacity of the soil to resist liquefaction expressed as a cyclic resistance ratio (CRR).

The cyclic shear stress ratio, *CSR*, induced by earthquake shaking at a depth z below the ground surface can be estimated:

$$CSR = 0.65 \frac{a_{max}}{g} \frac{\sigma_{v0}}{\sigma'_{v0}} r_d \tag{2.6}$$

where a_{max} is the maximum horizontal acceleration at the ground surface, g is Earth's gravitational field, σ_{v0} and σ'_{v0} are the total and effective vertical stress at depth z respectively, and the parameter r_d is a stress reduction coefficient to account for flexibility in the soil column. The factor of 0.65 is used to convert the peak cyclic shear stress ratio to a cyclic stress ratio that is representative of the most significant cycles over the full duration of loading (Seed & Idriss 1971). The magnitude of an earthquake governs the number of significant cycles of loading, and consequently can be accounted for by applying a magnitude scaling factor to the CSR (Seed et al. 1983).

The cyclic strength and resulting capacity of soil to resist liquefaction is expressed as a cyclic resistance ratio, *CRR*, and can be determined using a number of methods, which involve either sample extraction and subsequent laboratory testing, or in situ testing. The recovery of high quality undisturbed samples and subsequent laboratory testing is the most reliable and accurate method to evaluate the cyclic strength of sand (Ishihara 1993). The CRR can be determined using cyclic triaxial or cyclic simple shear tests, but the values obtained are not equivalent given the different loading conditions imposed (Robertson & Wride 1998). Unfortunately, obtaining such samples of loose, cohesionless soil is generally uneconomical (Youd et al. 2001). Methods using in situ field tests provide a more simple and economical alternative to laboratory testing, and have therefore become the state-of-practice (SOP) (Youd et al. 2001). In situ tests such as the standard penetration test (SPT), cone penetration test (CPT), shear wave velocity measurement (V_s) and the Becker penetration test (BPT) can be used. The advantages and disadvantages of the most common of these field tests used to assess the liquefaction resistance of a site are summarised in Table 2.1. The repeatability and the continuous profile of results obtained from CPTs make it the preferred in situ test where possible (Robertson & Wride 1998).

The liquefaction potential of soil is highly dependent on a number of parameters. A plethora of correction factors has been developed to account for variables including earthquake magnitude (Seed et al. 1983), fines content (Robertson & Wride 1998), and high overburden stresses (Robertson & Wride 1998, Boulanger 2003). In addition, modifications intended to account for the effect of structures on both the CRR of the soil below and surrounding the structure and the induced CSR near a structure have been developed (Rollins & Seed 1990).

Table 2.1 Comparison of advantages and disadvantages of various field tests for assessment of liquefaction resistance, after Youd et al. (2001)

Feature	SPT	CPT	V_s
Past measurements at liquefaction sites	Abundant	Abundant	Limited
Type of stress-strain behaviour	Partially drained, large strain	Drained, large strain	Small strain
Quality control and repeatability	Poor to good	Very good	Good
Detection of variability of soil deposits	Good	Very good	Fair
Soil types in which test is recommended	Non gravel	Non gravel	All
Soil sample retrieved	Yes	No	No
Property measured	Index	Index	Engineering

Empirical charts for liquefaction analysis have been developed, which present field correlations between measurements obtained from in situ field tests in Table 2.1 and CSR values known to have caused liquefaction during past earthquakes (Seed et al. 1983, 1985, Robertson & Wride 1998). These graphs display limiting curves of CRR which separate regions of no liquefaction from those where liquefaction is expected to occur, as shown in Figure 2.4. It is standard practice to use these charts worldwide for liquefaction assessment of a site, including in the European design standard Eurocode 8 (CEN 2004). However, this simple approach can be misleading for multiple reasons. Firstly, this method considers each layer in isolation and does not consider the system response. Manifestation of liquefaction at sites in Christchurch, New Zealand, with practically identical critical layer characteristics was found to be dependent on the thickness and vertical continuity of the critical zones (Cubrinovski et al. 2018). The simplified procedure would have incorrectly characterised these sites as having the same susceptibility to liquefaction. Secondly, this binary approach is problematic as it implies that all sites which fall below the liquefaction line, in the "no liquefaction" zone in Figures 2.4(a,b), are not susceptible to any damage associated with behaviour related to liquefaction. Potential damage to infrastructure due to the generation of positive excess pore pressures, without a complete loss of vertical effective stress, is not accounted for.

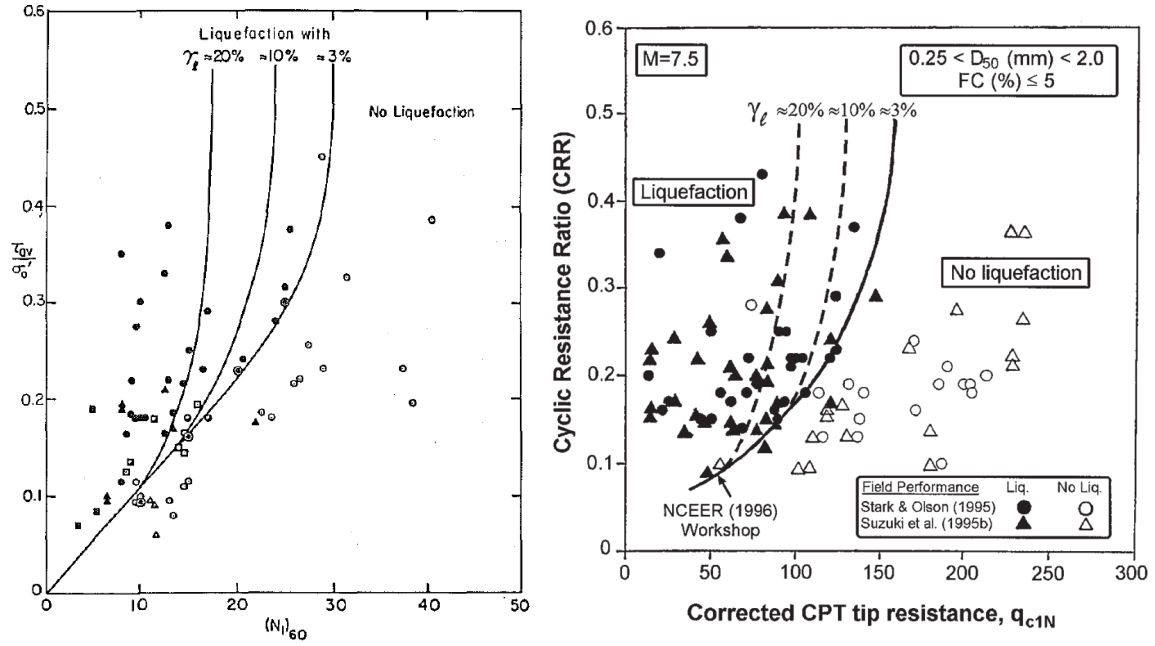

(a) (b)

Fig. 2.4 Empirical charts for liquefaction analysis (a) Relationship between cyclic stress ratio, N_1 values from SPT and limiting strains for natural deposits of clean sand (Seed et al. 1985) (with permission from ASCE), (b) Recommended cyclic resistance ratio for clean sands under level ground conditions based on CPT (Robertson & Wride 1998). γ_l is limiting shear strain.

2.2 Performance of structures with shallow foundations located on liquefied soil

Shallow foundations refer to systems of isolated pad footings and tie beams, foundation-beams and rafts, and are preferential over deep foundations (such as piles) for economical reasons if suitable ground conditions are present (Little 1961).

Damage caused by earthquake induced liquefaction of soil supporting structures with shallow foundations is a common occurrence. Liquefaction has caused significant building settlement and rotation in historic (Kishida 1966, Ohsaki 1966, Yoshimi & Tokimatsu 1977, Adachi et al. 1992, Tokimatsu et al. 1994, Hwang et al. 2003, Gazetas et al. 2004) and recent (Cubrinovski et al. 2011, Bertalot et al. 2013, Bray & Dashti 2014) earthquakes. Fortunately, very little liquefaction induced damage to buildings with shallow foundations on level ground results in catastrophic collapse (Hsu et al. 2002). However, demolition is often required due to structures being rendered unserviceable because of differential movement relative to neighbouring buildings and infrastructure (Hausler & Sitar 2001). In some cases, demolition

is needed due to pronounced structural distortion and cracking (Cubrinovski et al. 2011). To estimate the magnitude of liquefaction induced damage, and to develop methods to mitigate it, the mechanisms causing liquefaction induced building settlement and rotation of structures must be understood, and the building, soil and earthquake parameters affecting them must be ascertained. The recurrence of liquefaction induced damage to structures with shallow foundations suggests that there are gaps in the current understanding of these phenomena.

Dynamic centrifuge modelling and numerical simulations have been used to investigate this multifaceted problem and to understand the dominant mechanisms, which are summarised in Table 2.2 and Figure 2.5. The magnitude and rate of settlement of structures has been observed to be greater during the co-seismic period than in the post-seismic period (Liu & Dobry 1997, Sasaki & Tamura 2004, Coelho et al. 2007, Dashti et al. 2010*a*, Mitrani & Madabhushi 2010, Zeybek & Madabhushi 2016, Adamidis & Madabhushi 2018*a*). For this reason, co-seismic mechanisms are of most importance, and will therefore be considered first.

Generation of positive excess pore pressure, and the near zero vertical effective stress state that ensues, results in very large stiffness and strength degradation in the soil below and to the sides of a structure. This strength loss can result in partial bearing failure, which has been identified to be a cause of punching settlement of structures in the centrifuge (Dashti et al. 2010*b*, Adamidis & Madabhushi 2018*a*) and in the field (Cubrinovski et al. 2011). Cascone & Bouckovalas (1998) proposed that the reduction in bearing capacity could be modelled through the use of an equivalent critical state friction angle which was set to degrade with increasing excess pore pressure ratio. However, this is not a logical approach

Table 2.2 Primary mechanisms of ground and building displacement of structures with shallow foundations on level ground, after Dashti et al. (2010*b*)

Strains	Mechanisms of displacement	Location
Deviatoric	**Partial bearing failure** due to strength loss in the foundation soil **SSI-induced building ratcheting** due to cyclic loading of foundation	Under and adjacent to structures
Volumetric	**Localised volumetric strains** due to partial drainage **Sedimentation** after liquefaction **Consolidation** due to excess pore pressure dissipation	All locations
Other	Ground loss due to soil **ejecta**	All locations

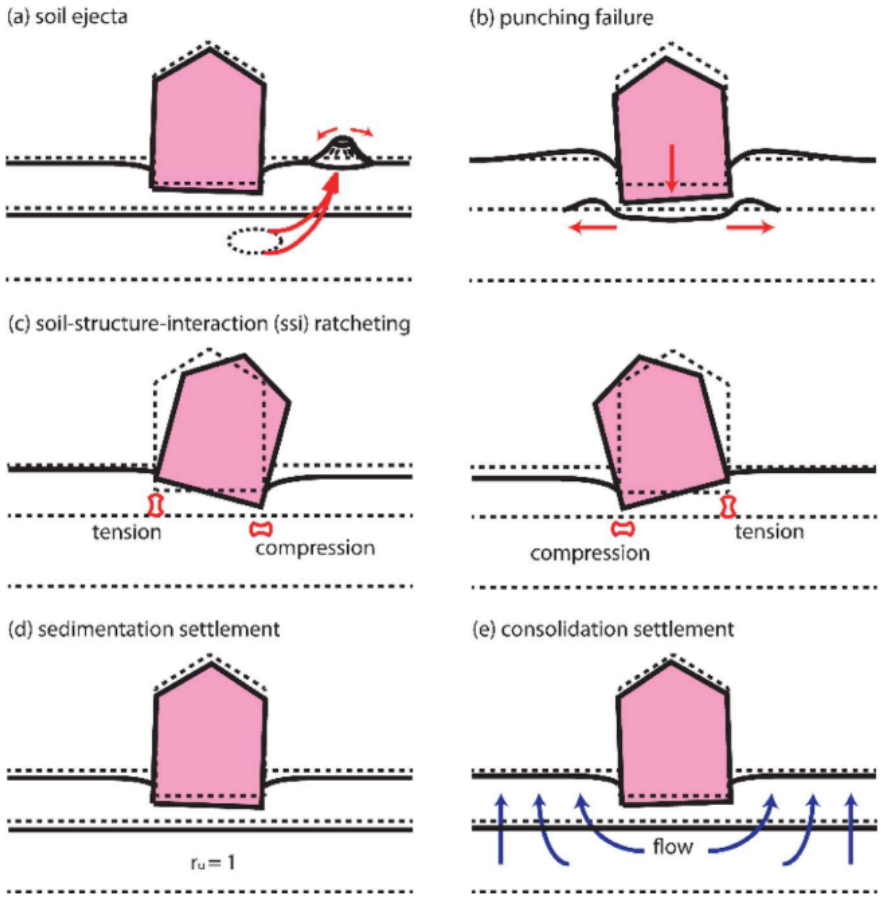

Fig. 2.5 Liquefaction induced building displacement mechanisms for structures with shallow foundations on level ground: (a) ground loss due to soil ejecta, (b) punching failure, (c) soil-structure-interaction (SSI) ratcheting, (d) sedimentation, (e) post liquefaction reconsolidation (Dashti & Bray 2013, Bray & Macedo 2017).

because the critical state friction angle is a material parameter which governs the mechanical behaviour of soil, and it does not change when excess pore pressures are generated.

Strength degradation is reduced when smaller positive excess pore pressures are generated relative to the initial vertical effective stress. This can be illustrated through the complex influence building weight has on settlement. If the foundation area is constant, an increase in building weight causes an increase in confining pressure below the structure. Soil under higher confinement requires larger cyclic shear strains to develop positive excess pore pressures (Yoshimi & Tokimatsu 1977, Dashti et al. 2010*b*, Zeybek & Madabhushi 2016). In addition, an increase in bearing pressure applied to shallow foundations increases the in-situ static shear stress around the edge of the foundation. This can prevent shear stress reversal and therefore inhibit pore pressure generation (Bertalot & Brennan 2015). Pore pressure generation can also

be inhibited by the tendency of soil to dilate when the ratio of shear stress to corresponding vertical effective stress is high (Bertalot & Brennan 2015). Consequently, heavier structures can settle less than lighter structures when the intensity and duration of shaking are not excessive (Yoshimi & Tokimatsu 1977, Zeybek & Madabhushi 2016). However, soil under higher confinement is capable of generating higher excess pore pressures for a given pore pressure ratio. Therefore, if the shaking is strong enough to overcome the higher cyclic resistance, heavier structures can settle more than lighter structures (Yoshimi & Tokimatsu 1977). This complex relationship between building weight and settlement is illustrated in field data of liquefaction induced settlement of structures with shallow foundations in the Niigata 1964, Luzon 1990, and Maule 2010 earthquakes. An increase in normalised settlement, defined as settlement/depth of liquefiable layer, was observed as bearing pressure increased from 20 kPa to 80 kPa followed by a decrease in normalised settlement as the bearing pressure increased from 80 kPa to 130 kPa (Bertalot et al. 2013). However, the suitability of the normalisation of these results with respect to depth of the liquefiable layer is questionable. Soil displacements obtained from digital image correlation during dynamic centrifuge testing of a plane strain model in a container with a transparent window has shown that the liquefaction induced failure mechanism beneath structures with shallow foundations is dependent on the depth of the liquefiable layer (Adamidis & Madabhushi 2018*a*).

When significant strength degradation occurs below a structure, settlement is worsened by soil-structure interaction induced building ratcheting. During this process, rocking of the structure causes the weakest underlying soil to be displaced laterally away from underneath the structure. Buildings with a high aspect ratio are more susceptible to settlement caused by ratcheting due to high dynamic overturning moments (Dashti et al. 2010*b*). In addition, the ease in which soil can be pushed laterally increases as the foundation width decreases, thereby increasing settlement caused by ratcheting.

The partially drained behaviour of soil during earthquake induced liquefaction can be captured in the centrifuge. Changes in soil permeability and development of heterogeneity caused when saturated soil approaches zero effective stress can be replicated (Schofield 1981), which has enabled displacement due to localised volumetric strains caused by partial drainage to be identified. The magnitude of these displacements are highly dependent on the hydraulic conductivity of the soil (Dashti et al. 2010*b*), which dramatically increases as effective stress decreases (Haigh et al. 2011). Reducing co-seismic hydraulic conductivity will reduce co-seismic volumetric strains due to partial drainage, however it will have the negative impact of increasing the magnitude and duration of elevated excess pore pressures in the soil (Brennan & Madabhushi 2002, Dashti et al. 2010*b*).

All of the co-seismic mechanisms of liquefaction induced building displacement identified in this section are intensified through increasing the seismic demand, which is achieved by increasing either the intensity or duration of the ground shaking (Dashti et al. 2010*b*, Mitrani & Madabhushi 2010, Karimi et al. 2018). These factors are encapsulated in the Arias intensity, I_a, which represents the energy of the ground motion (Arias 1970):

$$I_a(T) = \frac{\pi}{2g} \int_0^T a^2(t)dt \tag{2.7}$$

where a is the measured acceleration. The Arias intensity depends on the intensity, frequency content and duration of an earthquake. The rate roughly represents the rate of intensity build up. This explains the observation from centrifuge tests that the liquefaction induced settlement-time history of structures with shallow foundations follow the shape of the Arias intensity-time history for the earthquake motion (Dashti et al. 2010*a*, Adamidis & Madabhushi 2018*a*). Consequently, Dashti et al. (2010*a*) proposed a new measure of intensity called the shaking intensity rate, *SIR*:

$$SIR = \frac{I_{a5-75}}{t_{5-75}} \tag{2.8}$$

where I_{a5-75} is the change in Arias intensity from 5 to 75 % of its total value (equal to 0.7 I_a) and t_{5-75} is the corresponding time duration. SIR is the average rate of Arias intensity build up in this period. They argue that it captures the rate of soil particle disturbance, excess pore water pressure generation and seismic demand on structures, and therefore should correlate with the initiation, rate and amount of liquefaction induced settlement.

Liquefaction induced settlement can continue once shaking has ceased, albeit at a slower rate. Once earthquake shaking has ended, positive excess pore pressures gradually dissipate (Liu & Dobry 1997). Frictional contacts between soil grains are regained and settlement due to sedimentation occurs. Post sedimentation, whilst excess pore water pressures are continuing to dissipate, the increase in effective stress in the soil causes settlement due to consolidation. Dashti et al. (2010*b*) found post-seismic settlement due to consolidation to be independent of the rate of pore pressure dissipation, and to only be influenced by the net value of excess pore pressures at the end of cyclic loading and the soil compressibility. However, soil compressibility decreases as effective stress increases (Haigh et al. 2011), so it should be expected that settlement due to consolidation is in fact affected by the rate of pore pressure dissipation. Scaling the pore fluid viscosity to be only half of that of water at 1 g may have masked this effect in the centrifuge tests conducted by Dashti et al. (2010*b*). This

inconsistent scaling of viscosity compared to other scaled parameters will have resulted in a greater rate of excess pore pressure dissipation than would be expected in the field.

2.2.1 Estimating liquefaction induced settlement of structures

It is desirable to have methods available which practitioners can use to estimate liquefaction induced settlement. A number of widely used procedures exist for evaluating liquefaction induced settlements in the free-field by estimating post liquefaction volumetric strain. Tokimatsu & Seed (1987) estimated the volumetric strain expected for saturated sand deposits from the CSR and SPT N-count. Ishihara & Yoshimine (1992) produced graphs to estimate the post liquefaction volumetric strain for each layer of a sand deposit, given the factor of safety against liquefaction and the relative density of each layer. Zhang et al. (2002) correlated post liquefaction volumetric strain to equivalent clean sand normalised CPT tip resistance. Using any of these methods, the liquefaction induced settlement of the ground surface can then be calculated by integrating the volumetric changes throughout the depth. However, their suitability for calculating free-field settlements is questionable as they are founded on the inappropriate assumption that liquefaction is an undrained event, as discussed in Section 2.1.3. Furthermore, these methods are clearly not suitable for estimating liquefaction induced building settlements as they neglect displacements due to deviatoric strains caused by soil-structure interaction. Despite this, they are commonly used for this purpose (Dashti & Bray 2013).

Post earthquake field observations and model test results have been combined to develop charts to predict liquefaction induced settlement of structures with shallow foundations. Field observations from the Niigata 1964 earthquake and a number of 1 g model tests showed that, for a given liquefiable layer thickness, settlement decreased as the width of the building increased, and was independent of the number of stories (Yoshimi & Tokimatsu 1977). This data set was supplemented with centrifuge test results (Liu & Dobry 1997) and field observations from the 1990 Luzon earthquake (Adachi et al. 1992), and was then used to create a design chart to determine foundation settlement given the building width and depth of liquefiable soil (Liu & Dobry 1997). It has since been populated further with data from subsequent earthquakes and centrifuge tests by other researchers (Acacio et al. 2001, Bertalot et al. 2013). This design chart normalises building width and settlement with the thickness of the liquefiable layer. However, recent research shows that, whilst this method may work well in the presence of a sufficiently thick liquefiable layer, it may be misleading for thinner layers (Dashti et al. 2010*b*, Dashti & Bray 2013, Adamidis & Madabhushi 2018*a*).

Progress is being made; recently, a number of new methods have been proposed to predict the settlement of structures with shallow foundations on liquefiable soil during earthquakes.

A "simplified procedure" was presented by Bray & Macedo (2017), whereby displacement due to shear strains, volumetric strains, and ejecta are each calculated independently and then summed. Displacement due to shear strains are estimated using a complex equation developed from regression analysis of results obtained from non-linear, dynamic soil-structure interaction, effective stress analysis. Displacement due to volumetric strains are calculated using pre-existing empirical procedures developed for free-field ground deformation by Zhang et al. (2002). Ejecta-induced displacement are estimated based on observations from case histories. This "simplified procedure" emphasises the complexity of estimating liquefaction induced settlement of structures, as it is lengthy and it states in its requirements that a significant amount of "engineering judgement" is still needed (Bray & Macedo 2017). An alternative procedure, based on a semi-empirical, probabilistic model, has been proposed by Bullock et al. (2019). A vast numerical database of over 63000 virtual cases of building settlement were calculated using 3D, non-linear, effective stress analyses, which were subsequently validated with centrifuge data and adjusted using case history data to obtain an equation to predict the median expected settlement of a structure. Although insightful, this method is highly dependent on a numerical model which is unable to accurately model volumetric strains caused by liquefaction (Karimi & Dashti 2016).

An alternative approach is to investigate only the behaviour of a specific building of interest using numerical simulations. This is recommended for critical projects (Dashti & Bray 2013). However, it is difficult to accurately model the response of the soil and the soil-structure interaction during earthquake induced liquefaction given the very low vertical effective stresses that develop, and the large displacements that can occur. In addition, displacement due to ejecta cannot be captured by continuum based analyses. To enable numerical models to be used with confidence, they should be calibrated with centrifuge test data which correctly model the conditions of interest. Unfortunately this type of comparison is only valid for one input motion due to the sensitivity of the response to changes in seismic demand, which were discussed previously.

2.3 Performance of underground structures located in liquefied soil

Underground structures are commonplace across the world, particularly in densely populated urban centres where space is at a premium (Kawashima 1999). They include utility and pipeline distribution systems, storage containers, transportation networks, and residential and

commercial building space. Consequently, subsurface buildings and infrastructure are vital to everyday life.

Earthquake induced liquefaction of soil surrounding underground structures and infrastructure has caused significant structure displacement in both historic (Ohsaki 1966) and recent (Towhata 2008, Bhattacharya et al. 2011, Chian & Tokimatsu 2011, Tokimatsu et al. 2012, Wilkinson et al. 2012) earthquakes. Damage of this nature is primarily due to the floatation of light underground structures when the surrounding soil liquefies (Koseki et al. 1997).

Floatation of an underground structure located below the water table can be investigated by considering the vertical forces acting on it, These vertical forces are shown in Table 2.3, for both static conditions and the case when the surrounding soil liquefies. In static conditions, the weight of the structure and overlying soil, combined with the force due to shearing within the soil, are designed to be greater than the upward buoyancy force due to hydrostatic water conditions, which prevents uplift of the structure. When liquefaction occurs, the net vertical force acting on the same underground structure can become upward. The uplift force acting on the structure increases to greater than the hydrostatic value due to the generation of positive excess pore pressures. In addition, the shear resistance of the soil reduces significantly, to the extent that the shear resistance along the soil structure interface can be assumed to become negligible (Koseki et al. 1997). Zhang & Chian (2019) argue against this assumption, claiming that centrifuge test data showed that an increase in side wall friction resulted in an increase in resistance to liquefaction induced uplift of a buried structure. However, this effect was predominately due to one third of the soil-structure interface being above the water table. The increase in resistance is therefore likely to be due to the increase in shear resistance along the soil-structure interface in the dry layer above the water table, not within the liquefied layer of soil. When the net vertical force acting on an underground structure becomes upward, floatation is initiated (Koseki et al. 1997, Kang 2010, Chian et al. 2014, Zhang & Chian 2019). The subsequent rate and magnitude of uplift are dependent on soil-structure interaction.

Table 2.3 Vertical forces acting on an underground structure, for both static conditions and the case when the surrounding soil liquefies, after Chian & Madabhushi (2012)

Force	Static	Liquefied	Direction
Buoyancy force	✓	✓	↑
Weight of structure	✓	✓	↓
Weight of overlying soil	✓	✓	↓
Force due to shearing within soil	✓	×	↓
Excess pore pressure	×	✓	↑
Upward flow of fluid	×	✓	↑

Uplift of an underground structure will cause displacement of the surrounding liquefied soil. As an underground structure begins to float upward, any overlying soil is pushed aside by the uplifting structure (Chian et al. 2014, Madabhushi & Madabhushi 2015). A cavity can form beneath an uplifting structure (Koseki et al. 1997, Yang et al. 2004, Chian et al. 2014). Liquefied soil adjacent to the cavity laterally deforms towards and into this expanding void, and can cause further uplift of the structure (Koseki et al. 1997, Sasaki & Tamura 2004, Yang et al. 2004, Chian et al. 2014). Uplift accumulated through this mechanism can be reduced by increasing the width of the underground structure, as this reduces the ease in which liquefied soil can move towards the void by increasing the distance it must be displaced (Sasaki & Tamura 2004). An additional negative consequence of the lateral soil deformation towards and into this void is that it can increase the settlement of the ground surface adjacent to the structure.

Soil-structure interaction beneath the uplifting underground structure can affect the instantaneous rate of floatation. As the structure uplifts, the soil beneath it experiences negative excess pore pressures or suctions superposed onto the positive excess pore pressure, due to volumetric dilation (Chian & Madabhushi 2012, Madabhushi & Madabhushi 2015). If the stratigraphy of the soil around the underground structure allows partial drainage to occur, an increase in structure uplift can ensue due to movement of pore fluid toward the structure (Koseki et al. 1997). If movement of pore fluid is not possible, the rate of uplift can reduce due to a smaller upward force generated by excess pore pressures below the structure (Madabhushi & Madabhushi 2015). The uplift forces due to excess pore pressure generation and the upward flow of fluid can both also be affected by the permeability of any fill material immediately surrounding an underground structure relative to the adjacent native ground, as this determines the direction and speed of excess pore pressure dissipation (Yasuda & Kiku 2006).

Examination of the vertical forces acting on an underground structure suggests that uplift can be reduced by increasing the downward acting vertical forces. Increasing the weight of the overlying soil by increasing the burial depth can reduce liquefaction induced uplift for cases where the failure mechanism interacts with the ground surface (Chian & Madabhushi 2012, Chian et al. 2014). Unfortunately, increasing the depth of underground structures increases construction costs, therefore this approach is not widely adopted.

In addition, it is possible for post-seismic settlement of subsurface structures to occur. These can be a result of sedimentation and consolidation during excess pore pressure dissipation (Koseki et al. 1997). However, they are of lesser importance than the co-seismic mechanisms, as centrifuge test data have shown that the magnitude and rate of displacement

of underground structures are greater during the co-seismic period than in the post-seismic period (Yang et al. 2004, Chian et al. 2014).

2.3.1 Estimating liquefaction induced uplift of underground structures

It is desirable to have methods available which practitioners can use to estimate liquefaction induced uplift of underground structures. Following on from using the net vertical force to determine when uplift is initiated, one approach is to calculate the maximum uplift of an underground structure to be the point where vertical force equilibrium is regained (Kang 2010). However, this is a highly conservative approach and may provide an unrealistically large estimate of displacement, as earthquake loading may cease and uplift may stop before it is reached (Chian et al. 2014).

A different approach is to determine the uplift displacement of an underground structure from the equation of motion in the vertical direction. For highly instrumented cases, such as dynamic centrifuge tests, the time histories of the vertical forces listed in Table 2.3 can be considered, and displacement can be calculated by double integration of the net acceleration (Chian 2012). This is effectively applying the Newmark sliding block method to tunnel uplift (Newmark 1965). Alternatively, the uplift displacement can be determined by assuming that the soil behaves as a viscous fluid and the resistance force against uplift is proportional to uplift velocity (Sasaki & Tamura 2004). There is significant variability in the uplift calculated using this method, primarily due to the variation in the values for the viscosity of liquefied soil (Hwang et al. 2006). In addition, liquefied soil can dilate when sheared and cause a transient increase in resistance which will reduce uplift. This behaviour is not captured in a method which assumes liquefied soil to behave as a viscous fluid.

Numerical simulations can be used to estimate liquefaction induced uplift of underground structures for critical infrastructure projects. For example, numerical simulations were used to assess both the George Massey Tunnel (Yang et al. 2004) and the Bay Area Rapid Transit (BART) Offshore Transbay Tube (Chou et al. 2010) to establish whether ground improvement was required to reduce the occurrence and effect of liquefaction induced uplift on these important transportation tunnels.

2.4 Performance of buildings with basements located in liquefied soil

There is an increasing tendency for buildings to have basements. Urban centres are becoming densely populated and land prices are rising, making it desirable to use underground space

for parking and storage. In comparison to structures on shallow foundations and underground structures, there is sparse information on the effect of earthquake induced liquefaction on structure with basements.

Post earthquake reconnaissance missions following large earthquake events have provided some reports on the performance of structures with basements. Correlation of building width with average liquefaction induced settlement during the Niigata 1964 earthquake by Yoshimi & Tokimatsu (1977) included 4 buildings with basements without piles and 14 structures with a shallow foundation. From this data, it is evident that the structures with basements experienced comparable, if not slightly less, settlement than similar structures without basements which were normalised by number of storeys, and therefore assumed bearing pressure. Nothing was stated about the residual rotation of these structures. After the Chi-Chi 1999 earthquake it was observed that buildings with basements suffered less liquefaction induced settlement and rotation than those without basements (Hsu et al. 2002). For cases where the plan area of a basement did not match the plan area of the superstructure above, as expected from moment equilibrium, rotation occurred in the direction of the centre of gravity of the superstructure and away from the centre of buoyancy of the basement (Hsu et al. 2002, Tanaka 2003). More recently, differential displacement was observed across structures with basements as a consequence of liquefaction during the 2010-2011 series of earthquakes in Christchurch, New Zealand (Cubrinovski et al. 2011, Bray & Luque 2017). The basement storeys and the buildings above them behaved rigidly and as a result negligible distortion and minimal damage was noted (Cubrinovski et al. 2011). An observation worth noting was the failure of shear connections within a basement floor slab which were expected to be able to sustain 1.4 times the hydrostatic uplift force (Luxford 2014). This indicates that the pressure beneath a basement slab when soil liquefies is consistent with the liquefied soil behaving as a dense fluid.

Little research has investigated the co-seismic soil-structure interaction of structures with basements located in liquefiable soil. Rollins & Seed (1990) stated that the induced cyclic shear stress ratio (CSR) near a structure with a basement will depend on the extent to which the excavation for the basement floors compensate for the structure load. For a small number of cases studied, 3D finite-difference-based analyses by Unutmaz (2018) found the presence of a basement to reduce the CSR and therefore reduce the possibility of liquefaction. This is surprising as the presence of a basement reduces the vertical effective stress in the soil beneath it, thereby increasing susceptibility of contractive soils to liquefaction (Seed & Lee 1966).

One known series of physical model tests has been undertaken to investigate the effect of basements on liquefaction induced building settlement. Liu et al. (2014) conducted five 1 g

shaking table tests which found that the presence of a basement storey reduced the settlement of residential buildings. Although insightful, the research presented was brief and does not constitute a detailed investigation into the problem. Neither the co-seismic structure stability nor soil-structure interaction was assessed. In addition, realistic stress levels were not replicated as the investigation only consisted of a small number of model tests conducted at 1 g. There may, therefore, be important effects affecting the settlement of structures with basements which were not captured in these tests.

2.5 Liquefaction hazard mitigation methods

There are currently a number of methods used to reduce or remove the risk of earthquake induced liquefaction and the associated damage to surface and underground structures.

One of the most common methods used to reduce liquefaction induced damage is to modify the soil to prevent liquefaction from occurring (Hausler & Sitar 2001). This can be achieved by increasing the relative density of the sand, reducing the degree of saturation, or limiting the excess pore pressure ratio to acceptable levels.

The relative density of a sand layer can be increased using vibrocompaction. An increase in density increases the resistance to seismically induced pore pressure generation and strength loss. Following densification, if the sand remains on the loose or "wet" side of critical state, there will be a smaller void space available for volumetric compaction. If, however, the sand is now on the dense or "dry" side of critical state it will be dilative when sheared, which will cause a reduction in pore pressure and increase in effective stress in the soil. Consequently, an increase in density results in smaller volumetric strains which result in a reduction in structure displacement (Liu & Dobry 1997, Yang et al. 2004, Mitrani & Madabhushi 2010, Olarte, Dashti & Liel 2018). A consideration regarding the practicality of soil improvement is the volume of soil that must be improved (Coelho et al. 2007), both in terms of lateral extent of improvement next to the structure and the depth of improvement below.

The degree of saturation of a soil layer can be reduced using trenches or wells to lower the ground water table (Towhata 2008) or through air-injection into the soil layer (Okamura et al. 2011, Zeybek & Madabhushi 2016). Liquefaction resistance increases significantly with a decrease in the degree of saturation because of a reduction in the positive excess pore pressures generated during shaking (Yoshimi et al. 1989, Okamura et al. 2011, Zeybek & Madabhushi 2016). Consequently, liquefaction induced settlements are reduced when the degree of saturation is reduced, particularly for structures exerting a high bearing pressure (Zeybek & Madabhushi 2016).

Vertical prefabricated drains or stone columns can be installed in a liquefiable layer surrounding a structure. The greater hydraulic conductivity of the columns compared to the surrounding soil provides a preferential drainage path for pore fluid, thereby increasing the rate of dissipation of excess pore pressure (Brennan & Madabhushi 2002, Paramasivam et al. 2017, Kirkwood & Dashti 2019). Consequently, the inclusion of drains can reduce structure displacement (Paramasivam et al. 2017, Kirkwood & Dashti 2019).

Although possible through the methods detailed above, the prevention of soil liquefaction is not wholly beneficial. The substantial degradation of stiffness associated with soil liquefaction results in attenuation of the ground motion acceleration transferred to the structure which reduces the seismic demand of the structure (Liu & Dobry 1997). All three methods presented which modify the soil to prevent liquefaction from occurring have the undesirable effect of increasing the seismic demand of the structure (Liu & Dobry 1997, Mitrani & Madabhushi 2010, Zeybek & Madabhushi 2016, Olarte, Dashti & Liel 2018, Paramasivam et al. 2018).

An alternative approach to reducing liquefaction induced damage to structures is by using containment walls to restrict co-seismic strains. Stiff, impermeable, in-ground structural walls that extend below the bottom of the liquefiable layer significantly reduce the settlement of structures with shallow foundations (Yoshimi & Tokimatsu 1977, Mitrani 2006, Dashti et al. 2010*a*). This is achieved by minimising both volumetric and deviatoric strains beneath the structure, and also by transferring the load of the structure to stiffer stratum beneath the liquefiable layer. However, this may not be practical in locations where deep layers of liquefiable soil are present. The reduction in settlement decreases for cases where the containment walls do not extend below the liquefiable layer, particularly for events where shaking is sufficiently strong to cause liquefaction to occur below the bottom of the containment walls (Mitrani & Madabhushi 2010). A similar approach, using impermeable walls which were flexible was found to have minimal effect on structure settlement, even when they extended below the depth of the liquefiable layer (Dashti et al. 2010*a*). Restricting drainage reduced volumetric strains, but is likely to have amplified pore pressure generation and strength loss locally. Comparable methods using vertical containment walls have also proved successful in reducing the uplift of underground structures (Isoda et al. 2001).

Unfortunately, the implementation of mitigation methods on a single structure have been found to have severe consequences on the performance of nearby unmitigated structures (Kirkwood & Dashti 2018, 2019). The overlap of stress fields beneath adjacent structures can cause non-symmetric volumetric and deviatoric strains below the foundations, which can increase permanent rotation and differential settlement. Consequently, once mitigation methods have been developed which can successfully reduce liquefaction induced damage to

single, isolated structures, the approach should be extended to consider groups of adjacent structures, particularly in dense urban environments. However, this holistic approach is only possible when the details regarding the design and implementation of mitigation methods for isolated buildings are fully understood.

2.6 Summary

Earthquake induced liquefaction has caused significant damage in historic and recent earthquakes, particularly in the built environment. A need there remains to better understand the phenomenon of liquefaction with a view to mitigating damage to infrastructure.

Liquefaction induced displacement and rotation of structures is a multifaceted problem. Progress has been made to understand the dominant co-seismic and post-seismic mechanisms affecting the behaviour of both structures with shallow foundations and underground structures. However, a simplified method to predict displacement and rotation remains elusive as the mechanisms are highly dependent on a number of interdependent parameters.

The behaviour of structures partially buried in liquefiable ground, which is the case for many modern buildings with basements, is not well understood. This is concerning as there is an increasing tendency for buildings to have basements. Urban centres are becoming densely populated and land prices are rising, making it desirable to use underground space for parking and storage.

A number of mitigation methods are currently available which can reduce the liquefaction induced displacement and rotation of structures. However, methods which prevent the soil from liquefying are not wholly beneficial as they can result in increasing the seismic demand of the structure. There is a need to develop cost effective mitigation methods which reduce structural displacement and rotation whilst not increasing structure accelerations.

This research project addressed these gaps in knowledge, and investigates the co-seismic behaviour of structures with basements in liquefiable soil. Specifically, it investigates whether basement storeys can be used to reduce liquefaction induced settlement of structures by providing an uplift force during the liquefied period. The increase in habitable space that a basement provides in a property is anticipated to make this mitigation method an attractive option.

Chapter 3

Methodology

3.1 Introduction

Dynamic centrifuge modelling was the primary experimental method used in this research project. In this chapter the principles of this technique are discussed, the equipment used is presented, and the methodology that was followed is detailed.

3.2 Centrifuge modelling

Centrifuge modelling in geotechnics is the practice of subjecting a small physical model to an increased gravitational field by rotating it at a constant angular speed. When a 1:N scale model is subjected to an acceleration of $N \times g$, stresses and strains in the model are the same as those at homologous points of the prototype which it is modelling. Geotechnical centrifuge modelling therefore enables the correct stress-strain behaviour experienced in the field to be replicated, which in turn enables realistic failure mechanisms to develop. This is an extremely powerful method for investigating problems in geotechnical engineering because of the non-linear stress-strain relationship of soil. No prior assumptions about failure mechanisms, drainage conditions or soil-structure interaction (SSI) effects are required.

Scaling laws are used to relate the behaviour of the small-scale model in the centrifuge to that of the prototype, and consequently the behaviour of the full size structure in the field. Table 3.1 summarises a number of scaling laws that are applicable to this research project (Schofield 1980, 1981).

Table 3.1 Summary of centrifuge scaling laws, after Schofield (1980, 1981)

	Parameter	Scaling law $\frac{model}{prototype}$
General scaling laws	Length	1/N
	Mass	$1/N^3$
	Force	$1/N^2$
	Seepage velocity	N
	Time (consolidation)	$1/N^2$
	Stress	1
	Strain	1
Dynamic events	Time (dynamic)	1/N
	Frequency	N
	Velocity	1
	Acceleration/acceleration due to gravity (g)	N

3.3 Dynamic centrifuge modelling

Dynamic centrifuge modelling involves subjecting a small-scale model to lateral cyclic loading whilst in the centrifuge. This can be used to replicate earthquake induced shaking. A 1:N scale model subjected to a centrifugal acceleration of $N \times g$ which is then subjected to a cyclic lateral acceleration of $N \times a$ will experience the same behaviour as a prototype model subject to a horizontal acceleration of a (Schofield 1981).

Dynamic centrifuge modelling can be used to accurately model liquefaction problems (Madabhushi 2015). The changes in soil permeability and development of heterogeneity caused when saturated soil approaches zero effective stress can be replicated in centrifuge tests (Schofield 1981), and thus no prior assumptions about the drainage conditions (undrained or partially drained) are required. In addition, dynamic centrifuge modelling is an effective method to investigate and quantify dynamic SSI effects, which can be problematic and time consuming to investigate using numerical methods.

3.4 Centrifuge modelling at the University of Cambridge

The centrifuge model tests discussed in this thesis were conducted at the Schofield Centre at the University of Cambridge. The following sections detail the equipment used.

3.4.1 Turner beam centrifuge

The tests were conducted using the 10 m diameter Turner beam centrifuge, shown in Figure 3.1. This centrifuge is a 150 g-ton balanced beam centrifuge with swing platforms at either end - a model is placed at one end and a counterweight at the other end of the arm. The base of the model and counterweight are located at a radius of 4.125 m. Further details on the specification and operation of this centrifuge are given by Schofield (1980).

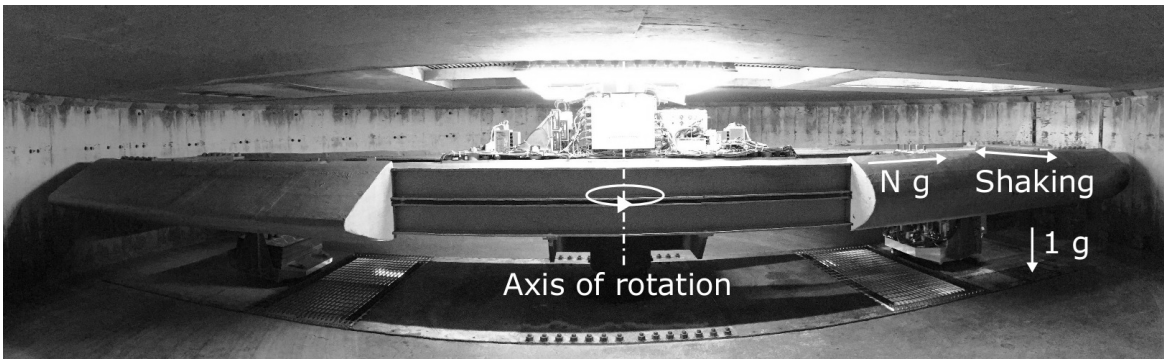

Fig. 3.1 Turner beam centrifuge, showing the direction of accelerations acting on a model during a dynamic centrifuge test. Photo taken when centrifuge was stationary, therefore test package and counterweight have not swung-up into position.

3.4.2 Earthquake actuators

An earthquake actuator was used to generate one-dimensional input motions, perpendicular to both the centrifugal acceleration, N g, and Earth's gravitational field, 1 g, as shown in Figure 3.1. Two different earthquake actuators were used during this research project. Their capabilities are summarised in Table 3.2 and discussed further in the sections below.

SAM earthquake actuator

The Stored Angular Momentum (SAM) earthquake actuator was used for the first four tests discussed in this thesis. It is capable of creating pseudo-harmonic motions with a predefined frequency, amplitude, and number of cycles. It is not able to generate small amplitude earthquakes. In the SAM earthquake actuator, the energy required for an earthquake is stored in a set of flywheels which are rotated by a simple three-phase motor. The flywheels turn a reciprocating rod through a cross-head. A fast acting hydraulic clutch is used to connect the reciprocating rod to a lever to laterally move the shaking table. Further details about the SAM are given by Madabhushi et al. (1998).

Servo-hydraulic earthquake actuator

The servo-hydraulic earthquake actuator was used for all the other tests discussed in this thesis. It is capable of generating sinusoidal and realistic earthquake input motions, and is able to reproduce very small amplitude earthquakes. In the servo-hydraulic earthquake actuator, the energy required for an earthquake is stored in hydraulic oil that is pressurised to 280 bar in four accumulators. The firing process for an earthquake opens the manifold between the accumulators and a servo-value, through which the high pressure oil then flows. This oscillates a double acting actuator which is rigidly connected to the shaking table. Further details about the servo-hydraulic earthquake actuator are given by Madabhushi et al. (2012).

Table 3.2 Capabilities of earthquake actuators, after Madabhushi et al. (1998, 2012)

Scale	Property	Unit	SAM	Servo-hydraulic
Model	Max operational centrifuge level	g	100	80
	Useful frequency range	Hz	0 - 150	20 - 150
	Maximum shaking acceleration	g	20	25
	Wave form		Sinusoidal	Any
Prototype at 60 g	Useful frequency range	Hz	0.17 - 0.83	0.33 - 2.5
	Maximum shaking acceleration	g	0.33	0.42
	Wave form		Sinusoidal	Any

Availability of earthquake actuators

Ideally, the servo-hydraulic earthquake actuator would have been used for all centrifuge tests. However, essential maintenance work meant that it was not available until part way through this research project. Time constraints meant that the start of the testing schedule could not be postponed, so the SAM earthquake actuator was used for the initial four tests discussed in this thesis. Consequently, very small amplitude earthquakes and realistic earthquake input motions were not possible for these four centrifuge tests.

3.4.3 Model container

Two types of model container were used during this research project.

Laminar container

The laminar container consists of 20 stacked, light, rectangular aluminium frames with stainless steel roller bearings between each frame. Details on the design of this container are

discussed by Brennan et al. (2006). Its most important feature is that the frames are able to roll across one another in the direction of shaking which means they effectively contribute no stiffness and minimal mass to the system. This is the model container best suited to liquefaction problems as it is able to simulate a soil layer of zero stiffness. An internal latex bag is used to make the container watertight.

Window container

The window container is a rigid container with a transparent polymethyl methacrylate (PMMA) window which allows digital image correlation to be conducted. Plane strain conditions are replicated when using this container to ensure that the visible cross section is characteristic of the model being tested. A layer of Duxseal is used at both ends of the container to limit the effect of the rigid boundaries (Steedman & Madabhushi 1991). Absorbing boundaries such as Duxseal layers are only partially effective, particularly when soil loses stiffness during liquefaction events.

It was important for this research to have a transparent sided model container in order to perform digital image correlation. Novel insight into the co-seismic soil-structure interaction and how displacement and rotation of the structures developed could be obtained by monitoring the cross-section of the model against the window. These benefits were felt to outweigh the limitations with respect to the boundary conditions compared to the laminar container.

3.4.4 Hostun sand

All the centrifuge tests were conducted using Hostun HN31 sand. This sand is commonly used in geotechnical laboratories, therefore its characteristic properties have been investigated by numerous researchers. Gay et al. (2003) and Heron (2013) reported $\phi_{crit} = 35^\circ$, which is comparable to the typical values of $\phi_{crit} = 33^\circ \pm 1^\circ$ or 2° for quartz sands (Bolton 1986). The properties of Hostun HN31 sand used in this thesis are given in Table 3.3.

Table 3.3 Properties of Hostun HN31 sand

Property	Symbol	Value	Reference
Average particle size (mm)	d_{50}	0.356	Silva (2018)
Minimum void ratio	e_{min}	0.555	Heron (2013)
Maximum void ratio	e_{max}	1.010	Heron (2013)
Critical state friction angle ($^\circ$)	ϕ_{crit}	35	Heron (2013), Silva (2018)
Specific gravity	G_s	2.65	

Figure 3.2 shows the particle size distribution curve for Hostun sand (Silva 2018) alongside the set of curves proposed by Tsuchida (1970) to identify soils which are susceptible to liquefaction based on grain-size. The particle size distribution of Hostun sand falls within the range of "most liquefiable soil", and is therefore considered to be highly liquefiable when present in a loose state.

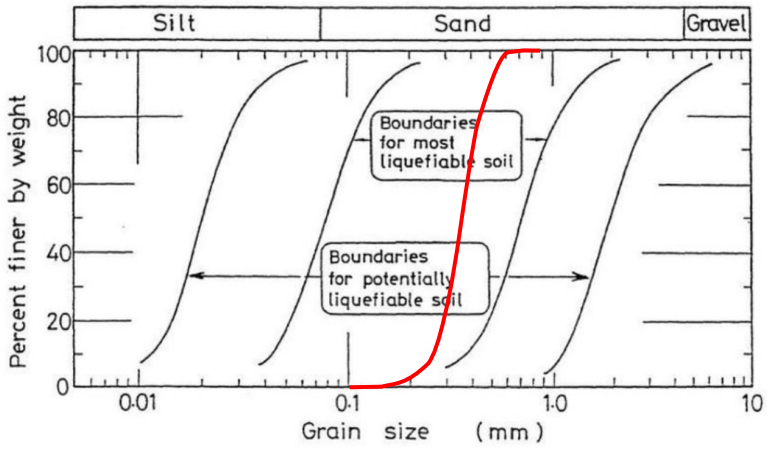

Fig. 3.2 Particle size distribution curve for Hostun sand shown in red, after Silva (2018), alongside grain size boundaries for liquefiable soil (Tsuchida 1970).

3.4.5 Pore fluid

The pore fluid used was a high viscosity aqueous solution of hydroxypropyl methylcellulose with a target viscosity of N cSt. A viscous pore fluid was required in order to overcome the inconsistency between the scaling laws of dynamic and seepage time in centrifuge modelling (Schofield 1981).

3.4.6 Instrumentation

Arrays of miniature instruments were placed at discrete locations in the soil and on the structure. The instruments were placed at locations anticipated to give insight into the seismic response of the soil, structure, and the soil-structure interaction. Columns of instrumentation were placed at the same depths in both the far-field and underneath the centre of each structure, and additional instruments were placed close to the basements of the structures. The location of where each instrument was placed during the preparation of the model was measured to $\pm$ 0.5 mm accuracy. Instrument calibration was conducted both before and after each centrifuge test, and is detailed in the following sections.

Pore pressure transducers

Pore Pressure Transducers (PPTs) measure pore pressure through the deflection of a strain-gauged diaphragm in the instrument. The PPTs used were PDCR 81 PPTs manufactured by Druck Ltd. Instruments with a 3 and 7 bar operating pressure range were used. A porous bronze stone was used to cover the entrance to the transducer and prevent sand grains from entering and potentially damaging the membrane. The PPTs were calibrated by applying known pressures at prescribed intervals to the instruments using an air pressure chamber.

Piezoelectric accelerometers

Piezoelectric accelerometers contain a piezoceramic element and mass. When vibrated, the mass exerts a pressure on the piezoceramic material, which releases an electric charge proportional to this stress. Charge amplifier leakage means only dynamic acceleration can be recorded. DJ Birchall (now DJB Instruments UK Ltd) A/23 piezoelectric accelerometers were positioned to measure both horizontal and vertical accelerations at discrete locations in the soil and on the model container. They were calibrated using a Brüel and Kjær calibrator which excited the instruments with a sinusoidal input acceleration with an amplitude of $\pm 10\ ms^{-2}$. The piezoelectric accelerometers were waterproofed by sealing them in wax.

Microelectromechanical system accelerometers

Micro-Electro-Mechanical System (MEMS) accelerometers are small electrical components which measure acceleration by measuring the force that a mass applies to a spring. They are therefore capable of recording both inertial and dynamic acceleration. MEMS accelerometers were used to monitor accelerations at discrete points on the structure. They are preferential to piezoelectric accelerometers due to their smaller size and mass. The MEMS accelerometers were waterproofed by sealing them in silicone.

Linear variable displacement transducers

Solartron DC50 Linear Variable Displacement Transducers (LVDTs) were used to measure vertical displacement of the structure and the soil surface. They are constructed using a static transformer primary winding and two secondary windings formed on a hollow bobbin through which a magnetic core can travel. This core moves with the object that is being tracked, and its position in the bobbin controls how much flux is coupled to each of the secondary coils, and therefore the output voltage.

Attachments were fixed to the ends of the LVDTs. A permeable plastic disk was attached to the bottom of the LVDT measuring displacement of the soil surface in the far-field to

prevent the LVDT from penetrating below the soil surface or floating on the surface of the pore fluid. Low friction polytetrafluoroethylene (PTFE) ends were connected to the LVDTs measuring structure displacement to prevent them from interfering with the behaviour of the structure.

Data acquisition

Amplification was set individually for each instrument within a junction box. Centrifuge test data was recorded at a sampling rate of 6 kHz. Data Acquisition System Laboratory (DASYLab) software was used for real-time data acquisition and analysis during the tests. The analogue to digital converters and computers were flown on the centrifuge. The data was saved as an ASCII file. MATLAB was used to post-process the centrifuge test data. Digital filtering was carried out during the post-processing of the centrifuge test data to remove noise and improve the quality of the signal. Eighth order Butterworth filters were used to enable a sharp cut-off at the desired frequency and avoid a gradual roll-off.

3.4.7 Miniature CPT

A miniature Cone Penetration Testing (CPT) device was used for two purposes. Firstly, to assess uniformity and repeatability of the soil specimen at the beginning of a centrifuge test. Secondly, to observe any change in cone resistance caused by the earthquake events.

The miniature CPT device used had an external diameter of 6.35 mm and a shaft length of 200 mm, with a 60 ° cone tip, as shown in Figure 3.3. An inner rod, protected by a hollow sleeve, transmitted the tip forces to a load cell located at the top of the shaft. The load cell was calibrated before and after each centrifuge test. The CPT device was driven by an electric piston attached to the model container. Comparison of four cone resistance versus depth profiles recorded by this CPT for a dense layer of sand show the device obtains repeatable results (Carey et al. 2018).

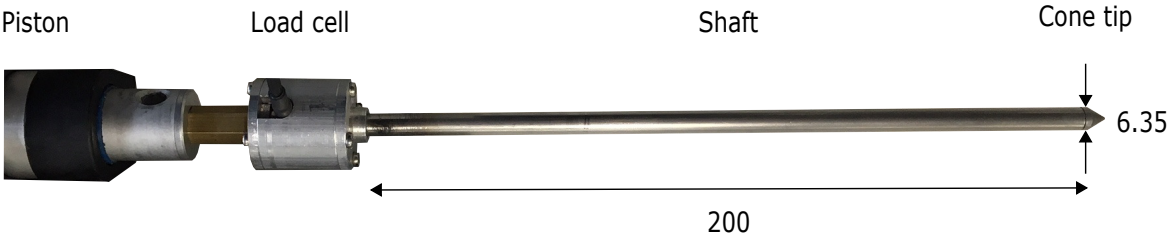

Fig. 3.3 Miniature CPT device, showing the electric piston, load cell, shaft and cone tip. Dimensions in mm at model scale.

CPTs were conducted during the final five centrifuge tests undertaken during this research project, all of which were in the window container. Two CPTs were conducted for each of these centrifuge tests – the first was post swing-up, before any earthquakes were fired, and the second was after all earthquakes had been fired, before swing-down. The CPT was driven in the same location at both instances, which in plan view was 55 mm from the transparent PMMA window and 80 mm from the edge of the Duxseal layer. The device was driven from 20 mm above the initial soil surface to 180 mm below it at a constant rate of penetration of 1.0 mm/s at model scale.

3.4.8 PIV

Particle image velocimetry (PIV) analysis was conducted using GeoPIV-RG to obtain displacements of the soil and structure (White et al. 2003, Stanier et al. 2015). A MotionBLITZ EoSens mini2 high speed recording camera, with 2 GByte internal memory, was used to record the cross section visible through the transparent window. For the first test conducted in the window container, 1696 $\times$ 1116 pixel images were captured at a frame rate of 804 Hz for 1.4 seconds at model scale using an exposure time of 100 μs. This was refined for all subsequent tests, where 1696 $\times$ 840 pixel images were captured at a frame rate of 1068 Hz for 1.4 seconds at model scale using an exposure time of 120 μs. For all tests, this corresponds to approximately 4.4 pixels to 1 mm in model scale. One third of the sand was dyed blue to increase the contrast in the images to improve the precision of the digital image correlation (Stanier & White 2013). The soil was tracked using patches of 50 $\times$ 50 pixels with the centres spaced at 25 pixels. Patches with a cross-correlation coefficient lower than 0.5 were removed from the analysis (Stanier et al. 2015). A grid of circular markers on the basement were used to track the basement of the structure.

The cross section of the model container was larger than the area that was visible through the transparent PMMA window. The high-speed camera was focused on the basement of each structure and the surrounding soil, but was unable to view the entire failure mechanism that developed. However, the region monitored gave valuable information about the co-seismic soil-structure interaction and how displacement and rotation of the structures developed.

The duration of capturing data at the frame rates used was limited by the memory capacity of the camera, therefore images were not captured for the entire post-seismic period whilst excess pore pressures were dissipated. Still images were taken after the dissipation period to observe final displacement and rotation.

3.5 Model structures

Two types of model structure were used in this research project. Both types of structure were single degree of freedom (SDOF) sway frames rigidly connected to a rigid basement structure. The friction angle between the structure and Hostun sand at 50 kPa is reported to be 28.8 ° (Adamidis 2017). The structures were designed to be representative of a 2-3 storey building with a 1 storey basement. To achieve the desired mechanical properties, both the thickness of the webs of the superstructure and the distribution of mass in the structure were varied. The fixed base natural frequency of each structure was found by conducting an impulse test at 1 g prior to testing in the centrifuge. The fixed base natural frequencies of the superstructures tested were between 0.8 - 1 Hz at prototype scale and are given in Tables 3.4 and 3.5.

The model basements were constructed out of sheet aluminium surrounding closed-cell polystyrene foam. The connections between the aluminium sheets were sealed with silicone to prevent leakage into the basement. Closed-cell polystyrene foam filled the space between the basement walls and was used two purposes. Firstly, it made the basement rigid. Secondly, it meant there was no space for fluid to collect in the basement.

Figure 3.4 shows the two types of superstructure and basement used. Structure type A was square in cross section and was used during tests in the laminar container. Structure type B was used during tests in the window container and was therefore designed to model plane strain behaviour. Type B structures were rectangular in cross section, with their length almost equal to the depth of the container.

3.5.1 Additional requirements for type B structures

Once the model was swung-up in the centrifuge, the configuration of the earthquake actuator and the camera meant that the force due to Earth's gravitational field was pulling the structure away from the transparent PMMA window. It was desirable for the structure to stay flush against the window for two reasons. Firstly, to ensure that the visible cross section was characteristic of the model being tested. Secondly, to allow for good tracking of the structure and soil using PIV. To ensure the structure stayed flush against the window, a pneumatic cylinder was attached to the back of the structure and the air pressure in it was set to provide a force equal in magnitude and opposite in direction to the weight of the structure at 1 g. This is shown in the schematic in Figure 3.5. A polytetrafluoroethylene (PTFE) cap attached to the end of the cylinder pushed against a sheet of high-density polyethylene (HDPE) attached to the back of the model container. The friction between the contact was limited to ensure that the structure was able to translate parallel to the window and rotate about an

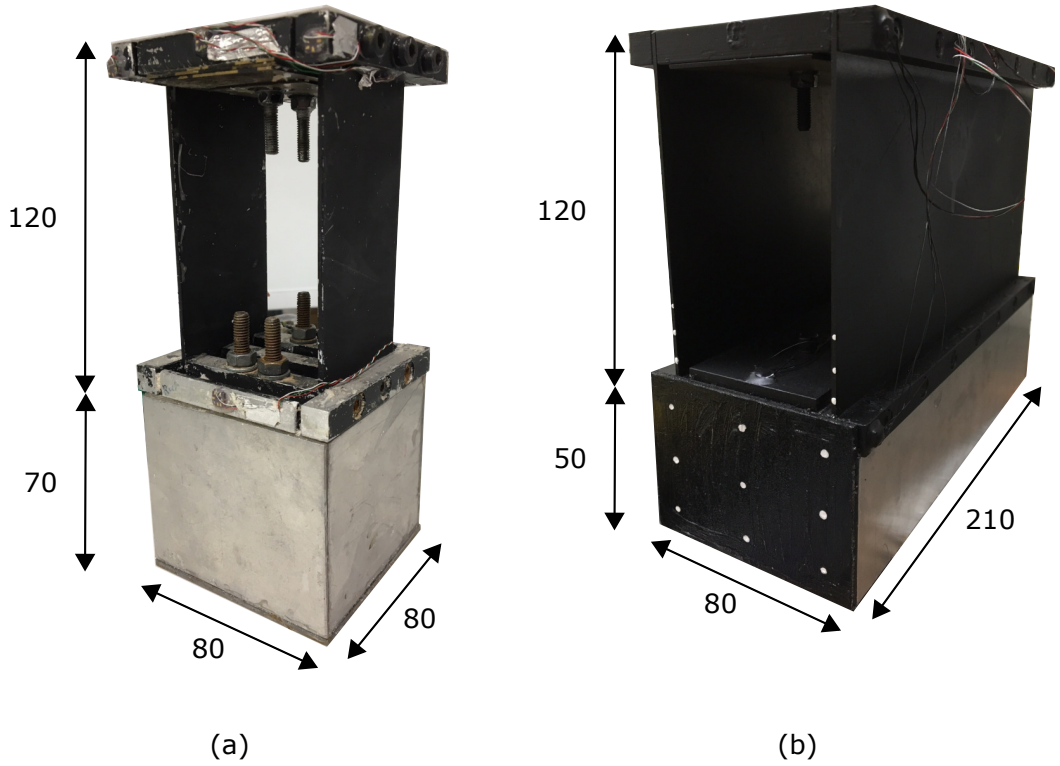

Fig. 3.4 Model structures: (a) Structure type A, for use in the laminar container, (b) Structure type B, for use in the window container. Dimensions in mm at model scale.

axis perpendicular to it (i.e. the structure had three degrees of freedom). The front of the basement was constructed from a sheet of black HDPE and covered with a thin layer of transparent silicone grease to minimise friction between the window and the structure. The HDPE sheet was black to reduce reflections in the high-speed images. For the same reason, the superstructure was spray painted black.

3.5.2 Design of basements

The basements of the structures were designed to provide an uplift force equal to a specified percentage of the total weight of the structure when the surrounding soil liquefied, the aim being to prevent the structure settling. This design philosophy is similar to that of "floating" or "compensated" foundations used to reduce structure settlement in locations with soft soil conditions (Tomlinson 2001), and can also be likened to designing for adequate buoyancy in boats.

Vertical forces acting on a structure with a basement in static conditions and in the event of complete soil liquefaction are shown in Figure 3.6. In static conditions, an upward

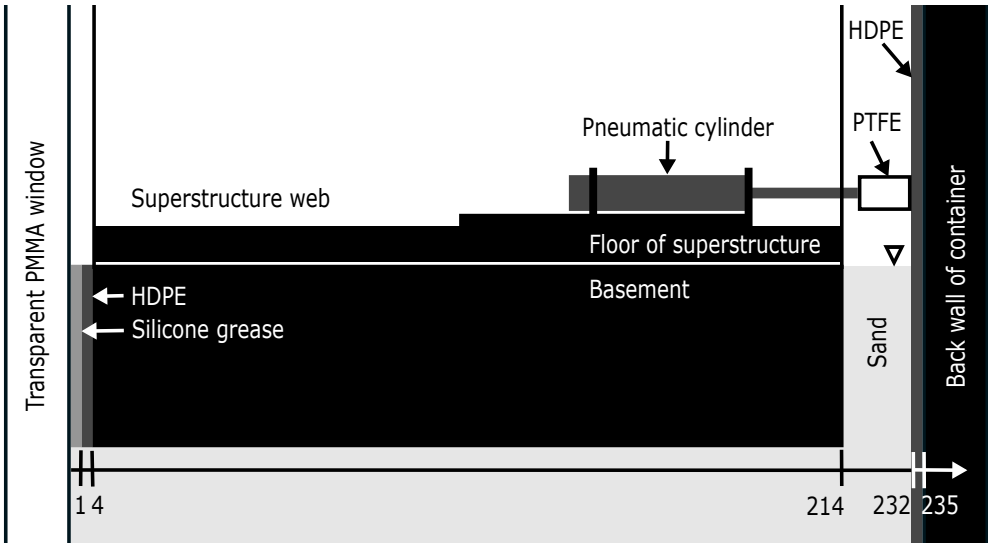

Fig. 3.5 Schematic of piston setup for type B structures. Dimensions in mm at model scale.

buoyancy force, $F_{U,h}$, is present due to hydrostatic water pressure, u_h:

$$F_{U,h} = u_h \times A = \gamma_w D \times A = \gamma_w \times V \tag{3.1}$$

where V, A and D are the volume, plan area and depth of the basement respectively and γ_w is the unit weight of water. This uplift force is resisted by the weight of the superstructure, F_S, and basement, F_B, and the shear resistance along the soil-structure interface, F_F, as shown in Figure 3.6(a). A resultant vertical force acts vertically downwards, which results in the effective bearing pressure given in Tables 3.4 and 3.5.

In the event of liquefaction, the shear resistance of the soil reduces significantly so the shear resistance along the soil-structure interface is assumed to be negligible (Koseki et al. 1997). In addition, the uplift force acting on the structure, $F_{U,L}$, increases to greater than the hydrostatic value, $F_{U,h}$. This is shown in the schematic in Figure 3.6(b). The uplift force during liquefaction can be considered in two ways.

Firstly, positive excess pore pressures, u_{ex}, are generated and act on the bottom of the basement in addition to the hydrostatic pressure present in the static analysis:

$$F_{U,L} = F_{U,h} + u_{ex} \times A \tag{3.2}$$

When liquefaction occurs, the positive excess pore pressure generated becomes equal to the initial vertical effective stress in the soil, and Equation 3.2 becomes:

$$F_{U,L} = F_{U,h} + \gamma'_s D \times A = (\gamma_w + \gamma'_s) \times V = \gamma_s V \tag{3.3}$$

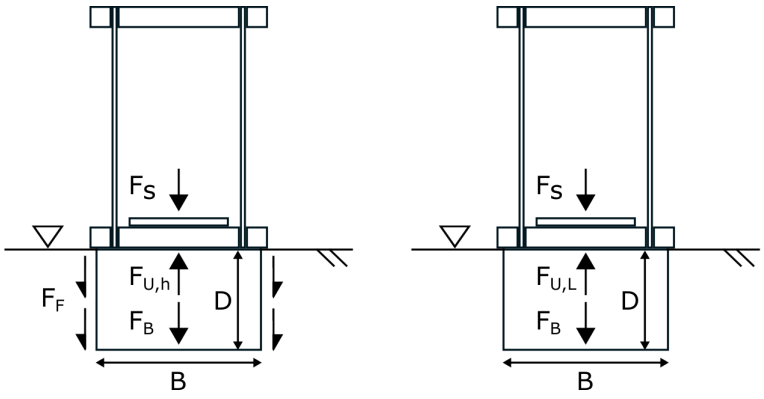

Fig. 3.6 Vertical forces acting on a structure with a basement (a) static conditions, (b) in the event of liquefaction. Forces are shown by single-headed arrows. Dimensions are shown by double-headed arrows.

where γ_s and γ_s' are the saturated and buoyant unit weight of the soil respectively.

Alternatively, the total uplift force can be calculated using Archimedes' principle, assuming the soil behaves as a dense fluid when liquefied. Archimedes' principle states that any body completely or partially submerged in a fluid at rest is acted upon by an upward, buoyant force, the magnitude of which is equal to the weight of the fluid displaced by the body:

$$F_{U,L} = \gamma_s V \tag{3.4}$$

Equations 3.3 and 3.4 show that these methods are equivalent when liquefaction occurs and the positive excess pore pressure generated is equal in magnitude to the initial vertical effective stress in the soil. The ratio of the uplift to total weight when the surrounding soil liquefies, U/W, given in Equation 3.5, was used as a design parameter for the structures tested in this research project:

$$\frac{U}{W} = \frac{F_{U,L}}{F_S + F_B} \tag{3.5}$$

3.5.3 Structure properties

Structure properties, in prototype scale, are given for type A structures in Table 3.4 and for type B structures in Table 3.5. Total and effective bearing pressures are respectively the total and effective vertical stress applied by the combined superstructure and basement to the soil directly beneath the bottom of the basement.

Table 3.4 Properties of type A structures (prototype scale)

Property	Symbol	FEH02	FEH03	FEH04
Width of basement (m)	B	4.8	4.8	-
Depth of basement (m)	D	4.2	4.4	-
Static buoyancy force (kN)	$F_{U,h}$	748	784	-
Width of superstructure (m)	b	4.8	4.8	4.8
Height of superstructure (m)	h	7.2	7.2	7.2
Symmetric superstructure		Y	Y	Y
Fixed base natural frequency (Hz)	f_n	1	1	1
Length of structure (m)	L	4.8	4.8	4.8
Total bearing pressure (kPa)	q_b	70.5	82.3	59.5
Static effective bearing pressure (kPa)	q'_b	33.3	43.2	59.5
Ratio of uplift to total weight during liquefaction	U/W	1.06	0.96	0
CoG height above top of basement (m)	y_{CoG}	2.0	1.7	4.1
CoG horizontal distance from centreline (m)	x_{CoG}	0	0	0

Table 3.5 Properties of type B structures (prototype scale)

Property	Symbol	FEH05	FEH06	FEH07	FEH08	FEH09	FEH10	FEH11
Width of basement (m)	B	4.8	9.6	9.6	9.6	4.8	4.8	4.8
Depth of basement (m)	D	3.0	3.0	3.0	3.0	3.0	3.0	3.0
Extenders, direction ^		-	-	-	-	V	V	H
Extenders, dimensions (m)	w × d	-	-	-	-	0.2 × 3.0	0.2 × 3.0	2.4 × 0.2
Static buoyancy force (kN)	$F_{U,h}$	1420	2860	2860	2860	1420	1420	1420
Width of superstructure (m)	b	4.8	4.8	4.8	4.8	4.8	4.8	4.8
Height of superstructure (m)	h	7.2	7.2	7.2	7.2	7.2	7.2	7.2
Symmetric superstructure		Y	Y	Y	N	Y	Y	Y
Fixed base natural frequency (Hz)	f_n	1	1	1	0.83	1	1	1
Length of structure (m)	L	12.6	12.6	12.6	12.6	12.6	12.6	12.6
Total bearing pressure (kPa)	q_b	65.3	68.1	55.0	55.2	68.1	59.4	59.5
Static effective bearing pressure (kPa)	q'_b	38.5	40.1	29.0	29.2	41.4	32.5	32.6
Ratio of uplift to total weight during liquefaction	U/W	0.79	0.75	0.93	0.92	0.80	0.91	0.93
CoG height above top of basement (m)	y_{CoG}	2.15	-0.044	0.526	1.3	2.1	2.1	2.1
CoG horizontal distance from centreline (m)	x_{CoG}	0	0	0	-0.184	0	0	0

^ V = vertical extenders, H = horizontal extenders

3.6 Experimental procedure

The sand layer was poured by spot air pluviation using an automatic sand pourer (Madabhushi et al. 2006) to obtain a uniform and repeatable sand layer, as shown in Figure 3.8(a). A nozzle diameter of 8 mm and a drop height of 400 mm were used. Figure 3.7 shows the cone resistance of the CPTs conducted post swing-up, before any earthquakes were fired, during the final five centrifuge tests. The gradient of each of these profiles is approximately constant, which shows that a uniform sand layer was produced. The blip in the cone resistance measured at approximately 5 m below the initial ground surface in Tests FEH07 and FEH08 was caused by a notch in the drive shaft of the CPT momentarily stalling progression of the cone.

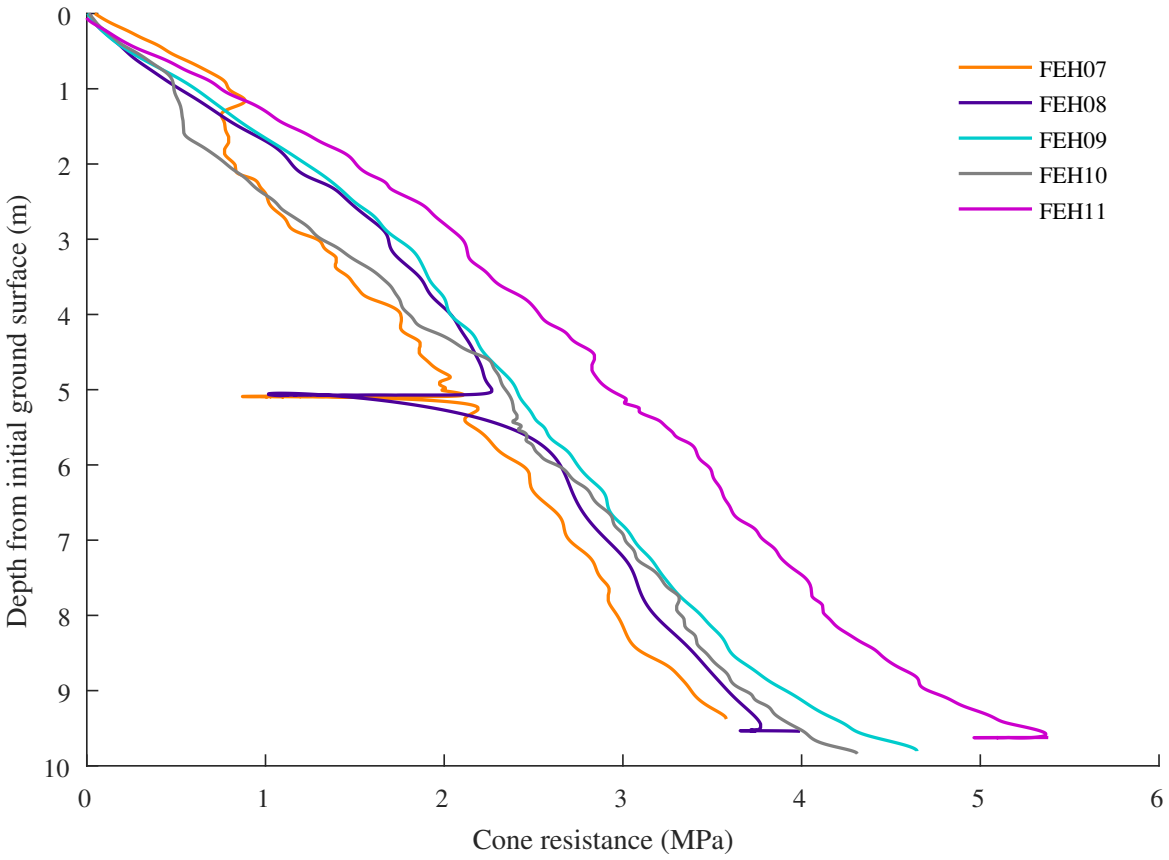

Fig. 3.7 Comparison of cone resistance post swing-up, before any earthquakes were fired.

For a given depth, the values of cone resistance across the centrifuge tests were comparable. The cone resistances in Tests FEH07, FEH08, FEH09 and FEH10 were within $\pm$ 0.4 MPa for the entire soil layer. The cone resistance measured in Test FEH11 was greater than the other four tests by approximately 25 %. This may be due to model disturbance during

the process of it being loaded onto the centrifuge. The comparable values of cone resistance across the tests show that the method of sand pouring was repeatable.

Layers of instrumentation in the soil were placed sequentially during sand pouring, as shown in Figure 3.8(b). Figure 3.8(c) shows the placement of the model structure which was manually placed once sand pouring had reached the level of the bottom of the basement. Once sand pouring was complete, the model was enclosed in an airtight chamber and was placed under a suction of approximately -80 kPa. It was then flushed three times with carbon dioxide. Carbon dioxide is more soluble in water than air, so was used to maximise the degree of saturation achieved. The model was saturated using an automatic, pressure controlled system, CAM-Sat (Stringer & Madabhushi 2010), as shown in Figure 3.8(d), with a target mass flow rate of 0.3 kg per hour. To ensure that the phreatic surface remained above the entire sand surface during spinning in the centrifuge, saturation continued until the fluid level was approximately 8 mm above the sand surface. The model was loaded onto the centrifuge following saturation using an electric crane (Figure 3.8(e)). Where applicable, the CPT configuration and camera and lighting gantry were then attached to the model, as shown in Figure 3.8(f).

The air supply to the pneumatic cylinder was switched on immediately before swing-up. The temperature of the pore fluid and the depth of the sand layer were recorded. The centrifugal acceleration of the centrifuge was increased in steps of 10 g to the target g level, 60 g. Photographs were taken at each 10 g increment during tests conducted in the window container. The characteristics of the earthquakes fired during each test are given in Section 3.7. Operation of the earthquake actuators, and the procedures followed to fire earthquakes, are discussed by Madabhushi et al. (1998) and Madabhushi et al. (2012).

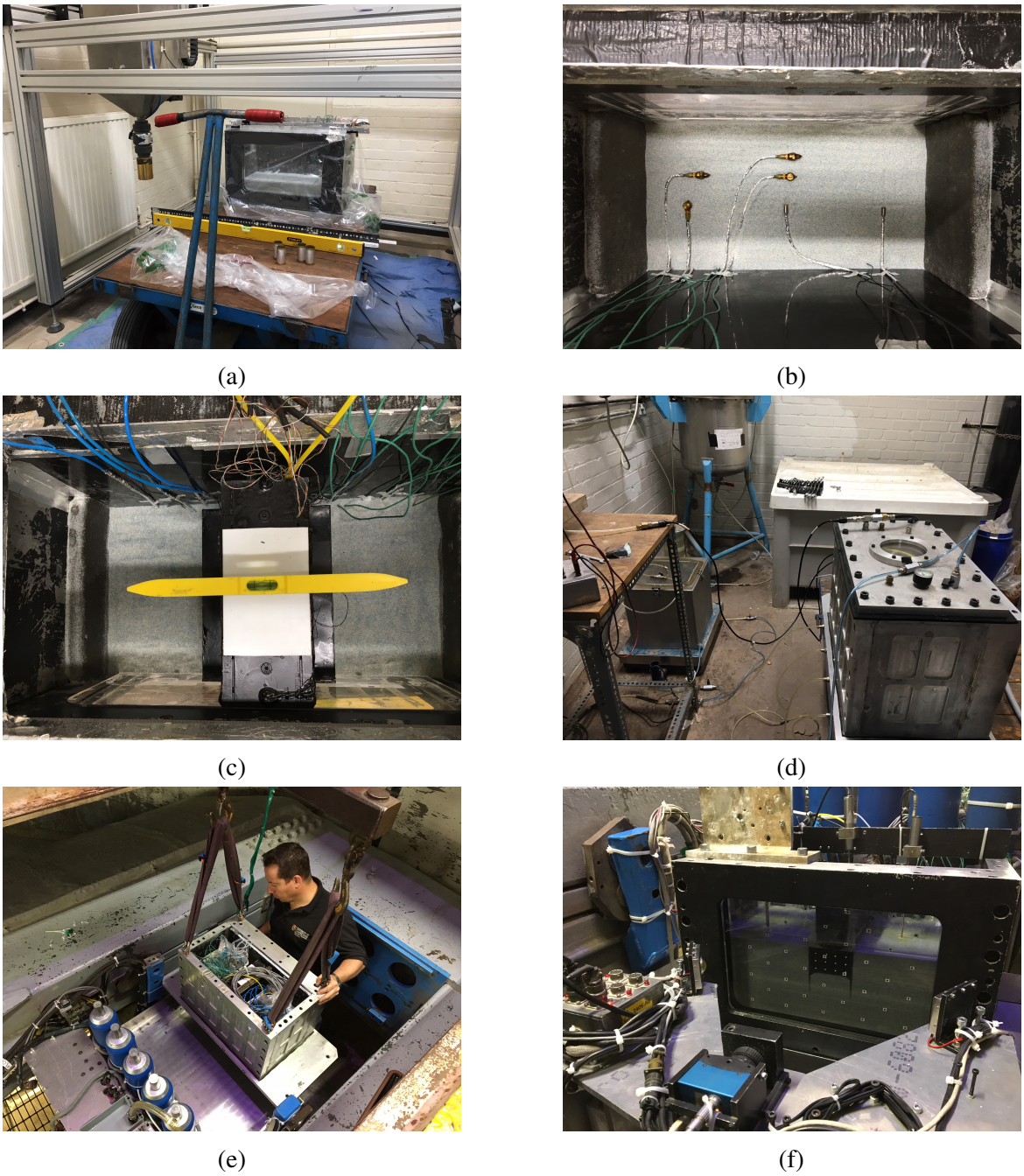

(a) (b)

(c) (d)

(e) (f)

Fig. 3.8 Photographs of centrifuge model preparation: (a) Sand pouring using an automatic sand pourer, (b) Placement of instrumentation during sand pouring, (c) Placement of structure with basement during sand pouring, (d) Saturation using an automatic, pressure controlled system, (e) Loading of the model onto the Turner beam centrifuge, (f) Model loaded onto the servo-hydraulic earthquake actuator.

3.7 Test program

Details of the dynamic centrifuge tests discussed in this thesis are detailed in this section.

3.7.1 Test FEH02

Aim	To observe the seismic response of a structure with a narrow basement
g level	60
Model container	Laminar
Structure type	A
Structure U/W	1.06
Relative density	45 %
Pre test model temp	16.6 ° C
Pore fluid viscosity	55 cSt
Earthquake actuator	SAM
Earthquakes fired	a) sinusoidal, 20 cycles, f = 60 Hz, peak input acc = 0.096 g b) sinusoidal, 20 cycles, f = 60 Hz, peak input acc = 0.379 g c) sine sweep, 20 cycles, f_{max} = 60 Hz, peak input acc = 0.296 g
CPT	Not used

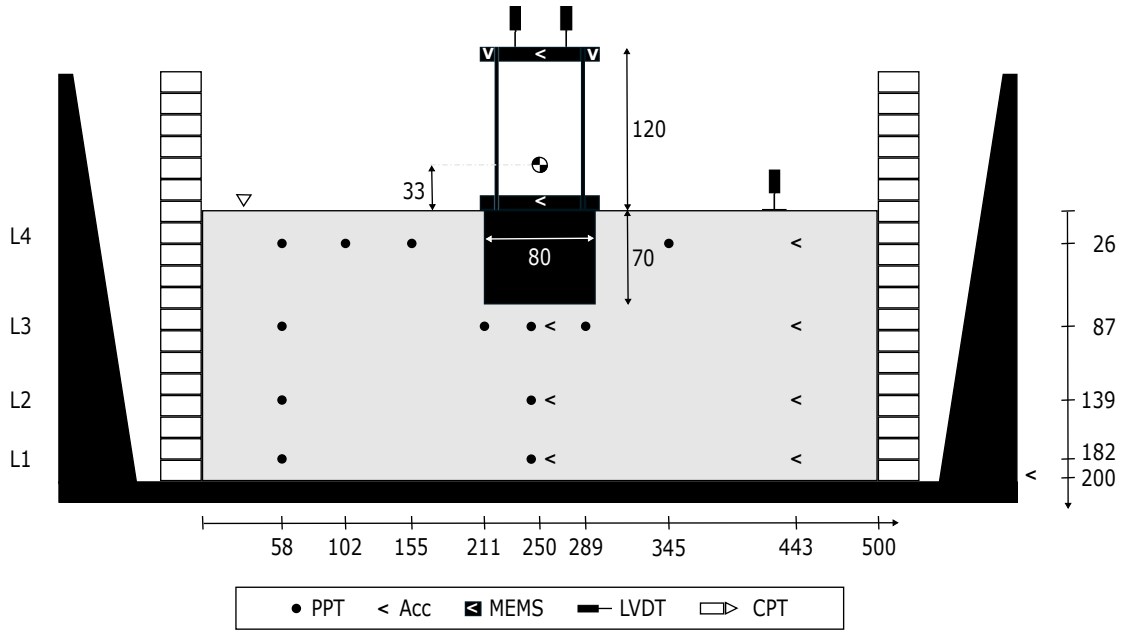

Fig. 3.9 Centrifuge model layout: FEH02. Dimensions in mm at model scale.

3.7.2 Test FEH03

Aim	To observe the seismic response of a structure with a narrow basement
g level	60
Model container	Laminar
Structure type	A
Structure U/W	0.96
Relative density	45 %
Pre test model temp	12.0 °C
Pore fluid viscosity	56 cSt
Earthquake actuator	SAM
Earthquakes fired	a) sinusoidal, 20 cycles, f = 60 Hz, peak input acc = 0.157 g b) sinusoidal, 20 cycles, f = 60 Hz, peak input acc = 0.306 g c) sine sweep, 20 cycles, f_{max} = 60 Hz, peak input acc = 0.181 g
CPT	Not used

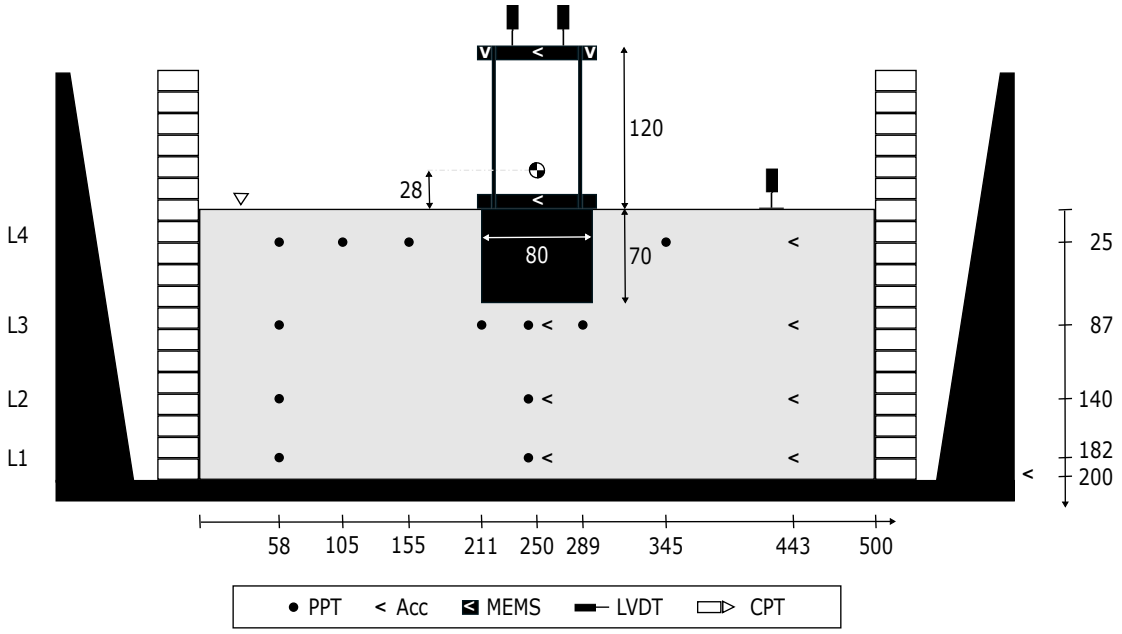

Fig. 3.10 Centrifuge model layout: FEH03. Dimensions in mm at model scale.

3.7.3 Test FEH04

Aim	To observe the seismic response of a structure on a shallow foundation with no basement
g level	60
Model container	Laminar
Structure type	A
Structure U/W	0
Relative density	45 %
Pre test model temp	12.6 °C
Pore fluid viscosity	63 cSt
Earthquake actuator	SAM
Earthquakes fired	a) sinusoidal, 20 cycles, f = 60 Hz, peak input acc = 0.215 g b) sinusoidal, 20 cycles, f = 60 Hz, peak input acc = 0.413 g c) sine sweep, 20 cycles, f_{max} = 60 Hz, peak input acc = 0.199 g
CPT	Not used

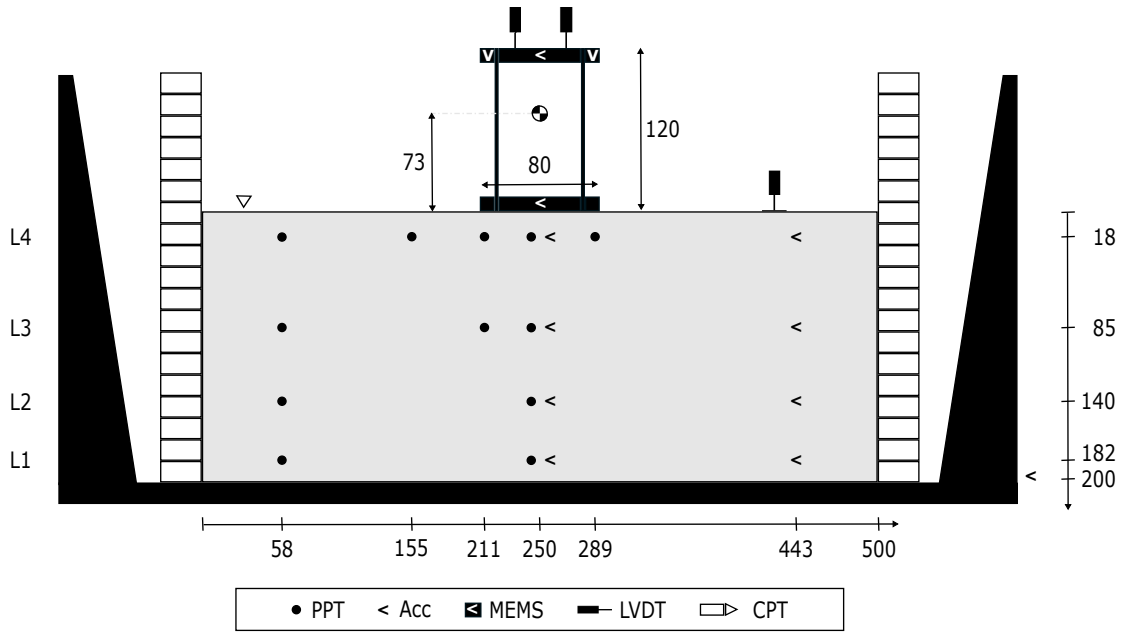

Fig. 3.11 Centrifuge model layout: FEH04. Dimensions in mm at model scale.

3.7.4 Test FEH05

Aim	To observe the seismic response of a structure with a narrow basement
g level	60
Model container	Window
Structure type	B
Structure U/W	0.79
Relative density	45 %
Pre test model temp	15.6 °C
Pore fluid viscosity	52 cSt
Earthquake actuator	SAM
Earthquakes fired	a) sinusoidal, 20 cycles, f = 60 Hz, peak input acc = 0.164 g b) sinusoidal, 20 cycles, f = 60 Hz, peak input acc = 0.312 g
CPT	Not used
Notes	No further earthquakes fired due to significant rotation of the structure

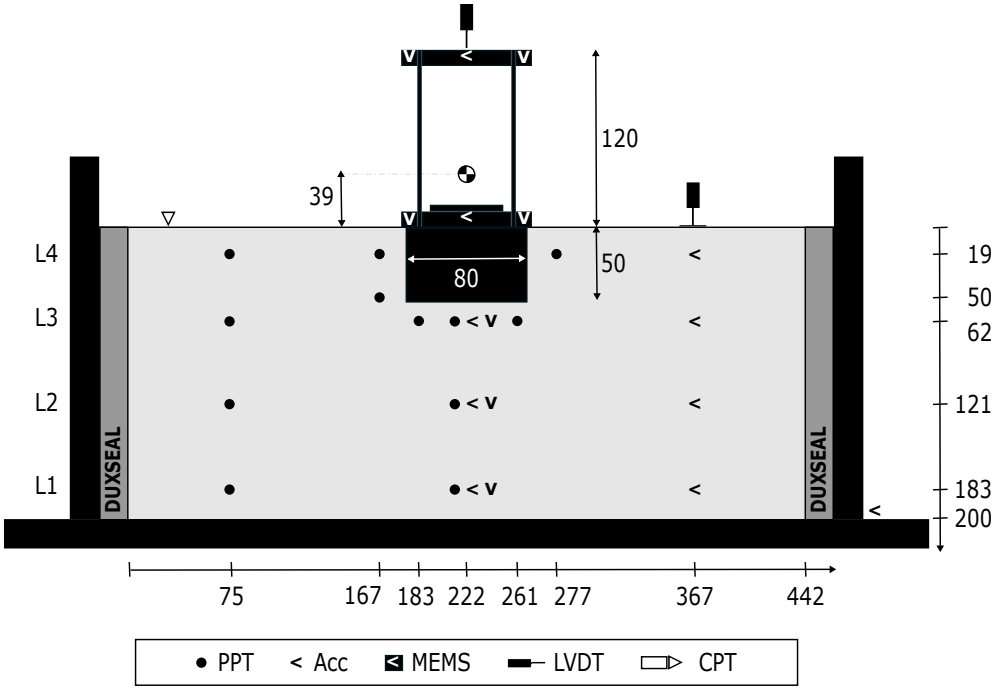

Fig. 3.12 Centrifuge model layout: FEH05. Dimensions in mm at model scale.

3.7.5 Test FEH06

Aim	To observe the seismic response of a structure with a wide basement
g level	60
Model container	Window
Structure type	B
Structure U/W	0.75
Relative density	43 %
Pre test model temp	12.0 °C
Pore fluid viscosity	56 cSt
Earthquake actuator	Servo hydraulic
Earthquakes fired	a) sinusoidal, 20 cycles, f = 60 Hz, peak input acc = 0.0347 g b) Imperial Valley wave form, peak input acc = 0.135 g c) sinusoidal, 20 cycles, f = 60 Hz, peak input acc = 0.392 g d) Kobe wave form, peak input acc = 0.289 g
CPT	Not used

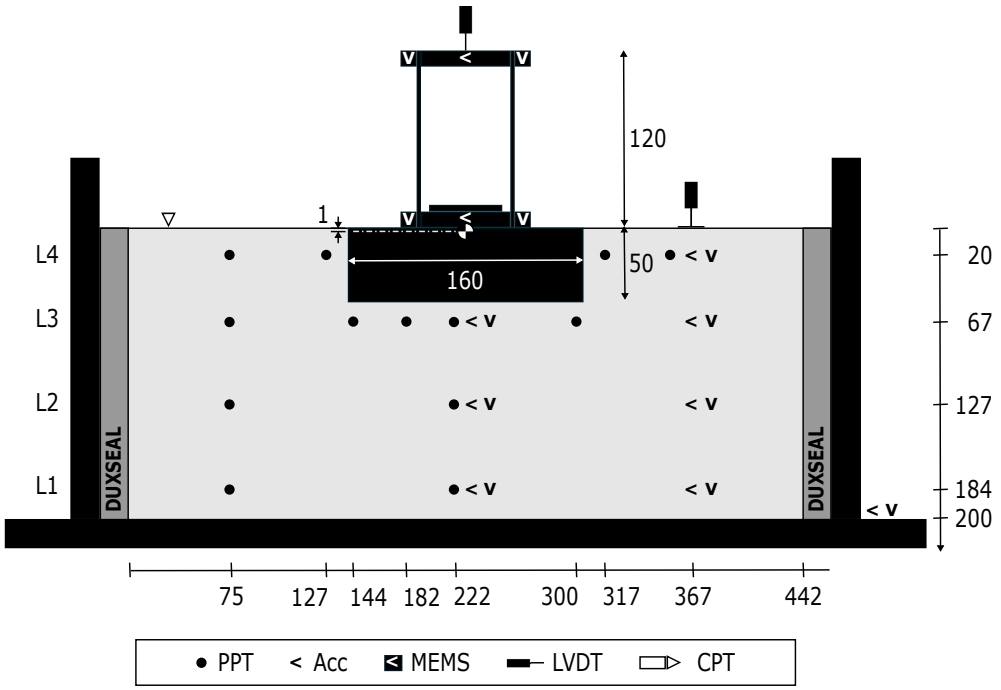

Fig. 3.13 Centrifuge model layout: FEH06. Dimensions in mm at model scale.

3.7.6 Test FEH07

Aim	To observe the seismic response of a structure with a wide basement
g level	60
Model container	Window
Structure type	B
Structure U/W	0.93
Relative density	44 %
Pre test model temp	16.0 °C
Pore fluid viscosity	64.3 cSt
Earthquake actuator	Servo hydraulic
Earthquakes fired	a) sinusoidal, 20 cycles, f = 60 Hz, peak input acc = 0.0352 g b) Imperial Valley wave form, peak input acc = 0.131 g c) sinusoidal, 20 cycles, f = 60 Hz, peak input acc = 0.424 g d) Kobe wave form, peak input acc = 0.284 g
CPT	Post swing-up, pre earthquakes Post earthquakes, pre swing-down

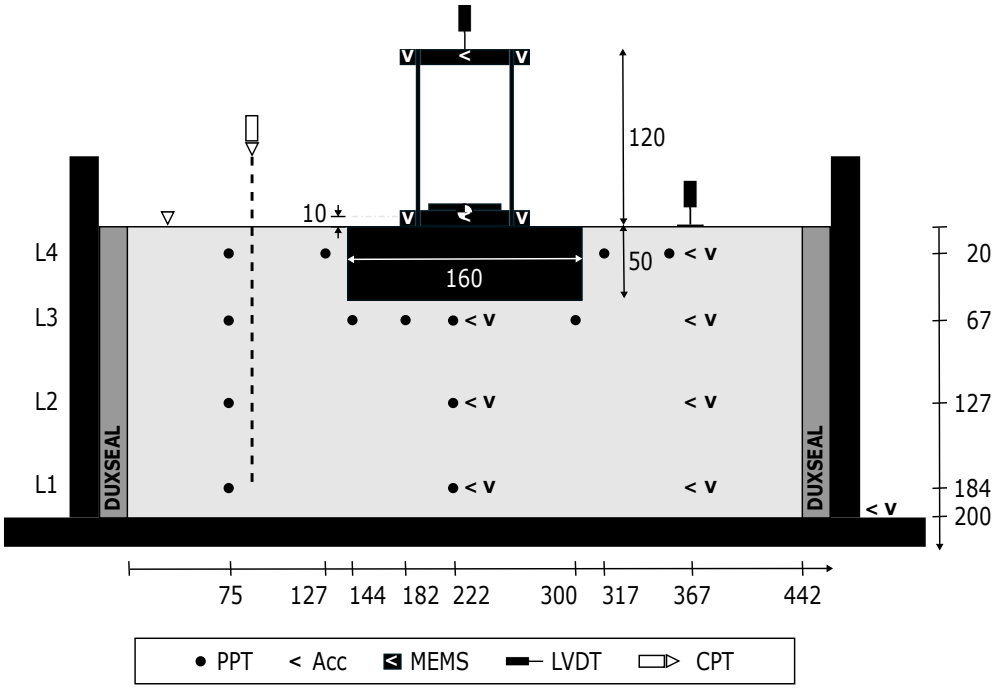

Fig. 3.14 Centrifuge model layout: FEH07. Dimensions in mm at model scale.

3.7.7 Test FEH08

Aim	To observe the seismic response of an asymmetrically loaded structure with a wide basement
g level	60
Model container	Window
Structure type	B
Structure U/W	0.92
Relative density	44 %
Pre test model temp	16.0 °C
Pore fluid viscosity	66.4 cSt
Earthquake actuator	Servo hydraulic
Earthquakes fired	a) sinusoidal, 20 cycles, f = 60 Hz, peak input acc = 0.0851 g b) Imperial Valley wave form, peak input acc = 0.123 g c) sinusoidal, 20 cycles, f = 60 Hz, peak input acc = 0.359 g
CPT	Post swing-up, pre earthquakes Post earthquakes, pre swing-down
Notes	No further earthquake fired due to significant rotation of the structure

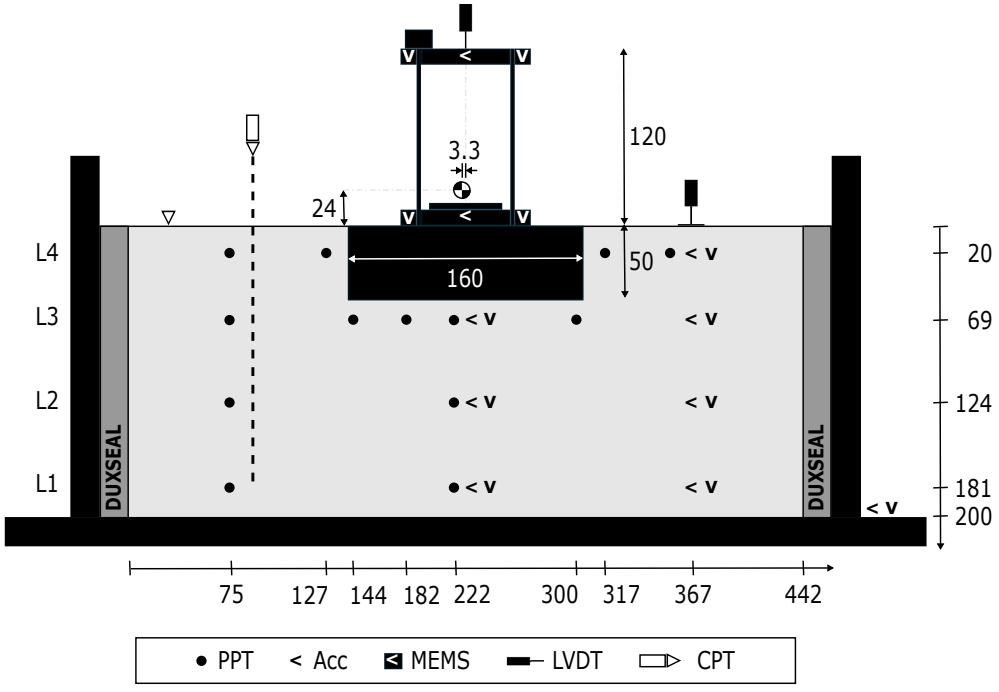

Fig. 3.15 Centrifuge model layout: FEH08. Dimensions in mm at model scale.

3.7.8 Test FEH09

Aim	To observe the seismic response of a structure with a narrow basement and vertical extenders
g level	60
Model container	Window
Structure type	B
Structure U/W	0.80
Relative density	45 %
Pre test model temp	12.0 °C
Pore fluid viscosity	55.8 cSt
Earthquake actuator	Servo hydraulic
Earthquakes fired	a) sinusoidal, 20 cycles, f = 60 Hz, peak input acc = 0.0322 g b) Imperial Valley wave form, peak input acc = 0.110 g c) sinusoidal, 20 cycles, f = 60 Hz, peak input acc = 0.437 g d) Kobe wave form, peak input acc = 0.295 g
CPT	Post swing-up, pre earthquakes Post earthquakes, pre swing-down

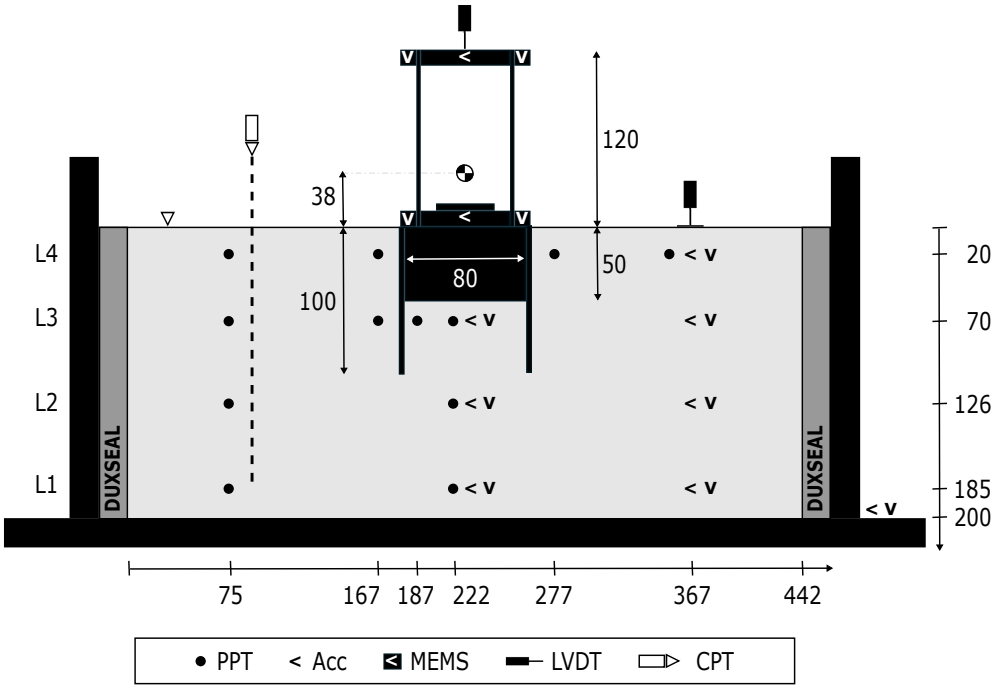

Fig. 3.16 Centrifuge model layout: FEH09. Dimensions in mm at model scale.

3.7.9 Test FEH10

Aim	To observe the seismic response of a structure with a narrow basement and vertical extenders
g level	60
Model container	Window
Structure type	B
Structure U/W	0.91
Relative density	40 %
Pre test model temp	8.0 °C
Pore fluid viscosity	57.2 cSt
Earthquake actuator	Servo hydraulic
Earthquakes fired	a) sinusoidal, 20 cycles, f = 60 Hz, peak input acc = 0.0333 g b) Imperial Valley wave form, peak input acc = 0.099 g c) sinusoidal, 20 cycles, f = 60 Hz, peak input acc = 0.419 g
CPT	Post swing-up, pre earthquakes Post earthquakes, pre swing-down
Notes	No further earthquake fired due to significant rotation of the structure

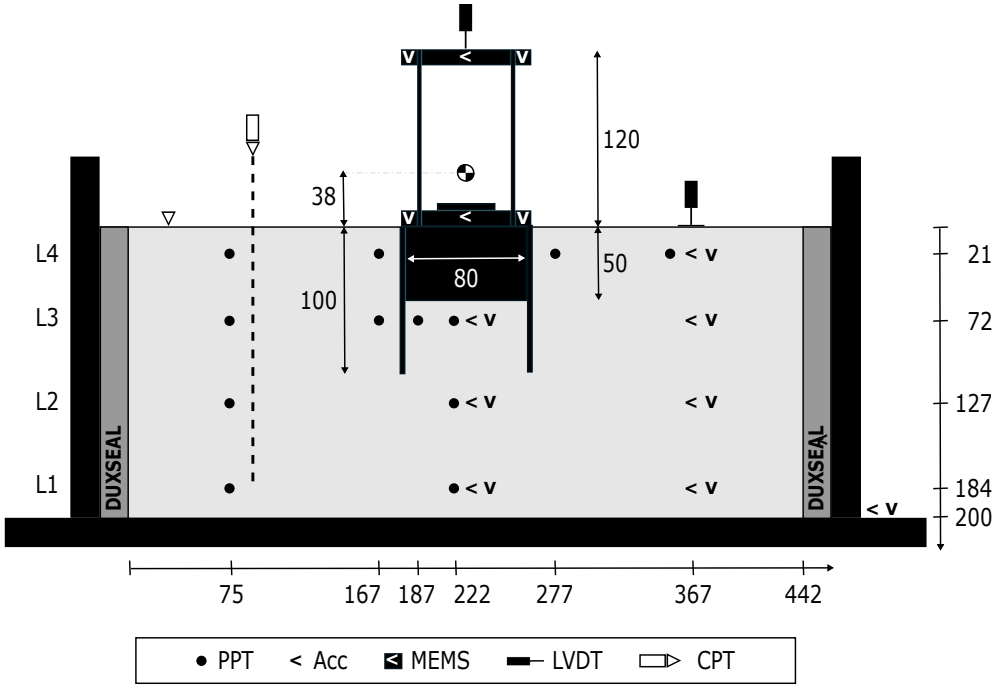

Fig. 3.17 Centrifuge model layout: FEH10. Dimensions in mm at model scale.

3.7.10 Test FEH11

Aim	To observe the seismic response of a structure with a narrow basement and horizontal extenders
g level	60
Model container	Window
Structure type	B
Structure U/W	0.93
Relative density	40 %
Pre test model temp	8.0 °C
Pore fluid viscosity	57.5 cSt
Earthquake actuator	Servo hydraulic
Earthquakes fired	a) sinusoidal, 20 cycles, f = 60 Hz, peak input acc = 0.0332 g b) sinusoidal, 20 cycles, f = 60 Hz, peak input acc = 0.0347 g c) Imperial Valley wave form, peak input acc = 0.110 g d) sinusoidal, 20 cycles, f = 60 Hz, peak input acc = 0.445 g e) Kobe wave form, peak input acc = 0.277 g
CPT	Post swing-up, pre earthquakes Post earthquakes, pre swing-down
Notes	Earthquake actuator malfunction meant it was necessary to swing down after earthquake a) and restart the test the following day

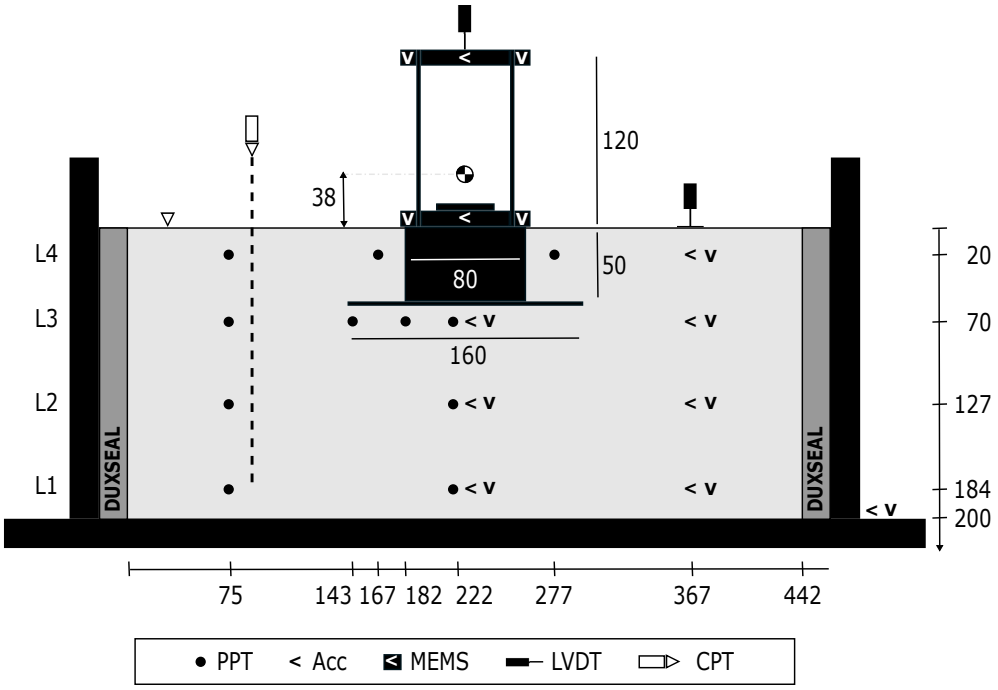

Fig. 3.18 Centrifuge model layout: FEH11. Dimensions in mm at model scale.

3.8 Errors and limitations in centrifuge modelling

It is necessary to discuss limitations of centrifuge modelling, and the errors that these limitations can lead to. In this section, the main limitations are discussed in relation to the research presented in this thesis. An extensive discussion of errors and limitations in centrifuge modelling is provided by Taylor (1995) and Madabhushi (2015).

3.8.1 Variation in gravity field

The Earth's gravitational field can be assumed to be constant for the height and geometry of a real structure. However, this is not the case in a geotechnical centrifuge. The circular motion of a centrifuge results in a centrifugal acceleration, Ng, that is a linear function of the distance from the centre of rotation:

$$Ng = r\dot{\theta}^2 \tag{3.6}$$

where r is the distance from the centre of rotation and $\dot{\theta}$ is the angular speed. Consequently, the gravitational field in a centrifuge model increases linearly with distance from the centre of rotation. The bottom of a centrifuge model therefore experiences a greater gravitational field than the top of the model, resulting in regions of over-stress and under-stress respectively compared to the average stress in the centrifuge model.

To minimise the error due to the variation in g level with depth within a centrifuge model, the ratio of the maximum under-stress and over-stress can be made to be equal. For this to be achieved, the effective radius must be measured from the axis of rotation to one third of the depth of the model above its base (Taylor 1995). For the centrifuge tests presented in this thesis, it was estimated that the maximum over-stress and under-stress errors were equal to 0.9 %. These errors are considered to have had a negligible effect on the tests presented in this thesis.

The proportionality of gravitational field with distance from the centre of rotation also results in differences in gravitational field in the radial direction within a centrifuge model. The difference increases with distance from the centreline of the centrifuge model. It was estimated that the maximum error due to the radial gravity field was 0.23 % for the centrifuge model layout used in the tests presented in this thesis. To avoid the radial gravity field influencing the co-seismic behaviour of the structures with basements being tested, each centrifuge test included only one model structure which was placed with its centreline coinciding with the centreline of the model container.

After swing-up of a package on the Turner beam centrifuge, the model container is in a horizontal position. The resulting acceleration field is therefore slightly out of the horizontal plane due to the presence of the Earth's gravitational field acting vertically downwards, as shown in Figure 3.1. For the angular speed of the centrifuge during testing, it was calculated that the angle of this resultant acceleration field was 0.95 ° to the horizontal. For the tests conducted in the window container, the configuration of the earthquake actuator and camera meant that once the model was spun up in the centrifuge, the force due to Earth's gravitational field was pulling the structure away from the transparent PMMA window. To ensure that the visible cross section was characteristic of the model being tested, the structure was kept flush against the window using a pneumatic cylinder which provided a force equal in magnitude and opposite in direction to the weight of the structure at 1 g. The effect of Earth's gravitational field on the structure was therefore negated.

3.8.2 Particle size effects

In centrifuge modelling, prototype dimensions are scaled by the gravity scaling factor N. However, the particle sizes are not scaled by the same factor. Clearly, scaling sand by a factor of 1:60 would result in particle sizes similar to clay, which would significantly change the stress-strain behaviour. In order to capture the true behaviour of the soil in the prototype, the same soil must be used in the centrifuge model. The soil is therefore being considered as a continuum (Madabhushi 2015).

Particle size effects must be considered when the centrifuge model dimensions approach the particle sizes. The average particle size of the Hostun sand used in this research project was 0.356 mm (Silva 2018). The miniature CPT device was the smallest model dimension used in the centrifuge tests. Bolton et al. (1999) found that to avoid CPT data in the centrifuge being influenced by the cone size, the cone diameter should be at least twenty times greater than the mean particle diameter. The cone used in this research project had a diameter of 6.35 mm which equates to 17.8 times the mean particle diameter. This is close to the recommended cone size, and is therefore not considered to have influenced the data obtained from the CPT. The narrowest of the basements tested were 225 times the average particle size. Therefore, the failure mechanisms for the structures with basements were unlikely to be affected by particle size effects.

3.8.3 Boundary conditions

Boundary conditions are an important consideration in any modelling technique used in geotechnical engineering due to the semi-infinite extent of soil horizontally. When investi-

gating dynamic geotechnical problems, boundary conditions are particularly important due to both the possibility of reflection of waves at boundaries and significant changes in soil stiffness during shaking. The two model containers used in this research project, the laminar and window containers, provided different boundary conditions.

The ability of the laminae to slide laterally across one another in the direction of shaking means that the walls of the laminar container effectively contribute no stiffness and minimal mass to the system, so the container will not restrain the soil movements within it. Consequently, the laminar container is the model container best suited to liquefaction problems. However, the laminar container does not allow digital image correlation to be conducted on a cross section of the model, which was important for this research project. The window container was used for this purpose. In this container, a layer of Duxseal was used at both ends of the window container to limit the effect of the rigid boundaries (Steedman & Madabhushi 1991). Absorbing boundaries such as Duxseal layers are only partially effective, particularly when soil loses stiffness during liquefaction events. The novel insight into the co-seismic soil-structure interaction that was facilitated by using the window container was felt to outweigh the limitations with respect to the boundary conditions compared to the laminar container.

For these reasons, possible boundary effects imposed by the model containers in the centrifuge tests conducted in this research project must be considered. Boundary effects specific to the data presented in Chapters 4 and 5 will be discussed in detail at the end of each of the respective chapters.

3.9 Summary

This chapter has presented the experimental techniques and equipment used in this research project to investigate the seismic behaviour of structures with basements in liquefiable soil. Geotechnical centrifuge modelling was the primary experimental method used as it enabled the correct stress-strain behaviour experienced in the field to be replicated, which in turn enabled realistic failure mechanisms to develop. In addition, no prior assumptions about drainage conditions, failure mechanisms or SSI effects were required. This was particularly important for this novel research topic. These strengths of centrifuge modelling were considered to far outweigh the limitations discussed in this chapter.

Chapter 4

Behaviour of structures with narrow basements located in liquefiable soil

4.1 Introduction

There is an increasing tendency for buildings to have basements. Urban centres are becoming densely populated and land prices are rising, making it desirable to use underground space for parking and storage. The behaviour of structures with basements located in liquefiable soil is not well understood.

Post earthquake reconnaissance missions following large earthquake events have provided some reports on the performance of structures with basements. Correlation of building width with average liquefaction induced settlement during the Niigata 1964 earthquake by Yoshimi & Tokimatsu (1977) included 4 buildings with basements without piles and 14 structures with a shallow foundation. From this data, it is evident that the structures with basements experienced comparable, if not slightly less, settlement than similar structures without basements which were normalised by number of storeys, and therefore assumed bearing pressure. Nothing was stated about the residual rotation of these structures. After the Chi-Chi 1999 earthquake it was observed that buildings with basements suffered less liquefaction induced settlement and tilt than those without basements (Hsu et al. 2002). For cases where the plan area of a basement did not match the plan area of the superstructure above, as expected from moment equilibrium, rotation occurred in the direction of the centre of gravity of the superstructure and away from the centre of buoyancy of the basement (Hsu et al. 2002, Tanaka 2003). More recently, differential displacement was observed across structures with basements as a consequence of liquefaction during the 2010-2011 series of earthquakes in Christchurch, New Zealand (Cubrinovski et al. 2011, Bray & Luque 2017). The basement

storeys and the buildings above them behaved rigidly and as a result negligible distortion and minimal damage was noted (Cubrinovski et al. 2011). Additional data on the behaviour of structures with basements is sparse.

Little research has investigated the co-seismic soil-structure interaction of structures with basements located in liquefiable soil. Rollins & Seed (1990) stated that the induced cyclic shear stress ratio (CSR) near a structure with a basement will depend on the extent to which the excavation for the basement floors compensate for the structure load. For a small number of cases studied, 3D finite-difference-based analyses by Unutmaz (2018) found the presence of a basement to reduce the CSR and therefore reduce the possibility of liquefaction.

In contrast, the behaviour of structures with shallow foundations located upon liquefiable layers has been widely investigated in post earthquake reconnaissance missions (Yoshimi & Tokimatsu 1977, Tokimatsu et al. 1994, Cubrinovski et al. 2011, Bertalot et al. 2013) and in the laboratory, primarily using dynamic centrifuge modelling (Liu & Dobry 1997, Dashti et al. 2010*b*, Bertalot & Brennan 2015, Adamidis & Madabhushi 2018*a*). Significant structure settlement and rotation have been observed, with the extent of both depending on several parameters including the depth of the liquefiable layer, shaking intensity, foundation bearing pressure, and building aspect ratio. The bearing pressure applied by a structure has been found to cause a bulb of stiffer soil, which does not liquefy, to form beneath the foundation (Coelho et al. 2007, Ghosh & Madabhushi 2007, Adamidis & Madabhushi 2018*a*). Decreasing the thickness of liquefied soil beneath this bulb, either by increasing the foundation bearing pressure or decreasing the thickness of the liquefiable layer, has been shown to cause an increase in accelerations transmitted to the structure (Adamidis & Madabhushi 2018*a*).

Another problem caused by liquefaction in the built environment that has been researched recently is the uplift of light subsurface structures that have a lower unit weight than the saturated soil surrounding them - for example pipe lines, empty storage tanks or underground car parks (Koseki et al. 1997, Yang et al. 2004, Chian & Madabhushi 2012). Excess pore pressures generated during shaking increase the uplift force acting on the submerged structure, and also decrease the resistance to uplift provided by shearing within the overlying soil and at the soil-structure interface (Koseki et al. 1997, Zhang & Chian 2019). Uplift is initiated when the net vertical force acting on the structure becomes upwards, and the instantaneous rate of floatation can be affected by soil-structure interaction beneath the uplifting structure (Chian & Madabhushi 2012, Madabhushi & Madabhushi 2015).

The dynamic centrifuge tests discussed in this chapter are the first tests of their kind to investigate the seismic behaviour of structures with basements located in liquefiable soil. This research is important given the increasing number of buildings with basements

in densely populated urban centres. In addition, it is a interesting topic to investigate because it is intuitive that partially buried buildings combine the propensity of structures with shallow foundations to settle and light subsurface structures to float. They may therefore perform advantageously during earthquake induced liquefaction by reducing the total vertical displacement of a structure. Some of the results presented in this chapter have been reported previously (Hughes & Madabhushi 2017, 2019*a*).

4.2 Preliminary test series

Three dynamic centrifuge tests were conducted in the laminar model container as a preliminary series to establish a starting point for the ratio of uplift to total weight when the surrounding soil liquefied, U/W. The properties of these structures are discussed in detail in Chapter 3, and are summarised below in Table 4.1.

Table 4.1 Properties of structures in preliminary test series (prototype scale)

Property	Symbol	FEH02	FEH03	FEH04
Total bearing pressure (kPa)	q_b	70.5	82.3	59.5
Static effective bearing pressure (kPa)	q'_b	33.3	43.2	59.5
Ratio of uplift to total weight during liquefaction	U/W	1.06	0.96	0
Symmetric superstructure		Y	Y	Y
Fixed base natural frequency (Hz)	f_n	1	1	1
Superstructure width (m)	b	4.8	4.8	4.8
Basement width (m)	B	4.8	4.8	-
Basement depth (m)	D	4.2	4.4	-

In the first two of the preliminary tests, FEH02 and FEH03, structures with basements were tested which were 4.8 m wide at prototype scale. Throughout this thesis, the term "narrow basement" is used to refer to a basement with this width. For the sake of brevity, the results from these two tests will not be discussed it detail. Their behaviour can be summarised in Figure 4.1, where vertical displacement and rotation of the structures are shown by solid lines and the displacement of the soil surface in the far-field is shown by dashed lines. It can be seen that the structures in Tests FEH02 and FEH03 both experienced uplift (Figure 4.1(a)) and clockwise (negative) rotation (Figure 4.1(b)). The uplift of the structure in Test FEH03 was surprising as the upward buoyancy force during liquefaction was less than the total weight of the structure. These two tests suggested that the ratio U/W was too large, and must be below 0.96 for no net vertical displacement to be achieved. This was not anticipated. However, since this was a novel test sequence, it was not possible to compare these observations to any previously conducted tests. To eliminate the possibility of

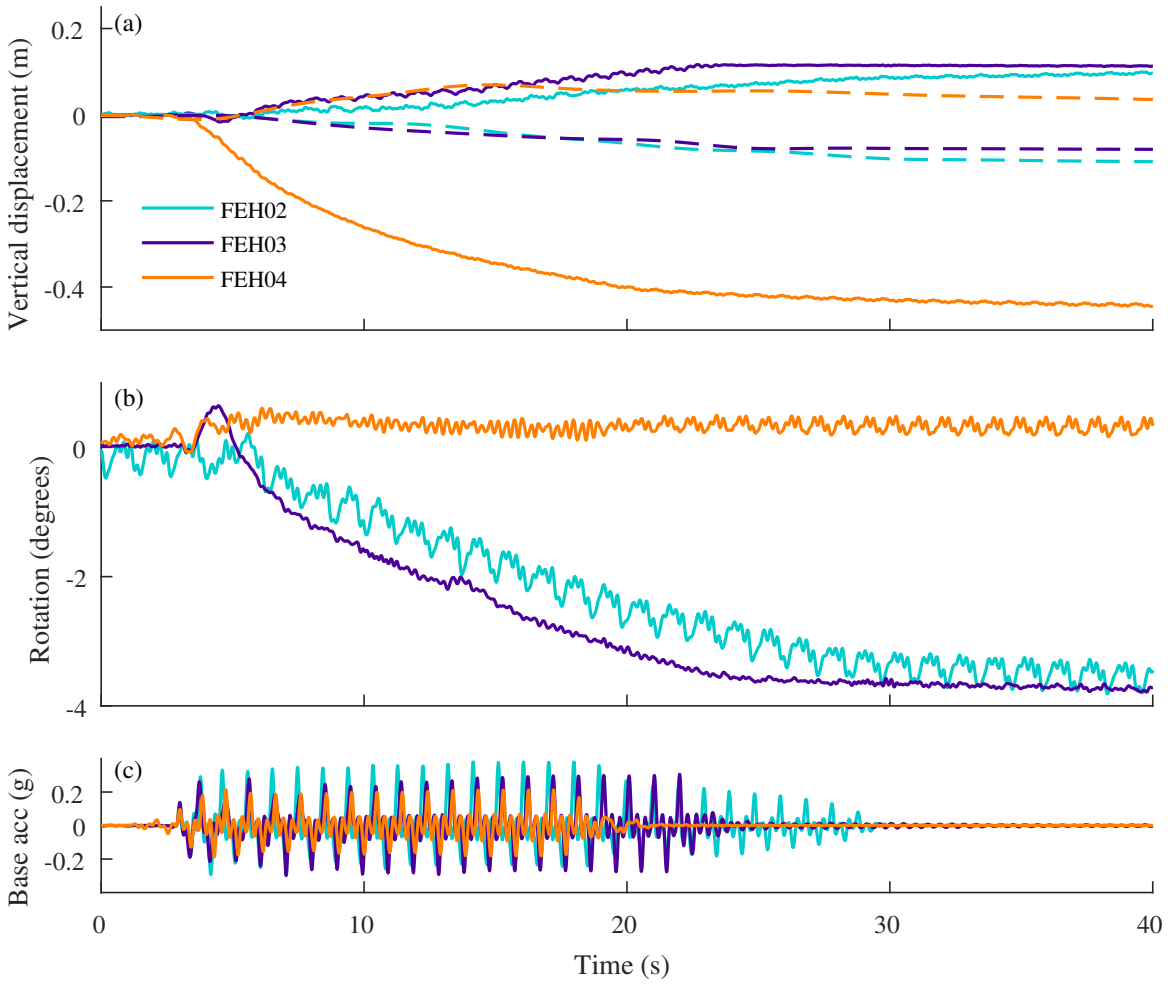

Fig. 4.1 Co-seismic vertical displacement and rotation, prototype scale. (a) Vertical displacement. Structure shown by the solid lines and far-field soil surface by the dashed lines. Settlement is negative vertical displacement and uplift is positive. (b) Rotation. Anticlockwise rotation is positive. (c) Base shaking horizontal acceleration.

model preparation and test setup producing spurious results, a benchmark test was conducted with a structure with a shallow foundation, without a basement, which could be compared to the results obtained by other researchers.

A structure with a shallow foundation was tested in Test FEH04. This structure suffered 0.43 m of settlement, shown in Figure 4.1(a), which is approximately the same liquefaction induced settlement observed by Adamidis & Madabhushi (2018*a*) for a rigid structure with a bearing pressure of 50 kPa, during an earthquake of comparable magnitude. It can therefore be concluded that the uplift of the structures in Test FEH02 and FEH03 were unlikely to be a result of model preparation and setup.

Following this preliminary test series, the decision was made to conduct all future tests in a model container with a transparent PMMA window which allowed digital image correlation to be conducted. The data from the structure with a shallow foundation in Test FEH04 was used as the benchmark test in this chapter. This test was not rerun in the window container due to the recent, extensive research conducted by Adamidis (2017) on the response of structures with shallow foundations to earthquake induced liquefaction, which was conducted in the same window container.

4.3 Influence of a shallow basement on liquefaction induced behaviour of a structure

In this section, the influence of a shallow basement on the co-seismic behaviour of a structure located on liquefiable soil will be presented. The results from two dynamic centrifuge tests will be compared. The properties of the structures are discussed in detail in Chapter 3, and are summarised in Table 4.2. Test FEH04 used a structure with a shallow foundation without a basement, and Test FEH05 used a structure with a basement which was 3 m deep at prototype scale. Throughout this thesis, the term "shallow basement" is used to refer to a basement with this depth. Both structures were single degree of freedom (SDOF) sway frames, with the same natural frequency of 1 Hz and width of 4.8 m at prototype scale. One base shaking event will be discussed for each of the structures. It was a sinusoidal input motion which consisted of 16 cycles with the same frequency as the fixed base natural frequency of the superstructures. The horizontal base shaking had a maximum amplitude of 0.22 g for FEH04 and 0.16 g for FEH05.

Table 4.2 Properties of structures (prototype scale)

Property	Symbol	FEH04	FEH05
Total bearing pressure (kPa)	q_b	59.5	65.3
Static effective bearing pressure (kPa)	q'_b	59.5	38.5
Ratio of uplift to total weight during liquefaction	U/W	0	0.79
Symmetric superstructure		Y	Y
Fixed base natural frequency (Hz)	f_n	1	1
Superstructure width (m)	b	4.8	4.8
Basement width (m)	B	-	4.8
Basement depth (m)	D	-	3.0

4.3.1 Initial vertical stress distribution

In static conditions, an upward buoyancy force, $F_{U,h}$, acts on a structure with a basement due to hydrostatic water pressure, u_h:

$$F_{U,h} = u_h \times A = \gamma_w D \times A = \gamma_w \times V \tag{4.1}$$

where V, A and D are the volume, plan area and depth of the basement respectively and γ_w is the unit weight of water. This uplift force is resisted by the weight of the superstructure, F_S, and basement, F_B, and the shear resistance along the soil-structure interface. Consequently, the effective weight of a structure, and therefore the effective bearing pressure, is reduced when a basement is present compared to when one is not.

The initial vertical effective stress distribution beneath each of the structures tested was found using the software Plaxis 2D (Plaxis 2000) and is shown in Figure 4.2. The superstructures and basement were modelled using effectively rigid, weightless plates with rigid fixities at the joints. The construction sequence was not considered and the structures were wished in place. Uniformly distributed loads were used to match the pressure applied by the superstructure and the basement. The soil was modelled as a Mohr-Coulomb material, with the material properties given in Table 4.3. A very small reference cohesion was required to achieve numerical convergence. $R_{interface}$ was the factor relating the interface strength at the basement-soil interface to the soil strength. Adamidis (2017) conducted shear box tests at a confining pressure of 50 kPa and found the corresponding interface friction angle between the soil and structure to be 28.8 $^\circ$.

The dilatancy angle can be calculated using the stress-dilatancy equations proposed by Bolton (1986), using Equations 4.2 - 4.5. The relative density of a sand, I_D, can be calculated:

$$I_D = \frac{e_{max} - e}{e_{max} - e_{min}} \tag{4.2}$$

where e is the void ratio, e_{max} is the maximum void ratio achievable in a quick-tilt test, and e_{min} is the minimum void ratio achievable by vibratory compaction. The relative crushability, I_C, can be calculated:

$$I_C = \ln \frac{\sigma_c}{p'} \tag{4.3}$$

where p' is the mean effective stress and σ_c is the aggregate crushing stress which is taken to be 20 000 kPa for quartz sand such as Hostun sand. The relative density index, I_R, can then be calculated:

$$I_R = I_D I_C - 1 \tag{4.4}$$

A positive relative density index implies that dilation will occur when the soil is sheared. A zero relative density index corresponds to critical state. In plane strain conditions, the following empirical correlation can subsequently be used to determine the dilatancy angle:

$$\phi_{max} - \phi_{crit} = 5I_R \tag{4.5}$$

At the mid-depth of the model, for the target relative density of 43 %, the relative density index was calculated to be 1.7 and the dilatancy angle was estimated to be 8.6 °. This is in reasonable agreement with published values of the dilatency angle of Hostun sand at low confining stress. For Hostun sand with a relative density of 20 %, Lancelot et al. (2006) showed the dilatency angle to decrease from approximately 5 ° at a confining pressure of 20 kPa to 0 ° at 200 kPa. Heron (2013) reported a dilatency angle of 10.1 ° for Hostun sand with a relative density of 51 % at 80 kPa.

Table 4.3 Plaxis 2D linear-elastic perfectly-plastic Mohr-Coulomb model parameters

Property	Symbol	Value	Reference
Saturated unit weight (kNm^{-3})	γ_s	18.8	
Reference stiffness (MPa)	E_{ref}	20	
Poissons ratio	ν	0.3	
Reference cohesion (kPa)	c_{ref}	0.1	
Critical state friction angle (°)	ϕ_{crit}	35	Heron (2013), Silva (2018)
Dilatancy angle (°)	ψ	8	
Interface reduction factor	$R_{interface}$	0.75	Adamidis (2017)

Figure 4.2(a) shows that, at a given depth, the initial vertical effective stress underneath the structure with a shallow foundation without a basement in Test FEH04 was greater than the initial vertical effective stress in the far-field. The difference was greatest at shallow depths, and decreased with increasing depth. In comparison, Figure 4.2(b) shows that for the structure with a basement in Test FEH05, directly beneath the bottom of the basement the initial vertical effective stress was comparable to that in the far-field at the same depth beneath the ground surface. The contours of constant initial vertical effective stress in Figure 4.2(b) are therefore almost horizontal, which is what would be observed for a level bed of homogenous soil. This makes intuitive sense as the excavation for the basement floors almost compensates for the structure load. Consequently, at the depth of the bottom of the basement, the total vertical stress in the far-field due to the column of soil above that point was only slightly less than the total stress applied by the structure.

The vertical effective stresses shown in Figure 4.2 were indicative of the conditions in the centrifuge models following spin up but prior to shaking. During shaking, soil-structure

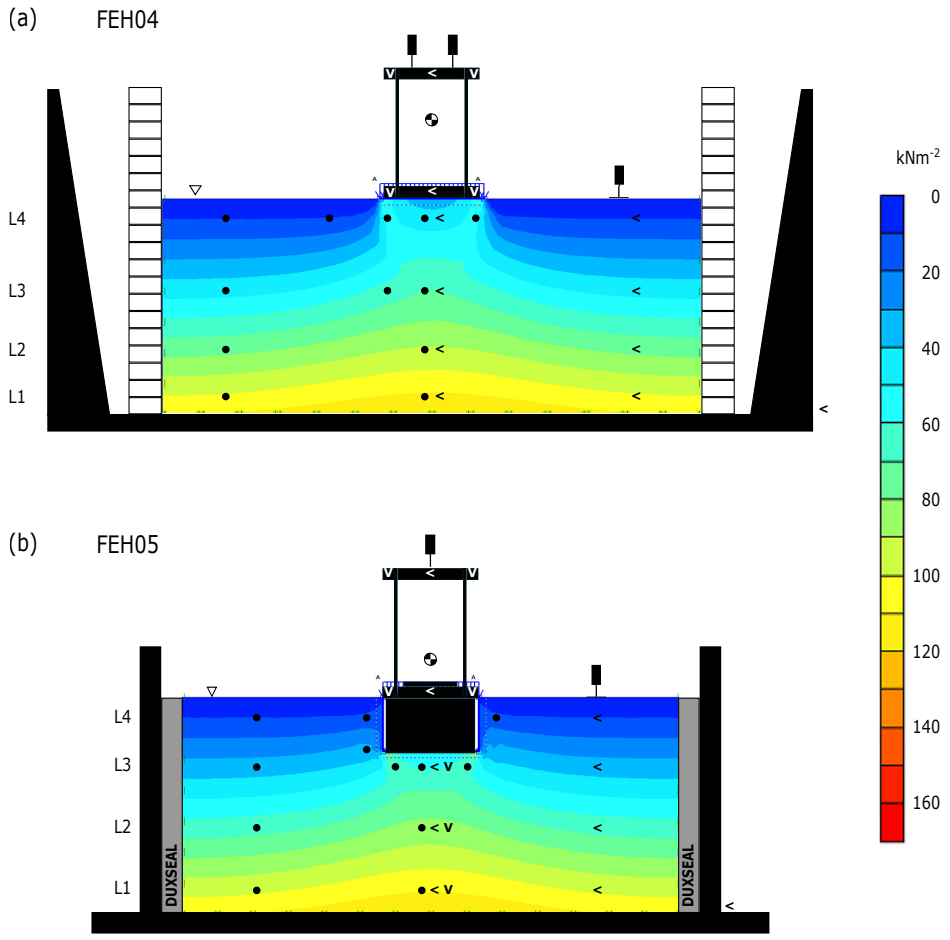

Fig. 4.2 Initial vertical effective stress contours for structures with and without a shallow basement obtained from Plaxis 2D analysis (Plaxis 2000). The initial location of the structure and instrumentation in each model test is shown.

interaction due to rocking and translation of the structure will affect the total vertical stress distribution in the soil. In addition, shearing of the soil can generate excess pore pressures. Both of these mechanisms affect the co-seismic vertical effective stress distribution.

4.3.2 Excess pore pressures

When loose, saturated, sandy soils are subjected to cyclic loading, the tendency to contract when sheared can result in the generation of positive excess pore pressures. When positive excess pore pressures are generated, the uplift force due to the basement, F_U, increases to greater than the hydrostatic value, $F_{U,h}$, because excess pore pressures, u_{ex}, act on the bottom

of the basement in addition to the hydrostatic pressure present in the static analysis:

$$F_U = F_{U,h} + (u_{ex} \times A) \tag{4.6}$$

If the soil is in vertical equilibrium, the maximum absolute pore pressure attainable is equal to the total vertical stress, which equates to the positive excess pore pressure being equal to the initial vertical effective stress. This corresponds to liquefaction. The uplift force during liquefaction, $F_{U,L}$, can be considered in two ways.

Firstly, the positive excess pore pressures generated, u_{ex}, act on the bottom of the basement in addition to the hydrostatic pressure present in the static analysis:

$$F_{U,L} = F_{U,h} + (u_{ex} \times A) = F_{U,h} + (\gamma_s' D \times A) = (\gamma_w + \gamma_s') \times V = \gamma_s V \tag{4.7}$$

where γ_s and γ_s' are the saturated and buoyant unit weight of the soil respectively.

Alternatively, the total uplift force can be calculated using Archimedes' principle, assuming the soil behaves as a dense fluid when liquefied. Archimedes' principle states that any body completely or partially submerged in a fluid at rest is acted upon by an upward, buoyant force, the magnitude of which is equal to the weight of the fluid displaced by the body:

$$F_{U,L} = \gamma_s V \tag{4.8}$$

Equations 4.7 and 4.8 show that these methods are equivalent when liquefaction occurs and the positive excess pore pressure generated is equal to the initial vertical effective stress in the soil.

Figure 4.3 shows the excess pore water pressures generated in Tests FEH04 and FEH05 in the instrumented columns of soil underneath the centre of the structures and in the far-field. Unfortunately, the pore pressure transducer (PPT) in L1 in the far-field for Test FEH05 malfunctioned during the test, and is therefore not shown. The dashed horizontal lines show the initial vertical effective stress at the corresponding instrument location, obtained from the Plaxis 2D analysis presented in Figure 4.2. When the excess pore pressure measured at an instrumented location approached the corresponding initial vertical effective stress, the instantaneous value of the vertical effective stress approached zero and liquefaction occurred.

The base shaking was sufficiently large to cause positive excess pore pressures to be quickly generated at all depths in the far-field and below the centre of the structures (Figure 4.3). In the far-field, the magnitude of the excess pore pressures quickly approached the value of the initial vertical effective stress indicating that liquefaction occurred. This occurred for all instrumented depths in Test FEH04 (Figures 4.3(b,d,f,h)), but only at shallow depths in

Test FEH05 (Figures 4.3(b,d)). The difference in behaviour at greater depths is anticipated to be a result of the greater amplitude of horizontal base shaking in FEH04 than FEH05 (0.22 g compared to 0.16 g). This difference in amplitude was not intentional, but a result of the limited control and repeatability of the SAM earthquake actuator used to simulate the earthquakes.

It is evident from Figure 4.3 that, for a given test and a given depth, the magnitude of the excess pore pressures generated in the far-field and underneath the structure were comparable. However, the dashed horizontal lines in Figure 4.3 and the contours in Figure 4.2 show that the corresponding initial vertical effective stresses were not the same. Consequently, liquefaction only occurred at the deepest instrumented depth (L1) beneath the structure with a shallow foundation without a basement (Figure 4.3(g)), and not at shallower depths where the initial vertical effective stress was greater than at the same depth in the far-field (Figure 4.3(a,c,e)). A region of non-liquefied soil formed at shallow depths in the column of soil beneath the structure, below and to the side of which liquefaction occurred. This is in agreement with the strains observed by Adamidis & Madabhushi (2018*a*) for a rigid structure, with a similar bearing pressure, resting on a deep liquefiable layer, during an earthquake of comparable magnitude.

At shallow depths below the structure with a basement, the initial vertical effective stress was less than at the equivalent depth below the structure without a basement, and was closer to the corresponding value at the same depth in the far-field. The excess pore pressure at the shallowest instrumented depth beneath the basement reached 72 % of the corresponding initial vertical effective stress (Figure 4.3(c)). This implies that liquefaction did not occur. However, significant soil softening will have occurred at this depth.

4.3.3 Transmission of horizontal accelerations

Horizontal accelerations caused by an earthquake are transmitted upwards through a soil layer by horizontally polarised, vertically propagating shear waves. The transmission of these accelerations to structures located on top of, or within, the soil results in horizontal inertia forces. These can damage structural components, depending on the amplitude and frequency of the accelerations in relation to properties of the structure.

Horizontal accelerations were measured at discrete locations in the soil body and on the structures. The left-hand column of Figure 4.4 shows the horizontal acceleration time histories for the roof and ground floor of the structures and the column of soil below the centre of the structures. The right-hand column of Figure 4.4 shows the horizontal acceleration time histories for the instrumented column of soil in the far-field. The general trend evident in Figure 4.4 is that the horizontal accelerations were attenuated as they were transmitted

upwards. However, the pattern was different beneath the two structures. Below the centre of the structure with a shallow foundation in Test FEH04, attenuation was progressive between each of the instrumented layers with the biggest decrease occurring between levels L1 (Figure 4.4(i)) and L2 (Figure 4.4(g)), deep in the soil layer. In contrast, beneath the basement of the structure in Test FEH05, the biggest decrease in amplitude of the horizontal acceleration occurred at a shallower depth between levels L2 (Figure 4.4(g)) and L3 (Figure 4.4(e)). These differences are consistent with the recorded excess pore pressures shown in Figure 4.3.

When the excess pore pressures approached the corresponding initial vertical effective stress, shown in Figure 4.3, the instantaneous vertical effective stress approached zero. The near zero vertical effective stress state caused a very large stiffness degradation, which reduced the ability of the soil to carry shear stress and therefore transmit shear waves. For the structure with a shallow foundation and no basement in Test FEH04, this occurred at the deepest layer of instrumentation, L1. This isolated the entire column of soil above: horizontal accelerations above this depth were attenuated despite liquefaction not occurring at the corresponding depth. In contrast, attenuation occurred at a much shallower depth, L3, where significant soil softening occurred.

In both tests, the horizontal accelerations transmitted to the ground floor of the structures, shown in Figure 4.4(b), were significantly smaller than those generated by the base shaking. Liquefaction beneath the structures therefore naturally isolated them from the base shaking acceleration. Horizontal accelerations transmitted to the ground floor of the structures were then amplified at the roof level, as shown in Figure 4.4(a), due to the flexible nature of the SDOF superstructure. The superstructures in both tests had a fixed base natural frequency equal to the frequency of the sinusoidal base shaking. However, the presence of the basement, specifically the effective stress at shallow depths directly beneath the structure and the embedment in the soil layer, is likely to have resulted in the natural frequency of the soil-structure systems differing. For the structure with a basement in Test FEH05 the amplitude of the accelerations at roof level remained less than the base shaking. The same is true for Test FEH04, however the amplitude of the horizontal accelerations at roof level incrementally increased during the last 10 seconds of base shaking. This observation is anticipated to be an consequence of differences in soil damping.

The observed drift in the measured horizontal acceleration of the structure in Test FEH05, shown in Figures 4.4(a,b), was caused by the accumulated rotation of the structure, which is discussed in detail in Section 4.3.4. As the accumulated rotation of the structure increased, the MEMS accelerometers recorded an increasing component of the centrifugal acceleration.

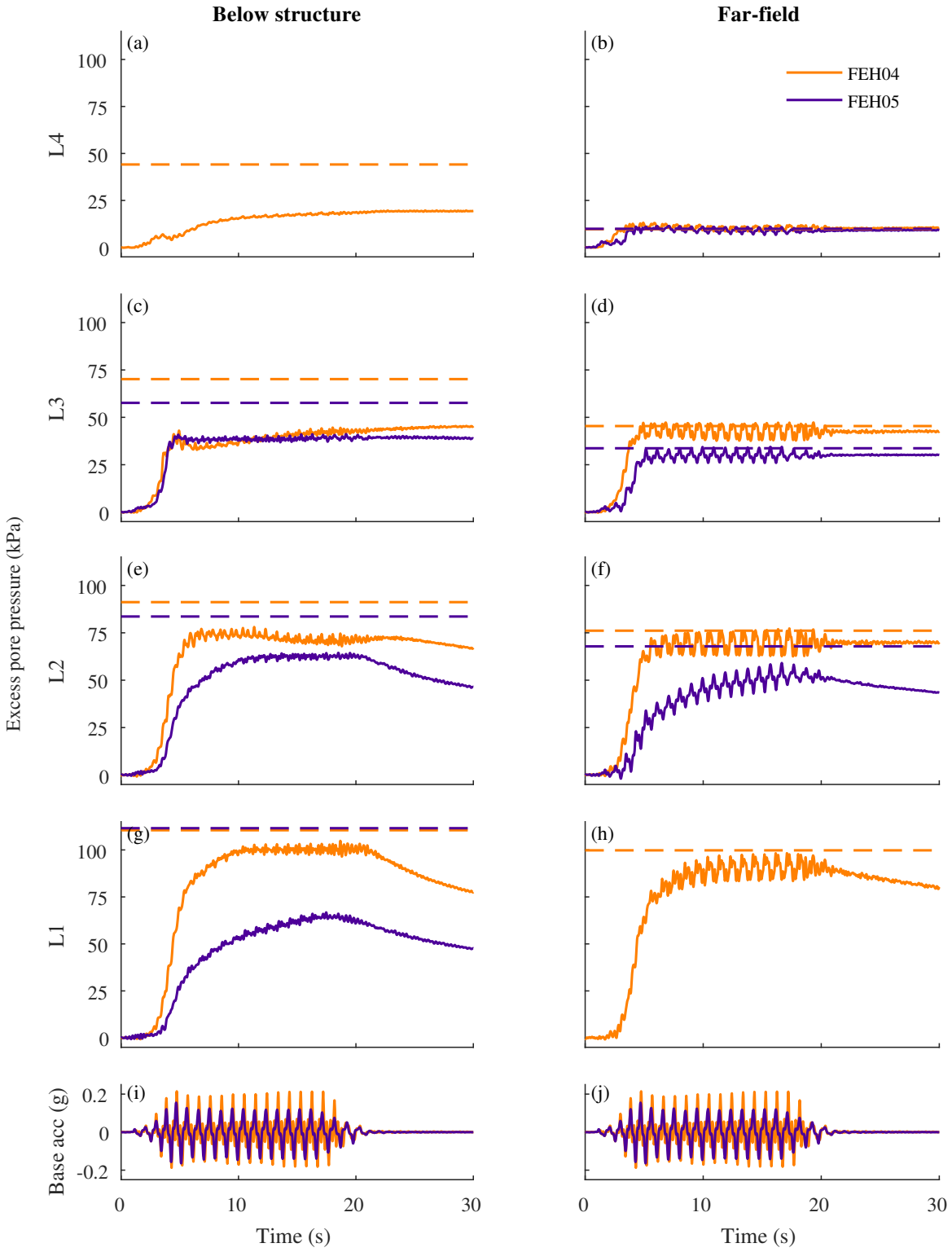

Fig. 4.3 Excess pore water pressure time histories for the instrumented column beneath the centre of the structure (left-hand column) and in the far-field (right-hand column). L*N* indicates the level of instrumentation, with *N* increasing with decreasing depth, as shown in Figure 4.2. Dashed lines indicate the initial vertical effective stress at the corresponding instrument location, obtained from Plaxis 2D analysis.

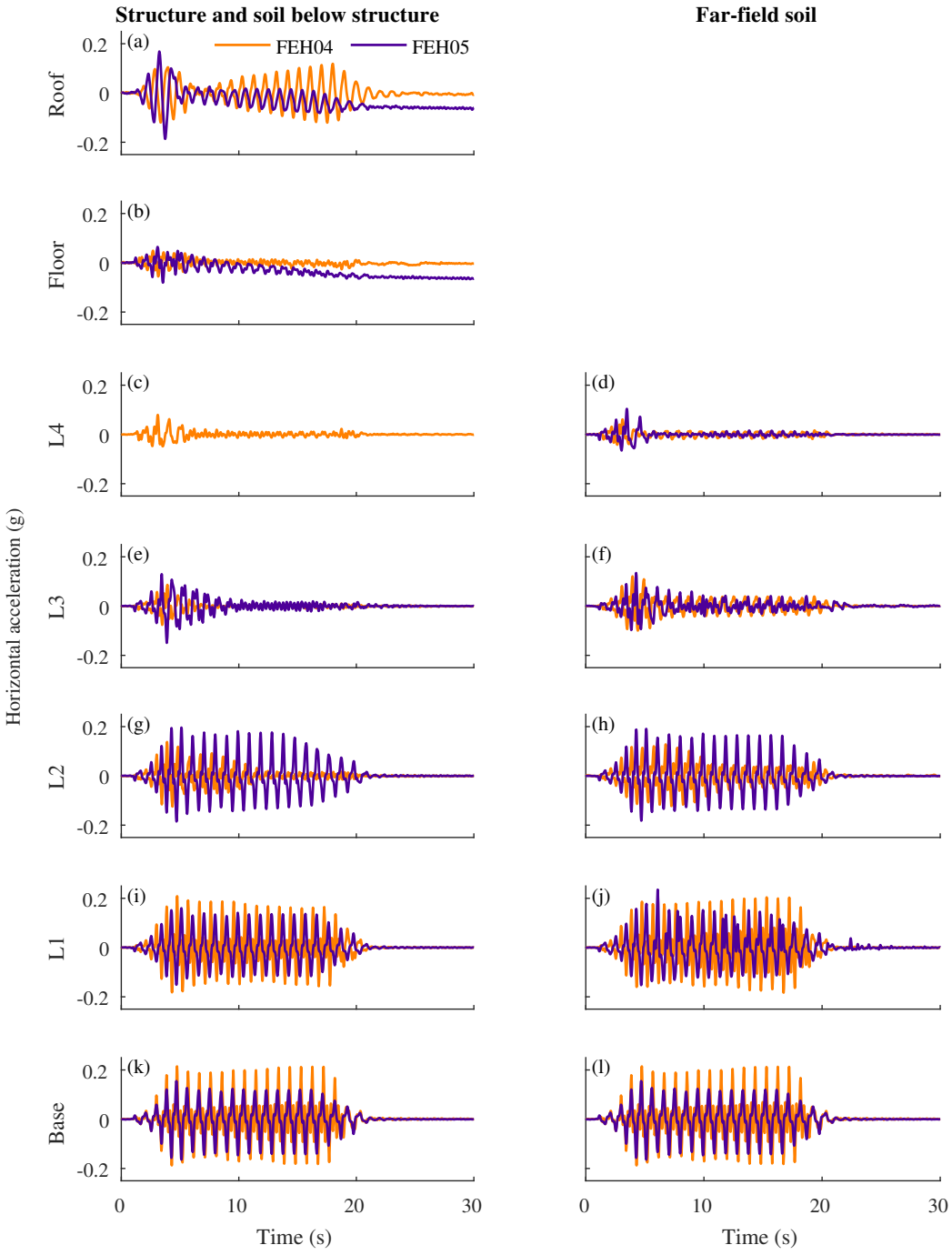

Fig. 4.4 Co-seismic horizontal acceleration time histories. Left-hand column: structure, the soil column below it and the input motion. Right-hand column: far-field and input motion. L*N* indicates the level of instrumentation in the soil, with *N* increasing with decreasing depth, as shown in Figure 4.2.

4.3.4 Displacement and rotation of the structures

It is desirable that a structure neither settles nor rotates during an earthquake. However, the increase in loading imposed by the structure on the surrounding soil and the concurrent decrease in resistance provided by the soil mean that, during earthquake shaking, structures can be susceptible to settlement and rotation.

The co-seismic change in vertical displacement and rotation of the structures in Tests FEH04 and FEH05 are shown by the solid lines in Figure 4.5. The displacements presented are for the centre of the bottom of the ground floor of the superstructure. Negative vertical displacement corresponds to settlement of the structure and positive vertical displacement corresponds to uplift. Anticlockwise rotation is taken to be positive. It is desirable that the structures do not experience displacement or rotation. For FEH05, the co-seismic vertical displacement and rotation were obtained using GeoPIV-RG (White et al. 2003, Stanier et al. 2015). The vertical displacement of the structure with no basement in Test FEH04 was measured using LVDTs. The vertical displacement of the soil surface adjacent to the structures is shown by the dashed lines in Figure 4.5(a), and was measured using an LVDT positioned to the right-hand side of each structure.

The structure with no basement in Test FEH04 settled 430 mm, prototype scale, as shown in Figure 4.5(a). Most of this was accumulated during the co-seismic period, with a small amount occurring post-shaking. This is a comparable magnitude to settlement found in dynamic centrifuge testing by other researchers investigating liquefaction induced settlement of structures with shallow foundations, without a basement, located on deep layers of liquefiable soil (Bertalot & Brennan 2015, Adamidis & Madabhushi 2018*a*). The structure in Test FEH04 experienced minimal residual rotation, totalling less than 0.5 °. The presence of a basement in Test FEH05 had the positive desired effect of notably reducing the settlement of the structure to 150 mm, as shown in Figure 4.5(a). However, greater rotation occurred. The structure with a basement accumulated anticlockwise rotation at an approximately constant rate during shaking, totalling 4.0 ° at the end of shaking, as shown in Figure 4.5(b). The structure did not self-right during shaking. Rotation and settlement of the structure stopped when shaking ceased.

The dashed lines in Figure 4.5(a) show the displacement of the soil surface in the far-field on the right-hand side of the structures. Settlement of the soil surface adjacent to the structure in Test FEH05 was of a comparable magnitude to that of the structure. In contrast, heave occurred adjacent to the structure with a shallow foundation in Test FEH04. This is likely to be due to a "punch-type" failure mechanism, which caused soil beneath the structure to be displaced sideways and upwards as the structure moved downwards into the soil layer. The differential displacement between the structure and the adjacent soil was therefore increased.

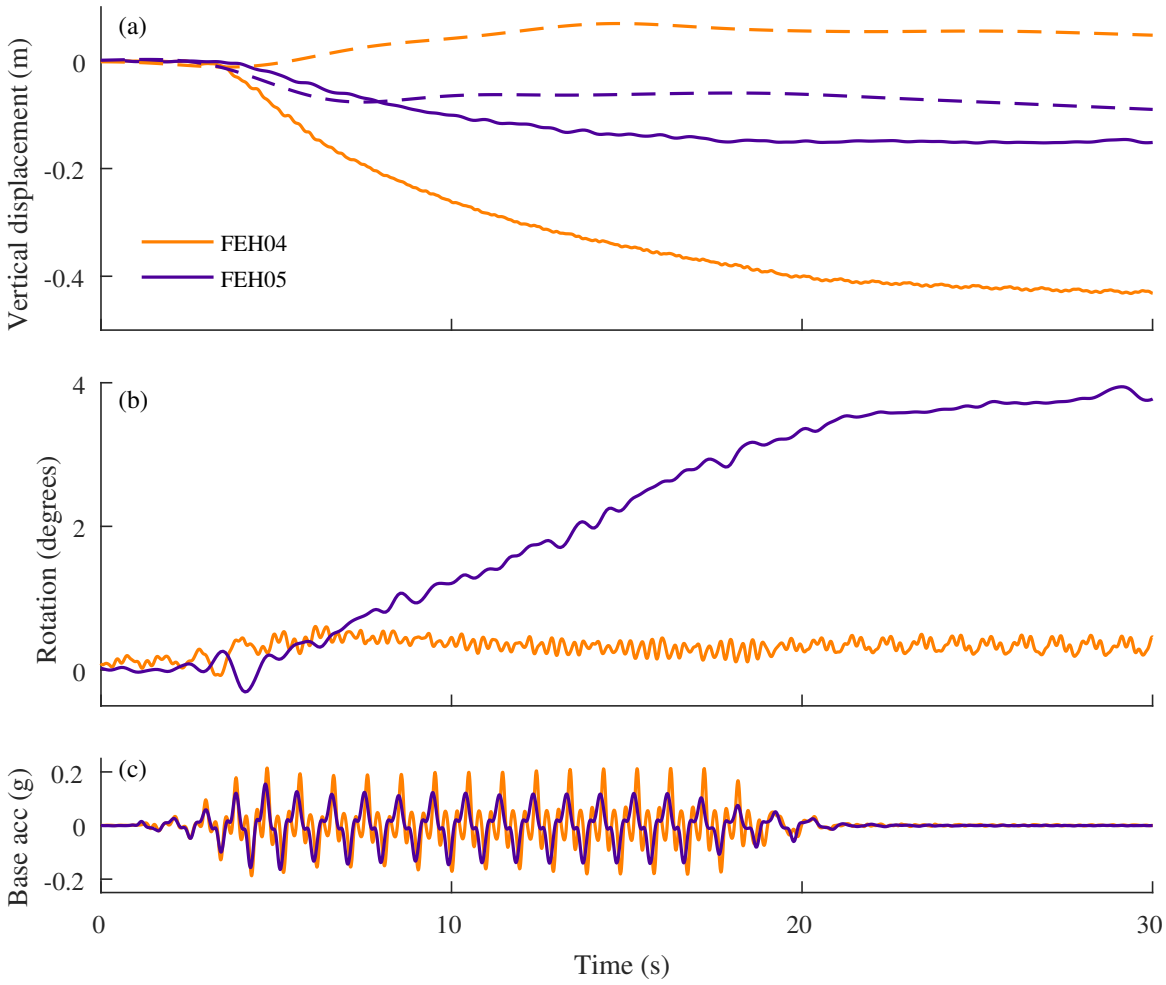

Fig. 4.5 Co-seismic vertical displacement and rotation, prototype scale. (a) Vertical displacement. Structure shown by the solid lines and far-field soil surface by the dashed lines. Settlement and uplift are negative and positive vertical displacement respectively. (b) Rotation. Anticlockwise rotation is positive. (c) Base shaking horizontal acceleration.

4.3.5 Analogy with stability of ships

The stability of structures with basements during earthquake induced liquefaction can be compared to the stability of ships. Both are partially submerged bodies with a buoyancy force of the same order of magnitude as their total weight, which are subjected to time varying horizontal loading - ships by waves and structures by earthquakes.

When a partially submerged object rotates its centre of buoyancy, CoB, moves, whilst its centre of gravity, CoG, remains at a fixed position. In naval engineering, the metacentre, MC, is defined as the point of intersection of a line drawn through the centre of buoyancy perpendicular to the water surface when the object is in equilibrium and the same line drawn

when the object is tilted (Biran 2003). This is shown in the schematics in Figure 4.6. For ships that are floating, the total uplift force, Δ, is equal to the total weight of the ship, W. Knowing the location of the metacentre is sufficient to know if the ship is stable, wherever it is rotating about. If the metacentre is above the centre of gravity, as in Figure 4.6(b), then the ship is stable because the couple acting on the titled ship due to the non-co-linear weight and buoyancy force will re-right the ship. If the metacentre is below the centre of gravity, as in Figure 4.6(c), then the ship is not stable, and will not self-right after being titled. Having the metacentre above the centre of gravity of a ship is relatively easy to achieve by positioning weight low down in the ship (i.e. cargo in the hull).

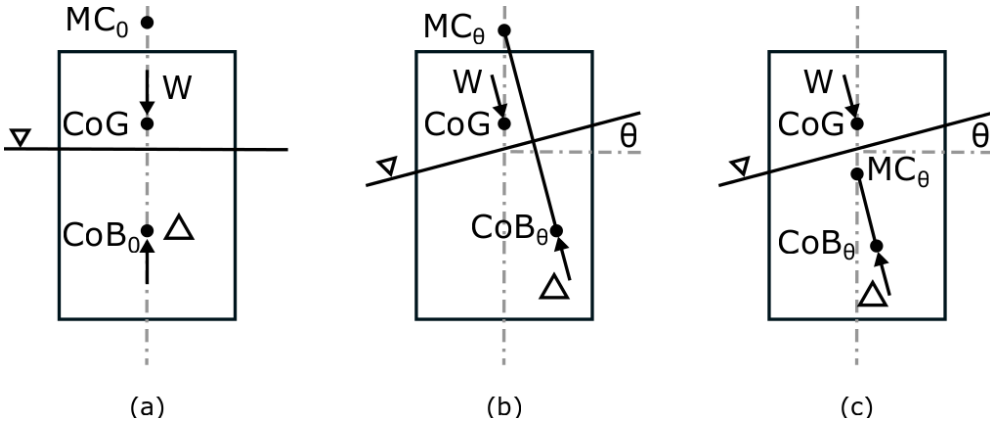

Fig. 4.6 Conditions of initial stability of a ship, after Biran (2003). The weight, W, acts through the centre of gravity, CoG. The buoyancy force, Δ, acts through the centre of buoyancy, CoB. (a) Upright, (b) Stable ship with metacentre, MC_θ, above the centre of gravity. Ship inclined by angle θ in the clockwise direction, (c) Unstable ship with metacentre, MC_θ, below the centre of gravity. Ship inclined by angle θ in the clockwise direction.

First let us assume that when liquefaction occurs, liquefied soil behaves as a dense fluid. We can then compare the co-seismic stability of structures with basements to the stability of ships. For structures with basements, it is more difficult to have the centre of gravity below the metacentre because the majority of the structure mass is above ground. An added complication to the analogy with the design and behaviour of ships is that the uplift provided by the basement during liquefaction is not necessarily equal to the total weight of the structure. This means that knowing the location of the metacentre is not sufficient to know if the structure is self-righting. If the metacentre is below the centre of gravity, analogous to Figure 4.6(c), the structure is not stable and will not self-right. If the metacentre is above the centre of gravity, analogous to Figure 4.6(b), then it is possible that the structure is stable and self-righting, but it is not guaranteed. Since the forces are not equal, the lever arm for

the forces about the centre of rotation is required to calculate the direction of the resultant moment.

Liquefied soil only momentarily behaves as a dense fluid. When sheared, liquefied soil can dilate and cause a transient increase in resistance. In contrast to ships, the stability of partially submerged structures in saturated soils, such as structures with basements, can therefore be increased by shearing of the soil adjacent to the structure. This is another reason why the location of the metacentre cannot define whether a structure with a basement is stable.

For the structure with a basement in Test FEH05, the metacentre was below the centre of gravity. Therefore, the couple due to the non-co-linear weight and buoyancy forces will not re-right the structure when it is rotated. The rotation of the structure shown in Figure 4.1(b) is evidence that the additional resistance provided by the shear dilation of the liquefied soil only hindered this rotation and was insufficient to prevent the structure from rotating completely.

4.3.6 Soil displacements

Soil displacements were obtained for the structure with a basement using GeoPIV-RG (White et al. 2003; Stanier et al. 2015). Total co-seismic soil displacements are shown as vectors in Figure 4.7(a) and as contours in Figures 4.7(b,c). The position of the basement at the end of shaking is shown. The soil displacements shown are relative to the movement of the rigid model container and are plotted at the initial location of each tracked patch. In these figures the horizontal edges of the container are at 0 and 25 m on the x-axis and the base is at 0 m on the y-axis.

As expected from the structural rotation shown in Figure 4.5(b), asymmetry in the soil displacements was observed below the structure with a basement in Test FEH05 presented in Figure 4.7. The generation of positive excess pore pressure and associated stiffness and strength loss in the soil below and to the sides of the basement allowed soil-structure induced building ratcheting to cause the weakest underlying soil to be displaced laterally away from underneath the structure. Rotation occurred about the bottom right-hand edge of the basement. Therefore, the greatest soil displacements occurred to the left of, and below the bottom left of, the basement as the structure moved into this space. Below the bottom of the basement and at a distance of $B/3$ from the left-hand corner (where B is the width of the basement), soil displaced vertically downwards with no horizontal component. To the left and right of this, vertical displacement was accompanied by horizontal displacement, to the left and right respectively, as shown in Figure 4.7(b). No gap was formed underneath the basement.

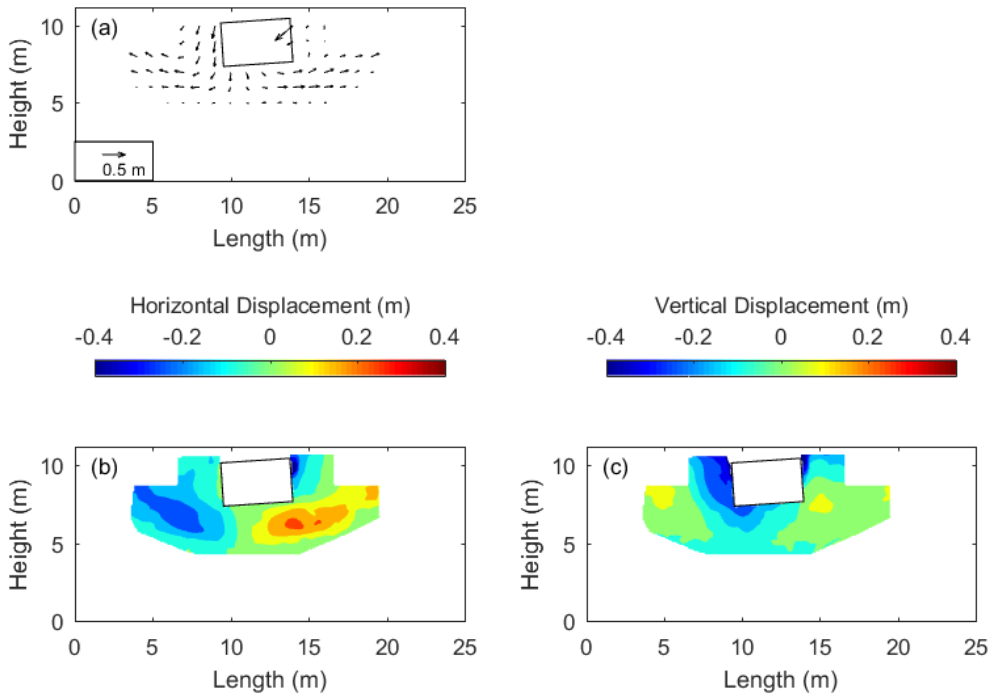

Fig. 4.7 Total co-seismic soil displacement around a structure with a basement in Test FEH05 (a) Displacement vectors, (b) Horizontal displacement contours, (c) Vertical displacement contours. Location of basement at the end of shaking shown. Note: soil displacements are plotted with a magnification factor of 3 relative to the basement and model container.

Instead, the liquefied soil moved with the rotating basement. Sand accumulated below the basement, resulting in accumulation of permanent rotation, as seen in Figure 4.5(b).

This can be compared to the liquefaction induced soil displacements observed by Adamidis (2017) for a rigid structure with a shallow foundation and a bearing pressure of 50 kPa, located on a 11 m deep layer of saturated, loose Hostun sand, which are shown in Figure 4.8. Given the comparable bearing pressure, depth of liquefiable soil and liquefaction induced settlement, it is logical to assume that these soil displacements are representative of the behaviour that occurred in Test FEH04. Figure 4.8 shows that the accumulated vertical and horizontal displacements were almost symmetric about the centreline of the structure. Vertical displacement was greatest in magnitude directly below the structure, and decreased with increasing depth. Heave of the soil was observed adjacent to the structure.

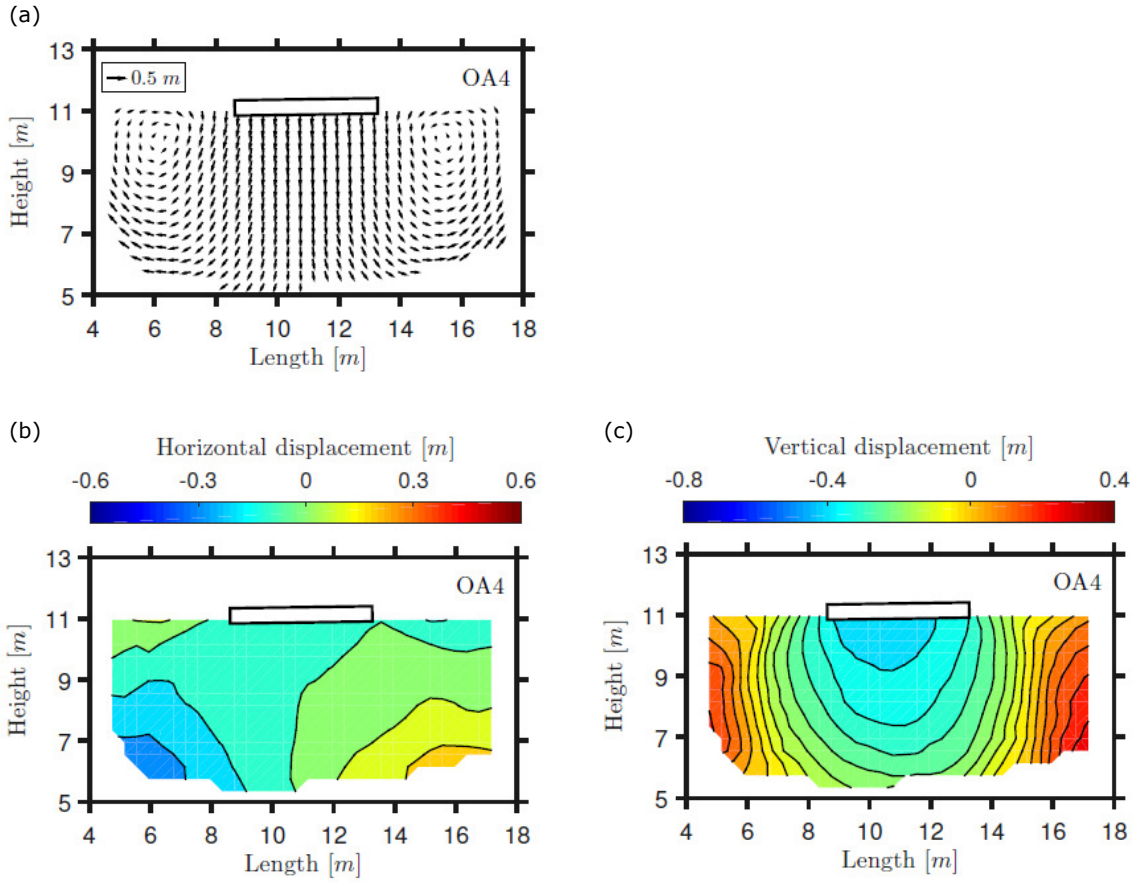

Fig. 4.8 Soil displacement beneath a structure with a shallow foundation, 50 kPa bearing pressure, on an 11 m deep layer of saturated, loose Hostun sand following 16 cycles of sinusoidal shaking with a peak acceleration of 0.22 g from Adamidis (2017). (a) Displacement vectors, (b) Horizontal displacement contours, (c) Vertical displacement contours.

4.3.7 Effect of a shallow basement of liquefaction induced behaviour of a structure

In this section, the influence of a shallow basement on the co-seismic behaviour of a structure located on liquefiable soil has been presented. The presence of a basement was shown to have the desirable effect of notably reducing the liquefaction induced settlement of the structure. The buoyancy force provided by the basement prevented the structure with a basement settling as much as a structure without a basement. However, the presence of a basement caused increased rotation of the structure. Rotation occurred about the bottom edge of the basement and was accumulated at an approximately constant rate during shaking. The couple due to the non-co-linear weight and buoyancy force did not re-right the structure. Insufficient resistance was provided by the shear dilation of the liquefied soil adjacent to the structure to prevent the structure rotating.

Liquefaction had the beneficial effect of reducing the seismic demand of the structures. The presence of a basement changed the mechanism through which isolation occurred. For the structure with a shallow foundation and no basement, significant soil softening occurred deep in the soil layer beneath a bulb of non-liquefied soil that formed at shallow depths directly beneath the structure. In contrast, the positive excess pore pressures generated directly below the structure with a basement reached 72 % of the corresponding initial vertical effective stress, which sufficiently softened the soil to isolate the structure.

It is interesting to compare this behaviour to conventional remediation methods used to reduce liquefaction induced settlement of structures. Ground improvement methods are commonly used to remove or reduce the tendency for soil to liquefy, for example soil improvement (Coelho et al. 2007, Mitrani & Madabhushi 2010, Olarte, Dashti, Liel & Paramasivam 2018, Olarte, Dashti & Liel 2018), reducing the degree of saturation of the soil (Zeybek & Madabhushi 2016) and improving drainage using vertical drains (Paramasivam et al. 2017). However, these methods have the result of increasing the seismic demand of the structure (Zeybek & Madabhushi 2016, Olarte, Dashti, Liel & Paramasivam 2018, Olarte, Dashti & Liel 2018). By reducing the extent of soil liquefaction the natural isolation provided by attenuation of horizontal accelerations in liquefied soil is removed.

It is proposed that basement storeys can be used to reduce the liquefaction induced settlement of structures whilst maintaining the natural isolation provided by liquefied soil. However, a means to reduce rotation and improve stability must be found.

4.4 Using rigid extenders to improve the seismic stability of structures with basements

A series of dynamic centrifuge tests were conduced to investigate methods to improve the stability of structures with basements during earthquake induced liquefaction, whilst keeping the width and depth of the basement unchanged. Methods used in naval engineering to improve the stability of ships were used as inspiration (Biran 2003). The use of a bilge keel to reduce a ship's tendency to roll suggested that vertical extenders protruding below the bottom of a basement should improve the co-seismic stability of structures with basements during liquefaction. Likewise, the use of outriggers to improve a ship's stability suggested that horizontal extenders protruding from a basement should also improve the stability of the structures being considered.

4.4.1 Dynamic behaviour of basement-structure system

Three dynamic centrifuge tests were conducted using structures with narrow, shallow basements and rigid, impermeable extenders. The properties of the structures are discussed in detail in Chapter 3, and are summarised in Table 4.4. All three tests included a symmetric, single degree of freedom (SDOF) superstructure which was rigidly connected to a basement of the same width. The enclosed basements had the same dimensions as the basement used in Test FEH05, which was discussed in Section 4.3. Images obtained from the high-speed camera during shaking showed that the extenders attached to the basements did not bend.

Test FEH09 had the same U/W as Test FEH05. The displacements observed in Test FEH09, which will be discussed in detail in Section 4.4.6, resulted in U/W being increased

Table 4.4 Properties of structures with narrow basements and extenders (prototype scale)

Property	Symbol	FEH09	FEH10	FEH11
Total bearing pressure (kPa)	q_b	68.1	59.4	59.5
Static effective bearing pressure (kPa)	q'_b	41.4	32.5	32.6
Ratio of uplift to total weight during liquefaction	U/W	0.80	0.91	0.93
Fixed base natural frequency (Hz)	f_n	1	1	1
Basement width (m)	B	4.8	4.8	4.8
Basement depth (m)	D	3.0	3.0	3.0
Extrusions from basement		Vertical	Vertical	Horizontal
Dimensions of extrusions (m)	b × d	0.2 × 3.0	0.2 × 3.0	2.4 × 0.2
Extrusion bending stiffness (MNm^2)	EI	402	402	402

for Tests FEH10 and FEH11. Tests FEH09 and FEH10 included rigid vertical extenders made of sheet aluminium which were rigidly connected to either side of the basement. They extended 3.0 m below the bottom of the basement and therefore extended to half the depth of the liquefiable soil layer. They were included for two purposes. Firstly, to investigate whether they could be used to improve the co-seismic stability of the structure. This is analogous to the use of a bilge keel to reduce a ship's tendency to roll. Secondly, they were included to more accurately replicate a realistic basement. In practice, construction of shallow basements often involves the installation of diaphragm walls prior to excavating to the required depth, and subsequently casting the base slab (Tomlinson 2001). The diaphragm walls usually extend to a depth of 2 – 3 m below the depth of the base slab to ensure that the excavation is stable and heave is prevented before the slab is cast. They are normally left in place following construction. Temporary props at intermediate depths are also required in some ground conditions for stability. This method of construction can be used to minimise the impact of construction on neighbouring structures.

Test FEH11 included a rigid horizontal extender made of sheet aluminium rigidly connected to the bottom of the basement. It extended 2.4 m either side of the basement. It was included to try to improve co-seismic stability, and is analogous to the use of an outrigger to improve a ship's stability. In practice, these horizontal extrusions could be horizontal grouted anchors (Figure 4.9). It would be possible to construct a continuous wide bottom slab, using diaphragm walls as previously described, and then construct a basement above with a narrower width than this slab. However, this is unlikely to be economical. Careful consideration of the structural capacity of the horizontal extenders would be required in practice, particularly the capacity in bending and the shear connection to the basement.

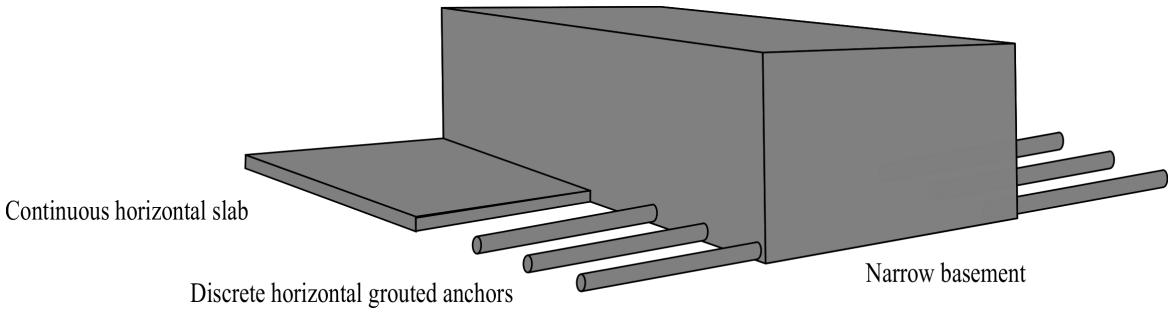

Fig. 4.9 Horizontal extrusions: a continuous horizontal slab or discrete horizontal grouted anchors.

Three base shaking events are discussed in this chapter for each of the structures with basements and extenders. The base shaking events differed in duration, peak acceleration, and frequency content. The first earthquake, EQ1, had a low amplitude, sinusoidal input

motion, consisting of 20 cycles with the same frequency as the fixed base natural frequency of the corresponding superstructure shown in Table 4.4. EQ1 had a peak acceleration of approximately 0.03 g. The second earthquake, EQ2, had the same frequency content as the 1979 Imperial Valley earthquake, which was characterised by its long duration and high frequency content, and was scaled to have a peak acceleration equal to 0.1 g. The third earthquake, EQ3, was a high amplitude, sinusoidal input motion with the same frequency as EQ1. It consisted of 20 cycles for Tests FEH09 and FEH10, and 15 cycles for Test FEH11. EQ3 had a peak acceleration of approximately 0.4 g.

The soil relative density prior to each earthquake event varied slightly, because soil densification occurred as a result of each of the sequential shaking events. For example, for Test FEH10, the relative density was 47 %, 47 % and 54 %, before EQ1, EQ2 and EQ3 respectively. These relative densities were calculated using the mass of sand in the model container and the volume occupied before each shaking event commenced. The pre-seismic soil condition remained susceptible to liquefaction prior to each earthquake, therefore it is assumed that the soil behaviour during each of the seismic events can be compared.

4.4.2 Initial vertical stress distribution

The initial vertical effective stress distribution beneath each of the structures tested was found using the software Plaxis 2D (Plaxis 2000) and is shown in Figure 4.10. The basements and extenders were modelled using effectively rigid, weightless plates with rigid fixities at the joints. Uniformly distributed loads were used to match the pressure applied by the superstructure and the basement. The soil was modelled as a Mohr-Coulomb material, with the material properties given in Table 4.3. The soil-structure interface was modelled to have an interface friction angle of 28.8 °, which corresponds to the interface friction angle between the soil and structure obtained by Adamidis (2017) from shear box tests at a confining pressure of 50 kPa.

In static conditions an upward buoyancy force, $F_{U,h}$, acts on the structures due to hydrostatic water pressure. This uplift force is resisted by the weight of the superstructure, F_S, and the basement, F_B, and the shear resistance along the soil-structure interface. Both vertical and horizontal extenders increase the resistance to uplift in static conditions. The vertical extenders increase the resistance by increasing the surface area of the soil-structure interface, whilst the horizontal extenders increase resistance due to the weight of soil overlying them. A resultant vertical force acts downwards, which results in an effective bearing pressure on the soil below.

Figure 4.10 shows that, at a given depth, the initial vertical effective stress underneath each of the basements was greater than the initial vertical effective stress in the far-field.

However, the difference was small and reduced with increasing depth. Exceptions to this are the points below the bottom of the vertical extenders where there were localised areas of increased vertical effective stress. These show that the extenders transferred some of the load of the structures to deeper in the soil layer. This is more pronounced in Test FEH09 because the structure was heavier than that in Test FEH10. The contours of constant initial vertical effective stress in Figure 4.10 are therefore almost horizontal, which is what would be observed for a level bed of homogenous soil. This makes intuitive sense as the excavation for the basement floors almost compensates for the structure load. Consequently, at the depth of the bottom of the basement, the total stress in the far-field due to the column of soil above that point was only slightly less than the total stress applied by the structure.

The vertical effective stresses shown in Figure 4.10 were indicative of the conditions in the centrifuge models following spin up but prior to shaking. During shaking, soil-structure interaction due to rocking and translation of the structure will affect the total stress distribution in the soil. In addition, shearing of the soil can generate excess pore pressures. Both of these mechanisms affect the co-seismic vertical effective stress distribution.

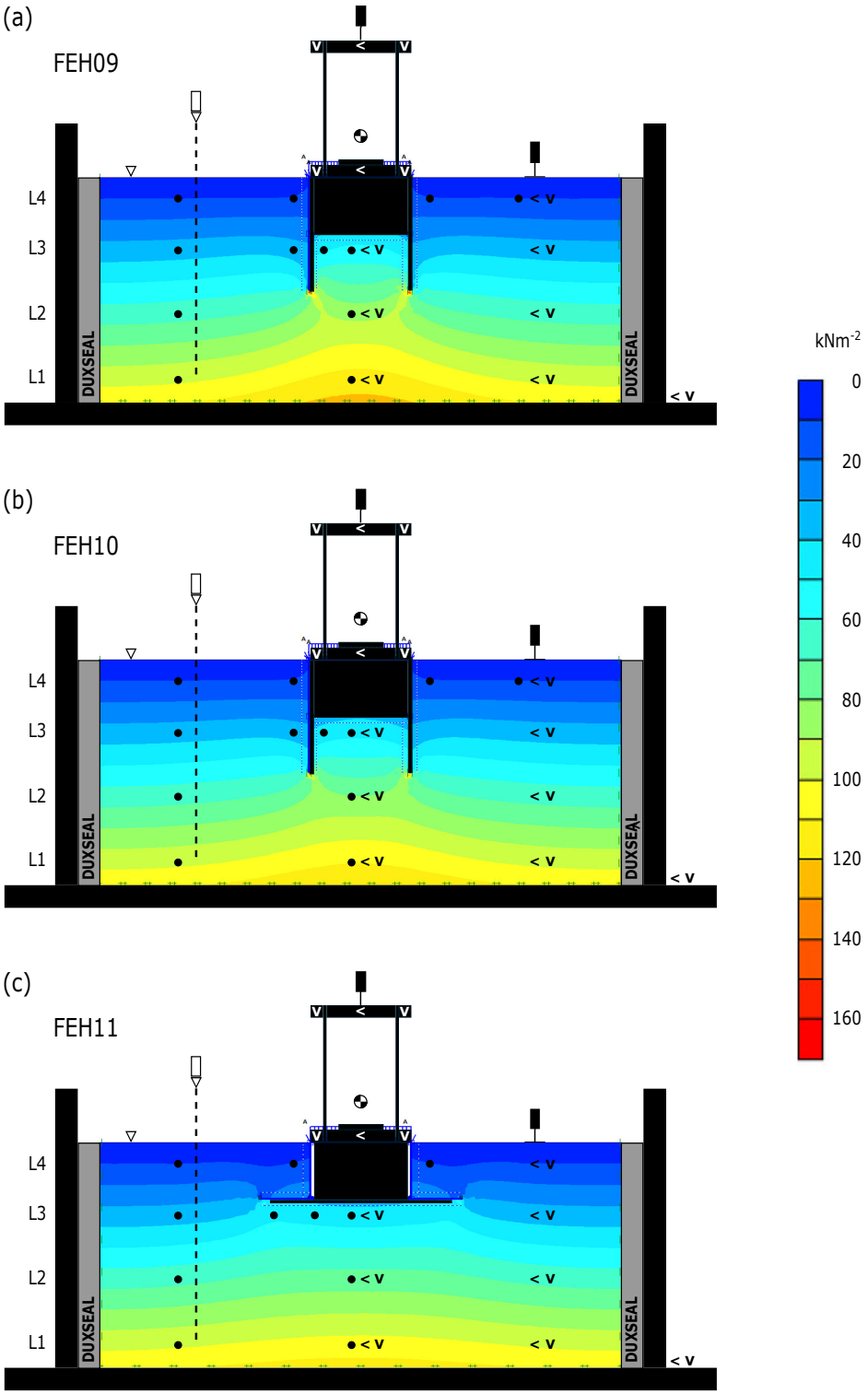

Fig. 4.10 Initial vertical effective stress contours for structures with basements and rigid extenders, obtained from Plaxis 2D analysis (Plaxis 2000). The initial location of the structure and instrumentation in each model test is shown.

4.4.3 Excess pore pressures

When loose, saturated, sandy soils are subjected to cyclic loading, the tendency to contract when sheared can result in the generation of positive excess pore pressures. When positive excess pore pressures are generated, the uplift force acting on a structure with a basement increases to greater than that during hydrostatic conditions, which consequently reduces the effective bearing pressure. Intuitively, this will strongly affect the co-seismic behaviour of structures with basements and extenders.

Figure 4.11 shows the excess pore water pressures generated in the instrumented column of soil in the far-field during the three earthquakes. Figure 4.12 shows the same for the instrumented column of soil beneath the centre of each of the basements. The dashed horizontal lines show the initial vertical effective stress at the corresponding instrument location, obtained from the Plaxis 2D analysis presented in Figure 4.10. When the excess pore pressure measured at an instrumented location approached the corresponding initial vertical effective stress, the instantaneous value of the vertical effective stress approached zero and liquefaction occurred.

In the far-field during EQ1, small positive excess pore pressures were generated in Tests FEH09 and FEH10 whilst almost none was generated in Test FEH11 (Figure 4.11). The cone resistance obtained from the post swing-up cone penetration test (CPT), shown in Figure 3.7, was greater for Test FEH11 than FEH09 and FEH10, indicating that the initial relative density of the soil layer was slightly higher in Test FEH11. The models were all poured using an automatic sand pourer with the same nozzle diameter and drop height. The difference is therefore likely to be a result of model disturbance during loading onto the centrifuge. The low amplitude of the base shaking of EQ1, which had a peak acceleration of 0.03 g, was sufficient to cause contraction of the loose soil skeleton in Test FEH09 and FEH10, but insufficient to do the same in Test FEH11.

It is interesting to note that during EQ1 greater excess pore pressures were generated underneath the centre of the basement of the structures with vertical extenders in Test FEH09 and FEH10 (Figures 4.12(a,b)) than at the corresponding depths in the far-field (Figures 4.11(d,e) respectively). The vertical extenders were impermeable, and therefore prevented horizontal water flow for the region of soil confined between them. Vertical water flow was not possible due to the impermeable basement structure above, therefore drainage during shaking was reduced. The excess pore pressures remained lower than the initial vertical effective stress obtained from the Plaxis 2D analysis, shown by the dashed lines in Figure 4.12, which indicates that liquefaction did not occur. It is important to note that stress redistribution from the basement onto the vertical extenders may have concurrently occurred and caused a reduction in vertical stress beneath the basement. It is not possible to

quantify this redistribution from the data obtained from the centrifuge test however, it is not anticipated to change the observation that liquefaction did not occur underneath the centre of the basement of the structures with vertical extenders in EQ1.

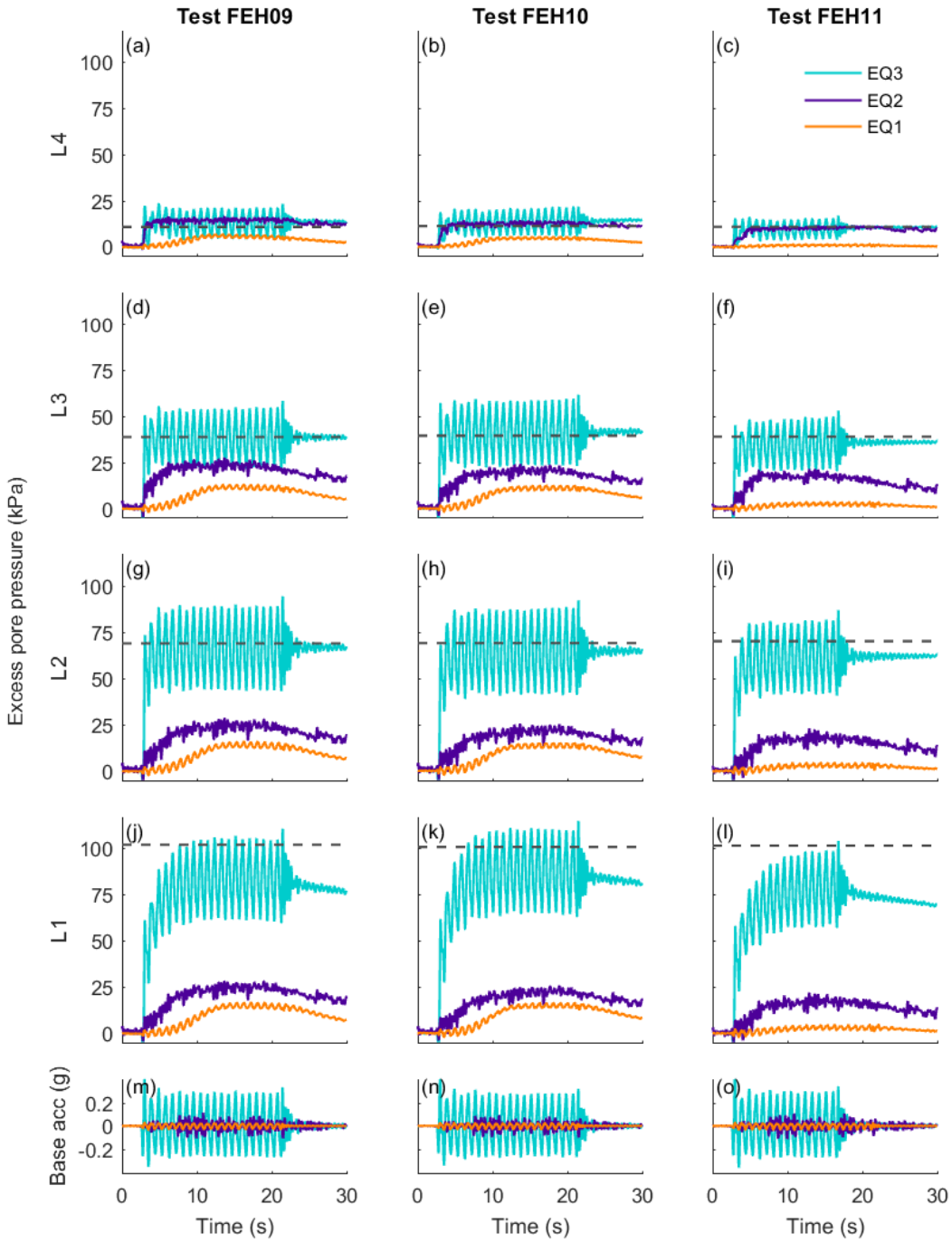

Fig. 4.11 Excess pore water pressure time histories for the instrumented column in the far-field during EQ1, EQ2 and EQ3. L*N* indicates the level of instrumentation, with *N* increasing with decreasing depth, shown in Figure 4.10. Dashed lines indicate the initial vertical effective stress at the corresponding instrument location, obtained from Plaxis 2D analysis.

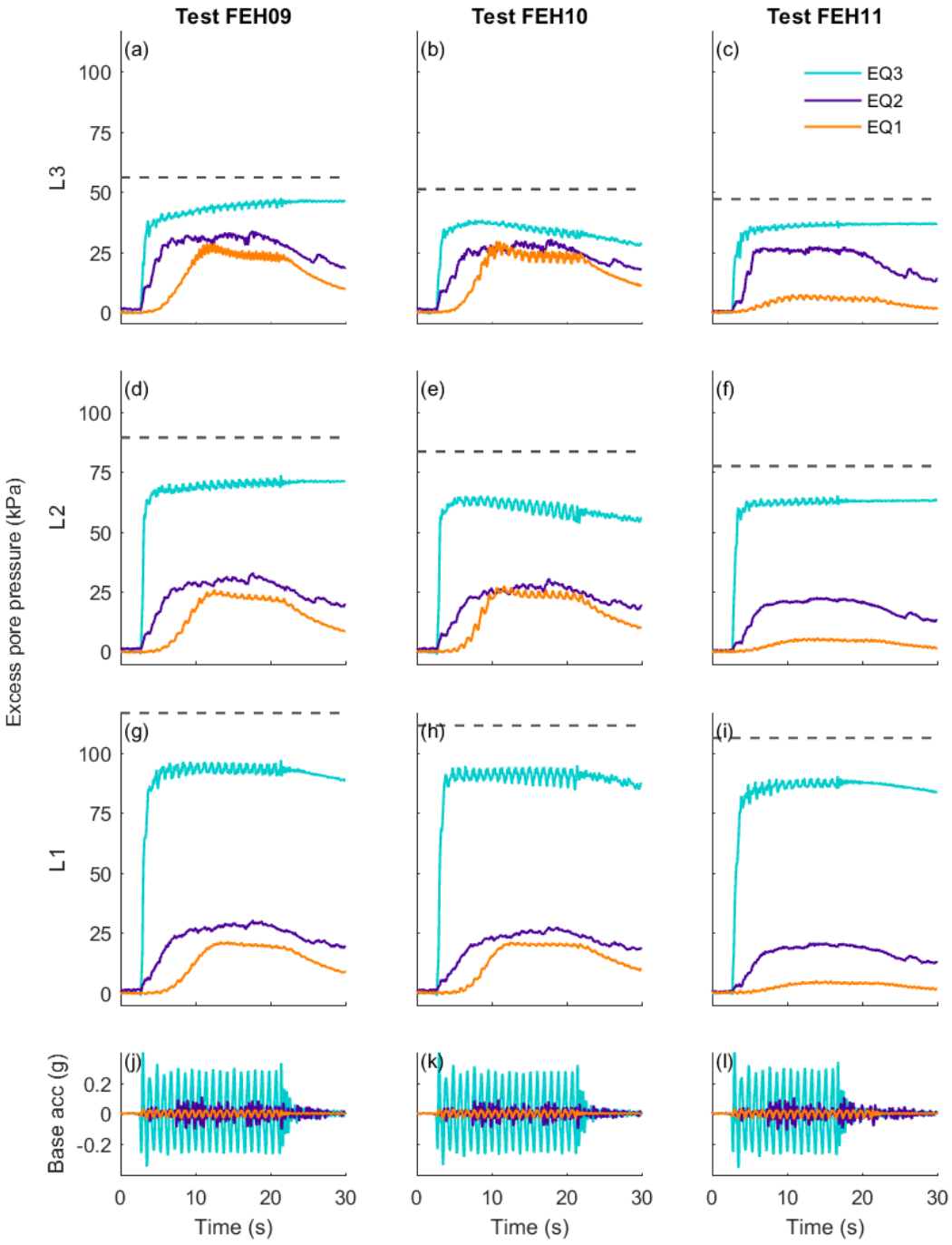

Fig. 4.12 Excess pore water pressure time histories for the column of soil underneath the centre of the structures during EQ1, EQ2 and EQ3. L*N* indicates the level of instrumentation, with *N* increasing with decreasing depth, shown in Figure 4.10. Dashed lines indicate the initial vertical effective stress at the corresponding instrument location, obtained from Plaxis 2D analysis.

In EQ2, positive excess pore pressures were generated at all depths in all three tests, both in the far-field, shown in Figure 4.11, and below the centre of the basements, shown in Figure 4.12. The rate of generation of excess pore pressure decreased with increasing depth because the vertical effective stress increased and therefore greater shearing was required to cause contraction of the soil skeleton. Liquefaction occurred at the shallowest instrumented depth in the far-field, shown in Figures 4.11(a,b,c). At the other instrumented locations, where liquefaction did not occur, the excess pore pressures generated were approximately the same magnitude during the co-seismic period, and fluctuated with the change in amplitude of the base shaking acceleration. Despite liquefaction not occurring, soil softening will have occurred and will have been proportional to the excess pore pressures generated with respect to the initial vertical effective stress.

The base shaking in EQ3 was sufficiently large to cause positive excess pore pressures to be quickly generated at all depths in the far-field, as shown in Figure 4.11, and below the centre of the basements, shown in Figure 4.12. These figures show that the excess pore pressures approached the corresponding values of initial vertical effective stress at all instrumented depths in the far-field, meaning that liquefaction occurred in the entire depth of the soil layer in the far-field. Beneath the centre of the structures, the excess pore pressures became equal to approximately 80 % of the corresponding value of initial vertical effective stress. The increase and decrease in steady state excess pore pressure measured at L3 in Tests FEH09 (Figure 4.12(a)) and Test FEH10 (Figure 4.12(b)) respectively, are likely to be due to the vertical displacement of the pore pressure transducer caused by the co-seismic movement of the structures. The displacement and rotation of these structures will be discussed in detail in Section 4.16.

The effect of vertical containment walls on the excess pore pressure generated below structures with shallow foundations with no basements has previously been investigated using 1 g shaking table tests (Yoshimi & Tokimatsu 1977) and dynamic centrifuge testing (Mitrani 2006). Their results are presented in terms of excess pore pressure ratio, which is equal to the excess pore pressure divided by the corresponding initial vertical effective stress. Yoshimi & Tokimatsu (1977) found that the excess pore pressure ratio was limited to a maximum value of 0.18 for soil within vertical containment walls that extended for the full depth of the liquefiable layer, whilst liquefaction occurred outside of the walls. This was explained to be because the "shear strain of the sand within the walls was restrained by the walls" and the structure with a shallow foundation "further confined the sand within the embedded walls" (Yoshimi & Tokimatsu 1977). For a similar containment wall configuration, the maximum excess pore pressure ratio within the containment walls was found to be 0.6 in dynamic centrifuge testing conducted by Mitrani (2006). Vertical containment walls that only

extended for half the depth of the liquefiable layer were also tested by Mitrani (2006). The depth of liquefaction in the far-field was found to govern the maximum excess pore pressure ratio within the containment walls. When liquefaction in the far-field was limited to depths shallower than the bottom of the containment walls, a maximum excess pore pressure ratio of 0.6 was measured within the walls. However, when liquefaction in the far-field occurred below the depth of the bottom of the containment walls, the excess pore pressure ratio within the containment walls reached a value of one. Mitrani (2006) proposed that there was room for soil shearing to occur within the containment walls. The pattern of excess pore pressures measured within the vertical extenders below structures with basements presented in Figure 4.12 are comparable to those observed by Mitrani (2006).

Oscillations in excess pore pressure about the mean value occurred during shaking due to cyclic shearing of the liquefied soil. The amplitude of these oscillations was greater in the far-field (Figure 4.11) than underneath the structure (Figure 4.12), and increased with increasing depth. Greater oscillations imply a greater amplitude of cyclic shear strain and consequently increased local contraction and dilation. In both the far-field and underneath the structure these oscillations occurred at the same frequency as the base shaking.

4.4.4 Migration of pore fluid

The rigid, impermeable extenders attached to the basements will have influenced the migration of pore water in the surrounding soil. This can be investigated by calculating the hydraulic gradient, $i(t)$, between any two instruments:

$$i(t) = \frac{-\Delta H(t)}{|\Delta s|} \tag{4.9}$$

where $H(t)$ is the potential head, which is equal to the sum of the pressure and elevation head, and Δs is the distance between the two points being considered. Flow occurs down the potential gradient, from areas of higher to lower potential head. When the hydraulic gradient is equal to zero, no flow occurs. Time histories of the vertical hydraulic gradient between L2 and L3 of instrumentation in both the column beneath the centre of the basements and in the far-field are plotted in Figure 4.13. In this figure, a positive hydraulic gradient corresponds to upward flow, and a negative hydraulic gradient corresponds to downward flow. For Tests FEH09 and FEH10, the hydraulic gradient below the basements shown in Figure 4.13 is between two points located 1.7 m above and 1.4 m below the bottom of the vertical extenders at prototype scale, where pore pressure transducers (PPTs) were located.

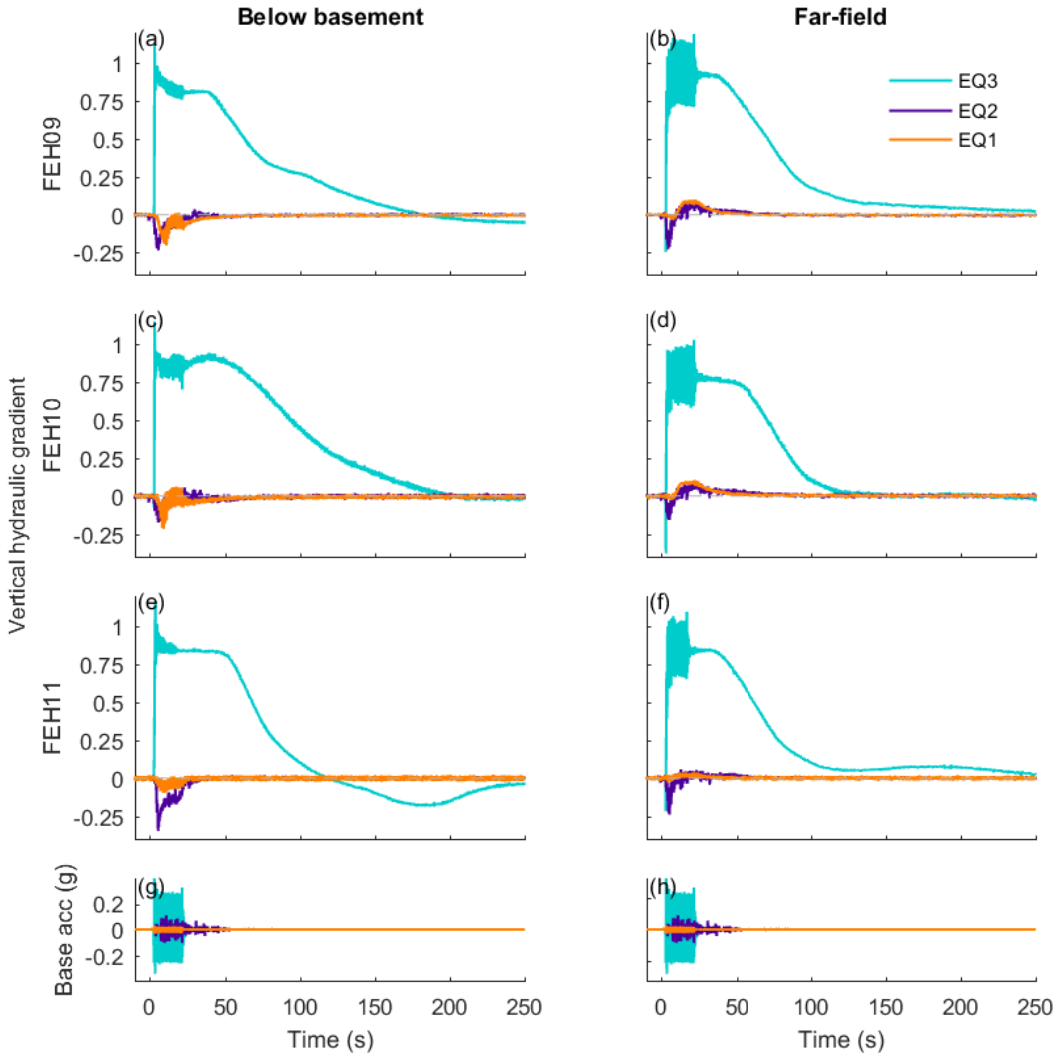

Fig. 4.13 Vertical hydraulic gradient time histories between L2 and L3 of instrumentation, below the basement (left column) and in the far-field (right column), during EQ1, EQ2 and EQ3. (a) FEH09 below basement, (b) FEH09 far-field, (c) FEH10 below basement, (d) FEH10 far-field, (e) FEH11 below basement, (f) FEH11 far-field, (g,h) Base shaking horizontal acceleration for FEH09.

Before shaking started, the hydraulic gradient was equal to zero so there was no flow of pore fluid. This was expected because in hydrostatic conditions the potential head at all points within the model is the same. When excess pore pressures are generated, a difference in potential head can occur.

During the entirety of the smaller amplitude earthquakes, EQ1 and EQ2, the hydraulic gradient beneath the structures was negative and flow was downward (Figures 4.13(a,c,e)). This means that a greater potential head occurred at shallower depths, where the positive excess pore pressure generated was closer to the corresponding value of initial vertical effective stress. The same was observed in the far-field, for approximately the initial 8 seconds of these two earthquakes (Figures 4.13(b,d,f)). Flow was initially downward because the rate of excess pore pressure generation was slower at deeper depths. Subsequently, the direction of flow reversed and was upward in the far-field for the remainder of EQ1 and EQ2.

During the large amplitude shaking in EQ3, the hydraulic gradient was always positive and flow was upward, with the exception of after 120 seconds during FEH11. Upward flow was a result of an increase in excess pore pressure with increasing depth. It was expected, as an increase in initial vertical effective stress with depth equates to an increase in maximum achievable excess pore pressure during strong base shaking. Indeed, in some layered soil configurations, upward flow from deep layers which have liquefied can be sufficient to cause fluidisation of shallow layers which would otherwise not have been expected to liquefy during the strong motion itself (Seed & Lee 1966).

After shaking ceased in EQ3, excess pore pressure dissipation occurred from the bottom of the soil layer upwards. Upward flow occurred in the far-field and, initially, beneath the structures with basements. This is consistent with the understanding of post-seismic dissipation of excess pore pressures proposed by Florin & Ivanov (1961). Below the structures with vertical extenders in Tests FEH09 and FEH10, the hydraulic gradient post-shaking was roughly bilinear, implying two different regimes of pore pressure dissipation. Initially, pore water was dissipated upwards into the soil confined between the impermeable vertical extenders. Concurrently, upward flow was occurring in the far-field. Dissipation in the far-field ceased at approximately 110 seconds in Figures 4.13(b,d), 90 seconds after shaking stopped. Subsequently, once excess pore pressures had been dissipated in the far-field, downward dissipation out of the soil confined between the vertical extenders occurred. The hydraulic gradient was being measured between points above and below the bottom of the vertical extenders, as opposed to between points above and level with the bottom of the vertical extenders. This is the reason why the sign of the hydraulic gradient did not change in Figures 4.13(a,c).

The hydraulic gradient post-shaking was roughly trilinear below the basement of the structure in Test FEH11, as shown in Figure 4.13(e). The change in sign of the hydraulic gradient at 120 seconds in Figure 4.13(e) suggests that the direction of vertical flow became downwards. This was not expected for the geometry of the impermeable horizontal extenders attached to the basement. To investigate this further, Figure 4.14 shows the horizontal

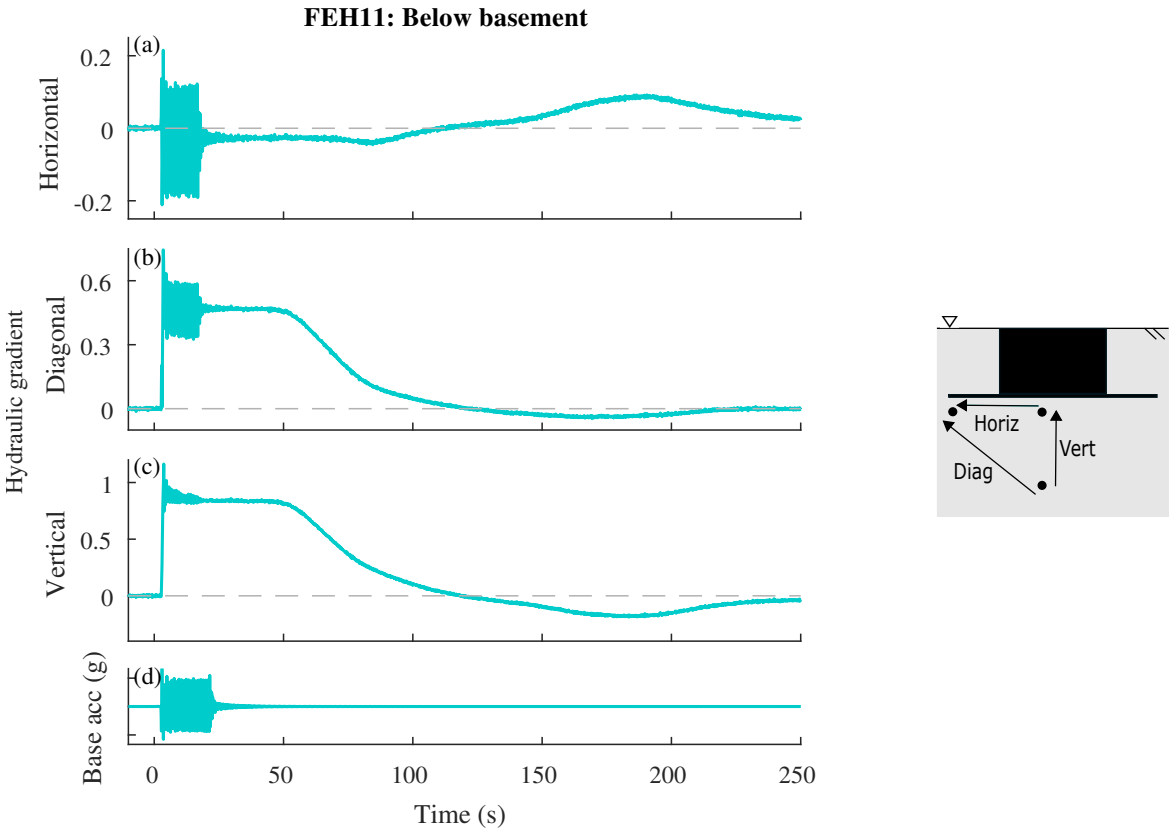

Fig. 4.14 Hydraulic gradient time histories below the basement during EQ3 in Test FEH11, (a) Horizontal, leftwards is positive, (b) Diagonal, upwards is positive, (c) Vertical, upwards is positive. Positive directions shown by the arrows in the schematic included.

and diagonal hydraulic gradient time histories below the basement in Test FEH11 during EQ3 alongside the vertical hydraulic gradient. Figure 4.14 shows that excess pore pressure dissipation began approximately 30 seconds after shaking ceased, and was initially vertically and diagonally upwards. The horizontal extenders prevented vertical dissipation from the soil below them. Dissipation of excess pore pressure horizontally beneath the extenders only began at 85 seconds in Figure 4.14(a), corresponding to the time when dissipation in the vertical direction almost ceased (Figure 4.14(c)). Pore pressure dissipated horizontally beneath the horizontal extenders, before then being dissipated upwards outside of the plan area of the extenders.

An increase in hydrostatic pore pressure measured pre and post shaking by the three PPTs used to generate Figure 4.14 shows that settlement of the instruments occurred during shaking. This settlement is most likely to have occurred during shaking, when displacement of the structure occurred, and will have increased the pressure head and decreased the elevation head in comparison to the values calculated which used the initial location of the instrument.

Instrument settlement is likely to be the cause of the negative vertical hydraulic gradient at 120 seconds in Figure 4.14(c), rather than it being a result of downward vertical flow.

4.4.5 Transmission of horizontal accelerations

Horizontal accelerations caused by an earthquake are transmitted upwards through a soil layer by horizontally polarised vertically propagating shear waves. The transmission of these accelerations to structures located on top of, or within, the soil results in horizontal inertia forces. These can damage structural components, depending on the amplitude and frequency of the accelerations in relation to properties of the structure.

Horizontal accelerations were measured at discrete locations in the soil body and on the structures. Figure 4.15 shows the horizontal acceleration time histories for the roof and ground floor of the structures and the column of soil below the centre of the basements.

During EQ1 and EQ2 the horizontal accelerations in the soil body were neither amplified nor attenuated as they were transmitted upwards. Consequently, in each of these cases, the amplitude of the shaking of the ground floor of the structure, shown in Figures 4.15(d,e,f), was of approximately the same amplitude as the base shaking. The flexible nature of the SDOF superstructures resulted in the accelerations at the roof level, shown in Figures 4.15(a,b,c), being greater than those experienced at the ground floor level. The accelerations experienced at roof level were therefore of greater amplitude than the base shaking. This was more pronounced during EQ1, where the frequency of the base shaking was equal to the fixed base natural frequency of the superstructures. It is worth reiterating that liquefaction did not occur at depths deeper than the bottom of the basements for any of the three tests during EQ1 or EQ2 (Figures 4.11 and 4.12).

In contrast, during EQ3 the horizontal accelerations were progressively attenuated as they were transmitted upwards through the liquefied soil (Figure 4.15). The transmission of horizontal accelerations from the base of the model through the soil body was therefore highly dependent on whether liquefaction occurred or not. When the excess pore pressures approached the corresponding initial vertical effective stress, shown in Figure 4.12, the instantaneous vertical effective stress approached zero. The near zero vertical effective stress state caused a very large stiffness degradation, which reduced the ability of the soil to carry shear stress and therefore transmit shear waves. The horizontal accelerations transmitted to the ground floor of the structures, shown in Figures 4.15(d,e,f), were therefore significantly smaller than those generated by the base shaking. Liquefaction of the soil beneath the basements therefore naturally isolated the structures from the base shaking acceleration. Horizontal accelerations transmitted to the ground floor of the structures were then amplified at the roof level, due to the flexible nature of the superstructure. In contrast to EQ1, in EQ3

the accelerations at roof level remained less than the base shaking, except for during the first cycle of shaking before positive excess pore pressures were generated (Figures 4.15(a,b,c)). The observed drift in the measured horizontal acceleration of the structure in Test FEH10 EQ3, shown in Figures 4.15(b,e), was caused by the accumulated rotation of the structure, which is discussed in detail in Section 4.4.6. As the accumulated rotation of the structure increased, the MEMS accelerometers recorded an increasing component of the centrifugal acceleration.

The horizontal accelerations in the structure and the soil column beneath the basements in EQ3, shown in Figure 4.15, show the same pattern of progressive attenuation that was observed for the structure with a basement without extenders in Test FEH05, shown in Figure 4.4. The presence of the horizontal and vertical extenders therefore did not affect the horizontal accelerations during large amplitude base shaking. Liquefaction of the soil beneath the basements occurred for the structures with and without extenders, and therefore naturally isolated the structures from the base shaking acceleration.

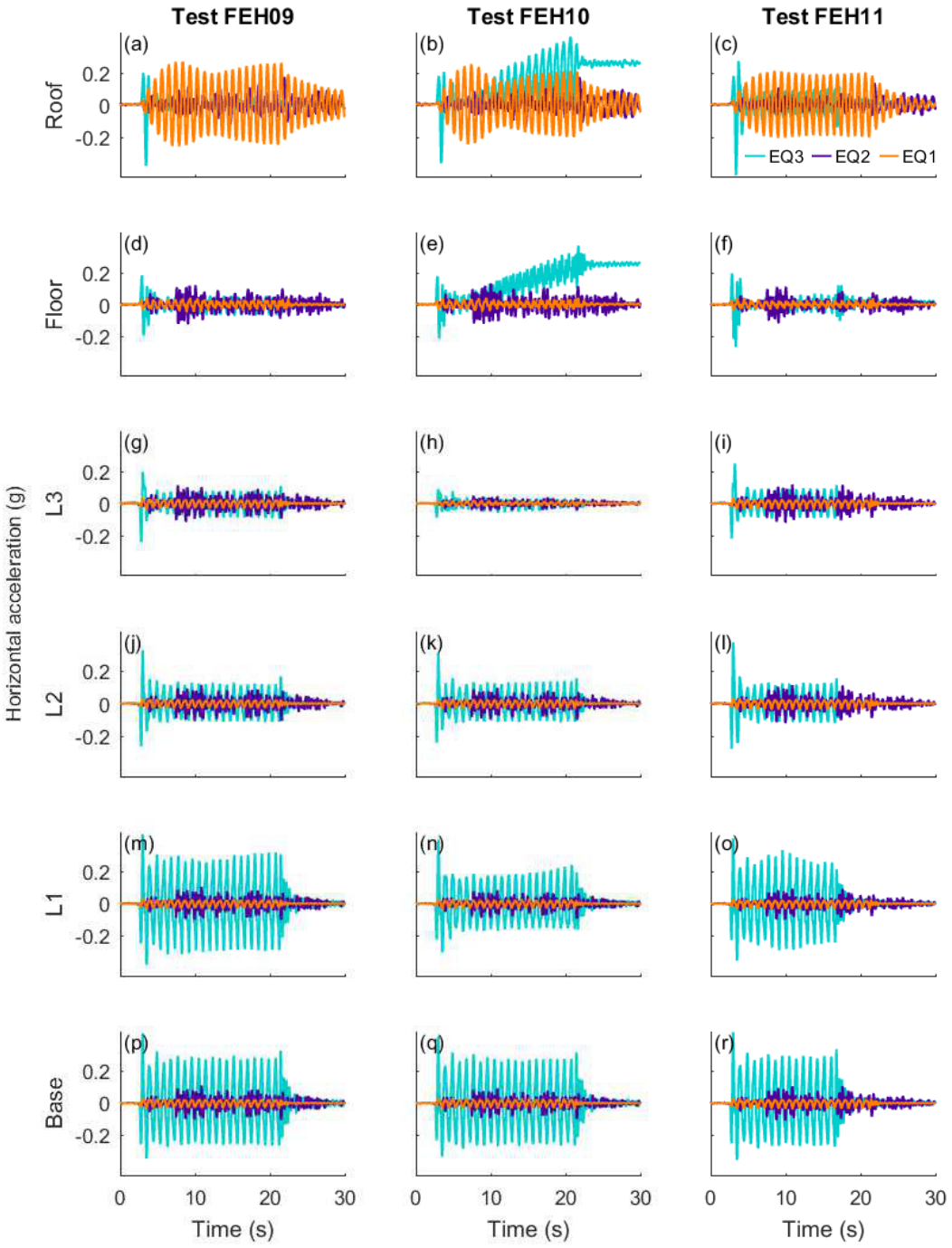

Fig. 4.15 Co-seismic horizontal acceleration time histories for the structure, the soil column below the basement and the input motion during EQ1, EQ2 and EQ3. L*N* indicates the level of instrumentation in the soil, with *N* increasing with decreasing depth, as shown in Figure 4.10.

4.4.6 Displacement and rotation of the structures

It is desirable that a structure neither settles nor rotates during an earthquake. However, the increase in loading imposed by the structure on the surrounding soil and the concurrent decrease in resistance provided by the soil mean that, during earthquake shaking, structures can be susceptible to settlement and rotation.

The co-seismic change in vertical displacement and rotation of the basement, which was rigidly connected to the ground floor of the superstructure, are shown by the solid lines in Figure 4.16 and are summarised in Table 4.5. The displacements presented are for the centre of the top of the basement/the bottom of the ground floor of the superstructure. Negative vertical displacement corresponds to settlement of the structure and positive vertical displacement corresponds to uplift. Anticlockwise rotation is taken to be positive. It is desirable that the structures do not experience displacement or rotation. For EQ3, the co-seismic vertical displacement and rotation were obtained using GeoPIV-RG (White et al. 2003, Stanier et al. 2015). The resolution of the images taken using the high-speed camera meant that this method was not accurate for the smaller amplitude earthquakes. The vertical displacement of the structures presented for EQ1 and EQ2 were measured using LVDTs. The vertical displacement of the soil surface adjacent to the structures is shown by the dashed lines in Figure 4.16(a,b,c), and was measured using an LVDT positioned to the right-hand side of the structures.

During EQ1, the structures in all three tests experienced small settlement, of the order of 10 mm, shown in Figures 4.16(a,b,c), and negligible rotation, shown in Figures 4.16(d,e,f). Comparable displacements occurred in the far-field. Liquefaction did not occur anywhere in the soil layer during EQ1 (Figures 4.11 and 4.12).

During EQ2, liquefaction occurred at shallow depths adjacent to the basements during all three tests (Figures 4.11(a,b,c)) and resulted in settlement of the soil surface in the far-field

Table 4.5 Accumulated vertical displacement and rotation of the structures with basement and extenders (prototype scale)

	Earthquake	FEH09	FEH10	FEH11
Vertical displacement (mm)	EQ1	-11.4	-8.8	-6.2
	EQ2	-1.3	-1.6	-8.4
	EQ3	-370	-180	-36 [a]
Rotation (°)	EQ1	< 0.05	< 0.05	< 0.05
	EQ2	< 0.05	< 0.05	< 0.05
	EQ3	0.6	16	1.1

Note: [a] peak = -62 mm

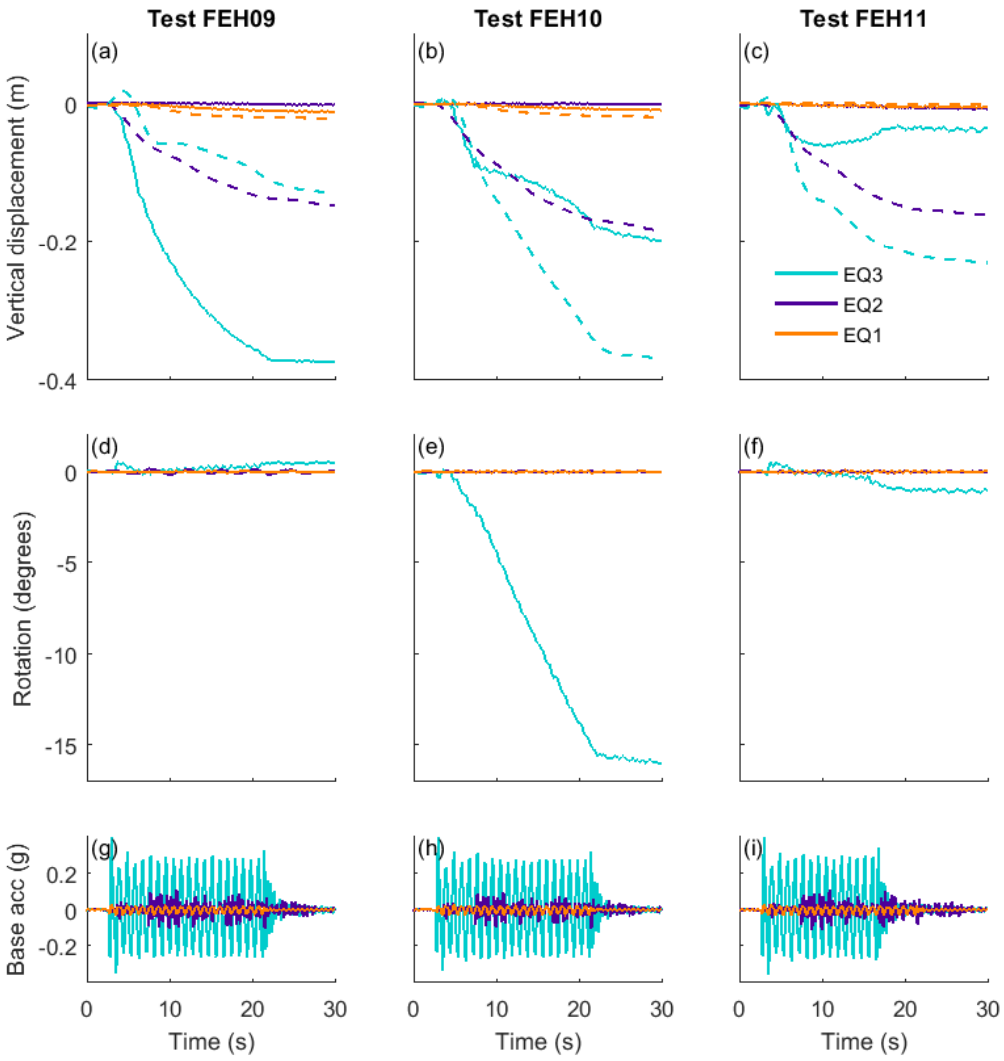

Fig. 4.16 Co-seismic vertical displacement and rotation, prototype scale. Top row: vertical displacement for (a) FEH09, (b) FEH10, and (c) FEH11. Structure shown by the solid lines and far-field soil surface by the dashed lines. Middle row: rotation for (d) FEH09, (e) FEH10, and (f) FEH11. Bottom row: base shaking horizontal acceleration for (g) FEH09, (h) FEH10, and (i) FEH11. Settlement is negative vertical displacement and anticlockwise rotation is positive.

by approximately 150 mm, shown in Figures 4.16(a,b,c). The structures, however, only accumulated minimal settlement and negligible rotation. Therefore, when liquefaction was restricted to only shallow depths, structures with basements with either vertical or horizontal extenders performed positively.

The settlement and rotation during EQ3 is of most interest as the behaviour observed across the three tests differed considerably. It will therefore be discussed in more detail, and will be investigated further during the remainder of this chapter. Unless otherwise stated, all discussions henceforth will be regarding EQ3.

During EQ3, the structure in Test FEH09 settled by a large amount, accumulating 370 mm of vertical displacement by the end of shaking (Figure 4.16(a)). This is a comparable magnitude to the liquefaction induced settlement of the structure with a shallow foundation in Test FEH04 and is notably greater than the settlement of the structure with a basement in Test FEH05 which had approximately the same ratio of uplift to total weight when the surrounding soil liquefied, U/W. This difference will in part be due to a difference in amplitude of shaking. Nevertheless, it appears that the vertical extenders worsened the liquefaction induced settlement of a structure with a basement when U/W was approximately 0.8. The structure in Test FEH09 accumulated less than 0.5 $^\circ$ of rotation, meaning that the vertical extenders had the positive effect of reducing the rotation of a structure with a basement with U/W of approximately 0.8.

The structure in Test FEH10 had the same geometry as the structure in Test FEH09 but it was lighter and therefore had a greater ratio of U/W, which was equal to 0.91. In Test FEH10, the structure accumulated clockwise rotation at an approximately constant rate during shaking, totalling 16.0 $^\circ$, shown in Figure 4.16(b). The mean rotation accumulated per cycle of sinusoidal shaking was 0.8 $^\circ$. Settlement of 180 mm occurred. The reduced weight of the structure therefore reduced the settlement of the structure with a basement with vertical extenders, however it considerably worsened the rotation.

Vertical extenders therefore worsened the behaviour of a structure with a basement during earthquake induced liquefaction. This is concerning as this is the likely geometry of structures with basements when the construction process is considered. This was not expected as it is in contrast to the finding that a similar principle, using vertical containment walls, has been successfully used to reduce liquefaction induced settlement of structures with shallow foundations (Yoshimi & Tokimatsu 1977, Dashti et al. 2010*a*, Mitrani & Madabhushi 2012). Vertical containment walls below structures with shallow foundations were found to be most successful when they extended to the full depth of the liquefiable layer, however they remained beneficial even when they only extended to half the depth of the liquefiable layer (Mitrani 2006). It may be the case that vertical extenders would be successful at limiting settlement and rotation of structures with basements if they extended to the full depth of the liquefiable layer. However, the reduction in effective bearing pressure due to the basement reduces the need to transfer the structure load to stiffer stratum below the liquefiable layer.

The structure in Test FEH11 had the same U/W as Test FEH10, but had horizontal instead of vertical extenders. This difference in geometry had a dramatic effect on the displacement and rotation of the structure, as shown in Figure 4.16. The structure in Test FEH11 initially settled (peak 62 mm) before uplifting, which reduced the total settlement at the end of shaking to 36 mm. This implies that a beneficial ratio of U/W was achieved, which prevented the structure from settling further. Small rotation, totalling 1.1 °, was accumulated during shaking (Figure 4.16(f)). The inclusion of horizontal extenders therefore had the desirable effect of maintaining the beneficial effect of the basement on minimising settlement of the structure, whilst also reducing rotation.

Intuitively, the displacement of the soil surface adjacent to the structures should have been the same in the three tests as the base shaking was approximately the same. However, it is evident in Figure 4.16(a,b,c) that this was not the case. It is apparent that the displacement and rotation of the structure strongly influenced the displacement of the soil surface adjacent to it. This will be explored further in the following sections. The structure in Test FEH11 experienced minimal displacement and rotation, therefore it will be assumed that it had minimal impact on the settlement of the soil surface.

4.4.7 Soil displacements

The cross section of the model container was larger than the area that was visible through the transparent PMMA window, which is shown in Figure 4.17. The high-speed camera was focused on the basement of each structure and the surrounding soil but was unable to view the entire failure mechanism that developed. However, the region monitored gave valuable information about the co-seismic soil-structure interaction and how displacement and rotation of the structures developed. The following section looks at the soil displacements and the soil-structure interaction during shaking. Soil displacements during EQ3 were obtained using GeoPIV-RG (White et al. 2003, Stanier et al. 2015). All the soil displacements shown are relative to the movement of the model container. In these figures the horizontal edges of the container are at 0 and 25 m on the x-axis and the base is at 0 m on the y-axis.

Soil displacements during one cycle of shaking

The accumulation of displacement and rotation of the structures occurred incrementally during shaking, as shown in Figure 4.16. It is therefore of interest to look at the soil-structure interaction during two sequential half-cycles of shaking, to understand how and when settlement and rotation was accumulated for each of the structures with a basement and rigid extenders.

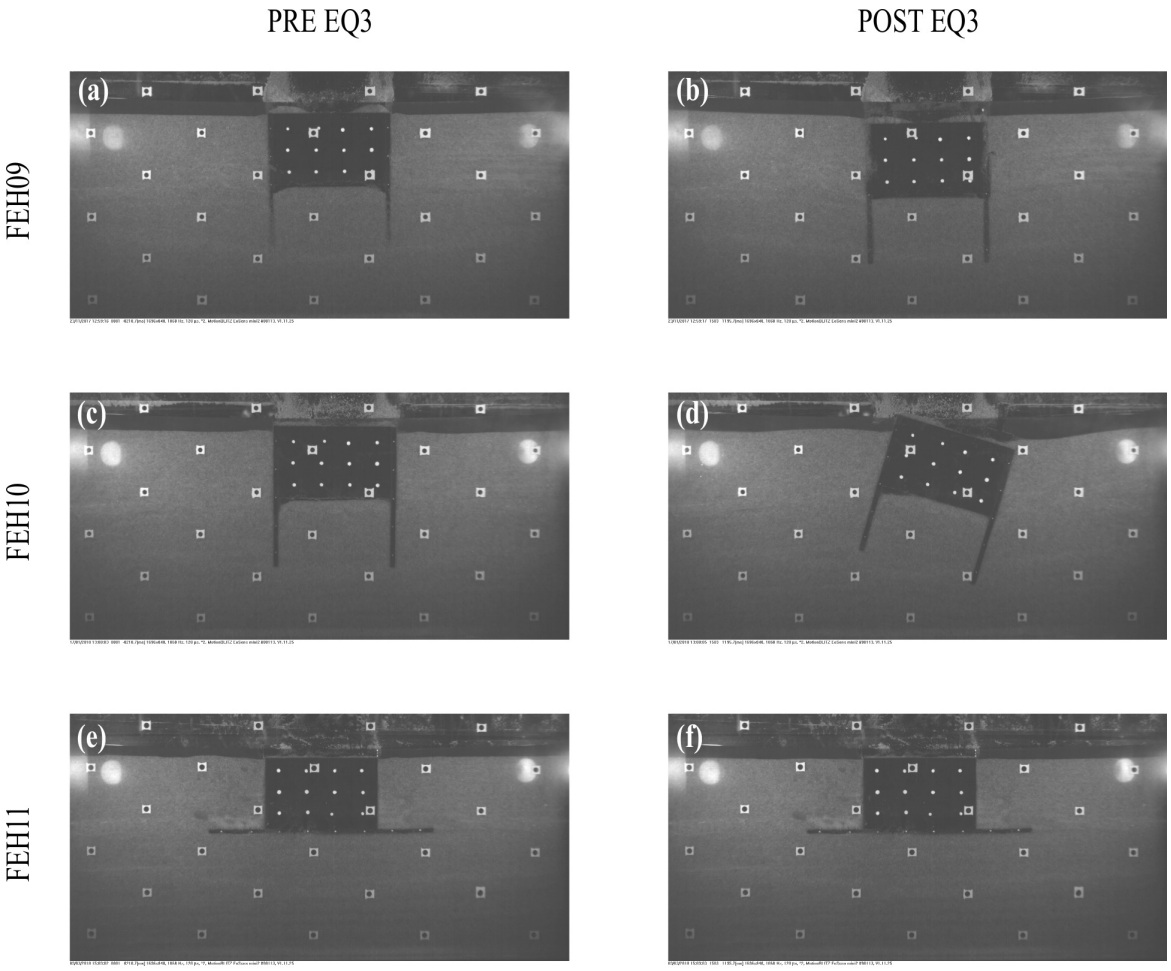

Fig. 4.17 Photos of the cross section of the models visible through the transparent PMMA window, both pre and post EQ3. (a) FEH09 pre EQ3, (b) FEH09 post EQ3, (c) FEH10 pre EQ3, (d) FEH10 post EQ3, (e) FEH11 pre EQ3, (f) FEH11 post EQ3.

Soil displacements accumulated during the 5^{th} and 6^{th} half-cycles of displacement of the model container during EQ3 are shown in Figure 4.18. The 5^{th} and 6^{th} half-cycles correspond to the time when the settlement rate of the structure in Test FEH09 was a maximum and the steady accumulation of rotation of the structure in Test FEH10 had begun, but before large displacement or rotation was accumulated (Figure 4.16). The initial cycles are not discussed as the servo-hydraulic earthquake actuator took two cycles to settle to a constant amplitude sinusoidal base shaking. The model container moved to the right in the 5^{th} half-cycle and then moved to the left in the 6^{th} half-cycle. The 5^{th} and 6^{th} half-cycles of displacement correspond to the 6^{th} and 7^{th} half-cycles of acceleration of the model container respectively.

In Test FEH09, during the 5^{th} half-cycle of displacement, shown in Figure 4.18(a), the soil within the model container moved to the left relative to the rigid base. The displacement

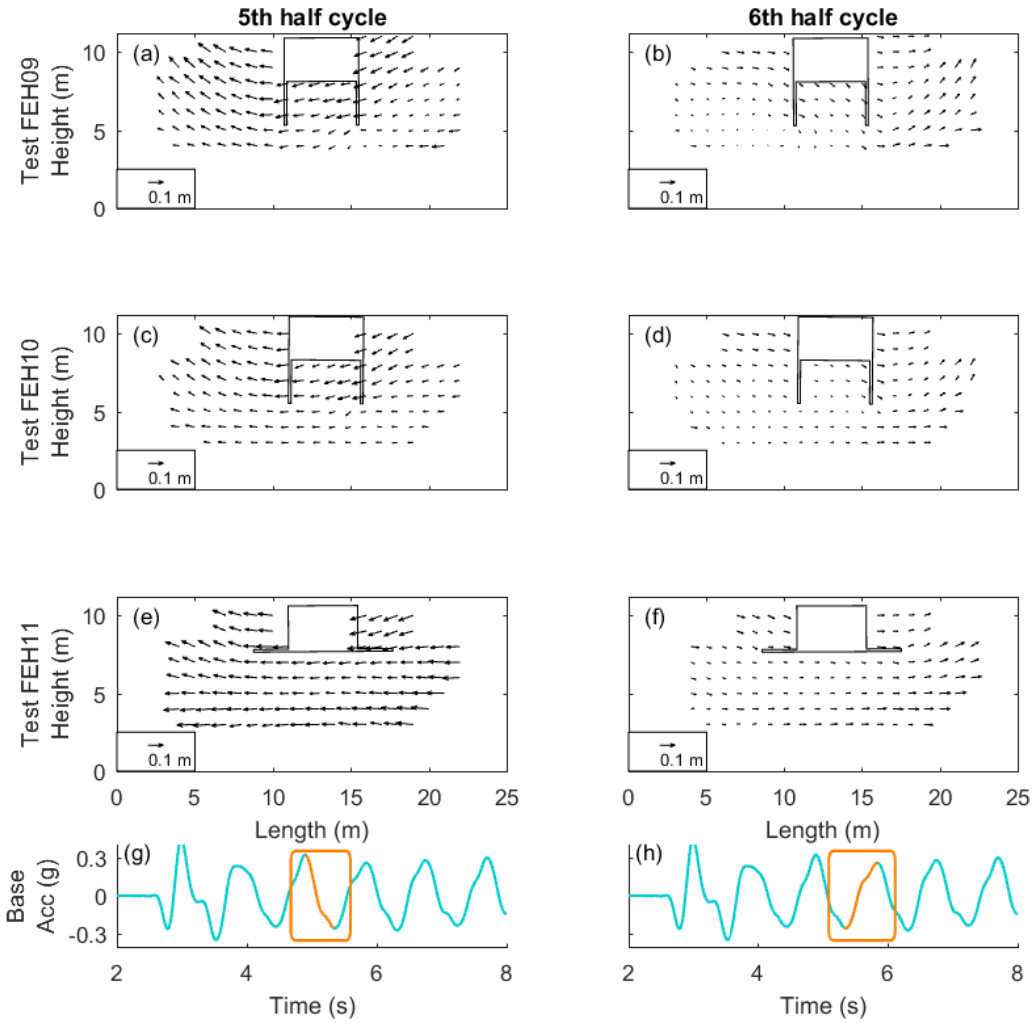

Fig. 4.18 Soil displacement during the 5^{th} (left-hand column) and 6^{th} (right-hand column) half-cycles of displacement of the model container. (a) FEH09 5^{th} half-cycle, (b) FEH09 6^{th} half-cycle, (c) FEH10 5^{th} half-cycle, (d) FEH10 6^{th} half-cycle, (e) FEH11 5^{th} half-cycle, (f) FEH11 6^{th} half-cycle. Location of basement at start of each half-cycle shown. Base shaking acceleration for Test FEH09 (bottom row), with corresponding half-cycle highlighted. Dimensions in prototype scale. Note: soil displacements are plotted with a magnification factor of 10 relative to the basement and model container.

vectors within the soil constrained between the vertical extenders were close to parallel and were approximately the same magnitude, indicating that it behaved as an almost rigid block. This rigid behaviour is apparent in the excess pore pressure time histories measured at L3 of instrumentation within the vertical extenders, shown in Figure 4.19(a). Oscillations in the excess pore pressure time histories were recorded either side of the basement in L4 of instrumentation, outside of the extenders, and were in antiphase. However, at L3 of instrumentation within the vertical extenders the oscillations were far smaller and there was no notable phase difference between those recorded on the centreline of the structure and to the left of it. Figure 4.18(a) shows that the downward component of displacement was small within the constrained block, and increased at the depth of the bottom of the extenders, with a greater magnitude under the right-hand edge of the structure than under the left-hand edge. The settling structure forced this soil to move downwards, and concurrently forced the soil to the left side of the basement upwards. During the 6^{th} half-cycle, shown in Figure 4.18(b), the displacement vectors were smaller in all locations. This was true for all three tests, and is likely to be a result of a slightly smaller peak-to-peak amplitude of base shaking acceleration shown in Figure 4.18(h). In Test FEH09, during the 6^{th} half-cycle of displacement, vertical displacement beneath the structure was greater than during the 5^{th} half-cycle, both between and below the extenders, which in turn caused greater upward soil movement to the right side of the structure.

The most significant difference between the soil displacement vectors during the 5^{th} and 6^{th} half-cycles in Test FEH10 (Figures 4.18(c,d)) to those observed in Test FEH09 (Figures 4.18(a,b)), was the vertical component of displacement below the bottom of the vertical extenders. Intuitively, this is a consequence of the reduced weight of the structure. In Test FEH10, below the bottom of the extenders, the vectors were close to horizontal, indicating that the displacement of the soil was purely horizontal with no vertical component. As a consequence, soil adjacent to the basement had a smaller upward component. Figure 4.19(b) shows that oscillations in excess pore pressure time histories either side of the basement in L4 of instrumentation, outside of the extenders, were in antiphase for the initial cycles of shaking. The magnitude and phase of oscillations in excess pore pressure changed considerably during shaking. This behaviour will be discussed in detail in the following section when total soil displacements are presented.

In Test FEH11 the soil displacement vectors below the horizontal extenders were horizontal indicating that the displacement of the soil was purely horizontal with no vertical component. During the 5^{th} half-cycle (Figure 4.18(e)), soil on top of the horizontal extenders had a downward component of displacement to the right of the basement, but was purely horizontal to the left of the basement. Local contraction and dilation were recorded by

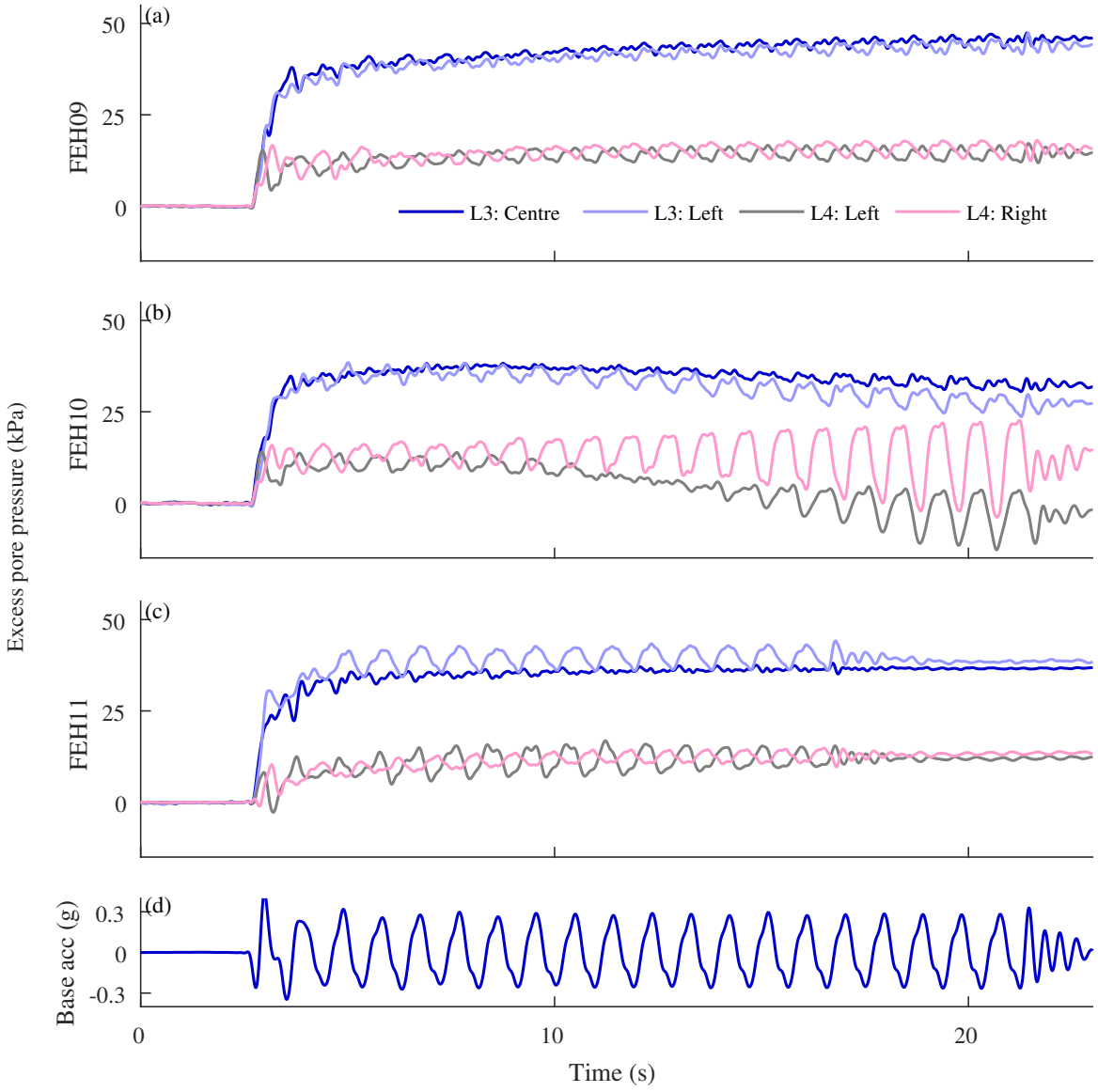

Fig. 4.19 Excess pore pressure time histories for the instrumented locations beneath (L3) and adjacent to (L4) the basements with extenders (a) FEH09, (b) FEH10, (c) FEH11, (d) Base shaking horizontal acceleration for FEH09.

pore pressure transducers in these respective locations (L4 right and left respectively in Figure 4.19(c)). To the left of the basement the displacement vectors transitioned to having a upward vertical component outside the edge of the horizontal extender. Excess pore pressures measured under the basement, in L3 of instrumentation, show local suction under the left edge of the horizontal extender during this half-cycle (Figure 4.19(c)). This was caused by extension in this region, shown in Figure 4.18(e). The pattern of soil displacements during the 6^{th} half-cycle, shown in Figure 4.18(f), was symmetric to that produced in the 5^{th} half-cycle about the vertical line through the centre of the structure.

Total co-seismic soil displacements

Further understanding of the failure mechanisms can be gained by looking at the total soil displacements accrued during the earthquake, both below and adjacent to the basements. Total co-seismic soil displacements accumulated during EQ3 are shown as vectors in Figure 4.20 and as contours in Figure 4.21, both plotted at the initial location of each tracked patch.

In Test FEH09, the total displacements shown in Figure 4.20(a) are symmetric about the vertical line through the centre of the structure. The soil beneath the basement and within the vertical extenders moved vertically downwards as the vertical extenders prevented lateral displacement (Figure 4.21(a)). Below the bottom of the extenders the magnitude of the lateral displacement of the soil increased moving away from the centreline of the structure to the extenders (Figure 4.21(a)). This soil was forced sideways and adjacent soil flowed upwards as the structure settled downwards into the soil layer, which was no longer able to support its effective weight. This upward flowing soil reduced the net settlement of the soil surface adjacent to the structure (Figure 4.16(a)). Points of zero displacement formed either side of the basement, between the downward moving basement and the upward moving soil, as shown in Figure 4.20(a). The displacement vectors resemble the flow that would be expected around a piston in a fluid, where there is no shear. The structure appears to ‘squeeze out’ the liquefied soil beneath it, which then flowed upwards.

In Test FEH10, a semi-cylinder of soil with a diameter roughly equal to the length of the vertical extenders rotated with the structure (Figure 4.20(b)). Rotation occurred about the axis through the centre of the bottom of the basement. This is in contrast to rotation occurring about the edge of the bottom of the basement for the structure in Test FEH05 which had the same width and depth but no vertical extenders, as shown in Figure 4.7. Figure 4.21(c) shows that the displacement of the soil between the lower half of the vertical extenders in Test FEH10 had a large horizontal component as the constraint provided by the vertical extenders forced this soil to move with the rotating structure. The horizontal and rotational resistance provided by the adjacent soil was insufficient to prevent the structure from rotating.

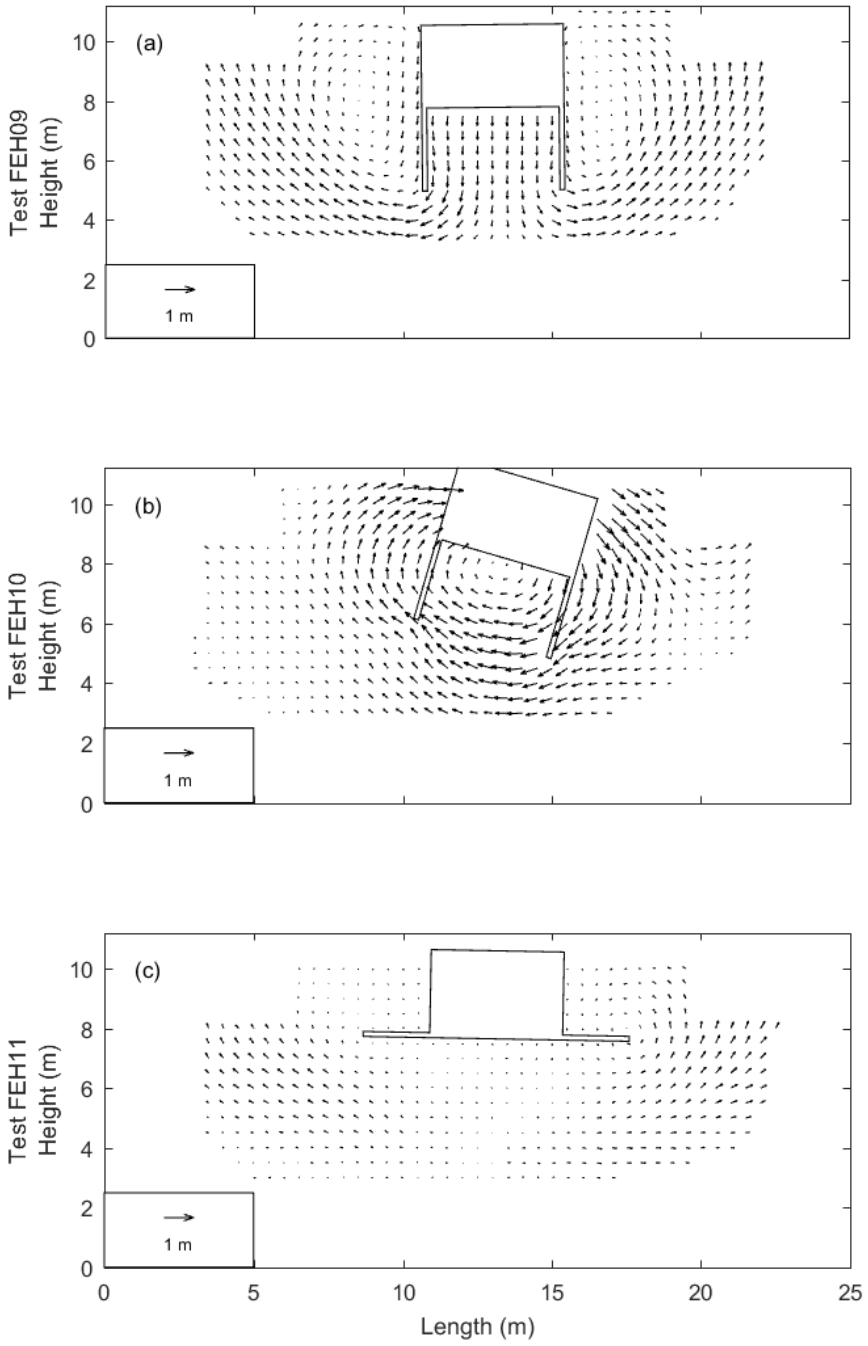

Fig. 4.20 Total co-seismic soil displacement vectors accumulated during EQ3. (a) FEH09, (b) FEH10, (c) FEH11. Location of basement at the end of shaking shown.

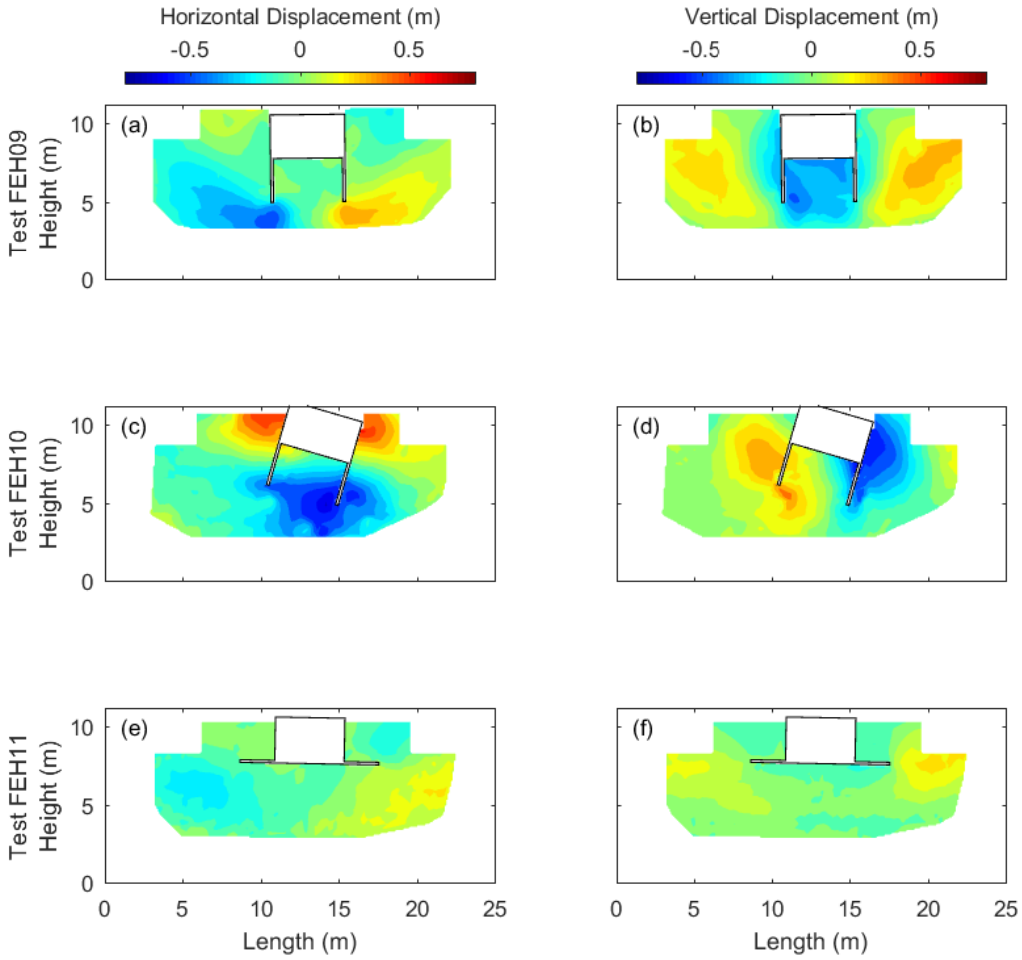

Fig. 4.21 Total co-seismic soil displacement contours accumulated during EQ3. (a) FEH09 horizontal displacement, (b) FEH09 vertical displacement, (c) FEH10 horizontal displacement, (d) FEH10 vertical displacement, (e) FEH11 horizontal displacement, (f) FEH11 vertical displacement. Rightwards is positive horizontal displacement and leftwards is negative. Settlement is negative vertical displacement and heave is positive. Location of basement at the end of shaking shown. Contours are not extrapolated outside of the region monitored.

The excess pore pressure time histories measured in the soil adjacent to the basement in L4 of instrumentation, shown in Figure 4.19(b), show that during shaking the amplitude of the suction spikes increased on both sides of the basement in Test FEH10, and to the left of the basement the steady state excess pore pressure decreased to approximately zero. These trends in excess pore pressure are in agreement with the rotation of the structure causing horizontal extension of the soil to the left of the basement, as shown in Figure 4.20(b). At some instances, the excess pore pressure oscillated to negative values meaning that the recorded absolute pore pressure was less than the hydrostatic pore pressure. The reduction in excess pore pressure and resulting increase in vertical effective stress will have caused an increase in resistance to rotation in the soil where the pore pressure transducer (PPT) was located, which was 0.8 m from the edge of the basement at prototype scale (shown by the turquoise circle in Figure 4.22). However, this increase in resistance was not transferred to the structure. Instead, lateral extension of the soil in this region caused localised piping along the side of the upper half of the basement. This can be seen in Figure 4.22 which was taken by the high speed camera during the 16^{th} half-cycle of shaking. Liquefaction of the soil layer created an upward hydraulic gradient and lateral extension of the soil created a channel through which this could be dissipated adjacent to the basement. This opening shows that contact was lost between the basement and soil adjacent to it. The gain in resistance implied by the suction spikes in Figure 4.19(b), which were measured by the PPT located in the position shown by the turquoise circle in Figure 4.22, will not have been transferred to the structure. Movement of the PPT during shaking may have contributed to the change in measured excess pore pressure, but is not believed to be the primary cause of the trends that have been presented in this section.

Figure 4.20(b) shows that the rotating structure in Test FEH10 caused heave of the soil surface to the left of the basement and increased settlement to the right, the latter being the side where the soil surface LVDT was positioned which measured the soil displacement shown in Figure 4.16(b). This explains why settlement of the soil surface adjacent to the structure in Test FEH10 (Figure 4.16(b)) was greater than in Test FEH09 (Figure 4.16(a)).

In Test FEH11, the soil underneath the basement experienced negligible displacement, both horizontally, shown in Figure 4.21(e), and vertically, shown in Figure 4.21(f), reflecting the movement of the structure presented in Figures 4.16(c,f). Soil displacements were greater below and outside the edges of the horizontal extenders, as soil was displaced to allow the small vertical displacement of the structure.

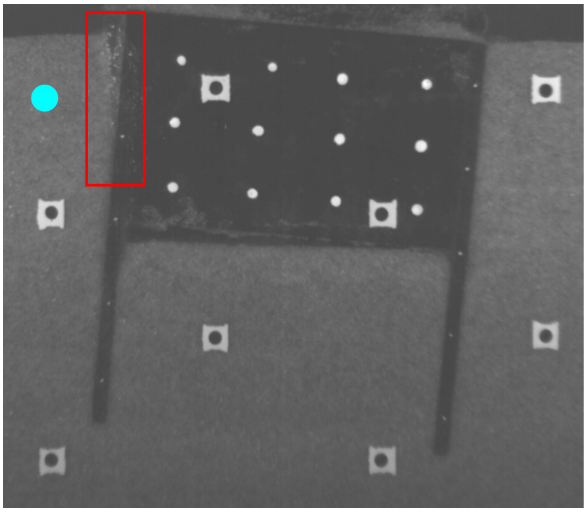

Fig. 4.22 Localised piping along the left-hand side of the basement in Test FEH10 during the 16^{th} half-cycle of shaking in EQ3. Location of pore pressure transducer measuring suction in Figure 4.19(b), L4: Left, shown in turquoise.

Total co-seismic strains

During shaking, soil can accumulate both shear and volumetric strains. The magnitude and spatial distribution of these strains is of interest as it can give insight into the cyclic loading of the soil by the combined effect of the earthquake and the structure.

The total shear and volumetric strains accumulated during EQ3 were calculated using GeoPIV-RG (White et al. 2003, Stanier et al. 2015) and are shown in Figure 4.23. Both are plotted at the initial location of each patch. Clockwise shear strains and contractive volumetric strains are positive. Interpretation of these strains should be done with care, due to the limited resolution of the images taken using the high-speed camera. It was important to record data at a high frame rate to enable the co-seismic soil-structure interaction to be investigated on a cycle-by-cycle basis. However, the specification of the high-speed camera available meant that this was a trade off with the resolution of the images. Calculation of strains requires taking the derivative of displacements of the tracked patches. Consequently, any errors in measuring displacement are amplified in strains.

In Test FEH09, Figure 4.23(a) shows that the distribution of shear strains was roughly of equal magnitude but opposite direction on either side of the basement, as expected from the symmetric behaviour of the structure (Figure 4.16(a,d)) and soil displacements (Figure 4.20(a)). The greatest shear strains were recorded directly beneath the ends of the vertical extenders, where soil was forced to move horizontally by the settling structure. Soil within the extenders accumulated minimal shear strain as lateral movement was restricted. The trends for volumetric strains accumulated below the structure shown in Figure 4.23(b) were

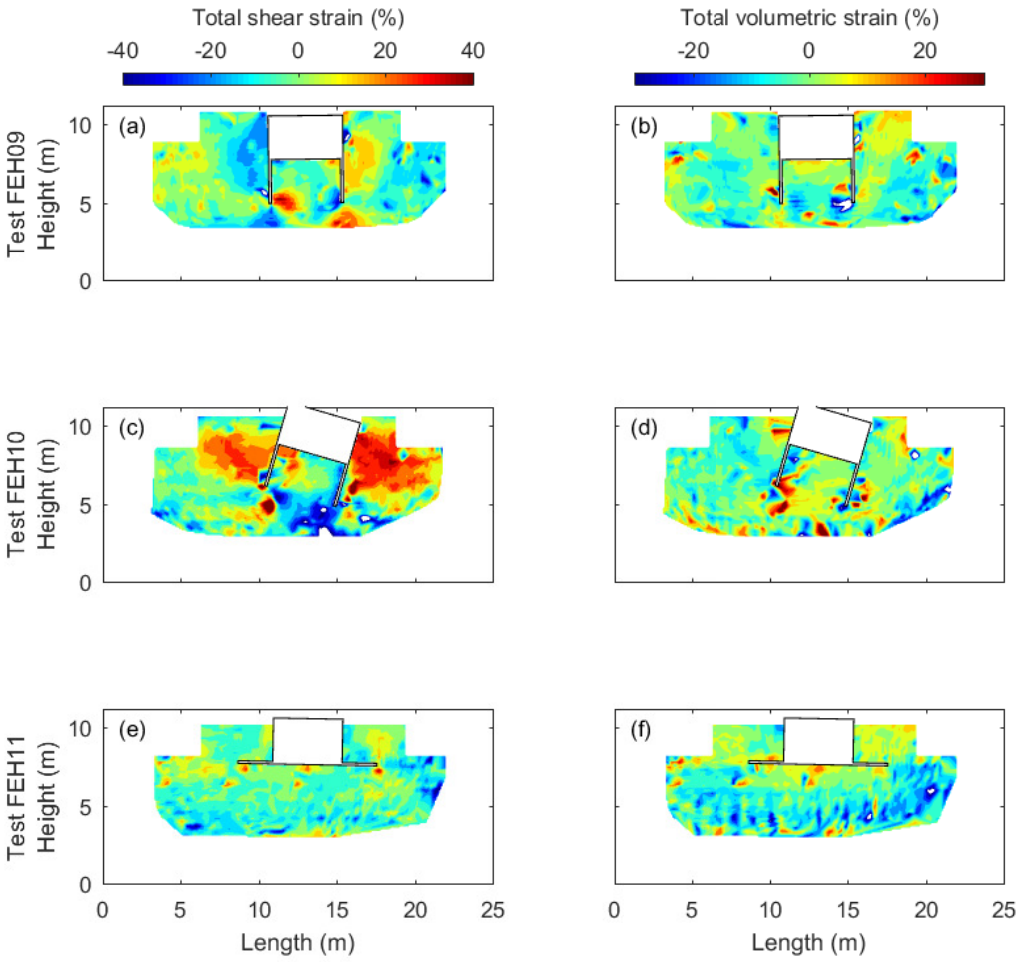

Fig. 4.23 Total co-seismic strains accumulated during EQ3. (a) FEH09 shear strains, (b) FEH09 volumetric strains, (c) FEH10 shear strains, (d) FEH10 volumetric strains, (e) FEH11 shear strains, (f) FEH11 volumetric strains. Location of basement at the end of shaking shown. Clockwise shear strains and contractive volumetric strains are positive.

not as clear as for shear strains, due to insufficient resolution of the images. Volumetric contraction occurred below the basement as the structure moved vertically downwards. In contrast, the upward flowing soil adjacent to the basement experienced volumetric dilation.

Figure 4.23 shows that the distribution of shear and volumetric strain in Test FEH10 was very different from that observed in Test FEH09. A much larger volume of soil accumulated a large magnitude of shear strain in Test FEH10. Shear strains were a maximum within the semi-cylinder of soil that rotated with the structure (Figure 4.23(c)). This region of soil experienced minimal volumetric strains (Figure 4.23(d)) implying that it remained the same volume throughout shaking. Large shearing also occurred at the bottom of the extenders,

with regions of both large volumetric contraction and dilation. The rigid body rotation of the basement, which included the soil confined between the vertical extenders, resulted in smaller shear strains being accumulated in the soil confined between the vertical extenders than outside these extenders (Figure 4.23(c)).

No significant shear strains were accumulated in Test FEH11, shown in Figure 4.23(e), because the displacement and rotation of the structure were small. Volumetric strains were also small around the structure, as shown in Figure 4.23(f). The alternating ripples of volumetric contraction and dilation at deeper depths may result from insufficient resolution of the images, as discussed previously by Stanier et al. (2016).

4.4.8 Resultant co-seismic vertical force

The generation of positive excess pore pressures during shaking, and the ensuing increase in uplift provided by a basement, mean that the effective weight of structures with basements in liquefiable soils can change considerably during shaking. This will have strongly affected the co-seismic soil-structure interaction which has been presented in the preceding sections.

The resultant vertical force acting on the structures during EQ3 can be calculated using the pore pressures recorded during the dynamic centrifuge tests. The effective weight, $W'(t)$, of the structure was calculated by subtracting the uplift force provided by the basement during shaking, $F_U(t)$, from the combined weight of the superstructure, F_S, and the basement, F_B:

$$W'(t) = F_S + F_B - F_U(t) \tag{4.10}$$

where

$$F_U(t) = [u_h + u_{ex}(t)] \times A \tag{4.11}$$

Equation 4.11 shows that two upward acting pressures contributed to the uplift force, which were summed and multiplied by the plan area of the basement, A. The first pressure was the hydrostatic pressure, u_h, and the second was the excess pore water pressure acting on the bottom of the basement, $u_{ex}(t)$. The latter of these two terms varied with time due to soil-structure interaction. When liquefaction occurred, the steady state value of the uplift force was equal to the uplift calculated using Archimedes' principle, assuming that the liquefied soil behaved as a dense fluid (see Equations 4.7 and 4.8).

Figure 4.24(a) shows that, in all three tests, the effective weight of the structures significantly reduced during EQ3. Positive excess pore pressures were generated and the uplift provided by the basement increased, whilst the weight of the structure remained unchanged. Concurrently, the generation of positive excess pore pressures reduced the instantaneous vertical effective stress, and therefore caused a reduction in stiffness and strength in the

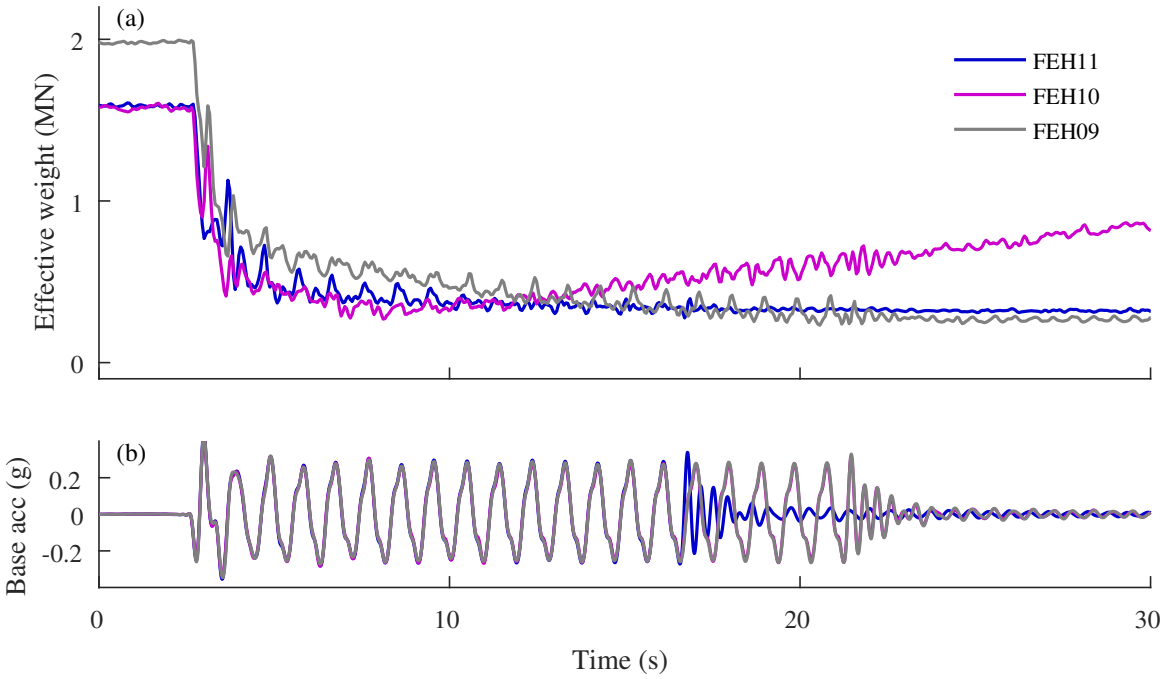

Fig. 4.24 Time histories of effective weight of the structures during EQ3. (a) Effective weight, (b) Base shaking horizontal acceleration.

soil below, and to the sides of, the basement. The bearing capacity of cohesionless soils is dependent on the vertical effective stress below and adjacent to a partially buried structure, therefore it is logical to assume that it will reduce with the generation of positive excess pore pressures. From the comparable excess pore pressures recorded adjacent to (Figure 4.11(a,b,c)) and directly below (Figure 4.12(a,b,c)) the basements, it will be assumed that the reduction in bearing capacity during EQ3 was comparable in the three tests. Therefore, differences in structure settlement and rotation were a result of differences in structure geometry and/or effective weight.

For the initial 8 seconds shown in Figure 4.24(a), the effective weight of the structures in FEH10 and FEH11 were approximately the same, and were less than that of FEH09. The calculated increase in effective weight of the structure in FEH10 after 8 seconds was not a physical effect, but was a consequence of displacement of the PPT at the shallowest instrumented depth, caused by the rotation of the structure. The difference in the effective weight of the structures in Tests FEH09 and FEH10 during the initial 8 seconds presented in Figure 4.24 can be used to understand the very different settlement and rotation during EQ3, shown in Figure 4.16. It is worth reiterating that both structures had the same geometry.

The structure in Test FEH09 settled during EQ3 (Figure 4.16(a)). It can be inferred that this was because the effective weight of the structure, shown in Figure 4.24(a), exceeded the

degraded bearing capacity provided by the soil below. A combination of factors prevented the structure from rotating. Firstly, the forced vertically downward movement of the block of soil between the vertical extenders prevented rotation. For rotation to occur, a section of this block would have been required to move vertically upwards. Secondly, vertical confinement of the soil below the extenders provided resistance to rotation. This reasoning is consistent with the findings of Mitrani (2006) on vertical containments walls beneath structures with shallow foundations, which had a greater effective weight than the structure in Test FEH09. When liquefaction occurred to a depth below the bottom of the vertical containment walls, Mitrani (2006) found that a structure with a shallow foundation did not accumulate notable rotation. In addition, the presence of the vertical extenders in Test FEH09 increased the resistance to rotation because, in comparison to the structure with a basement without vertical extenders in Test FEH05, they increased the volume of soil that would need to be displaced for rotation to be accumulated.

Greater resistance to rotation, due to a larger volume of soil being required to be displaced for rotation to be accumulated, was insufficient to prevent rotation of the structure in Test FEH10. This structure had exactly the same geometry as the structure in Test FEH09, but was lighter, as evidenced by the difference in effective weight during the initial 8 seconds in Figure 4.24(a), before displacement of the PPT lead to inaccuracies in the calculated effective weight.

The vertical extenders resulted in the mobilisation of a bigger failure mechanism compared to the case with no vertical extenders in Test FEH05 (see Figure 4.7). Although the point of rotation changed, rotation still occurred because the liquefied soil adjacent to the extenders could not offer sufficient resistance as it had close to zero strength. In addition, the soil confined between the vertical extenders had close to zero vertical effective stress so did not provide any resistance to rotation, and instead was forced to rotate with the basement, as shown in Figure 4.20(b). In contrast, rotation did not occur when vertical confinement was increased in Test FEH09. Therefore, the key to minimising residual rotation lies in the vertical confinement at the instant of rotation - a greater vertical effective stress corresponds to a greater horizontal stress, which in turn results in increased resistance provided by the soil. This was illustrated in Test FEH09, and by Mitrani (2006) for structures with shallow foundations with vertical containment walls which extended to half the depth of the liquefied layer. This is analogous to the ease in which an object can be concurrently lifted and rotated, compared to pushed against another body and rotated. It can be concluded, that for cases where vertical confinement is insufficient to result in resistance to rotation, vertical extenders must extend into stiffer soil below the liquefied layer if they are to successfully prevent rotation.

The effective weight of the structure with horizontal extenders in Test FEH11, shown in Figure 4.24(a), progressively reduced during the first five cycles of shaking, before reaching a constant mean value for the remainder of shaking. The structure accumulated small settlement during the initial cycles of shaking (Figure 4.16(c)). It can be inferred that this was because, during this time, the effective weight of the structure, shown in Figure 4.24(a), was greater than the degraded bearing capacity provided by the soil. Subsequently, settlement ceased and the structure accumulated small uplift. This implies that it is likely that the effective weight of the structure reduced to below zero, meaning a resultant upward vertical force acted on the structure. This was not calculated using the data obtained from the centrifuge test. Errors in instrument location or soil unit weight could have reduced the accuracy of the calculated values of effective weight presented in Figure 4.24(a).

4.5 Boundary effects

It is important to discuss the possible boundary effects imposed by the model container. The width of the model container used for these centrifuge tests can be compared to the basement width, B, and depth, D. The rigid horizontal and vertical extenders increased the projected width and depth to B_{ext} and D_{ext} respectively. Compared to the basements with vertical extenders in Tests FEH09 and FEH10, the width of the model container was $6B$, which is equal to $5D_{ext}$. This equates to the edge of the basement being located a horizontal distance 2.6B from the edge of the model container, which is equal to $2.1D_{ext}$. For the basement with horizontal extenders in Test FEH11, the edges of the extenders were located a horizontal distance $1.05B_{ext}$ from the edge of the model container. It would have been desirable to have had a greater horizontal distance between the basements and the boundary, however this was not possible due to the size of the model containers available to use with the earthquake actuators on the centrifuge at the time of this research.

In Figures 4.18, 4.20, 4.21 and 4.23 the horizontal edges of the container are at 0 and 25 m on the x-axis, and the base is at 0 m on the y-axis. The soil displacement vectors shown in Figure 4.20 show that soil displacements occurred at the edges of the region monitored using the high-speed camera. The logical continuation of these displacement vectors outside the region monitored infers that the displacement mechanisms extended to the container boundaries. However, this does not invalidate the results and discussion presented in this chapter. For the structures with vertical extenders, the most significant difference between the soil displacements during the early cycles of shaking in EQ3 was the vertical component of displacement below the bottom of the extenders, as shown in Figure 4.18. The difference in the calculated effective weight of the structures accounted for this change, which in turn

governed the failure mechanisms that are shown in Figure 4.20. Rotation of the structure with vertical extenders in Test FEH10 occurred about the axis which minimised the volume of soil that needed to be displaced for rotation to be accumulated. Likewise, the behaviour of the structure with a horizontal extender in Test FEH11 was explained by considering its change in effective weight during shaking. Consequently, it is not felt that the model container boundaries either prevented failure mechanisms from developing or caused them to form. However, it is possible that the horizontal movement of soil was limited close to the model container boundaries. It is therefore not possible to determine the area of influence of the structures with basements with extenders due to the potential restriction of horizontal displacement due to the width of the model container.

To reduce the possibility of boundary effects when investigating the behaviour of structures in liquefiable soils it may be desirable to use larger levels of centrifugal acceleration or to commission a wider model window container. Both of these options would increase the width of the column of soil between the basement edge and the model container edge.

4.6 Structure installation effects

It is necessary to discuss the possible installation effects caused by the method used to prepare the centrifuge models. During the preparation of the centrifuge models, the model structures were manually placed once sand pouring had reached the level of the bottom of the basement. This was simple for all the structures, excluding the structures with basements with vertical extenders. For these structures, i.e. Tests FEH09 and FEH10, installation of the structure involved pushing the vertical extenders through the poured layer of sand until the bottom of the basement was level with the top of the soil layer. Pushing was done uniformly and slowly, with the basement held level and flush against the model container window. A consequence of this procedure was that soil adjacent to the extenders was dragged downward by the extenders due to the build up of skin friction. This resulted in small gaps of no soil in the corners where the extenders joined the basement, meaning that the bottom of the basements were not flush with the soil across their entire cross sectional area. Post sand pouring, these small gaps were full of air. After saturation of the model they were full of pore fluid.

For the cross section visible through the transparent PMMA window, the percentage of the total width of the basement in contact with the soil beneath it after swing up was measured to be approximately 85 % for Test FEH09 and 81 % for Test FEH10. It is assumed that this was representative of the entire length of each structure. The bearing pressure applied by the structures was therefore greater than if 100 % of the basement had been in contact with the

soil, which means the initial vertical effective stress obtained from the Plaxis 2D analysis was an underestimate.

Local densification is likely to have occurred in the soil immediately adjacent to the extenders during installation of the structures. In Test FEH09 the soil constrained within the vertical extenders behaved as an almost rigid body (Figures 4.18(a,b)). Therefore it can be assumed that there were negligible differences in the soil conditions within this region. In addition, it is not felt that the small gaps altered the co-seismic behaviour of the soil between the vertical extenders. Large excess pore pressures were generated in this region during large amplitude shaking in EQ3. This was expected due to the low initial relative density of the sand and was consistent with the behaviour observed by Mitrani (2006) for vertical containment walls that extended for half the depth of a liquefiable layer below a structure with a shallow foundation. The small gaps are not believed to have governed this behaviour. Therefore, it is not felt that the installation method had a notable impact on the behaviour of the structures with vertical extenders presented in this chapter.

A number of alternative model construction methods were considered to minimise installation effects. Installing the vertical extenders and basement separately, at the point at which the sand pour reached the level of their respective base, and subsequently connecting them together, was considered. Following trial runs, this option was discarded as it was not possibly to produce a rigid connection between the basement and extenders whilst keeping the structure flush against the container window but not stuck to it, without significantly disturbing a large volume of the poured soil layer. Another option considered was to conduct the sand pour with the model container rotated by 90 °, as is commonly done when preparing centrifuge models containing a pre-installed tunnel. This method of model construction would have ensured that the structure was flush against the window and the sand following pouring. However, it would not have allowed discrete instrumentation to be sequentially placed within the soil layer. The method of structure installation used for the centrifuge tests presented in this chapter was the most suitable given the model requirements and the equipment available.

4.7 Conclusions

The focus of this chapter was on the influence of a shallow, narrow basement on the seismic behaviour of a structure located on liquefiable soil. Emphasis was placed on the performance of these structures when rigid extenders were attached to the basement.

In static conditions, an upward buoyancy force acted on the basements due to hydrostatic water pressure. During liquefaction, this uplift force increased due to the generation of

positive excess pore pressure. Consequently, the effective weight of the structures reduced. The centrifuge tests showed that this had the positive desired effect of reducing liquefaction induced settlement of the structure, compared to structures with shallow foundations without basements. This was in spite of the positive excess pore pressures concurrently reducing the stiffness and strength of the soil, which degraded the bearing capacity of the soil. In addition, the reduced effective bearing pressure of the structure allowed the positive excess pore pressures in the column of soil below the structure to approach the corresponding values of initial vertical effective stress. This had the beneficial effect of naturally isolating the structure from the base shaking.

The presence of a basement was found to increase rotation during earthquake induced liquefaction. The couple due to the non-co-linear weight and buoyancy force did not re-right the structure. Insufficient resistance was provided by the shear dilation of the liquefied soil adjacent to the basement to prevent rotation of the structure.

Methods used in naval engineering to improve the stability of ships were used as inspiration to improve the stability of the structures with basements during earthquake induced liquefaction. Rigid, vertical extenders, which were attached to the sides of the basement and extended for half the depth of the liquefiable layer, were found to adversely affect the behaviour of the structures. When the effective weight of the structure exceeded the degraded bearing capacity provided by the soil below, settlement occurred. The forced vertical downward movement of the block of soil within the vertical extenders, and the confinement of the soil below, was sufficient to prevent the structure from rotating. In contrast, when the effective weight of the structure was reduced, the vertical effective stress in the soil below decreased. This reduced the horizontal stress, and therefore the resistance to rotation. The vertical extenders resulted in the mobilisation of a bigger failure mechanism compared to the case with no vertical extenders. However, rotation still occurred because the liquefied soil could offer insufficient resistance as it had close to zero strength. In summary, vertical extenders protruding below shallow, narrow basements worsened settlement for heavier structures and rotation for lighter structures. This is concerning as this is the likely geometry of structures with basements when the construction process is considered; diaphragm walls extending below the bottom of a basement are commonly used for construction and then left in place.

The use of horizontal extenders were found to have the desirable effect of maintaining the beneficial effect of the basement on minimising settlement of the structure, whilst also reducing rotation. This behaviour suggests that the width of the widest section of the basement and the net weight of the structure during liquefaction are the key design parameters to ensure

that structures with basements located in liquefiable soils accumulate minimal liquefaction induced settlement and rotation.

Chapter 5

Behaviour of structures with wide basements located in liquefiable soil

5.1 Introduction

The dynamic centrifuge tests presented in Chapter 4 showed that basements can be used to reduce the liquefaction induced settlement of structures. However, resistance to rotation provided by the soil was found to be reduced due to a reduction in vertical effective stress below the basements. Stability of a structure with a narrow basement was found to be improved by including rigid, horizontal extenders protruding horizontally from the sides of the basement. In this chapter, the behaviour of structures with wide basements is discussed. These structures are representative of hotels or shopping malls with a wide ground floor which could have a basement extending below it, and a taller central tower above (see Elghazouli (2017)).

Within the extensively researched area of liquefaction induced settlement of structures with shallow foundations, the effect of foundation width has been widely investigated. For a given depth of liquefiable soil, increasing the foundation width has been found to reduce the settlement of a structure (Yoshimi & Tokimatsu 1977, Adachi et al. 1992, Acacio et al. 2001, Bertalot et al. 2013). For a given bearing pressure, an increase in the width of the foundation makes it more difficult to displace soil laterally from beneath the structure, and therefore reduces settlement due to ratcheting (Dashti et al. 2010*b*). Liu & Dobry (1997) compiled field and centrifuge data and proposed a design chart to determine foundation settlement given the building width and depth of liquefiable soil. This chart has since been populated further with data from subsequent earthquakes and centrifuge tests by other researchers (Acacio et al. 2001, Bertalot et al. 2013). Recent research shows that, whilst this method may work well in

the presence of a sufficiently thick liquefiable layer, it may be misleading for thinner layers (Dashti et al. 2010*b*, Dashti & Bray 2013, Adamidis & Madabhushi 2015, 2018*a*).

The effect of foundation width on the liquefaction induced residual rotation of structures with shallow foundations has been indirectly studied by investigating the effect of aspect ratio. If the height of the centre of mass of a structure remains unchanged, reducing the foundation width increases the aspect ratio. Following the 1999 Kocaeli earthquake, it was observed that liquefaction induced residual rotation of structures increased with increasing aspect ratio (Gazetas et al. 2004). No visible rotation was observed for structures with an aspect ratio less than 0.8, whilst structures with an aspect ratio greater than 1.8 overturned. Intuitively, this pattern was attributed to the increase in dynamic over turning moment when the aspect ratio increased.

There are two reports on the liquefaction induced behaviour of structures with wide basements following the 2010 - 2011 series of earthquakes in Christchurch, New Zealand. The first structure had a 69 m $\times$ 82 m two storey basement, with superstructures located above approximately one half of the plan area of the basement. Differential vertical displacement of 130 - 150 mm was measured across the basement mat foundation, and was attributed to downward settlement of the basement below where the superstructures were located, and uplift where no superstructure was present (Bray & Luque 2017). The second structure had a 50.8 m $\times$ 37.7 m one storey basement beneath two symmetrically positioned superstructures. It experienced approximately 120 mm of differential settlement, but it is unknown whether this was due to differential settlement or differential heave, or both (Luxford 2014). There was failure of shear connections within the floor slab of this basement which were expected to be able to sustain 1.4 times the hydrostatic uplift force, indicating that the pressure beneath the slab far exceeded hydrostatic pressure. This is consistent with the liquefied soil behaving as a dense fluid.

The dynamic centrifuge tests discussed in this chapter are the first tests of their kind to investigate the seismic behaviour of structures with wide basements located in liquefiable soil. Some of the results presented in this chapter have been reported previously (Hughes & Madabhushi 2018*a*, 2019*b*).

5.2 Dynamic behaviour of basement-structure system

Three dynamic centrifuge tests were conducted using structures with wide basements. The properties of the structures are discussed in detail in Chapter 3, and are summarised in Table 5.1. All three tests included a single degree of freedom (SDOF) superstructure which was rigidly connected to a wide basement, which was 9.6 m wide at prototype scale. Throughout

Table 5.1 Properties of structures with wide basements (prototype scale)

Property	Symbol	FEH06	FEH07	FEH08
Total bearing pressure (kPa)	q_b	68.1	55.0	55.2
Static effective bearing pressure (kPa)	q'_b	40.1	29.0	29.2
Ratio of uplift to total weight during liquefaction	U/W	0.75	0.93	0.92
Symmetric superstructure		Y	Y	N
Fixed base natural frequency (Hz)	f_n	1	1	0.83
Basement width (m)	B	9.6	9.6	9.6
Basement depth (m)	D	3.0	3.0	3.0
CoG height above top of basement (m)	y_{CoG}	-0.044	0.526	1.3
CoG horizontal distance from centreline (m)	x_{CoG}	0	0	-0.184

this thesis, the term "wide basement" is used to refer to a basement with this width. Tests FEH06 and FEH07 used the same symmetric superstructure but with a different total structure weight. The structure used in Test FEH08 had the same total weight as that used in Test FEH07, but the superstructure was asymmetric. A mass was placed on the roof of the structure, centred over one of the columns. Symmetry and uniformity are desirable in the design of earthquake resistant buildings, as stated in Eurocode 8 Part 1 (CEN 2004); however, mass and stiffness eccentricities are inherent in structures due to the presence of features such as water storage tanks, lift shafts and entrances.

Three base shaking events are discussed in this chapter for each of the structures with wide basements. The base shaking events differed in duration, peak acceleration, and frequency content. The first earthquake, EQ1, had a low amplitude, sinusoidal input motion, consisting of 20 cycles with the same frequency as the fixed base natural frequency of the corresponding structure shown in Table 5.1. The second earthquake, EQ2, had the same frequency content as the 1979 Imperial Valley earthquake, which was characterised by its long duration and high frequency content, and was scaled to have a peak acceleration equal to 0.1 g. The third earthquake, EQ3, was a high amplitude, sinusoidal input motion with the same number of cycles and the same frequency as EQ1. EQ3 had a peak acceleration of approximately 0.4 g. EQ1, EQ2 and EQ3 had the same characteristics as the corresponding earthquakes fired during the centrifuge tests using narrow basements and rigid, impermeable extenders, which were discussed in Chapter 4, Section 4.4.

The soil relative density prior to each earthquake event varied slightly, because soil densification occurred as a result of each of the sequential shaking events. For example, for Test FEH07, the relative density was 49 %, 49 % and 53 %, before EQ1, EQ2 and EQ3 respectively. These relative densities were calculated using the mass of sand in the container and the volume occupied before each shaking event commenced. The pre-seismic

soil condition remained susceptible to liquefaction prior to each earthquake, therefore it is assumed that the soil behaviour during each of the seismic events can be compared.

5.2.1 Initial vertical stress distribution

The initial vertical effective stress distribution beneath each of the structures tested was calculated using the software Plaxis 2D (Plaxis 2000) and is shown in Figure 5.1. The basements were modelled using effectively rigid, weightless plates with rigid fixities at the joints. Uniformly distributed loads were used to match the pressure applied by the superstructure and the basement. The soil was modelled as a Mohr-Coulomb material, with the material properties given in Table 4.3.

Figure 5.1 shows that, at a given depth, the initial vertical effective stress underneath each of the basements was greater than the initial vertical effective stress in the far-field. However, the difference was small and reduced with increasing depth. The contours of constant initial vertical effective stress in Figure 5.1 are therefore almost horizontal, which is what would be observed for a level bed of homogenous soil. This makes intuitive sense as the excavation for the basement floors almost compensates for the structure load. Consequently, at the depth of the bottom of the basement, the total stress in the far-field due to the column of soil above that point was only slightly less than the total stress applied by the structure.

The vertical effective stresses shown in Figure 5.1 were indicative of the conditions in the centrifuge models following spin up but prior to shaking. During shaking, soil-structure interaction due to rocking and translation of the structure will affect the total stress distribution in the soil. In addition, shearing of the soil can generate excess pore pressures. Both of these mechanisms affect the co-seismic vertical effective stress distribution.

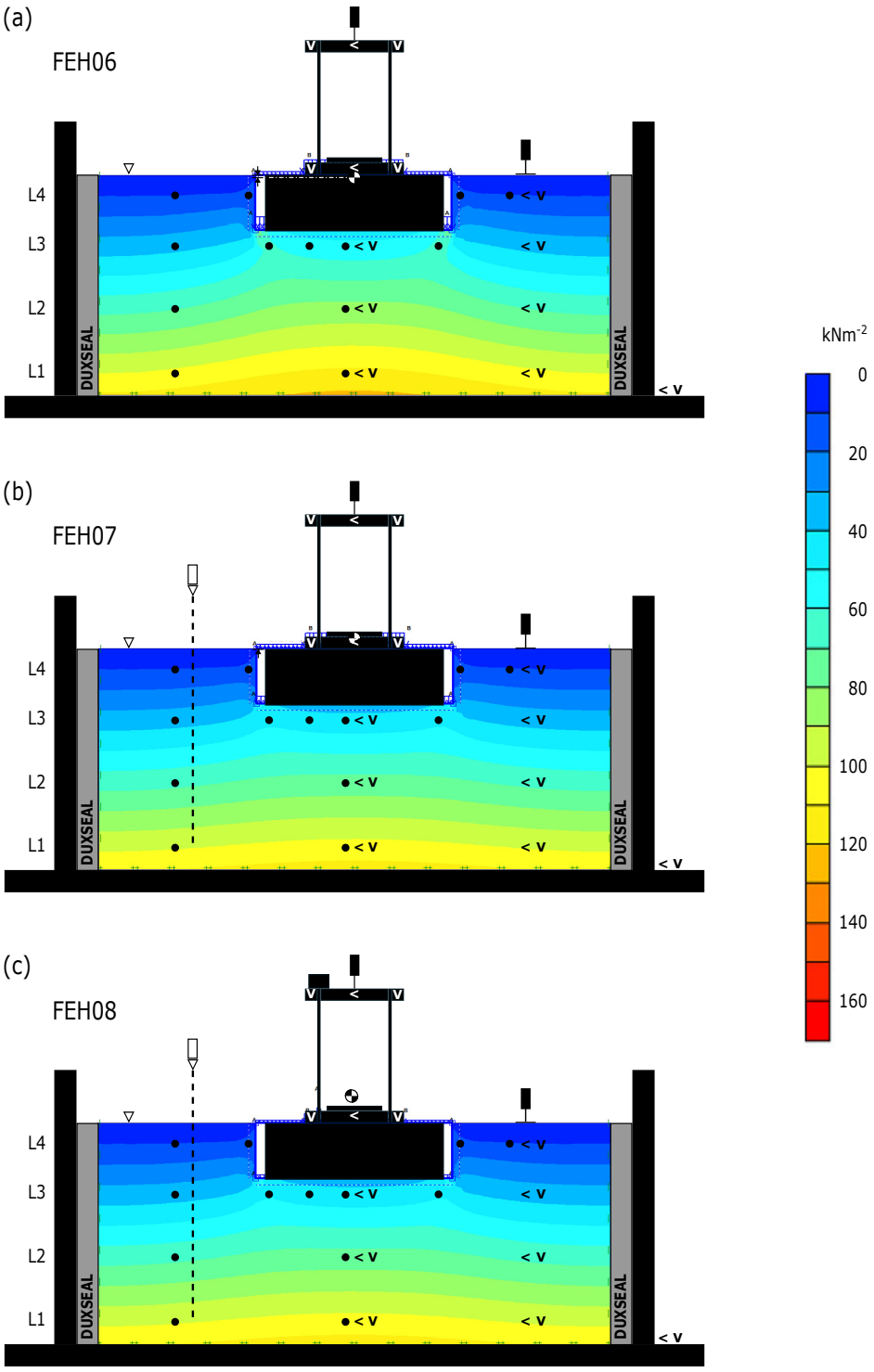

Fig. 5.1 Initial vertical effective stress contours for structures with wide basements obtained from Plaxis 2D analysis (Plaxis 2000). The initial location of the structure and instrumentation in each model test is shown.

5.2.2 Excess pore pressures

When loose, saturated, sandy soils are subjected to cyclic loading, the tendency to contract when sheared can result in the generation of positive excess pore pressures. When positive excess pore pressures are generated, the uplift force acting on a structure with a basement increases to greater than that during hydrostatic conditions, which consequently reduces the effective bearing pressure. Intuitively, this will strongly affect the co-seismic behaviour of structures with wide basements.

Figure 5.2 shows the excess pore water pressures generated in the instrumented column of soil in the far-field during the three earthquakes. Figure 5.3 shows the same for the instrumented column of soil beneath the centre of each of the wide basements. The dashed horizontal lines show the initial vertical effective stress at the corresponding instrument location, obtained from the Plaxis 2D analysis presented in Figure 5.1. When the excess pore pressure measured at an instrumented location approached the corresponding initial vertical effective stress, the instantaneous value of the vertical effective stress approached zero and liquefaction occurred.

For Tests FEH06 and FEH07, during EQ1 almost no excess pore pressures were generated in either the far-field (Figure 5.2) or beneath the structures (Figure 5.3), indicating that the low amplitude of the base shaking of EQ1, which had a peak acceleration of 0.035 g, was not sufficient to cause contraction of the loose soil skeleton. The amplitude of EQ1 was greater in Test FEH08 and had a peak acceleration of 0.085 g, as shown in Figures 5.2(o) and 5.3(l). This was not intentional, but a result of the frequency dependency of the transfer function of the servo-hydraulic shaker (Madabhushi et al. 2012). Consequently, positive excess pore pressures were generated, and were approximately the same magnitude, at all the instrumented depths for Test FEH08 during EQ1. Liquefaction occurred only at the shallowest instrumented depth in the far-field, shown in Figure 5.2(c).

In EQ2, positive excess pore pressures were generated at all depths in all tests, both in the far-field (Figure 5.2) and below the centre of the basements (Figure 5.3). The rate of generation of excess pore pressure decreased with increasing depth as the vertical effective stress increased and therefore greater shearing was required to cause contraction of the soil skeleton. Liquefaction occurred at the shallowest instrumented depth in the far-field, shown in Figures 5.2(a,b,c). At the other instrumented locations, where liquefaction did not occur, the excess pore pressures generated were approximately the same magnitude during the co-seismic period, and fluctuated with the change in amplitude of the base shaking acceleration. Despite liquefaction not occurring, soil softening will have occurred and will have been proportional to the excess pore pressures generated with respect to the initial vertical effective stress.

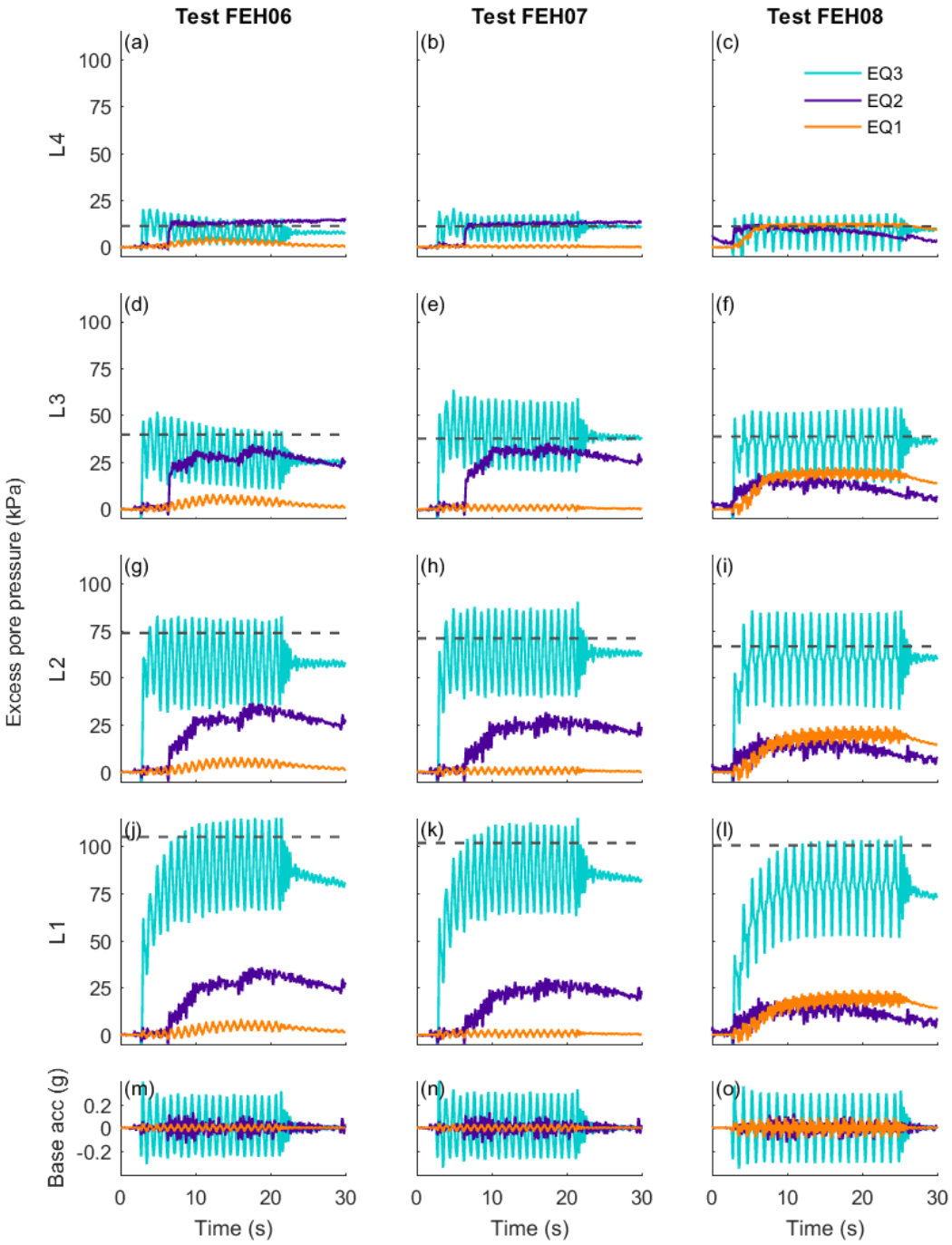

Fig. 5.2 Excess pore water pressure time histories for the instrumented column in the far-field during EQ1, EQ2 and EQ3. L*N* indicates the level of instrumentation, with *N* increasing with increasing depth, shown in Figure 5.1. Dashed lines indicate the initial vertical effective stress at the corresponding instrument location, obtained from Plaxis 2D analysis.

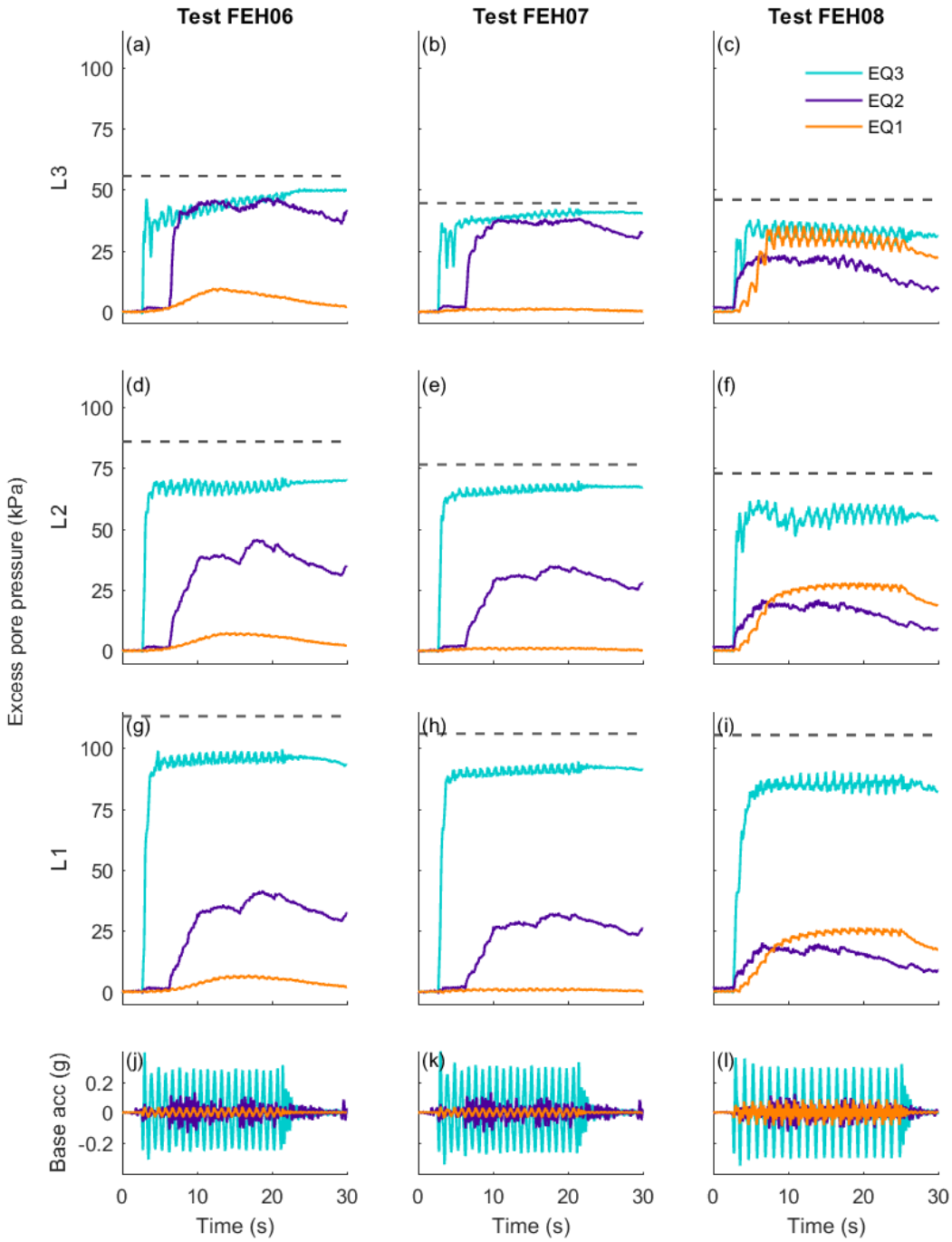

Fig. 5.3 Excess pore water pressure time histories for the column of soil underneath the centre of the structures during EQ1, EQ2 and EQ3. L*N* indicates the level of instrumentation, with *N* increasing with increasing depth, shown in Figure 5.1. Dashed lines indicate the initial vertical effective stress at the corresponding instrument location, obtained from Plaxis 2D analysis.

The base shaking in EQ3 was sufficiently large to cause positive excess pore pressures to be quickly generated at all depths in the far-field (Figure 5.2) and below the centre of the basements (Figure 5.3). These figures show that the excess pore pressures approached the corresponding values of initial vertical effective stress, meaning that liquefaction occurred at all locations, including at all depths below each of the structures with basements. This is in contrast to what has been observed to occur beneath structures with shallow foundations on liquefiable soil during strong shaking, and is a result of the very different effective bearing pressures applied by the structures.

For structures on shallow foundations which are not partially buried, the effective bearing pressure is equal to the total bearing pressure, and remains constant when positive excess pore pressures are generated. Two recent research efforts which have investigated the behaviour of structures with shallow foundations, using dynamic centrifuge testing, utilised structures with bearing pressures in the range of 30 - 130 kPa (Bertalot & Brennan 2015) and 50 - 100 kPa (Adamidis & Madabhushi 2018*a*). In contrast, the generation of positive excess pore pressures during shaking increased the uplift force on the structures with basements presented in this chapter whilst the total weight of the structures remained constant. Consequently, the effective bearing pressure of the structures with basements significantly reduced during liquefaction, and were 15.9, 2.82 and 2.18 kPa for the structures with wide basements in Tests FEH06, FEH07 and FEH08 respectively. The high effective bearing pressure applied by a structure with a shallow foundation has been found to prevent liquefaction occurring in the bulb of soil directly below the foundation (Coelho et al. 2007, Dashti et al. 2010*a*, Marques et al. 2012, Zeybek & Madabhushi 2016, Adamidis & Madabhushi 2018*a*). Figure 5.3 shows that the uplift force provided by the basements reduced the effective bearing pressure applied by the structures to a level below that preventing liquefaction from occurring. Comparable behaviour was observed below the centre of the structures with narrow basements with rigid extenders, shown in Figure 4.12, however the maximum excess pore pressures obtained were a slightly smaller percentage of the corresponding initial vertical effective stress.

Oscillations in excess pore pressure about the mean value occurred during shaking due to cyclic shearing of the liquefied soil. The amplitude of these oscillations was greater in the far-field (Figure 5.2) than underneath the centre of the structures (Figure 5.3) and increased with increasing depth. Greater oscillations imply a greater amplitude of cyclic shear strain and consequently increased local contraction and dilation. In both the far-field and underneath the structure these oscillations occurred at the same frequency as the base shaking.

5.2.3 Transmission of horizontal accelerations

Horizontal accelerations caused by an earthquake are transmitted upwards through a soil layer by horizontally polarised vertically propagating shear waves. The transmission of these accelerations to structures located on top of, or within, the soil results in horizontal inertia forces. These can damage structural components, depending on the amplitude and frequency of the accelerations in relation to properties of the structure.

Horizontal accelerations were measured at discrete locations in the soil body and on the structures. Figure 5.4 shows the horizontal acceleration time histories for the roof and ground floor of the structures and the column of soil below the centre of the basements.

During EQ1 and EQ2 the horizontal accelerations in the soil body were neither amplified nor attenuated as they were transmitted upwards. Consequently, in each of these cases, the amplitude of the shaking of the ground floor of the structure was of approximately the same magnitude as the base shaking, shown in Figures 5.4(d,e,f). The flexible nature of the SDOF superstructures resulted in the accelerations at the roof level, shown in Figures 5.4(a,b,c), being greater than those experienced at the ground floor level. The accelerations experienced at roof level were therefore of greater magnitude than the base shaking. This was more pronounced during EQ1, where the frequency of the base shaking was equal to the fixed base natural frequency of the superstructures. It is worthwhile reiterating that liquefaction did not occur in the deeper instrumented layers for any of the three tests during EQ1 or EQ2 (Figures 5.2 and 5.3).

In contrast, during EQ3 the horizontal accelerations were progressively attenuated as they were transmitted upwards through the liquefied soil (Figure 5.4). The transmission of horizontal accelerations from the base of the model through the soil body was therefore highly dependent on whether liquefaction occurred or not. When the excess pore pressures approached the corresponding initial vertical effective stress, shown in Figure 5.3, the instantaneous vertical effective stress approached zero. The near zero vertical effective stress state caused a very large stiffness degradation which reduced the ability of the soil to carry shear stress and therefore transmit shear waves. The horizontal accelerations transmitted to the structure were therefore significantly smaller than those generated by the base shaking. Liquefaction of the soil beneath the basements therefore naturally isolated the structures from the base shaking acceleration. Horizontal accelerations transmitted to the ground floor of the structures were then amplified at the roof level, due to the flexible nature of the superstructure. In contrast to EQ1, in EQ3 the accelerations at roof level remained less than the base shaking (Figures 5.4(a,b,c)). The observed drift in the measured horizontal acceleration of the structure in Test FEH08 EQ3, shown in Figures 5.4(c,f), was caused by the accumulated rotation of the structure, which is discussed in detail in Section 5.2.5. As

the accumulated rotation of the structure increased, the MEMS accelerometers recorded an increasing component of the centrifugal acceleration.

Despite the comparable amplitude of base shaking between the tests during EQ1, the amplitude of acceleration of the roof of the structure was significantly greater in Test FEH06 than either FEH07 or FEH08 (Figures 5.4(a,b,c)). This was not observed during EQ2, but also occurred during EQ3, but to a lesser extent. This is likely to be due to the proximity of the natural frequency of the soil-structure system to the constant frequency of the base shaking during EQ1 and EQ3. It should be reiterated that the frequency of the base shaking during EQ1 and EQ3 was the same frequency as the fixed base natural frequency of the structure being tested.

The Fast Fourier transforms (FFTs) of the horizontal acceleration of the structure during EQ2, shown in Figure 5.5, gives insight into this behaviour as the base shaking had a mixed frequency content. The base shaking acceleration during EQ2 had dominant frequencies at 1.7 Hz and around 2.6 Hz. The acceleration of the roof of the structure in FEH06 and FEH08 show dominant frequencies at 1 Hz (Figure 5.5(a)) and 0.8 Hz (Figure 5.5(c)) respectively, despite the base shaking not having a peak at these frequencies. These were the design fixed base natural frequencies of these superstructures, and for this reason were the frequency of the sinusoidal base shaking during EQ1 and EQ3. FEH07 did not have a clear peak in this frequency range (Figure 5.5(b)), despite the design fixed base natural frequency of the superstructure being 1 Hz. During EQ1 and EQ3, the structures in Tests FEH06 and FEH08 were therefore shaken at the natural frequency of the soil-structure system, but FEH07 was not. This explains the differences in roof acceleration amplitude observed in Figures 5.4(a,b,c). It is not possible to estimate the natural frequency of the soil-structure system for FEH07 as the magnitude of the base shaking during EQ2 was not constant at all frequencies.

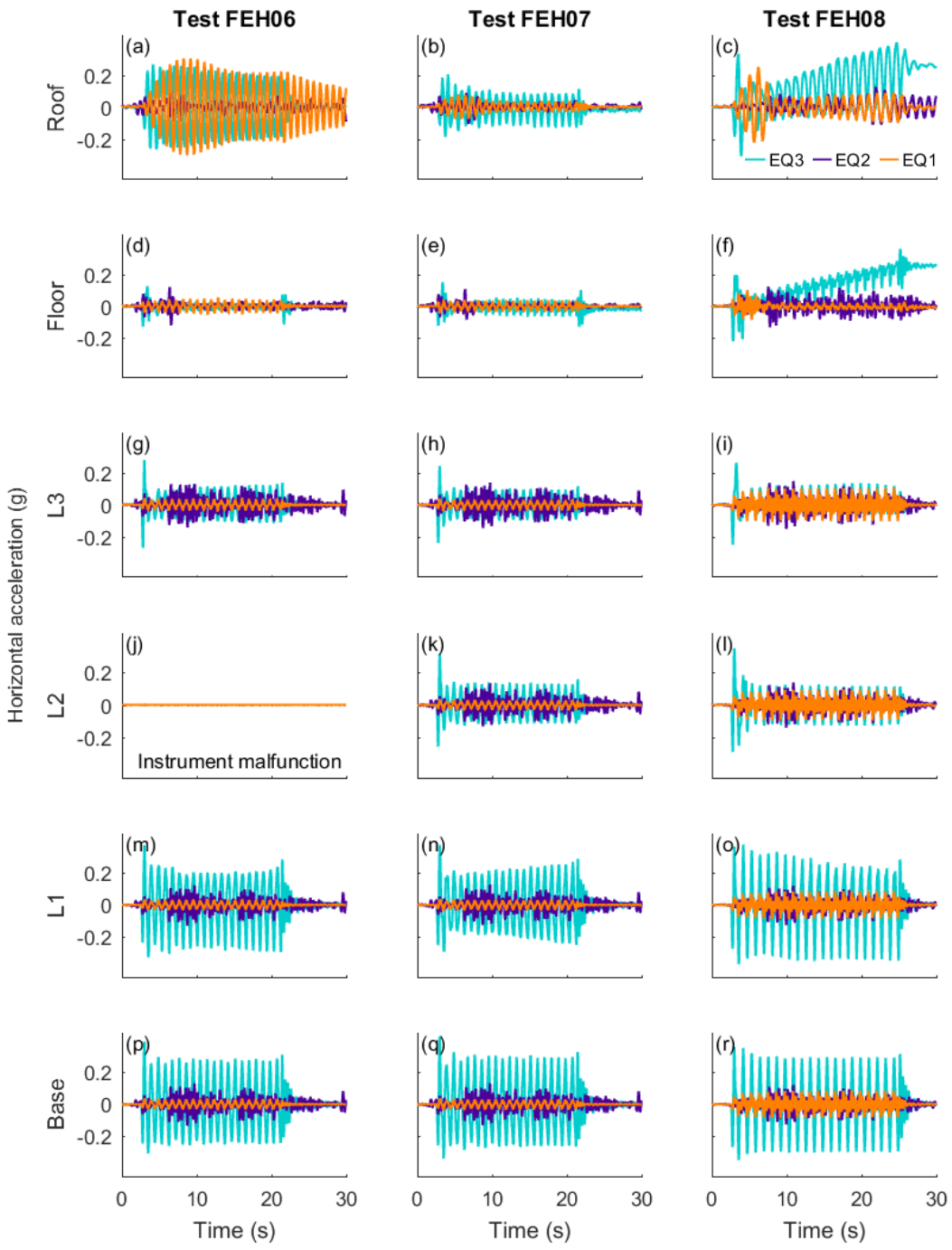

Fig. 5.4 Co-seismic horizontal acceleration time histories for the structure, the soil column below the basement and the input motion during EQ1, EQ2 and EQ3. L*N* indicates the level of instrumentation in the soil, with *N* increasing with increasing depth, as shown in Figure 5.1.

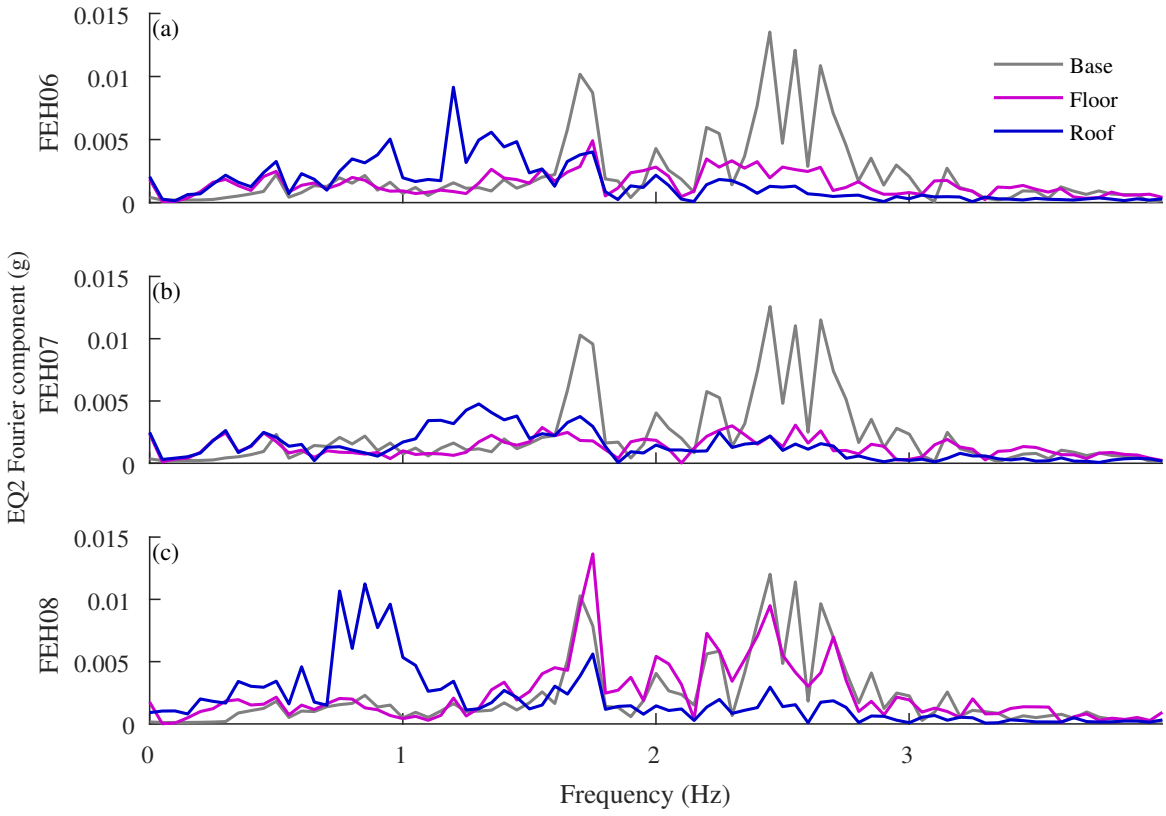

Fig. 5.5 Fast Fourier transform (FFT) of the horizontal acceleration at the base of the model container (Base) and the ground floor (Floor) and roof (Roof) of the structures with wide basements during EQ2.

5.2.4 Stress paths

The different soil behaviour during the three earthquakes can be investigated further by plotting the stress paths during shaking. Specifically, it is interesting to compare the behaviour in the far-field and under the centre of the basements. In these centrifuge tests, the excavation for the basement floors almost compensated for the structure load. As a consequence the initial vertical effective stresses were comparable (Figure 5.1) however, the vertical load in the far-field was purely due to the weight of the overlying soil, whilst beneath the basement it was a combination of the structure load and a thinner soil layer.

The stress paths at the depth of L2 of instrumentation, 7.1 m below the soil surface, in both the far-field and underneath the centre of the basements are presented in Figure 5.6 for the three earthquakes. The critical state line, *CSL*, is shown in grey. Vertical effective stress was calculated by subtracting the measured excess pore pressure from the corresponding initial vertical effective stress obtained from the Plaxis 2D analysis. Shear stress was calculated using acceleration data, following the methodology proposed by Elgamal et al. (1996). Redistribution of total vertical stress and shear stress caused by rocking and rotation of the structure was not included. This omission reduces the accuracy of the stress paths plotted. Nevertheless, Figure 5.6 provides insight into the different soil behaviour during the three earthquakes.

During EQ1 and EQ2, the stress paths in the far-field, shown in Figures 5.6(a,c,e), and underneath the basements, shown in Figures 5.6(b,d,f), showed comparable behaviour. Positive excess pore pressure generation resulted in a reduction in vertical effective stress and gradual progression of the stress paths leftward along the x-axis with each cycle of shear stress, toward the critical state line, *CSL*, which is shown in grey in these figures. The slope of the stress paths were shallower in the far-field than under the centre of the basements. This is a result of greater amplitude oscillations in excess pore pressure causing larger changes in vertical effective stress during each cycle of shaking.

During EQ3, the stress paths in the far-field and underneath the basements showed different behaviour. Underneath the centre of the basements, shown in Figures 5.6(b,d,f), a large reduction in vertical effective stress occurred within one cycle of shear stress, which rapidly moved the stress paths leftwards toward the critical state line. Beneath the basement in Test FEH08, the critical state line was reached, and the stress path changed direction when it did so (Figure 5.6(f)). Following the initial cycle, the stress paths below the basements cycled at an approximately constant vertical effective stress for the remainder of shaking.

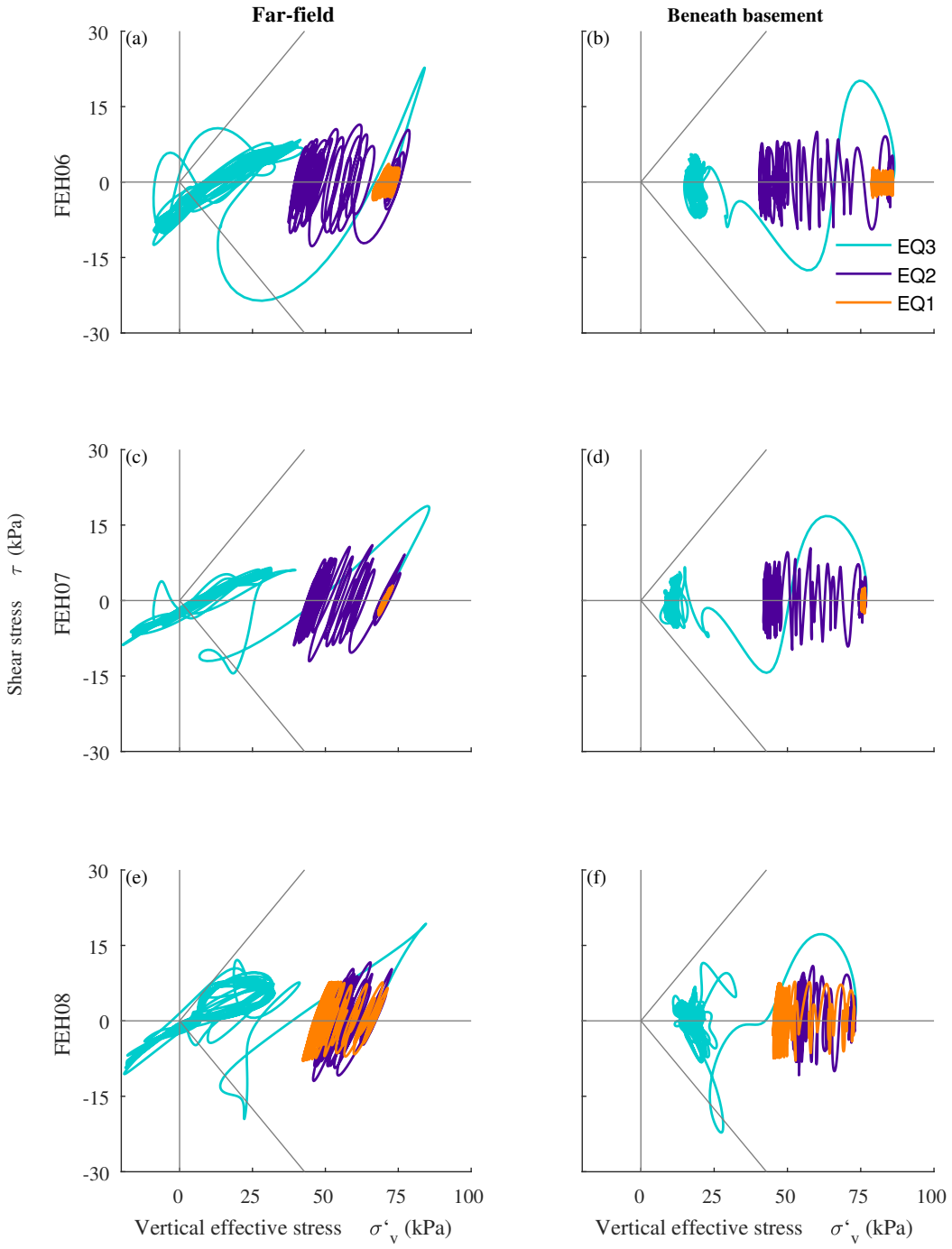

Fig. 5.6 Stress paths at the depth of L2 of instrumentation, 7.1 m below the soil surface, in both the far-field (left column) and underneath the centre of the basements (right column) during EQ1, EQ2 and EQ3. Critical state line shown in grey. (a) FEH06 far-field, (b) FEH06 beneath basement, (c) FEH07 far-field, (d) FEH07 beneath basement, (e) FEH08 far-field, (f) FEH08 beneath basement.

In the far-field, the same large reduction in vertical effective stress occurred within the initial cycle of shear stress, at which point the stress paths reached the critical state line in all three tests, as shown in Figures 5.6(a,c,e). It is expected that after initial liquefaction, the stress paths will follow the critical state line in stress space. Figures 5.6(a,c,e) show that the stress paths in fact cycled up and down a straight line with a shallower gradient than the critical state line. This suggests that the oscillations in instantaneous vertical effective stress during each cycle of shaking are overestimated in Figure 5.6. These were calculated by subtracting the measured excess pore pressures from the initial vertical effective stress at the corresponding location, obtained from Plaxis 2D analysis. This may be an artefact of not accounting for settlement of the instrument during shaking. Alternatively, it may be because the soil was not in vertical equilibrium.

Oscillations in excess pore pressure ratio with peaks notably greater than one have been shown to be due, in part, to the soil body no longer being in vertical equilibrium when liquefaction occurs (Hughes & Madabhushi 2018*b*). Following this logic, the instantaneous vertical effective stresses can be recalculated, using a methodology which does not assume the soil body to be in vertical equilibrium.

The vertical forces at an instrument location can be assessed. The downwards vertical force, $F_1(t)$ in Figure 5.7, is due to the weight of the sand and the pore fluid above the pore pressure transducer (PPT):

$$F_1(t) = A[\gamma_{sat} \times z] = A \times \sigma_{v0} = A[\sigma'_{v0} + u_h] \tag{5.1}$$

where z is the depth of the PPT, γ_{sat} is the saturated unit weight of the soil, A is the plan area being considered, and σ_{v0} and σ'_{v0} are the total and effective initial vertical stresses respectively.

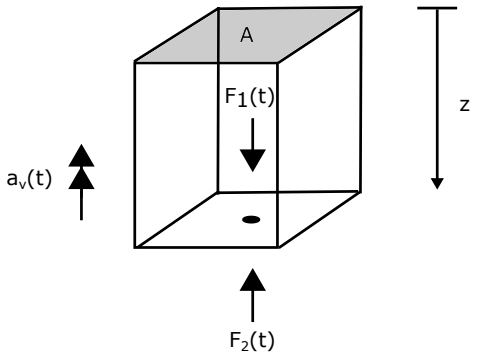

Fig. 5.7 Vertical forces, $F(t)$, and resulting vertical acceleration, $a_v(t)$, acting on a volume of saturated sand, depth z and plan area A, above a pore pressure transducer (PPT) located at depth z below the ground surface. PPT shown by black circle.

Terzaghi's effective stress principle is reliant on a soil body being in equilibrium (Terzaghi 1943). Starting from this principle, the upwards vertical force, $F_2(t)$ in Figure 5.7, is the sum of the vertical effective stress, $\sigma'_v(t)$, the hydrostatic pore water pressure, u_h, and the excess pore water pressure generated, $u_{ex}(t)$:

$$F_2(t) = A[\sigma'_v(t) + u_h + u_{ex}(t)] \tag{5.2}$$

However, it will not be assumed that vertical equilibrium is maintained. Newton's second law can be used to calculate the resultant vertical force from the recorded vertical accelerations in the soil body, $a_v(t)$, which were measured using piezo accelerometers.

$$F_2(t) - F_1(t) = ma_v(t) \tag{5.3}$$

where m is the mass being accelerated, which will be assumed to be the mass of the soil and pore fluid above the location of the instrument, which is equal to $\gamma_{sat}Az/g$. The instantaneous vertical effective stress can be calculated:

$$\sigma'_v(t) = \frac{\gamma_{sat} z a_v(t)}{g} + \sigma'_{v0} - u_{ex}(t) \tag{5.4}$$

Figure 5.6 is replotted in Figure 5.8 with the recalculated vertical effective stress, given in Equation 5.4, which accounts for the measured vertical accelerations. It is observed that the gradient of the "butterfly loops" in the stress path, where the critical state line is first reached and liquefaction is initiated, now closely match the gradient of the critical state line in Figures 5.8(c,e). Likewise, following initial liquefaction, the stress paths now fit closer to the critical state line. The stress paths in the far field are now closer to what is traditionally expected in geotechnical engineering (Ishihara 1985).

Comparing Figures 5.6 and 5.8, it is evident that accounting for the measured vertical accelerations has a greater effect on the stress paths during EQ3 compared to during EQ1 and EQ2. Vertical accelerations were largest when the amplitude of the base shaking was greatest, and when liquefaction occurred. In addition, comparison of Figures 5.6 and 5.8 show that accounting for the measured vertical accelerations had a greater effect on the stress paths in the far-field than underneath the centre of the structures. This shows that vertical accelerations were greater in the far-field than underneath the structures, likely because of rocking of the basements during shaking. At L2 of instrumentation during EQ3, the amplitude of vertical accelerations were approximately 0.1 g and 0.03 g in the far-field and in the column of soil underneath the centre of the basements respectively. It should be noted

that redistribution of total vertical stress and shear stress during shaking are not accounted for in Figure 5.8.

In the far-field, the recalculated vertical effective stress reduced to values below zero after liquefaction was initiated, as shown in Figures 5.8(c,e). Physically, it is not possible to have negative vertical effective stress as it implies that the sand particles were in tension. Instead, the negative values are likely to be a result of a combination of two effects that were not considered in the calculation methodology detailed in Equations 5.1 - 5.4. Firstly, instrument settlement was not included. Changes in pre and post earthquake hydrostatic pore pressure show settlement of PPTs occurred at all instrumented locations in the far-field during EQ3. However, settlement was not included in the calculations because, during shaking, it is difficult to decouple changes in pore pressure measurements due to instrument settlement from those due to soil shearing and soil-structure interaction. The vertical effective stresses calculated and shown in Figure 5.8 will therefore be an underestimate after any instrument settlement occurred. This will have shifted the stress paths leftwards along the x-axis because the increase in hydrostatic pore pressure was not accounted for. Secondly, when vertical acceleration occurred, Equation 5.4 may still have overestimated the oscillations in instantaneous vertical effective stress during each cycle of shaking as it does not consider shearing relative to the free field.

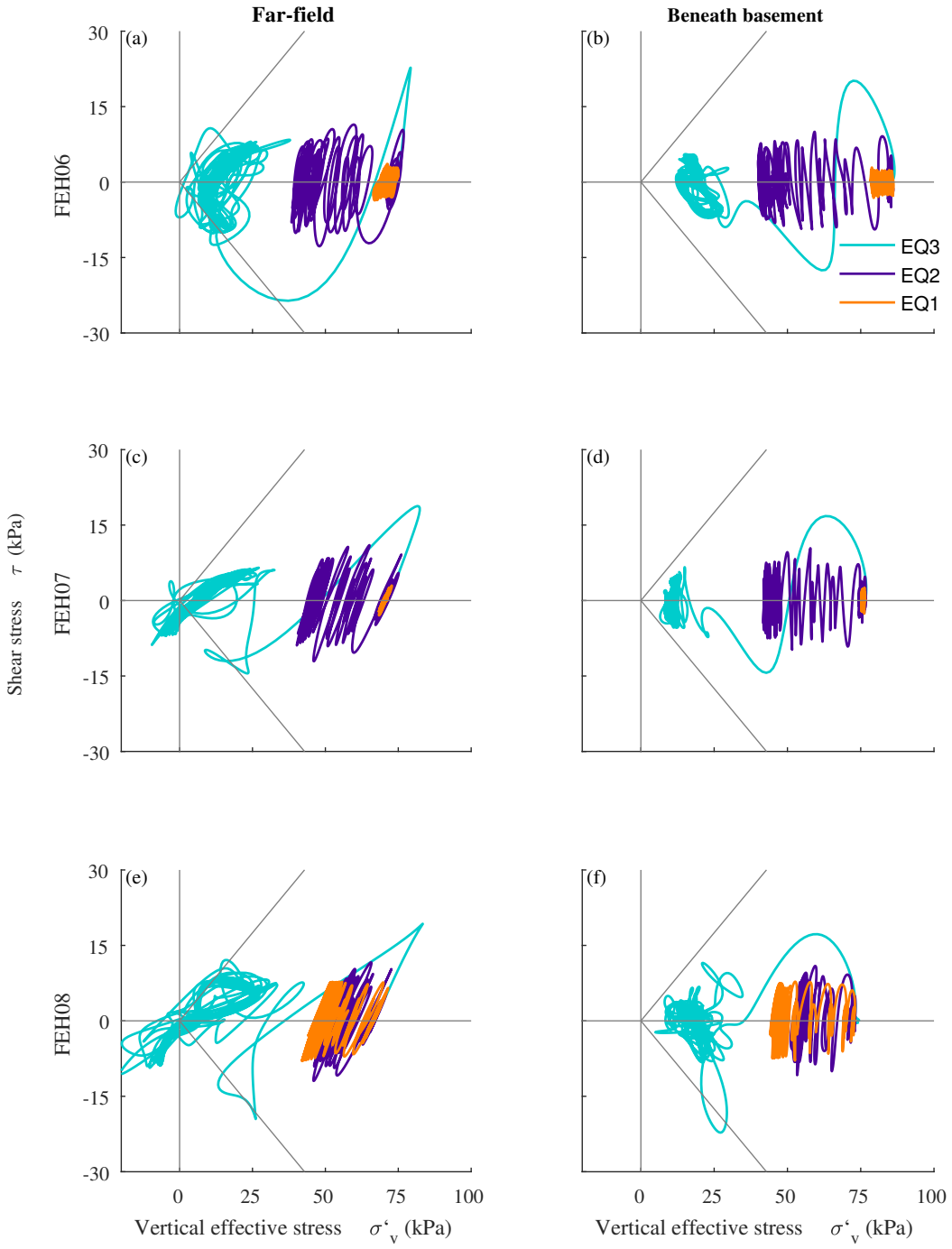

Fig. 5.8 Modified stress paths at the depth of L2 of instrumentation, 7.1 m below the soil surface, in both the far-field (left column) and underneath the centre of the basements (right column) during EQ1, EQ2 and EQ3. Equation 5.4 used to account for vertical accelerations in the calculation of instantaneous vertical effective stress. Critical state line shown in grey. (a) FEH06 far-field, (b) FEH06 beneath basement, (c) FEH07 far-field, (d) FEH07 beneath basement, (e) FEH08 far-field, (f) FEH08 beneath basement.

5.2.5 Displacement and rotation of the structures

It is desirable that a structure neither settles nor rotates during an earthquake. However, the increase in loading imposed by the structure on the surrounding soil and the concurrent decrease in resistance provided by the soil mean that, during earthquake shaking, structures can be susceptible to settlement and rotation.

The co-seismic change in vertical displacement and rotation of the basement, which was rigidly connected to the ground floor of the superstructure, are shown by the solid lines in Figure 5.9 and are summarised in Table 5.2. The displacements presented are for the centre of the top of the basement/the bottom of the ground floor of the superstructure. Negative vertical displacement corresponds to settlement of the structure and positive vertical displacement corresponds to uplift of the structure. Anticlockwise rotation is taken to be positive. It is desirable that the structures do not experience displacement or rotation. For EQ3, the co-seismic vertical displacement and rotation were obtained using GeoPIV-RG (White et al. 2003, Stanier et al. 2015). The resolution of the images taken using the high-speed camera meant that this method was not accurate for the smaller amplitude earthquakes. The vertical displacements of the structures presented for EQ1 and EQ2 were measured using LVDTs. The vertical displacement of the soil surface adjacent to the structures is shown by the dashed lines in Figure 5.9, and was measured using an LVDT positioned to the right-hand side of the structures.

During EQ1, the structures in Tests FEH06 and FEH07 experienced negligible settlement, less than 1 mm (Figures 5.9(a,b)). The structure in Test FEH08 settled 11 mm (Figure 5.9(c)), owing to the base shaking having a slightly greater amplitude and therefore causing liquefaction at shallow depths (Figure 5.2(c)). All three structures accumulated negligible rotation, as shown in Figures 5.9(d,e,f). Liquefaction occurred at shallow depths in EQ2 during all three tests (Figures 5.2 and 5.3) and resulted in settlement of the structures shown

Table 5.2 Accumulated vertical displacement and rotation of the structures with wide basements (prototype scale)

	Earthquake	FEH06	FEH07	FEH08
Vertical displacement (mm)	EQ1	-0.10	-0.20	-11
	EQ2	-70	-30	-5.0
	EQ3	-630	-35 [b]	-140
Rotation (°)	EQ1	< 0.05	< 0.05	< 0.05
	EQ2	< 0.05	< 0.05 [c]	< 0.05
	EQ3	-0.061 [a]	-0.70	17

Note: [a] peak = 0.35 °, [b] peak = -120 mm, [c] peak = 0.3 °

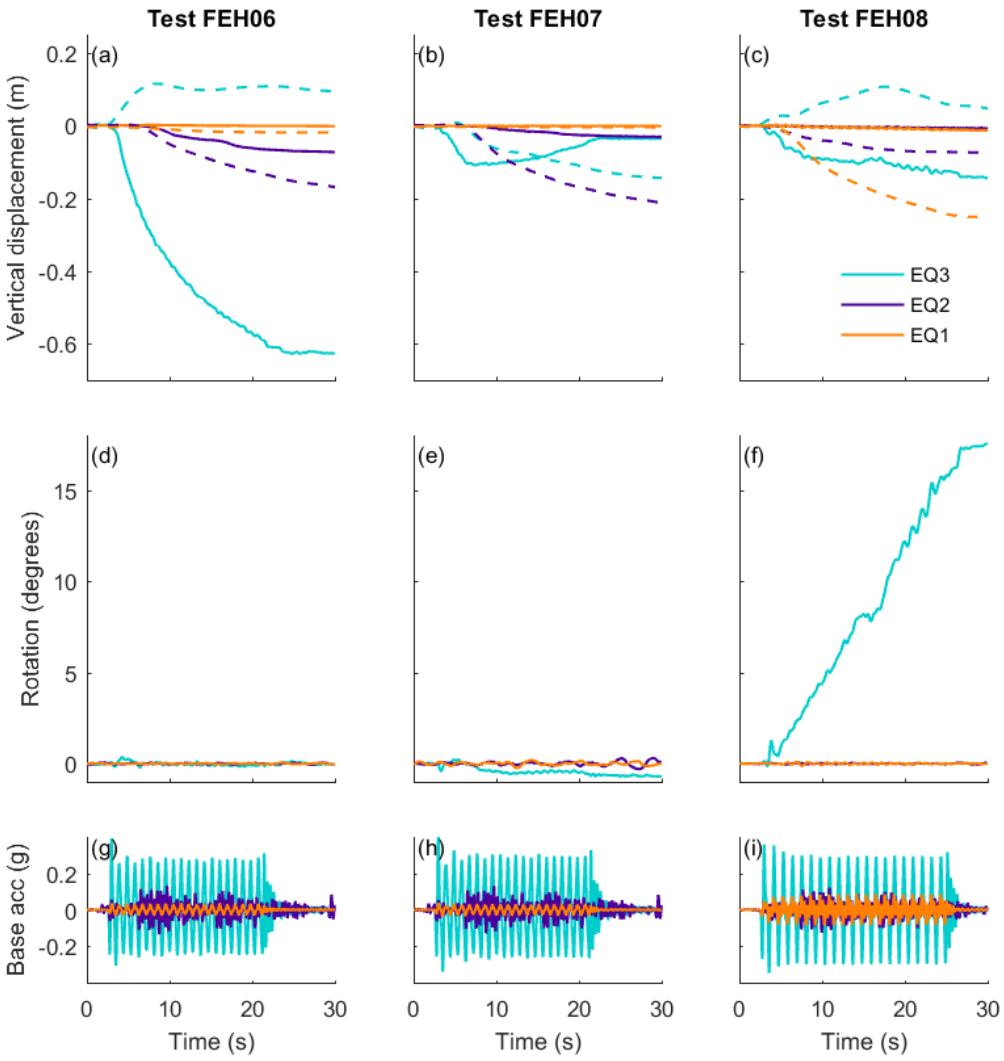

Fig. 5.9 Co-seismic vertical displacement and rotation, prototype scale. Top row: vertical displacement for (a) FEH06, (b) FEH07, and (c) FEH08. Structure shown by the solid lines and far-field soil surface by the dashed lines. Middle row: rotation for (d) FEH06, (e) FEH07, and (f) FEH08. Bottom row: base shaking horizontal acceleration for (g) FEH06, (h) FEH07, and (i) FEH08. Settlement is negative vertical displacement and anticlockwise rotation is positive.

in Figures 5.9(a,b,c). The structure in Test FEH06 experienced the greatest settlement due to having the greatest effective bearing pressure. Again, none of the structures accumulated rotation.

Co-seismic settlement of the soil surface adjacent to the structures with wide basements occurred in all three tests during EQ1 and EQ2, shown by the dashed lines in Figures 5.9(a,b,c). As expected, the settlement greatly increased when positive excess pore water pressures were generated in the far-field and liquefaction occurred (Figure 5.2). For Test FEH08, far-field settlement was greater during EQ1 than EQ2. The excess pore pressures generated in the far-field were of comparable magnitude during these two earthquakes, shown in Figure 5.2(c), therefore the densification that resulted after EQ1 reduced the settlement caused by a subsequent earthquake of similar amplitude.

The settlement and rotation during EQ3 is of most interest as the behaviour observed across the three tests differed considerably (Figure 5.9). It will therefore be discussed in more detail, and will be investigated further during the remainder of this chapter. Unless otherwise stated, all discussions henceforth will be regarding EQ3.

During EQ3, the structure in Test FEH06 settled by a large amount, accumulating 630 mm of vertical displacement by the end of shaking, as shown in Figure 5.9(a). This is significantly greater than the 150 mm settlement of the structure with a narrow basement of half the width in Test FEH05, shown in Figure 4.5, which had approximately the same ratio of uplift to total weight when the surrounding soil liquefied, U/W. On first inspection, this difference is surprising as the structures had the same bearing pressure. Additionally, the reduction in settlement of structures with shallow foundations following an increase in basement width (Yoshimi & Tokimatsu 1977, Adachi et al. 1992, Acacio et al. 2001, Bertalot et al. 2013) was anticipated to translate to structures with basements. However, the difference in settlement between Tests FEH05 and FEH06 is likely to be predominantly due to the difference in magnitude of the base shaking. For the earthquakes being compared in Tests FEH05 and FEH06, the respective peak accelerations were 0.16 g and 0.39 g and Arias intensities were 1.3 and 9.99 ms^{-1}. For these shaking characteristics, Dashti et al. (2010*a*) estimate the rate of settlement of a structure with a shallow foundation without a basement to differ by a factor of 3. This highlights the effect base shaking magnitude can have, however the numerical value may not directly transfer to structures with basements because the dominant mechanisms causing settlement are different.

In contrast to Test FEH06, the structure tested in Test FEH07 experienced significantly less vertical displacement (Figures 5.9(b)). During the same base shaking, the structure initially settled (peak 120 mm), before uplifting. This reduced the total settlement at the end of shaking to 35 mm. These vertical displacements suggest that a beneficial ratio of uplift to total weight when the surrounding soil liquefied, U/W, was achieved, which prevented the structure from settling further. This is corroborated by almost exactly the same vertical displacement for Test FEH11, shown in Figure 4.16(c), for a structure with the same U/W

but with a narrow basement with rigid horizontal extenders. In contrast, an uplift of 0.11 m was observed for the structure in Test FEH03 which had a comparable U/W and a narrow basement with no rigid extenders, shown in Figure 4.1(a). Soil-structure interaction means that the beneficial ratio of U/W is dependent on the width of the widest section of the basement. This will be investigated further in the soil displacement vectors in Section 5.3. Figures 5.9(d,e) show that neither of the structures in Test FEH06 or FEH07 accumulated significant rotation.

The asymmetric structure in Test FEH08 accumulated rotation at an approximately constant rate during the shaking, totalling 17 ° at the end of shaking (Figure 5.9(e)). The mean rotation accumulated per cycle of sinusoidal shaking was 0.9 °. As expected, this rotation occurred in the direction of the eccentric mass. Rigid body rotation of the structure accounted for 90 mm of the total 140 mm settlement of the centre of the top of the basement shown in Figure 5.9(c). Whilst the centre of the structure did not experience substantial vertical displacement, the sizeable accumulation of rotation resulted in one edge of the structure settling considerably and the other uplifting, as can be seen in Figure 5.10(f). In practice this would render the structure unusable, and would be particularly problematic for any adjacent structures or utilities.

For FEH06 and FEH08, where the structures experienced large settlement and rotation respectively, heave of the soil surface occurred adjacent to the structures, shown by the dashed lines in Figures 5.9(a,c). In contrast, settlement of the soil surface occurred when the structure accumulated only small settlement and rotation in FEH07. This is particularly concerning as the problems caused by large settlement and rotation of the structures will be exacerbated by the resulting differential displacement between the structure and adjacent soil. The interdependency of the behaviour of the structure and the displacement of the soil surface adjacent to it will be explored further in Section 5.3.

5.3 Soil displacements

The cross section of the model container was larger than the area that was visible through the transparent PMMA window shown in Figure 5.10. The high-speed camera was focused on the basement of each structure and the surrounding soil but was unable to view the entire failure mechanism that developed. However, the region monitored gave valuable information about the co-seismic soil-structure interaction and how displacement and rotation of the structures developed. The following section looks at the soil displacements and the soil-structure interaction during shaking. Soil displacements during EQ3 were obtained using GeoPIV-RG (White et al. 2003, Stanier et al. 2015). All the soil displacements shown are

relative to the movement of the model container. In these figures the horizontal edges of the container are at 0 and 25 m on the x-axis and the base is at 0 m on the y-axis.

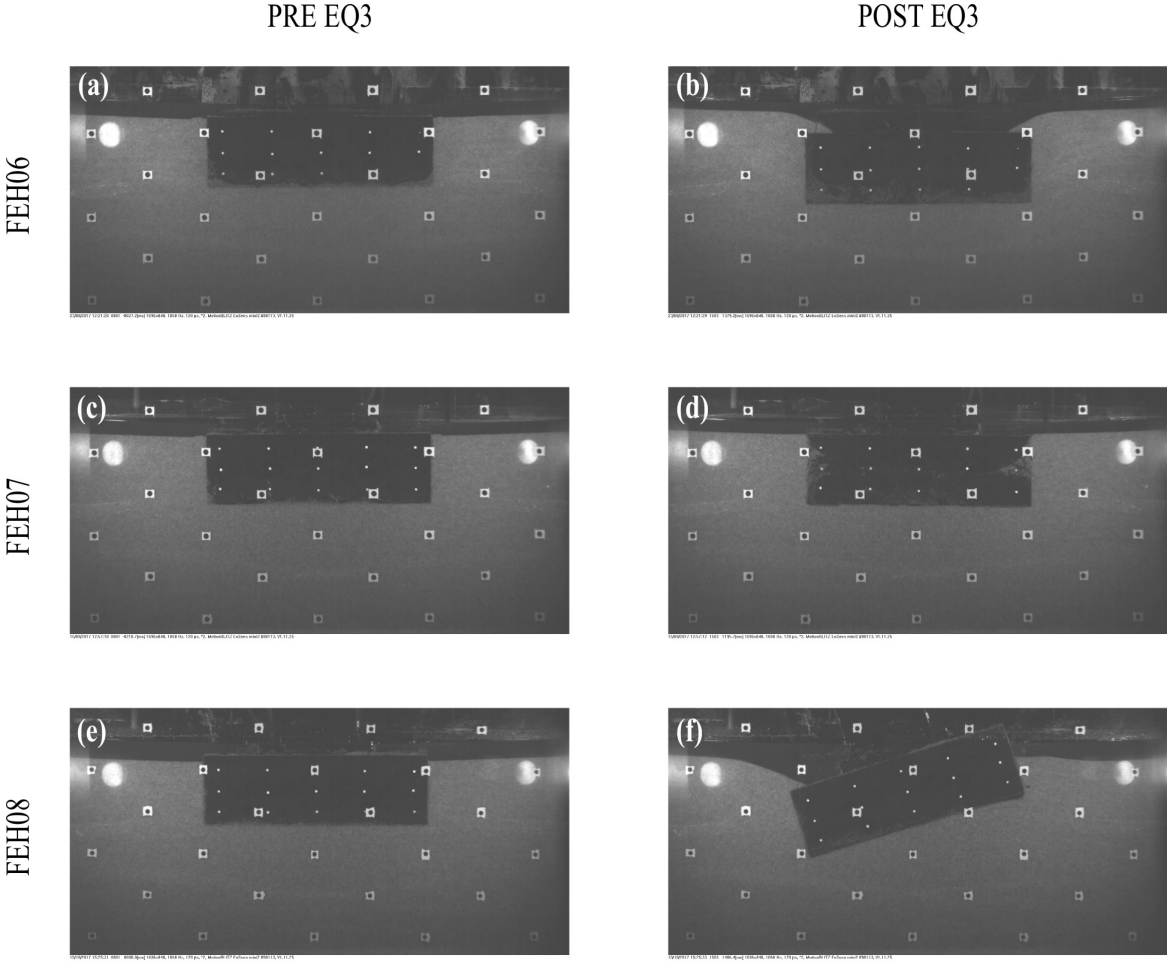

Fig. 5.10 Photos of the cross section of the models visible through the transparent PMMA window, both pre and post EQ3. (a) FEH06 pre EQ3, (b) FEH06 post EQ3, (c) FEH07 pre EQ3, (d) FEH07 post EQ3, (e) FEH08 pre EQ3, (f) FEH08 post EQ3.

5.3.1 Soil displacements during one cycle of shaking

The accumulation of displacement and rotation of the structures occurred incrementally during shaking, as shown in Figure 5.9. It is therefore of interest to look at the soil-structure interaction during two sequential half-cycles of shaking to understand how and when settlement and rotation was accumulated for each of the structures with a wide basement.

Soil displacements accumulated during the 5^{th} and 6^{th} half-cycles of displacement of the model container during EQ3 are shown in Figure 5.11. The 5^{th} and 6^{th} half-cycles correspond

to the time when the settlement rate of the structure in Test FEH06 was a maximum and the steady accumulation of rotation of the structure in Test FEH08 had begun, but before large displacement or rotation was accumulated (Figure 5.9). The initial cycles are not discussed as the servo-hydraulic earthquake actuator took two cycles to settle to a constant amplitude sinusoidal base shaking. The model container moved to the right in the 5^{th} half-cycle and then moved to the left in the 6^{th} half-cycle. The 5^{th} and 6^{th} half-cycles of displacement correspond to the 6^{th} and 7^{th} half-cycles of acceleration of the model container respectively.

In Test FEH06, during the 5^{th} half-cycle of displacement, shown in Figure 5.11(a), the soil underneath the structure moved to the left relative to the rigid base. The structure forced the soil underneath the basement to move downwards, with a greater magnitude under the right-hand half of the structure than under the left-hand half. As the structure moved downwards into the liquefied soil layer, it forced the soil to the left of the basement upwards. During the 6^{th} half-cycle, shown in Figure 5.11(b), the displacement field was symmetric to that produced in the 5^{th} half-cycle about the vertical line through the centre of the symmetric structure. The symmetric soil displacement in consecutive half-cycles is apparent in the equal amplitude of oscillations in excess pore pressure under the opposite edges of the basement shown in Figure 5.12(a). This data shows that the structure was rocking from side to side, with equal amplitude in both directions. The oscillations were in antiphase, indicating that suction and contraction spikes were simultaneously occurring under opposite edges of the basement. The acceleration time histories of the roof and floor of the structure shown in Figure 5.12(d) concur with the structure rocking from side to side with equal amplitude in both directions.

Beneath the structure in Test FEH06, contraction spikes were recorded under the edge which the basement was rocking towards. This corresponds to beneath the right-hand side of the structure during the 5^{th} half-cycle, where it can be seen in Figure 5.11(a) that vertical compression of the soil occurred due to the movement of the basement. Suction spikes were recorded in the excess pore pressure time histories under the opposite edge, where dilation occurred due to horizontal extension in the soil. Concurrently, rocking of the structure will have caused a change in the distribution of total vertical stress beneath the basement. Therefore, changes in vertical effective stress at the instrumented locations will not have been equal to the changes in excess pore pressure shown in Figure 5.12(a). Negligible rotation was accumulated over the two half-cycles due to the symmetry in the soil displacements. However, settlement occurred as shown in Figure 5.9(a). The soil displacement vectors in Figures 5.11(a,b) show that this was primarily due to ratcheting when the structure rocked from side to side.

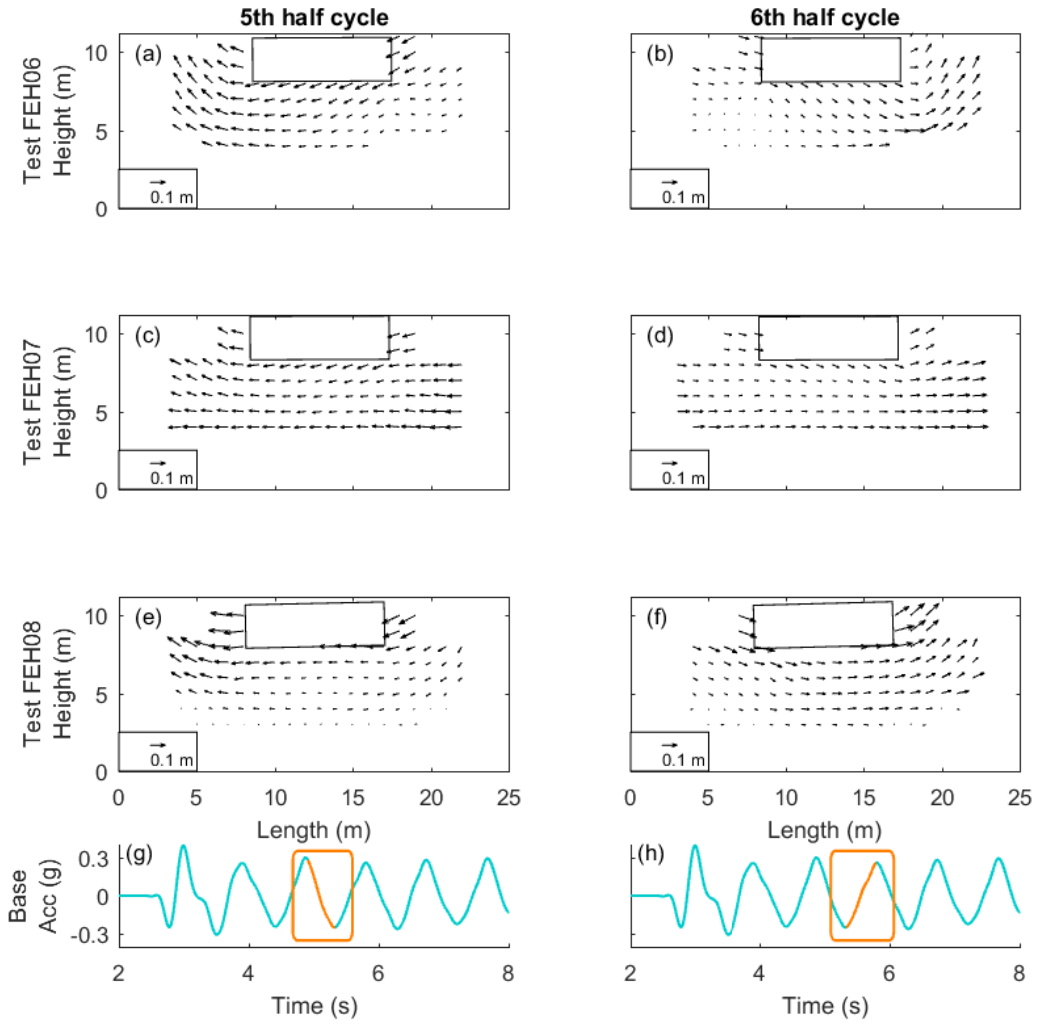

Fig. 5.11 Soil displacement during the 5^{th} (left column) and 6^{th} (right column) half-cycles of displacement of the model container. (a) FEH06 5^{th} half-cycle, (b) FEH06 6^{th} half-cycle, (c) FEH07 5^{th} half-cycle, (d) FEH07 6^{th} half-cycle, (e) FEH08 5^{th} half-cycle, (f) FEH08 6^{th} half-cycle. Location of basement at start of each half-cycle shown. Base shaking acceleration for Test FEH06 (bottom row), with corresponding half-cycle highlighted. Dimensions in prototype scale. Note: soil displacements are plotted with a magnification factor of 10 relative to the basement and model container.

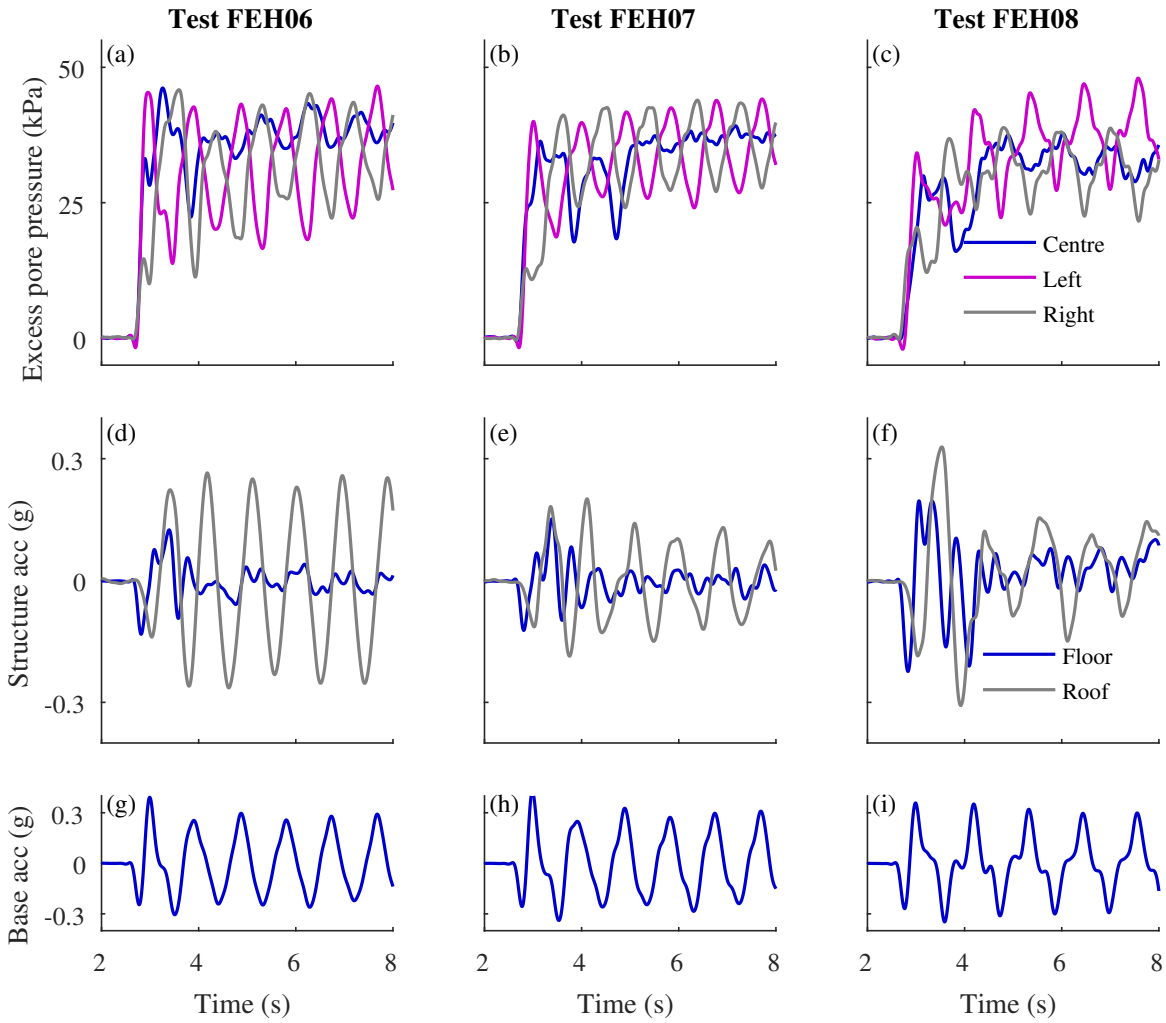

Fig. 5.12 Phase relationships during the initial cycles of shaking. Top row: excess pore pressures generated below the bottom of the basement in L3 of instrumentation for (a) FEH06, (b) FEH07, and (c) FEH08. Middle row: absolute horizontal acceleration of ground floor and roof of structure for (d) FEH06, (e) FEH07, and (f) FEH08. Bottom row: Base shaking horizontal acceleration for (g) FEH06, (h) FEH07, and (i) FEH08.

During Test FEH07, once again the symmetric structure resulted in symmetric displacements of the soil for the two consecutive half-cycles shown in Figures 5.11(c,d). However, the magnitude of the displacements was reduced compared to during Test FEH06. In comparison to Test FEH06, there was a smaller vertical component of downward soil movement beneath the basement in both half-cycles, caused by the small initial settlement of the structure (Figure 5.9(b)). Adjacent to the basement, soil movement had a vertical component, which was upwards to the left of the basement for the 5^{th} half-cycle and to the right for the 6^{th} half-cycle. This was caused by the rocking of the submerged basement and the proximity from the Duxseal at the container boundary may have also contributed to it. Contraction and suction spikes were recorded in the excess pore pressure time histories shown in Figure 5.12(b) under the edges of the basement, and were caused by the same mechanisms discussed in the preceding paragraph for Test FEH06. The magnitude of these spikes were reduced due to the reduction in the soil displacements, and consequently reduced local soil compression and extension (Figure 5.11).

In Test FEH08, the movement of the soil around the basement relative to the rigid base was notably larger compared to the previous two tests discussed, shown by the larger displacement vectors in Figure 5.11(e,f). During the 5^{th} half-cycle there was minimal vertical movement of the soil underneath the structure. Excess pore pressures measured under the basement show local suction under the left edge and contraction under the right during this half-cycle (Figure 5.12(c)). This was caused by horizontal extension and contraction respectively, shown in Figure 5.11(e). In the subsequent half-cycle, shown in Figure 5.11(f), there was a considerable downward movement of soil under the left-hand side of the basement, accompanied by vertically upward movement under the right-hand side. Excess pore pressures in Figure 5.12(c) show contraction under the left edge and suction under the right, this time caused by vertical contraction and extension respectively. These oscillations in excess pore pressure were greatest in magnitude under the left-hand edge, due to the larger soil displacements in this area. In both half-cycles, rocking of the structure will have resulted in a redistribution of total vertical stress. This means that changes in vertical effective stress at the instrumented locations will not have been equal to the changes in excess pore pressure shown in Figure 5.12(c). Instead of a gap being formed underneath the structure, the liquefied soil moved with the rotating basement. Sand accumulated below the uplifting side of the basement in Figure 5.11(f), resulting in accumulation of permanent rotation. The asymmetry in the soil displacements was a result of the geometry of the superstructure. The overturning moment generated by the eccentric mass will be discussed in detail in Section 5.4.

The plots of excess pore pressure in Figure 5.12(a,b,c) show that absolute suction did not occur beneath the basements during shaking, which would have resulted in negative excess

pore pressures. However, the large peak-to-peak amplitude of the oscillations in excess pore pressure (approximately 20 kPa) indicate that strength was regained during shaking due to dilation of the soil. The liquefied soil only momentarily behaved as a dense fluid, before it dilated and returned to behaving like a soil. This resulted in an increase in resistance which restricted the rate of settlement of the structure in Test FEH06 and prevented the structure in Test FEH08 toppling uncontrollably.

It is not possible to quantify the increase in vertical effective stress during dilation of the liquefied soil from the excess pore pressures shown in Figure 5.12 because of the concurrent change in total vertical stress distribution due to rocking of the structure:

$$\sigma'_v(t) = \sigma_v(t) - u_{ex}(t) - u_h \tag{5.5}$$

where, at a given time t, $\sigma'_v(t)$ is the vertical effective stress, $\sigma_v(t)$ is the total vertical stress, and $u_{ex}(t)$ and u_h are the excess and hydrostatic pore pressure respectively. This highlights why is it not appropriate to use the traditional definition of excess pore pressure ratio, $r_u(t)$, where the excess pore pressures generated, $u_{ex}(t)$, are normalised by the corresponding initial vertical effective stress, σ'_{v0}:

$$r_u(t) = \frac{u_{ex}(t)}{\sigma'_{v0}} \tag{5.6}$$

Using Equation 5.6, liquefaction is defined as occurring when $r_u(t)$ is equal to one. This implies that liquefaction occurs, and the current vertical effective stress becomes equal to zero, when the excess pore pressure generated becomes equal the initial vertical effective stress. However, this is not the case in soil surrounding a structure, due to changes in total vertical stress during shaking.

5.3.2 Total co-seismic soil displacements

Further understanding of the failure mechanisms can be gained by looking at the total soil displacements accrued during the earthquake, both below and adjacent to the basements. This is of particularly important in practice, as the area of influence of a structure can impact the performance of adjacent structures and utilities. Total co-seismic soil displacements accumulated during EQ3 are shown as vectors in Figure 5.13 and as contours in Figure 5.14, both plotted at the initial location of each tracked patch.

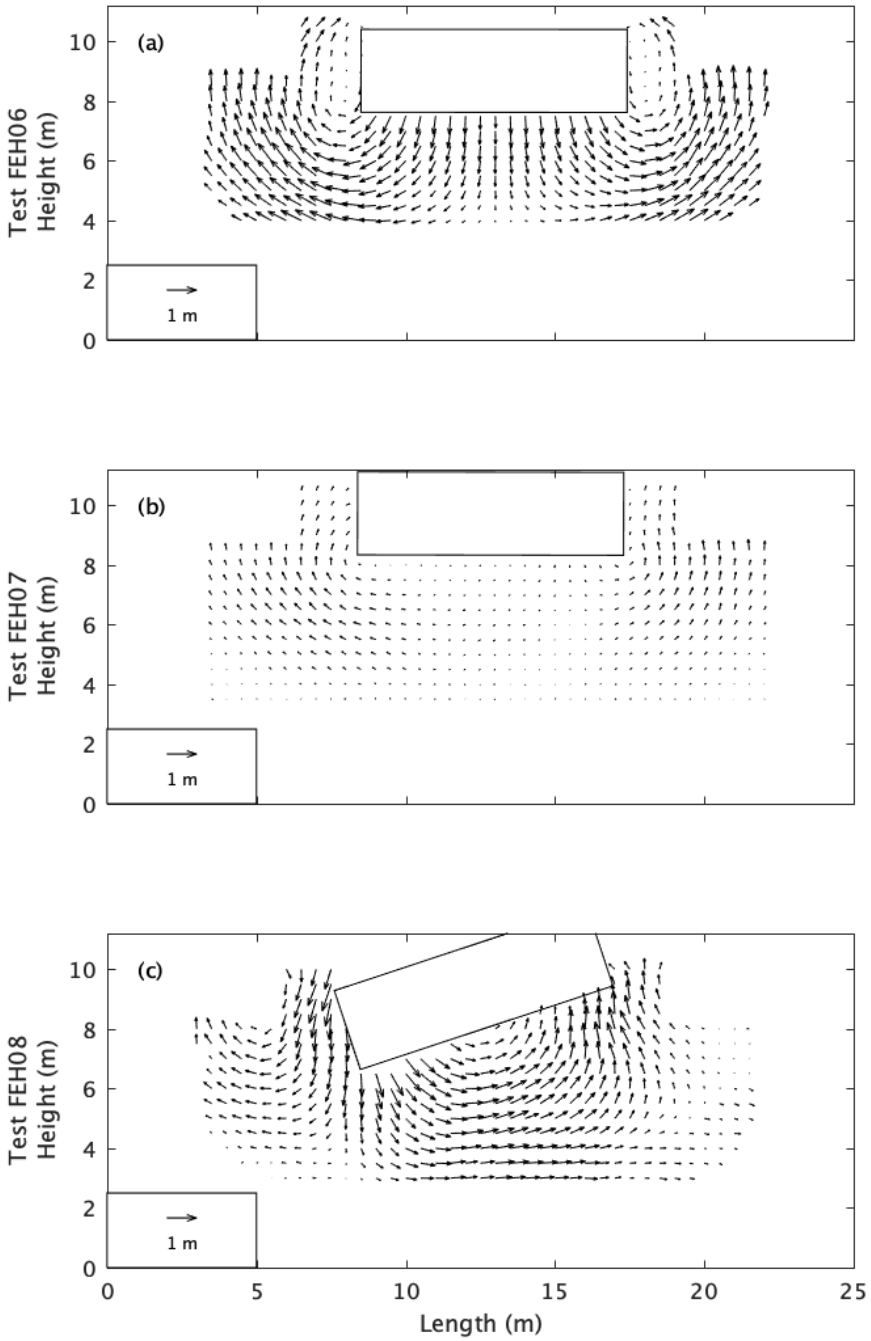

Fig. 5.13 Total co-seismic soil displacement vectors accumulated during EQ3. (a) FEH06, (b) FEH07, (c) FEH08. Location of basement at the end of shaking shown.

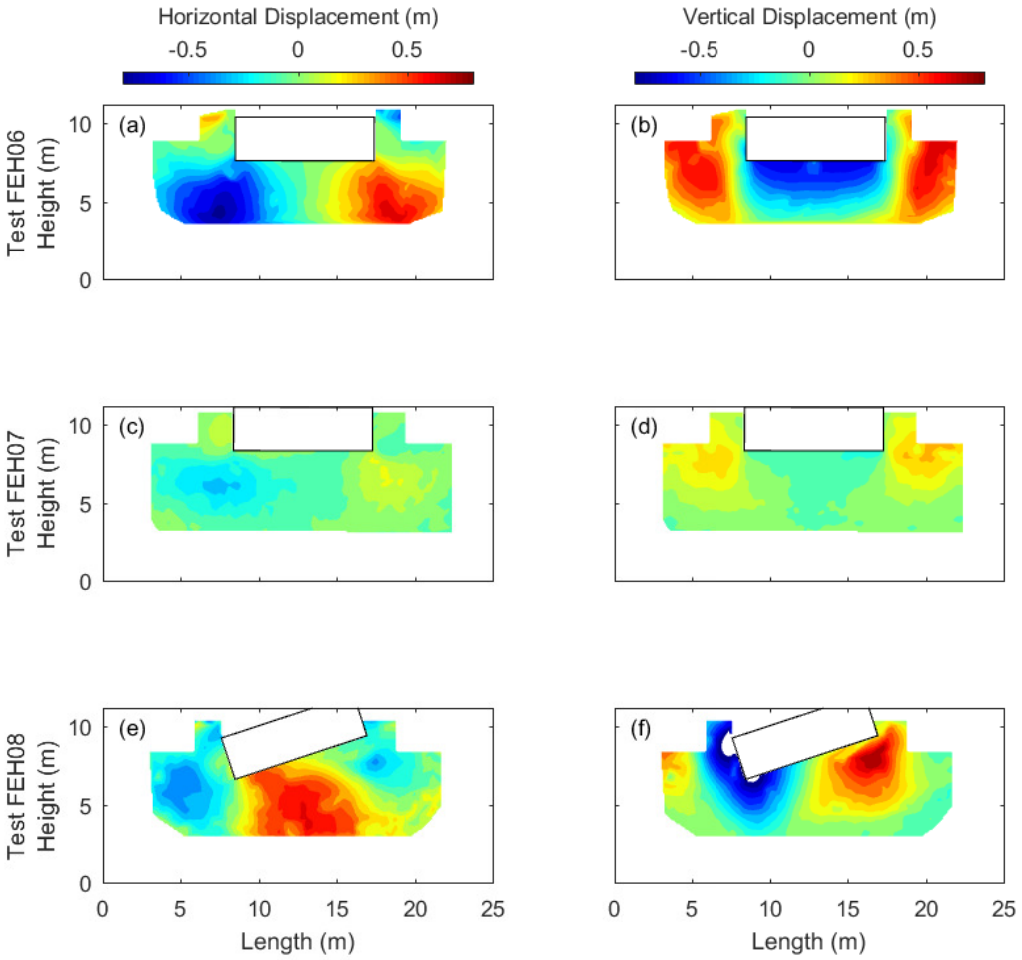

Fig. 5.14 Total co-seismic soil displacement contours. (a) FEH06 horizontal displacement, (b) FEH06 vertical displacement, (c) FEH07 horizontal displacement, (d) FEH07 vertical displacement, (e) FEH08 horizontal displacement, (f) FEH08 vertical displacement. Rightwards is positive horizontal displacement and leftwards is negative. Settlement is negative vertical displacement and heave is positive. Location of basement at the end of shaking shown. Contours are not extrapolated outside of the region monitored.

In Test FEH06, the soil underneath the centre of the structure moved vertically downwards (Figure 5.13(a)). The magnitude of the vertical component of displacement, shown in Figure 5.14(b), decreased with increasing depth and reduced to approximately zero at a depth of roughly $B/2$ below the bottom of the basement, where B is the width of the basement. The model container extended for approximately another $B/2$ below this depth, but unfortunately this region was not visible due to the construction of the model container. The magnitude of horizontal displacement of the soil increased moving away from the centre of basement towards its edges, and increased with increasing depth (Figure 5.14(a)). Figure 5.13(a) shows that the structure forced soil sideways as it settled downwards into the soil layer, which caused an upward flow of soil adjacent to the basement. The movement of soil beneath the basement is comparable to that below light structures with shallow foundations on liquefied soil (Adamidis & Madabhushi 2018*a*). However, in this case the effective bearing pressure is significantly lower. The movement of the soil adjacent to the basement has similarities to the flow of liquefied soil around buried pipes, which have a resultant upward vertical force during liquefaction (Chian et al. 2014). The intuition that structures with basements combine the propensity of structures with shallow foundations to settle and light subsurface structures to float is therefore observed in the co-seismic soil displacements in Figure 5.13(a).

In FEH07, soil also flowed upwards adjacent to the basement, but with a significantly smaller magnitude (Figure 5.13(b)) as the settlement of the structure was far less. The soil underneath the basement experienced negligible displacement, horizontally (Figure 5.14(c)) or vertically (Figure 5.14(d)), reflecting the movement of the structure shown in Figure 5.9(b).

In contrast, Figure 5.13(c) shows that the column of soil beneath the structure in Test FEH08 experienced very large displacements. A semi-cylinder of soil with a diameter of approximately B rotated with the structure - soil beneath the left-hand side displaced downwards and rightwards whilst soil beneath the right-hand side displaced upwards. No gap was formed underneath the structure. Large displacements were also accumulated in the soil to the left of the basement as the structure moved into this region. Vertical displacement became negligible at the deepest depth visible (Figure 5.14(f)), which was also observed for Test FEH06 in Figure 5.14(b).

From overlaying the initial and final high-speed images shown in Figure 5.10, the point of rotation for all the structures with wide basements was found to be the centre of the bottom of the basement. This is in contrast to the behaviour of a structure with a basement of half the width in Test FEH05 which was observed to rotate about the edge of the bottom of the basement, as shown in Figure 4.7. It is therefore appropriate to consider the effect a change in point of rotation has on the moment imposed by the structure and resistance provided by the soil. A greater moment is imposed on the surrounding soil if rotation occurs about the

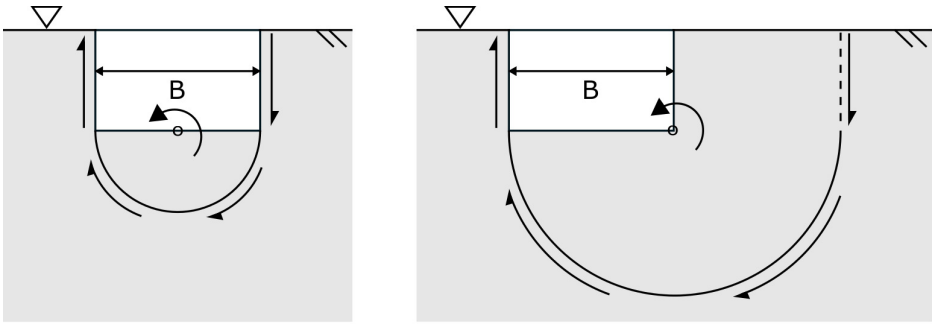

Fig. 5.15 Schematic of failure mechanisms for anticlockwise rotation about point O. (a) Rotation about the centre of the bottom of the basement. (b) Rotation about the right-hand edge of the bottom of the basement.

bottom edge of the basement compared to the centre, due to the increased lever arm for all the vertical forces acting on the structure. However, the soil provides greater resistance to rotation about the basement edge than about the basement centre. For simplicity, this can be be considered by assuming that a semi-cylinder of soil rotates with the structure, which is an approximation of what was observed for Test FEH08 in Figure 5.13(c). When rotating about the centre of the basement, this semi-cylinder has a diameter equal to the width of the basement, B, as shown in Figure 5.15(a). In comparison, when rotating about the edge of the basement, this semi-cylinder has a diameter equal to double the width of the basement, $2B$, as shown in Figure 5.15(b). The latter therefore involves shearing along a plane with over double the cross sectional area and displacing at least four times the volume of soil, both which provide increased resistance to rotation, including when the soil is liquefied.

This implies that the moment loading imposed by the structure with a wide basement in Test FEH08 about the edge of the basement was less than the resistance provided by the soil against rotation about this point. However, the moment loading about the centre of the basement was greater than resistance provided by the soil against rotation about this point. The narrower basement in Test FEH05, resulted in reduced resistance to rotation provided by the soil, so rotation could occur about the edge of the basement, where moment loading was greatest.

A corollary to this reasoning is that, for a given basement width, a threshold moment is anticipated to exist, below which rotation occurs about the centre of the basement, and above which rotation occurs about the edge of the basement. Likewise, for a given dynamic moment loading, a threshold basement width exists, below which rotation occurs about the basement edge and above which it occurs about the basement centre. Additional centrifuge

tests, using an increased range of basement widths and base shaking amplitudes, is required to confirm this corollary.

5.3.3 Total co-seismic strains

During shaking, soil can accumulate both shear and volumetric strains. The magnitude and spatial distribution of these strains can give insight into the cyclic loading of the soil by the combined effect of the earthquake and the structure.

The total shear and volumetric strains accumulated during EQ3 were calculated using GeoPIV-RG (White et al. 2003, Stanier et al. 2015) and are shown in Figure 5.16. Both are plotted at the initial location of each patch. Clockwise shear strains and contractive volumetric strains are positive. Interpretation of these strains should be done with care, due to the limited resolution of the images taken using the high-speed camera. It was important to record data at a high frame rate to enable the co-seismic soil-structure interaction to be investigated on a cycle-by-cycle basis. However, the specification of the high-speed camera available meant that this was a trade off with the resolution of the images. Calculation of strains requires taking the derivative of displacements of the tracked patches. Consequently, any errors in measuring displacement are amplified in strains.

In Test FEH06, Figure 5.16(a) shows that very large shear strains were accumulated below the edges of the basement for the entire depth monitored. Soil in this region was displaced horizontally as the structure ratcheted downwards and settled into the liquefied soil (Figure 5.13(a)). Large shearing also occurred in the soil adjacent to the basement because, during shaking, the structure rocked and moved horizontally within the liquefied soil. Underneath the structure, shearing was recorded in the area directly below the structure, up to a depth of approximately B/4. Below this depth, shear strains were limited due to the downward movement of the structure forcing soil in this region to move vertically downwards. The trends for volumetric strains accumulated below the structure, shown in Figure 5.16(b), were not as clear as for shear strains, due to insufficient resolution of the images. This problem has been discussed previously by Stanier et al. (2016).

In Test FEH07 localised shearing occurred around the edges of the bottom of the basement, shown in Figure 5.16(c). Unlike for Test FEH06, these regions did not extend throughout the full depth monitored, but were restricted to a depth of approximately B/4 below the basement edges. Figure 5.16(d) shows that volumetric dilation was recorded in the triangular prisms directly adjacent to the sides of the basement, with contraction recorded at these depths outside of these prisms. Volumetric strains were small beneath the structure, with areas of larger volumetric dilation at deeper depths anticipated to have been facilitated by fluid flow stemming from the soil below.

In Test FEH08 the majority of the soil region monitored experienced large shear strains, shown in Figure 5.16(e). The asymmetric structure rocked and accumulated rotation during shaking, displacing the liquefied soil below and adjacent to it. Shear strains were a maximum along the edge of the semi-cylinder of soil that rotated with the structure, which was identified by the displacement vectors plotted in Figure 5.13(c). Particularly large shear strains were also recorded in the region of soil directly beneath the right-hand third of the basement. The trends for volumetric strains accumulated below the structure were not as clear as for shear strains. Figure 5.16(f) shows that large volumetric contraction occurred around the right-hand edge of the structure, close to the soil surface where the drainage path was short. Areas of volumetric contraction and dilation were recorded at deeper depths.

The shear strains accumulated in the soil surrounding the wide basements shown in Figure 5.16 can be compared to those accumulated below structures with shallow foundations located on deep layers of liquefiable soil. In the column of soil directly beneath structures with shallow foundations, the effective bearing pressure applied by the structure prevents liquefaction from occurring (Coelho et al. 2007). Within this region of non-liquefied soil, shear strains are limited due to better confinement and therefore increased stiffness (Adamidis & Madabhushi 2018*a*). Adjacent to this region, in the liquefied soil, large shearing does occur. This spatial distribution of shear strains is comparable to the shear strains in the soil surrounding the structure in Test FEH06 which settled, as shown in Figure 5.16(a). However, liquefaction was found to have occurred at all depths beneath the structure (Figure 5.3) as well as in the far-field (Figure 5.2). For the structure in Test FEH08 which accumulated significant rotation, Figure 5.16(e) shows that large shear strains were accumulated within the majority of the soil region monitored. This different behaviour experienced by the structures with wide basement during EQ3 can be explored further by looking at the resultant co-seismic vertical force and moment acting on the structures, which were transmitted from the structure to the adjacent soil.

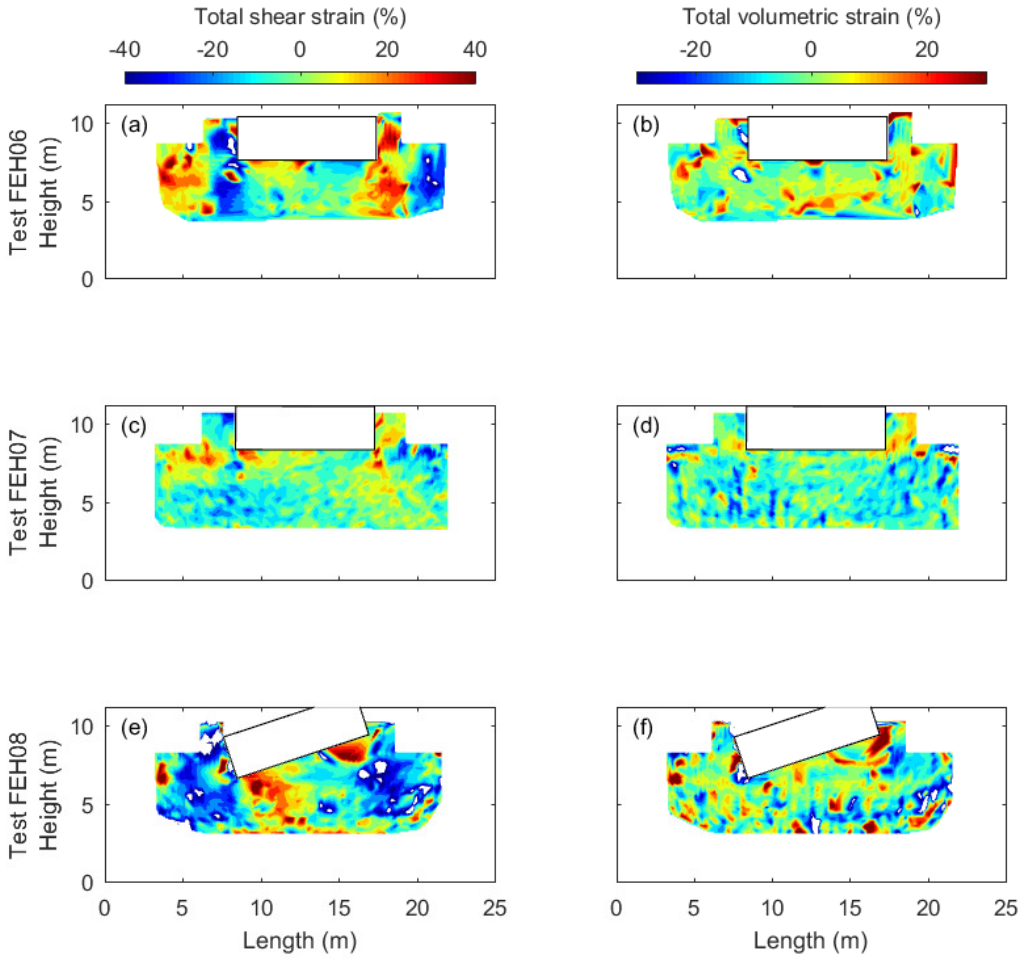

Fig. 5.16 Total co-seismic strains accumulated during EQ3. (a) FEH06 shear strains, (b) FEH06 volumetric strains, (c) FEH07 shear strains, (d) FEH07 volumetric strains, (e) FEH08 shear strains, (f) FEH08 volumetric strains. Location of basement at the end of shaking shown.

5.4 Resultant co-seismic vertical force and moment

Loading imposed by structures with wide basements in liquefiable soil can change considerably during shaking. This will have strongly affected the co-seismic soil-structure interaction which has been presented in the preceding sections.

The resultant vertical force and moment acting on the structures with wide basements during EQ3 can be calculated using the pore pressures, accelerations, displacements, and rotations recorded during the dynamic centrifuge tests. These were calculated at each instant an image was recorded using the high-speed camera. This was at a frequency of 18 Hz at prototype scale which corresponds to 18 times per cycle of sinusoidal shaking for FEH06 and FEH07, and 21 times per cycle for FEH08.

The effective weight, $W'(t)$, of the structure was calculated by subtracting the uplift force provided by the basement, $F_U(t)$, from the combined weight of the superstructure, F_S, and basement, F_B:

$$W'(t) = F_S + F_B - F_U(t) \tag{5.7}$$

where

$$F_U(t) = [u_h + u_{ex}(t)] \times A \tag{5.8}$$

Equation 5.8 shows that two upward acting pressures contributed to the uplift force, which were summed at each time step and multiplied by the plan area of the basement, A. The first pressure was the hydrostatic pressure, u_h, and the second was the excess pore water pressure acting on the bottom of the basement, $u_{ex}(t)$. The latter of these two terms varied with time due to soil-structure interaction. When liquefaction occurred, the steady state value of the uplift force was equal to the uplift calculated using Archimedes' principle, assuming that the liquefied soil behaved as a dense fluid.

The resultant moment transmitted from the structure to the surrounding soil was calculated at each time step using Equations 5.9 to 5.12:

$$M_{net}(t) = \sum M_1(t) + \sum M_2(t) - \sum M_3(t) \tag{5.9}$$

where

$$M_1(t) = \sum m_i[g + a_{i,y}(t)][y_i sin\theta(t) - (x_i + x_{i,drift}(t))cos\theta(t)] - F_U(t)[y_i sin\theta(t)] \tag{5.10}$$

$$M_2(t) = \sum m_i a_{i,x}(t)[y_i cos\theta(t)] \tag{5.11}$$

$$M_3(t) = \sum I_{Gi}\ddot{\theta}(t) \tag{5.12}$$

In order to calculate the resultant co-seismic moment, the structure was split into four rigid sections which are shown in Figure 5.17 - the eccentric mass (m_1) (where applicable), the roof (m_2), and the ground floor and basement (m_3) which were rigidly connected, plus the buoyancy force (F_U). The rigid sections had a mass moment of inertia, I_{Gi}, about their respective centre of gravity located at coordinates (x_i, y_i). The net moment applied by the structure consisted of three components. The first and most significant component, $M_1(t)$, was the $P-\delta$ effect due to the vertical forces not being co-linear (Equation 5.10). This was increased by the flexible nature of the superstructure, where the horizontal displacement of the roof, and when applicable the eccentric mass, lagged behind the ground floor and basement. The second component, $M_2(t)$, was provided by the horizontal inertial force of the masses accelerating due to the transmission of the base shaking through the soil body to the structure (Equation 5.11). The third contribution, $M_3(t)$, came from the rotational inertia of the components of the structure (Equation 5.12). The contribution of each rigid section to each component was summed at every time step. Moments were calculated about the centre of the bottom of the basement, point C in Figure 5.17. This was observed to be the point of rotation for all three structures with wide basements. Anticlockwise moments and rotations were taken as positive.

Figure 5.18 shows the time history of the effective weight, $W'(t)$, and resultant moment, $M_{net}(t)$, imposed by the structures on the surrounding soil. Figure 5.19 shows the co-seismic interaction between this loading and the movement of the structures, with each column sharing the same x-axis and each row sharing the same y-axis.

Figure 5.18(a) shows that, in all three tests, the effective weight of the structures significantly reduced during EQ3. Positive excess pore pressures were generated and the uplift provided by the basement increased, whilst the weight of the structure remained unchanged. Concurrently, the generation of positive excess pore pressures reduced the instantaneous vertical effective stress, and therefore caused a reduction in stiffness and strength in the soil below, and to the sides of, the basement. The bearing capacity of cohesionless soils is dependent on the vertical effective stress below and adjacent to a partially buried structure, therefore it is logical to assume that it will reduce with the generation of positive excess pore pressures. From the comparable excess pore pressures recorded adjacent to (Figure 5.2(a,b,c)) and directly below (Figure 5.3(a,b,c)) the basements, it will be assumed that the reduction in bearing capacity during EQ3 was comparable in the three tests. Therefore, differences in structure settlement and rotation were a result of differences in effective weight of the structure and/or distribution of mass in the superstructure.

The structures in Tests FEH07 and FEH08 accumulated minimal vertical displacement (Figure 5.19(c)) as the effective weight of the structures quickly reduced to approximately

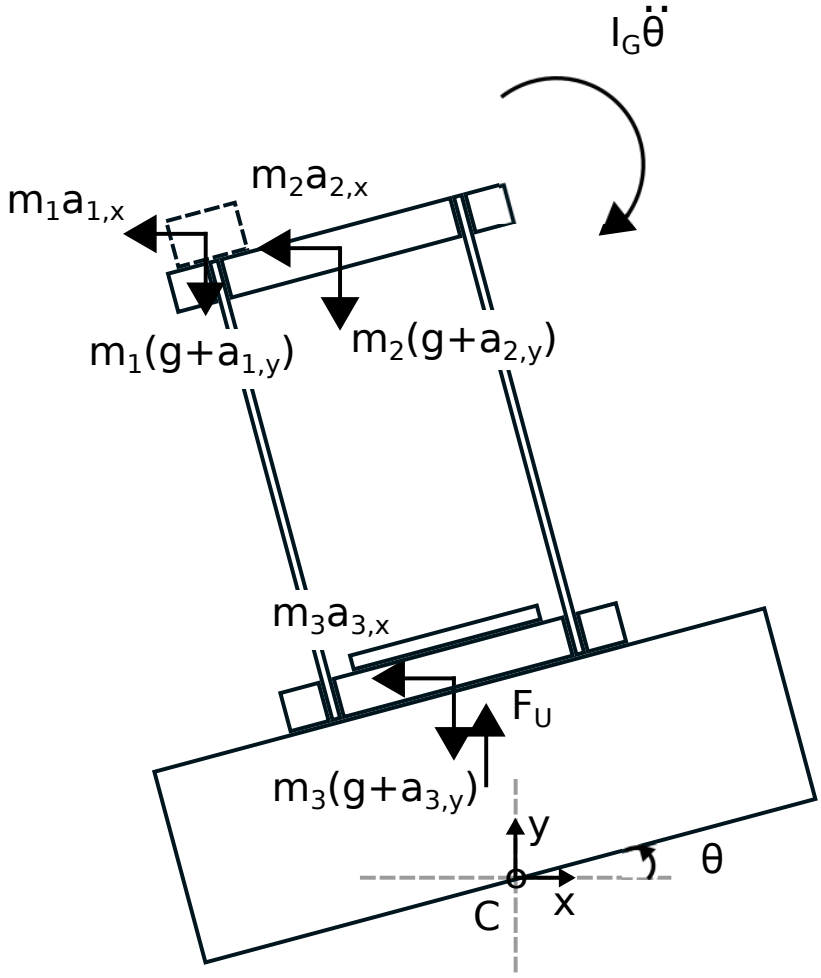

Fig. 5.17 Components of moment transmitted from the structure to the adjacent soil. Moments taken about the centre of the bottom of the basement, point C. For clarity, shown on a structure with significant accumulated rotation, θ.

zero, as shown in Figure 5.18(a). The calculated increase in effective weight of the structure in FEH08 after 12 seconds was not a physical effect, but was a consequence of displacement of the PPT at the shallowest instrumented depth beneath the basement, caused by the rotation of the structure. In contrast, during Test FEH06 the effective vertical weight of the structure remained above zero. This structure settled for the duration of shaking, as shown in Figure 5.9(a). It can be inferred that this was because the effective weight of the structure, shown in Figure 5.18(a), exceeded the degraded bearing capacity provided by the soil below.

For the symmetric structures used in Tests FEH06 and FEH07, the resultant co-seismic moments transmitted from the structure to the surrounding soil were close to being equal in both the clockwise (negative) and anticlockwise (positive) directions, shown in Figure 5.18(b). The amplitude of the resultant moment was greater for Test FEH06, which had a greater mass.

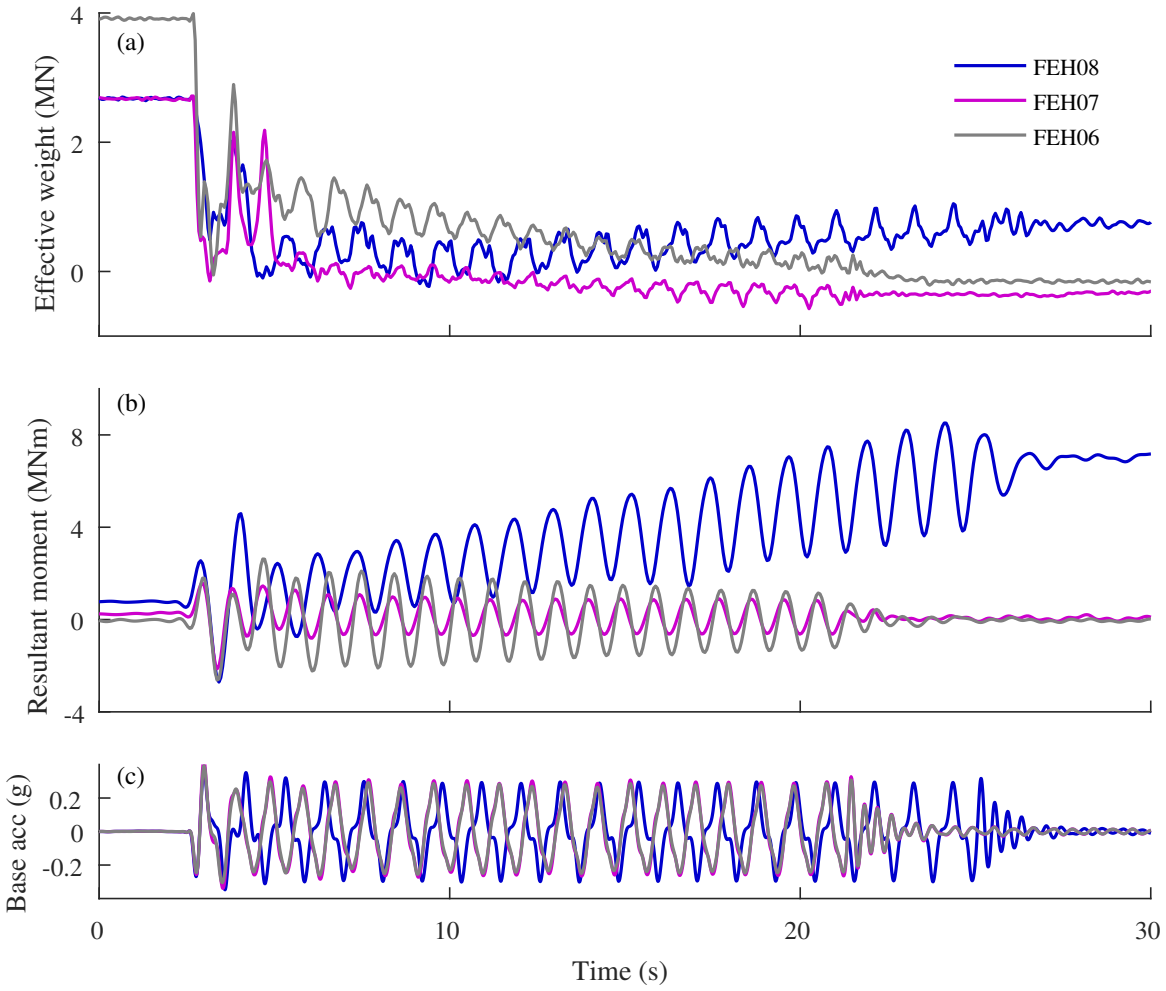

Fig. 5.18 Time histories of the structure loading on the surrounding soil during EQ3. (a) Effective weight, (b) Resultant moment, (c) Base shaking horizontal acceleration.

The structures were not self-righting. However, the sinusoidal base shaking, which was of almost equal amplitude in both directions, caused the structures to be re-centred and therefore not accumulate significant rotation during shaking, as shown in Figure 5.19(b). Although negligible rotation was accumulated for Test FEH06, settlement was accumulated for each cycle of rotation, shown in Figure 5.19(c). The soil displacements shown in Figure 5.11(a,b) show that this was primarily due to ratcheting when the structure rocked from side to side.

The behaviour of the symmetric structures with wide basements in Tests FEH06 and FEH07 can be compared to the moment-rotation behaviour of rigid, symmetric structures with shallow foundations on dry sand (Gajan et al. 2005, Gajan & Kutter 2008, Heron et al. 2015) and on liquefiable layers (Adamidis & Madabhushi 2018*c*). The amplitude of rotation of the symmetric structures in the present study were of the same order of magnitude however, the moment transmitted from the structures with basements to the surrounding soil

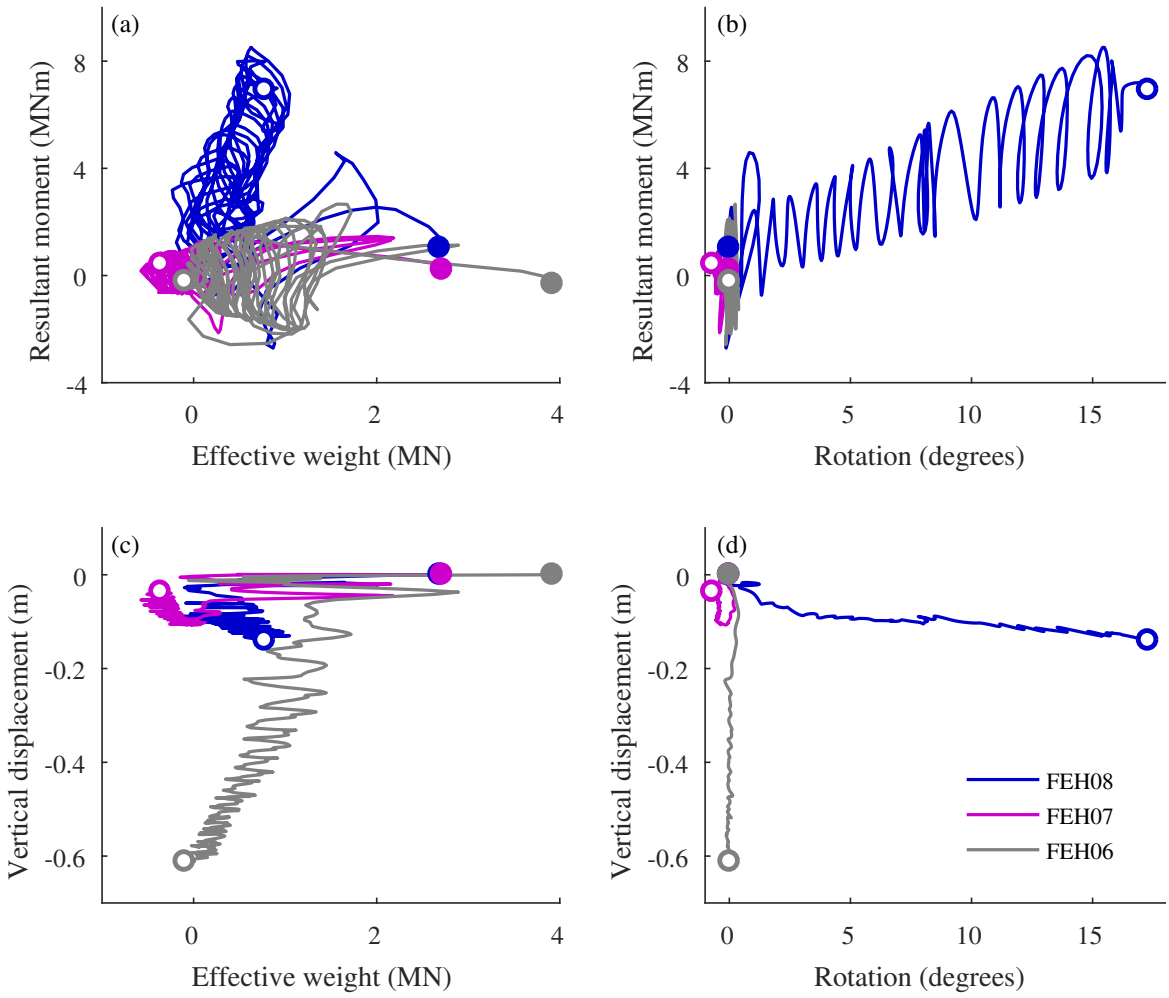

Fig. 5.19 Co-seismic interaction between the loading imposed on the surrounding soil and the movement of the structures with wide basements during EQ3. (a) Resultant moment - effective weight. (b) Resultant moment - rotation. (c) Vertical displacement - effective weight. (d) Vertical displacement - rotation. Each column shares the same x-axis and each row shares the same y-axis. Start of base shaking located by filled circle and end of base shaking by open circle.

shown in Figure 5.18(b) were far greater than for structures on shallow foundations without basements. The reason for this is twofold. Firstly, and most significantly, the lever arm for all inertia forces was greater since rotation was occurring about a plane below the soil surface. Secondly, the moment due to the $P-\delta$ effect was increased because there was an uplift force provided by the basement, and also due to interstorey drift of the flexible superstructures tested. This greater amplitude of co-seismic moment is believed to have been the cause of the increased ratcheting shown in the soil displacements in Figure 5.11. These data suggest that the increased ratcheting had a greater effect on the settlement of the structure in Test FEH06 than the reduction in effective bearing pressure due to the buoyancy force provided by the basement. This resulted in a comparable magnitude of settlement to centrifuge testing of structures with shallow foundations, without a basement, sited on deep layers of liquefiable soil (Bertalot & Brennan 2015, Adamidis & Madabhushi 2018*a*).

The eccentric distribution of weight of the structure in Test FEH08 resulted in a resultant moment being transferred from the structure to the surrounding soil in static conditions. This moment was resisted by the surrounding soil. During shaking, the peak co-seismic moment transmitted from this structure to the surrounding soil occurred during the first cycle of shaking (Figure 5.18(b)), before the soil was liquefied (Figures 5.2 and 5.3). The peak moment was greatest in the anticlockwise (positive) direction, due to the location of the eccentric mass. Rotation was accumulated in this direction as shaking progressed, as shown in Figure 5.19(b). The structure was not re-centred because of the asymmetry in the moments produced and the detrimental feedback loop this created. As positive rotation was accumulated, the resultant moment exerted by the structure on the soil increased, which in turn increased the rotation. Interestingly, the rate of accumulation of rotation did not increase (Figure 5.9(c)), despite the static component of the moment increasing (Figure 5.18(b)). These data suggest that the rate of accumulation of rotation was dependent on the dynamic component of the resultant moment, which did increase during shaking, but to a much lesser extent. The greatest contribution of the eccentric mass to the moment was through the P - δ term, $M_1(t)$, which increased throughout the earthquake as anticlockwise rotation was accumulated. $M_2(t)$ and $M_3(t)$ also increased, but not as notably.

The accumulation of rotation of the structure in Test FEH08 during EQ3 ceased at the end of shaking, as shown in Figure 5.9(f). This was despite the static component of the moment exerted on the soil being large (Figure 5.18(b)) and high excess pore pressures indicating that a near zero vertical effective stress state still remained (Figure 5.2 and 5.3). This is consistent with the current understanding of the phenomenon of liquefaction induced damage to structures - a near zero effective stress state is on its own insufficient, and must be

accompanied by soil particle disturbance created by the earthquake motion (Madabhushi & Haigh 2012).

The three structures with wide basements shown in Figure 5.19(d) either settled, rotated or did neither. None of the structures accumulated both large settlement and rotation. This is as anticipated given the sequential structure parameter selection process between the centrifuge tests conducted, which aimed at eliminating displacement and rotation. From an academic curiosity point of view, this poses the question as to whether large accumulation of both rotation and settlement can occur simultaneously. However, from a practical point of view, this is of little practical interest as neither are desirable.

5.5 Boundary effects

It is important to discuss the possible boundary effects imposed by the model container. Compared to the width of the wide basements, B, the width of the model container used for these centrifuge tests was 3.1B. This equates to the edge of the basement being located a horizontal distance 1.05B from the edge of the model container. It would have been desirable to have had a greater horizontal distance between the basement and the boundary, however this was not possible due to the size of the model containers available to use with the earthquake actuators on the centrifuge at the time of this research.

In Figures 5.11, 5.13, 5.14 and 5.16 the horizontal edges of the container are at 0 and 25 m on the x-axis, and the base is at 0 m on the y-axis. The soil displacement vectors shown in Figure 5.13 show that soil displacements occurred at the edges of the region monitored using the high-speed camera. The logical continuation of these displacement vectors outside the region monitored infers that the displacement mechanisms extended to the container boundaries.

For all three structures with wide basements, during EQ3 an upward flow of liquefied soil was observed around the basements as soil was displaced to accommodate the accumulation of displacement and rotation of the structures (Figure 5.13). Consequently, heave occurred at the soil surface adjacent to the structures, as shown by the dashed lines in Figure 5.9(a,c). It is possible that the horizontal movement of this soil was limited by the boundaries, and therefore exacerbated upwards displacement. It is also possible that sloshing of the liquefied soil occurred in the narrow width of the soil column between the basement edge and the container boundary. Both additional upward displacement and soil sloshing would result in increased energy dissipation, which could therefore have reduced displacement or rotation of the structures. This would mean that the results from the tests could be an underestimate of what would occur in reality. In addition, potential restriction of horizontal displacement due

to the width of the model container means it is not possible to determine the area of influence of the structures with wide basements.

However, these boundary effects do not invalidate the results and the discussions presented in this chapter. It is not felt that the boundaries either prevented failure mechanisms from developing or caused them to form. The co-seismic behaviour of the structures with wide basements was found to most significantly affect the soil in close proximity to the basement, shown in Figure 5.11, which in turn governed the co-seismic resistance provided by the soil. Comparison of the resultant force and moment transmitted by the structure to the soil with the co-seismic resistance provided by the soil can explain the accumulation of settlement and rotation which was observed in the tests.

To reduce the possibility of boundary effects when investigating the behaviour of structures with wide basements in liquefiable soils it may be desirable to use larger levels of centrifugal acceleration or to commission a wider model window container. Both of these options would increase the width of the column of soil between the basement edge and the model container edge.

5.6 Conclusions

The focus of this chapter was on the seismic behaviour of structures with wide basements, with emphasis placed on the performance of these structures during earthquake induced liquefaction. These structures are representative of hotels or shopping malls with a wide ground floor which could have a basement extending below it, and a taller central tower above.

During small magnitude shaking events, the structures with wide basements performed advantageously. They accumulated minimal settlement, despite shaking being strong enough to cause the adjacent soil surface to settle. Negligible rotation was accumulated, regardless of whether the mass distribution in the structure was symmetric or asymmetric. However, during a larger shaking event which caused liquefaction within the entire soil layer, the behaviour of these structures with wide basements differed considerably.

The very different behaviour of the three structures with wide basements during a large amplitude, sinusoidal base shaking event can be understood by considering the resultant co-seismic vertical force and moment imposed by the structures on the surrounding soil. When positive excess pore pressures were generated during shaking, the uplift force provided by the basement increased whilst the weight of the structure remained unchanged. Consequently, the effective weight of the structures significantly reduced. Concurrently, the generation of positive excess pore pressures and associated stiffness and strength loss in the soil below and

to the sides of the basement reduced the bearing capacity provided by the soil beneath the structure. Rotation and displacement were accumulated when the loading imposed by the structure exceeded the resistance provided by the soil. Settlement of the structure occurred in Test FEH06. It had the greatest effective weight of the three structures with wide basements, which remained above zero for the duration of shaking. Soil displacement vectors show that settlement was primarily due to ratcheting as the structure rocket from side to side. In contrast, the vertical effective weight of the structure in FEH07 quickly approached zero after the onset of shaking, therefore the structure did not settle. For these two structures the resultant co-seismic moment loading was almost symmetric, therefore rotation was not accumulated, despite the moment capacity of the soil being close to zero. Rotation was accumulated during FEH08 as the eccentric mass increased the moment imposed on the soil by the structure in one direction, which could not be resisted by the soil which had close to zero moment capacity. Local dilation of the soil during shaking increased the resistance to rotation and prevented the structure from toppling uncontrollably.

The soil displacements observed during these tests are consistent with the accumulated structure rotation and settlement being caused by the calculated resultant co-seismic loads imposed on the surrounding soil. Rotation was observed to occur about an axis through the centre of the bottom of the wide basements, despite the moment loading being greater about an axis through the basement edge. Accumulation of rotation about the centre of the basement however required both a smaller volume of soil to be displaced and shearing along a shallower plane with a smaller cross sectional area.

The accumulation of rotation of the eccentrically loaded structure in Test FEH08 during EQ3 ceased at the end of shaking. This was despite the static component of the moment exerted on the soil being large and high excess pore pressures indicating that a near zero vertical effective stress state still remained. This is consistent with the current understanding of the phenomenon of liquefaction induced damage to structures - a near zero effective stress state is on its own insufficient, and must be accompanied by soil particle disturbance created by the earthquake motion (Madabhushi & Haigh 2012).

In comparison to structures with shallow foundations without basements, the structures with wide basements performed advantageously during liquefaction because they had a significantly lower effective weight. However, they transmitted a greater moment to the surrounding soil, primarily due to the increased lever arm of all inertia forces as a result of rotation occurring about a plane below the soil surface. To successfully limit both rotation and displacement, the loading imposed by structures with basements on the surrounding soil during liquefaction must therefore be carefully considered.

Furthermore, the structures with wide basements are favourable as the presence of the basements reduced the accelerations transmitted to the superstructures. The reduction in effective bearing pressure due to the increased uplift force provided by the basements allowed liquefaction to occur beneath the structures. Horizontal accelerations were therefore attenuated beneath the structures, which naturally isolated the structures with basements from the base shaking and caused a reduction in structure accelerations.

Consequently, based on the research presented in this chapter, it is possible for basements to be used to reduce liquefaction induced settlement of structures in locations where there is sufficient land available to have a wide basement, and if the mass and stiffness distribution in the structure is reasonably symmetric.

Chapter 6

Cone Penetration Tests in liquefiable soil adjacent to structures with basements

6.1 Introduction

Cone Penetration Tests (CPTs) are a popular in-situ test for site investigation as they enable a continuous profile of penetration resistance to be obtained. This data is frequently interpreted to obtain soil parameters which are of interest in geotechnical design, and in seismic areas to conduct liquefaction susceptibility analysis.

Soil deformation around an advancing cone makes it difficult to link cone resistance, q_c, to soil properties. Villet & Mitchell (1981) demonstrated that there is no single unique relationship that is valid between relative density, I_D, cone resistance, q_c, and vertical effective stress, σ'_v, for all sands because of the influence of soil compressibility on cone resistance. Subsequently, numerous empirical correlations have been proposed to obtain I_D from CPT data for specific sands. The majority of these correlations have been obtained from calibration chamber tests. These laboratory tests involve independently applying a specified vertical and horizontal stress to a cylindrical specimen of artificially-sedimented sand, which subsequently has a cone penetrometer pushed through it.

From regression analysis of calibration chamber tests carried out on un-cemented, normally consolidated quartz sand, Jamiolkowski et al. (1985) proposed a correlation for relative density which was dependent on vertical effective stress, σ'_v. Dimensional analysis of CPT data obtained from centrifuge testing of Fontainbleau sand by Bolton et al. (1993) agreed with the correlation of relative density with vertical effective stress, σ'_v, and proposed that the factors influencing cone tip resistance could be expressed through the following dimensionless

groups:

$$\frac{q_c - \sigma_v}{\sigma'_v} = N_p\{\phi_{crit}, \frac{\sigma'_v}{p'_c}, OCR, I_D, \frac{z_m}{B_c}, \frac{B_c}{d_{50}}\} \tag{6.1}$$

where N_p is the dimensionless penetration coefficient, ϕ_{crit} is the critical state friction angle, p'_c is an aggregate crushing parameter defined by Bolton (1986), σ'_v is the vertical effective stress, OCR is the overconsolidation ratio, I_D is the relative density, B_c is the cone diameter, z_m is test depth, and d_{50} is the mean particle diameter. These dimensionless groups include intrinsic soil properties, ϕ_{crit} and p'_c, parameters describing the current soil state, σ'_v, OCR, and I_D, and the test geometry, z_m/B and B/d. In contrast, calibration chamber tests on Leighton Buzzard sand conducted by Houlsby & Hitchman (1988) showed that, for a given density of sand, the cone tip resistance depended on the in-situ horizontal effective stress, σ'_h, and not on the vertical effective stress, σ'_v. From cross correlation of centrifuge and laboratory tests (direct shear and triaxial tests), Gaudin et al. (2005) proposed that cone resistance is in fact controlled by mean stress, p', in addition to void ratio.

These aforementioned correlations are examples of the many that have been proposed to correlate cone resistance with the current soil state. From an academic perspective they have been developed to further the understanding of soil deformations around an advancing cone, whilst from a practical perspective they facilitate soil parameters to be determined from CPT data. It is evident from these correlations that there is a lack of consensus regarding the influence of the current soil state on cone resistance.

CPT data is also used in the current state-of-practice (SOP) for liquefaction susceptibility analysis, to quantify the resistance of ground to liquefaction. Reasonably good correlation is expected to exist because factors tending to increase the resistance to liquefaction, such as relative density, also tend to increase the penetration resistance of sand (Seed 1979). Consequently, correlations to estimate the capacity of soil to resist liquefaction have been made based on the cone penetration test. Empirical charts have been developed to compare the cyclic shear stress ratio (CSR) induced by an earthquake to the capacity of the soil to resist liquefaction, which is often expressed as a cyclic resistance ratio (CRR). These empirical charts have been developed using post earthquake observations and field testing to correlate manifestation of liquefaction (or not) to in-situ field test data from the site and the estimated CSR value imposed by the earthquake event. These charts display limiting curves of CRR which separate regions of no liquefaction from those where liquefaction occurred, as shown in Figure 6.1. To allow comparison, the CPT cone resistance must be corrected for unequal area affects and subsequently corrected for overburden stress effects to obtain the penetration resistance, q_{c1N}, that would be obtained in the same sand at an overburden stress of 1 atm if all other attributes remain constant. A number of correction factors have

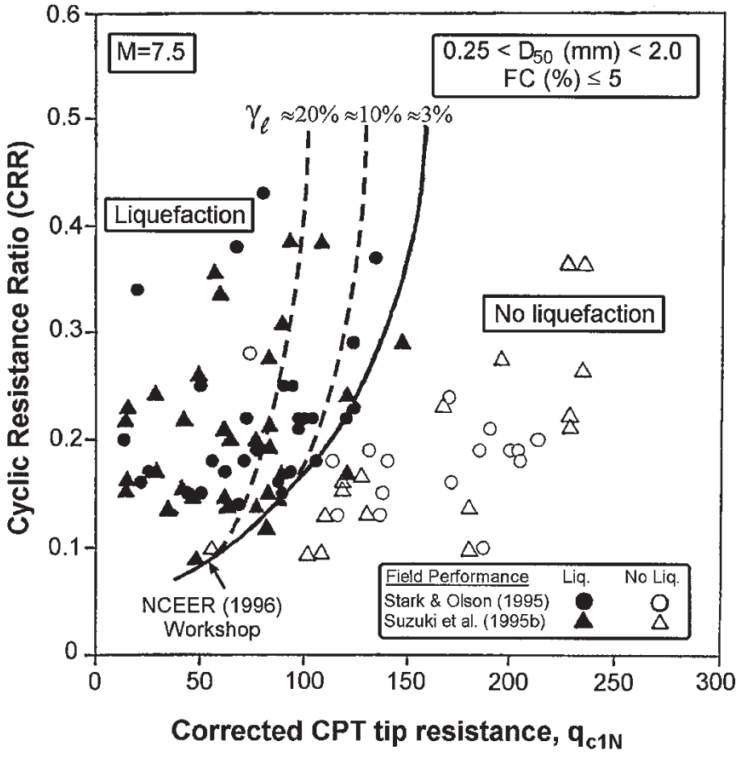

Fig. 6.1 Empirical chart for liquefaction susceptibility analysis using CPT tip resistance, for clean sands under level ground conditions (Robertson & Wride 1998).

been developed to account for variables including earthquake magnitude (Seed et al. 1983), fines content (Robertson & Wride 1998), and high overburden stresses (Robertson & Wride 1998, Boulanger 2003). It is standard practice to use the charts worldwide for liquefaction assessment of a site, including in the European design standard Eurocode 8 (CEN 2004).

This approach is simple and accessible, however, it can be misleading for a number of reasons. Firstly, this method considers each layer in isolation and does not consider the system response. Manifestation of liquefaction at sites in Christchurch, New Zealand, with practically identical critical layer characteristics was found to be dependent on the thickness and vertical continuity of the critical zones (Cubrinovski et al. 2018). The simplified procedure would have incorrectly characterised these sites as having the same susceptibility to liquefaction. Secondly, this binary approach is problematic as it implies that all sites which fall below the liquefaction line, in the "no liquefaction" zone, are not susceptible to any damage associated with behaviour related to liquefaction. Potential damage to infrastructure due to the generation of positive excess pore pressures, without a complete loss of vertical effective stress, is not considered.

In addition to being used in the field, miniature CPT devices have been used in the centrifuge by a number of researchers for similar purposes. Firstly, they have been used to obtain in-flight soil strength profiles (Darby et al. 2017, Beber et al. 2018). However, the same problems exist in the centrifuge as in the field for obtaining soil properties from the cone resistance due to soil deformation around an advancing cone. Secondly, there are a small number of cases where CPTs have been used in the centrifuge to correlate co-seismic behaviour with the pre-shaking properties of the soil (Sharp et al. 2010, Darby et al. 2017). Finally, miniature CPTs have been used in the centrifuge to check uniformity and repeatability of the soil specimen (Renzi et al. 1994, Bolton et al. 1999, Carey et al. 2018). This has been found to be particularly valuable for international collaborative projects, such as LEAP (Liquefaction Experiments and Analysis Projects) as an independent check on centrifuge model properties such as relative density (Carey et al. 2018). Care is required in the centrifuge to avoid data being influenced by the cone size or the proximity to a rigid boundary (Bolton et al. 1993, Gui & Bolton 1998).

6.2 In-flight Cone Penetration Testing

A miniature Cone Penetration Test (CPT) device was used in-flight during the final five centrifuge tests undertaken during this research project. Two CPTs were conducted during each of these tests. The first was conducted post spin-up, before any earthquakes were fired. In this chapter this will be referred to as the "Pre Test" CPT. A second CPT was conducted after all the earthquakes had been fired, before swing-down, and will therefore be referred to as the "Post Test" CPT. The CPT was driven in the same location at both instances, which is shown in Figure 6.2. Liquefaction occurred in the far-field between the Pre and Post CPTs for all of the tests (see Figures 4.11 and 5.2), therefore it is logical to assume that the cavity created by the Pre Test CPT closed during shaking and the location was once again representative of the surrounding soil conditions when the Post Test CPT was conducted. As a result, it is not felt that driving the CPT in the same location will have had an impact on the cone resistance obtained.

The miniature CPT was used for three primary purposes. Firstly, it was used to assess uniformity and repeatability of the soil specimen at the beginning of a centrifuge test. Secondly, it was used to compare the observations from the centrifuge tests to the state-of-practice methods used to determine liquefaction susceptible at a site. Finally, it was used to observe the change in cone resistance caused by the earthquake events. These three points will be explored in this chapter.

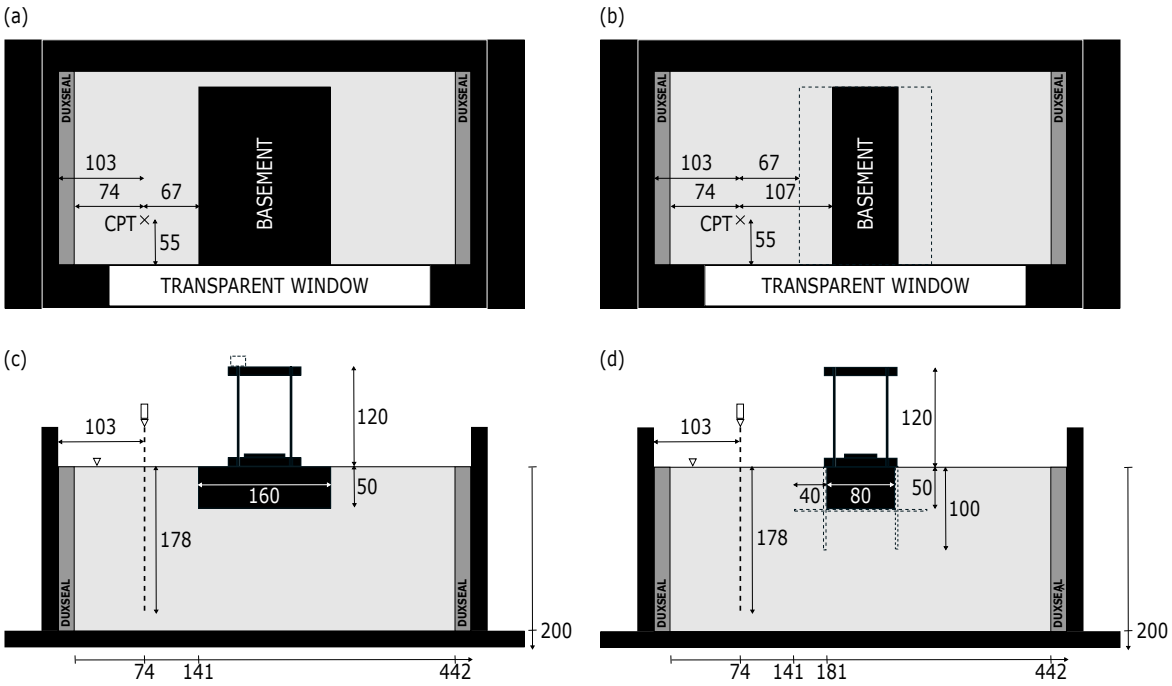

Fig. 6.2 Schematics of Cone Penetration Testing locations, dimensions in mm at model scale: (a) Plan view for tests with structures with wide basements, (b) Plan view for tests with structures with narrow basements, (c) Cross sectional view for tests with structures with wide basements, (d) Cross sectional view for tests with structures with narrow basements.

6.3 Uniformity and repeatability

In physical model testing, the continuous profile of cone resistance with depth obtained from CPTs provide a means to assess uniformity of a soil specimen and repeatability of the preparation method.

CPT profiles obtained from the Pre Test CPT, post spin-up, before any earthquakes were fired, are shown in Figure 6.3(a). The gradient of each of the profiles is approximately constant which shows that a uniform sand layer was produced. The blip in the cone resistance measured at approximately 5 m below the initial ground surface in Tests FEH07 and FEH08 was caused by a notch in the drive shaft of the CPT momentarily stalling progression of the cone.

Figure 6.3(a) shows that, for a given depth, the values of cone resistance across the centrifuge tests were comparable. The cone resistances in Tests FEH07, FEH08, FEH09 and FEH10 were within $\pm$ 0.4 MPa for the entire soil layer. The cone resistance measured in Test FEH11 was greater than the other four tests by approximately 25 %. The models were all poured using an automatic sand pourer with the same nozzle diameter and drop height. The difference is therefore likely to be a result of model disturbance during loading onto the

centrifuge. The comparable values of cone resistance across the tests show that the method of sand pouring was repeatable.

From regression analysis of calibration chamber tests on un-cemented, normally consolidated quartz sand, Jamiolkowski et al. (1985) proposed a correlation for relative density, I_D, which was dependent on vertical effective stress:

$$I_D(\%) = -98 + 66 log_{10}\left(\frac{q_c}{\sqrt{\sigma'_v}}\right) \tag{6.2}$$

where q_c is the cone resistance and σ'_v is the vertical effective stress, both in $tonne - force/m^2$. The sand used in the centrifuge tests was an un-cemented quartz sand, therefore Equation 6.2 was used to estimate the initial relative density of the models post spin-up, before any earthquakes were fired. Values of the initial vertical effective stress were found using the software Plaxis 2D (Plaxis 2000), presented in Sections 4.4.2 and 5.2.1. The estimation of relative density are shown in Figure 6.3(c).

The relative density calculated using Equation 6.2 is significantly lower at shallow depths (approximately shallower than 2 m) than at deeper depths (Figure 6.3(c)). This is not a physical change in density, but a consequence of two different phases of behaviour during cone penetration (Vesic 1963). The transition from one phase to another occurs at a critical depth which is dependent on the depth below the soil surface in comparison to the diameter of the cone (Gui & Bolton 1998). At shallow depths the failure mechanism surrounding a cone is characteristic of that of shallow foundations, whilst at deeper depths failure is characteristic of deep foundations. Centrifuge testing by Bolton et al. (1999) found the critical depth to be approximately 10 times the diameter of the cone, which for the tests presented in this chapter is a depth of 3.5 m below the soil surface at prototype scale. For this reason, the correlation of relative density with cone resistance using Equation 6.2 is deemed unsuitable for depths shallower than 3.5 m. This region is therefore shaded out in Figure 6.3(c).

The relative densities calculated using Equation 6.2 and shown in Figure 6.3(c) can be compared to the mean initial relative density of the soil layer which was calculated using the mass of sand and volume occupied in the model container presented in Chapter 3. The target relative density during model preparation was 44 %. For the five centrifuge tests discussed in this chapter, the mean relative density prior to loading the model onto the centrifuge was calculated to be in the range of 42 $\pm$ 3 %. Compression of the sand layer occurred during spin-up due to the increase in gravitational field and a corresponding increase in vertical and horizontal stress. This resulted in an increase in relative density. For the centrifuge tests discussed in this chapter, the mean relative density was estimated to increase to 48 $\pm$ 2 %, assuming that the increase in density was the same throughout the soil layer.

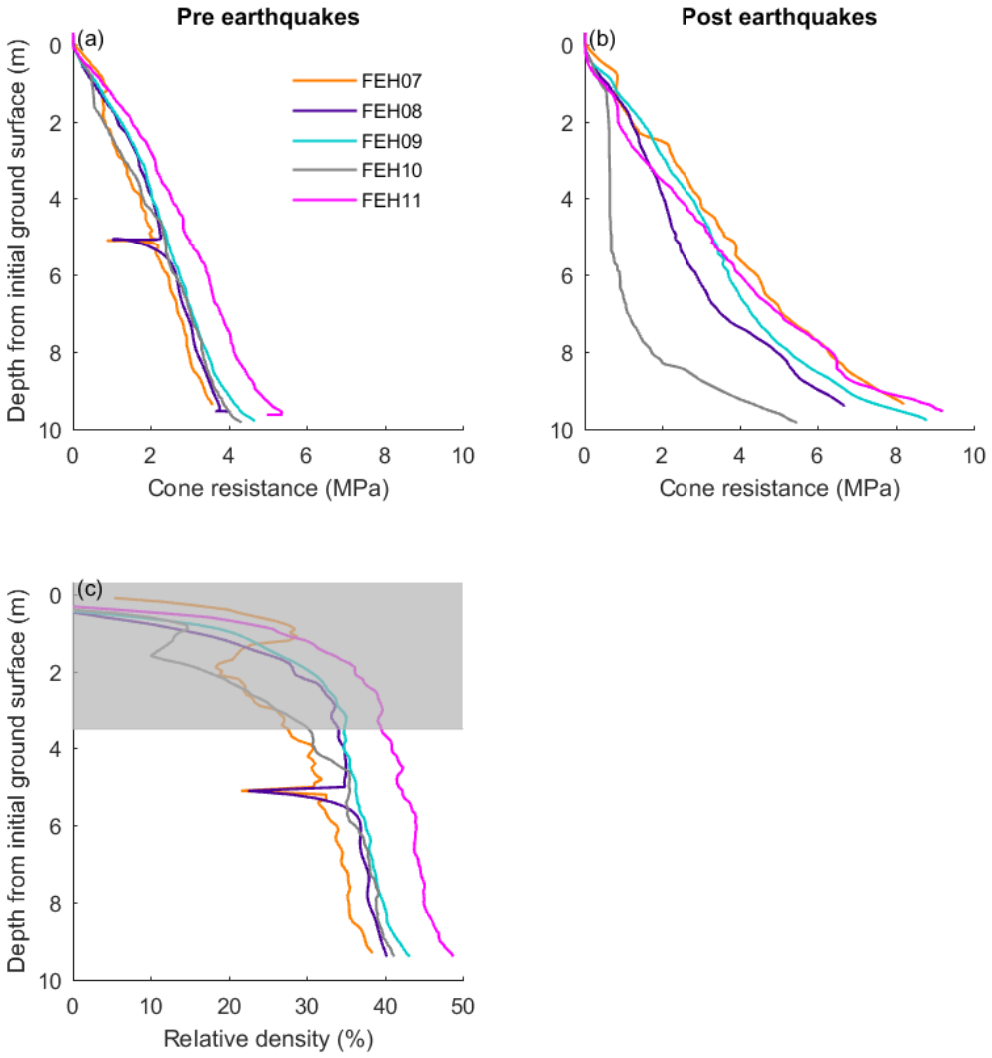

Fig. 6.3 Comparison of cone resistance between centrifuge tests: (a) Pre Test CPT, conducted after swing-up, pre earthquakes, (b) Post Test CPT, conducted post earthquakes, before swing-down. (c) Relative density calculated from Pre Test CPT using equation proposed by Jamiolkowski et al. (1985), detailed in Equation 6.2.

This is slightly greater than, but in reasonable agreement with, the relative densities calculated using Equation 6.2, shown in Figure 6.3(c).

The Pre Test cone resistances shown in Figure 6.3(a) can be compared to the Post Test cone resistances shown in Figure 6.3(b). These figures show that there was a considerable change in cone resistance between the Pre and Post Test CPTs, and that the magnitude and direction of the change was different for the five centrifuge tests presented. These changes will be discussed in detail in Section 6.5. For now it will be concluded from Figure 6.3(a) that the differences in cone resistance between the Post Test CPTs shown in Figure 6.3(b) were a result of changes during shaking, not because of differences during model preparation.

6.4 Liquefaction susceptibility analysis

The current state-of-practice to assess the susceptibility of a site to earthquake induced liquefaction is to use empirical charts to compare the cyclic shear stress ratio (CSR) induced by an earthquake to the capacity of the soil to resist liquefaction, which is often expressed as a cyclic resistance ratio (CRR). Correlations to estimate the capacity of soil to resist liquefaction have been made based on a number of standard field testing methods, including the CPT. These empirical charts have been developed using post earthquake observations and field testing to correlate manifestation of liquefaction (or not) to in-situ field test data from the site and the estimated CSR value imposed by the earthquake event. These charts display limiting curves of CRR which separate regions of no liquefaction from those where liquefaction is expected to occur (Figure 6.1).

This methodology was followed for the five centrifuge tests where CPTs were conducted. The following procedure was used for each test. Firstly, the Pre Test CPT was used to obtain the normalised CPT tip resistance, q_{c1N}, for the depths of discrete instrumentation in L1, L2 and L3 in the far-field of the model:

$$q_{c1N} = \frac{q_c - \sigma_{v0}}{P_a} \sqrt{\frac{P_a}{\sigma'_{v0}}} \tag{6.3}$$

where q_c is the cone resistance, σ_{v0} and σ'_{v0} are the initial total and effective vertical stress respectively, and P_a is atmospheric pressure in the same units as the aforementioned stresses. Secondly, the CSR imposed at each of these depths by each of EQ1, EQ2 and EQ3 was calculated:

$$CSR = 0.65 \frac{a_{max}}{g} \frac{\sigma_{v0}}{\sigma'_{v0}} \tag{6.4}$$

where a_{max}/g was the maximum normalised horizontal acceleration measured at the corresponding location. Finally, the maximum excess pore pressure ratio, $r_{u,max}$, at the corresponding location during each of the earthquakes was calculated:

$$r_{u,max} = \frac{u_{ex,max}}{\sigma'_{v0}} \tag{6.5}$$

where $u_{ex,max}$ is the maximum excess pore pressure measured during an earthquake and σ'_{v0} is the initial vertical effective stress at the corresponding location, obtained using Plaxis 2D analysis.

The boundary separating locations susceptible and not susceptible to liquefaction can be calculated for clean sands using the expressions given by Robertson & Wride (1998):

$$CRR = \begin{cases} 0.833\left[\frac{q_{c1N}}{1000}\right] + 0.05 & \text{for } q_{c1N} < 50 \\ 93\left[\frac{q_{c1N}}{1000}\right]^3 + 0.08 & \text{for } 50 \leq q_{c1N} < 160 \end{cases} \tag{6.6}$$

Field data was used to determine this boundary. It is worthwhile noting that the uniform, clean sand used in the centrifuge tests was very clean relative to clean sand in the field, which may have an effect on susceptibility. CRR increases with increased fines content (Seed et al. 1985), due to an increase in liquefaction resistance or a decrease in penetration resistance. An increase in fines content results in a leftward shift and vertical stretch of the boundary separating locations susceptible and not susceptible to liquefaction (Youd et al. 2001).

Figure 6.4 shows this data plotted in the form of a standard liquefaction susceptibility chart, where the normalised CPT tip resistance, q_{c1N}, is plotted on the x-axis, CSR is plotted on the y-axis, and the colour of each data point shows the maximum excess pore pressure ratio. Circular points show data for EQ1. These are the points plotted with most confidence because the CPT used to calculate q_{c1N} was conducted immediately prior to this earthquake. A CPT was not conducted immediately prior to EQ2 and EQ3, therefore the Pre Test CPT was also used to calculate q_{c1N} for the data points for these earthquakes. Data from EQ2 is plotted as squares and EQ3 as triangles. The black line represents the relationship between q_{c1N} and CRR using the expressions given by Robertson & Wride (1998) in Equation 6.6. This line separates locations anticipated to liquefy, which lie above the line, and those which are not susceptible to liquefaction, which lie below the line.

For the CRR line to be accurate for the centrifuge data plotted in Figure 6.4, all points located below it should be blue and those located above it should be red. It is clear from Figure 6.4 that for most, but not all, of the points this is correct. There are a number of yellow, green and turquoise points located both above and below this line. These points

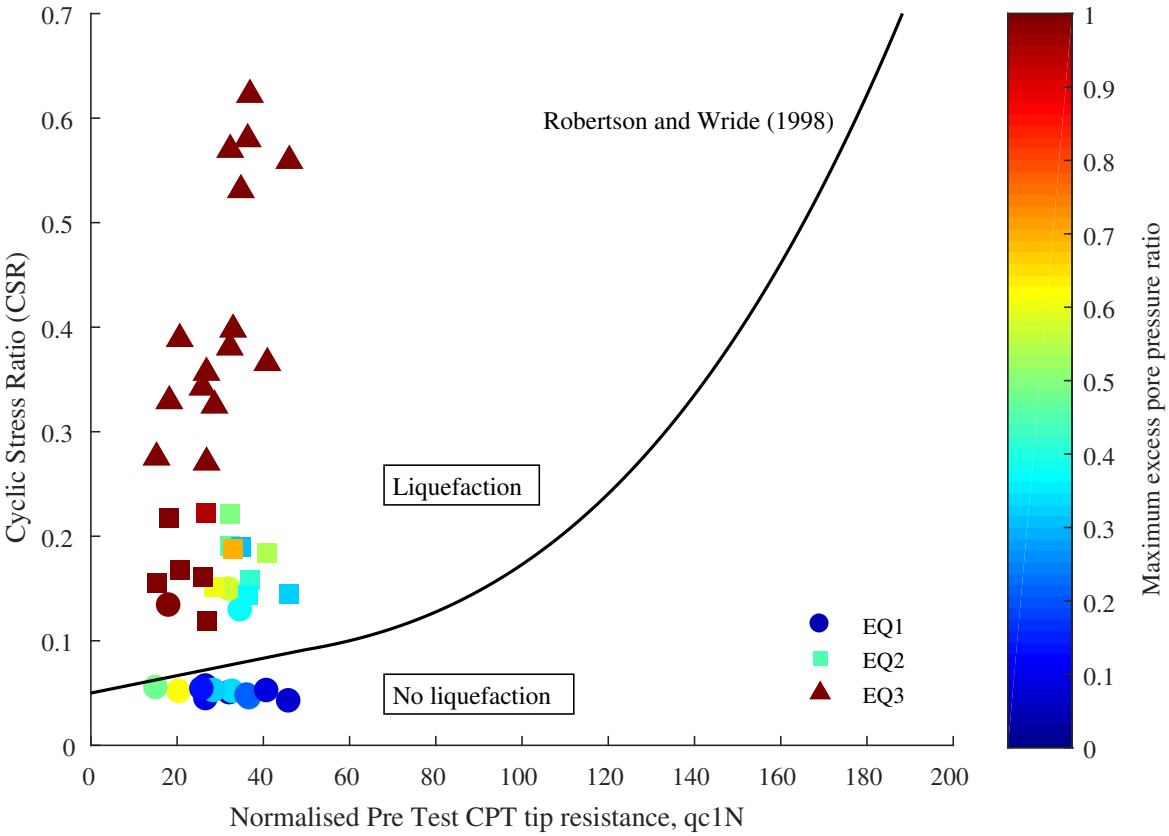

Fig. 6.4 Liquefaction susceptibility analysis using Pre Test CPT tip resistance, for EQ1 (circle), EQ2 (square) and EQ3 (triangle). The colour of the marker corresponds to the maximum excess pore pressure ratio recorded for the corresponding location and earthquake.

correspond to locations where liquefaction did not occur but significant positive excess pore pressures were generated and soil softening occurred due to a reduction in vertical effective stress. The CRR line is conservative for the yellow, green and turquoise points located above it but, worryingly, it is un-conservative for those located below it. The binary nature of this type of chart implies that the line separates regions which are "safe" and "not safe". From Figure 6.4 it is evident that this is not the case.

It should be considered whether the location of the data points for EQ2 and EQ3 in relation to the CRR line would have changed if a CPT had been conducted immediately prior to each of these earthquakes. This would have taken into account any changes in normalised CPT tip resistance, q_{c1N}, caused by the preceding earthquake(s) which would have resulted in the translation of data points in the x-axis direction. This is a worthwhile aspect to consider because most of the field data used to determine the CRR line will have been obtained from CPTs conducted during post earthquake reconnaissance work where CPTs were conducted to obtain a better understanding of the earthquake induced soil behaviour. Figure 6.5 shows

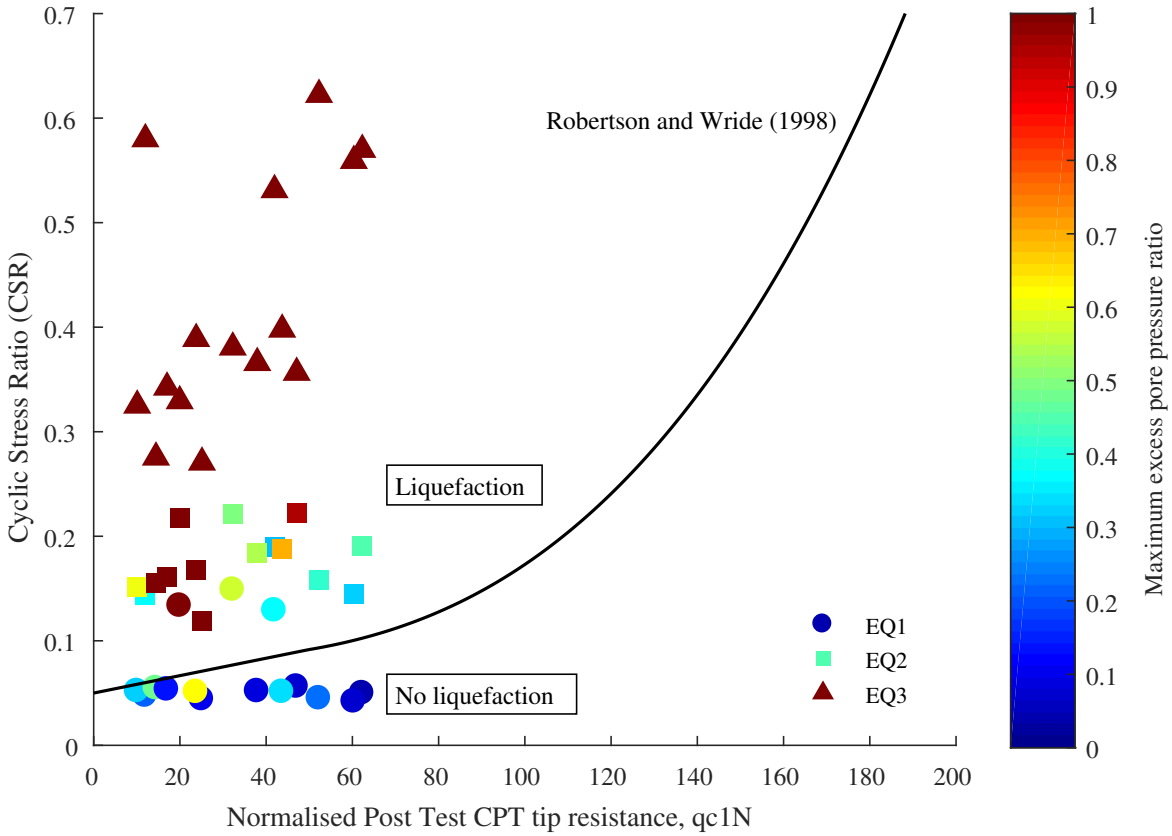

Fig. 6.5 Liquefaction susceptibility analysis using Post Test CPT tip resistance, for EQ1 (circle), EQ2 (square) and EQ3 (triangle). The colour of the marker corresponds to the maximum excess pore pressure ratio recorded for the corresponding location and earthquake.

the same liquefaction susceptibility analysis, but this time conducted using the Post Test CPT to obtain the normalised CPT tip resistance, q_{c1N}. By comparing Figure 6.4 to Figure 6.5 it can be seen that the data points have moved in the x-axis direction. However, their position relative to the CRR line has not changed. Therefore, the classification of whether the sites were susceptible to liquefaction or not has not changed. This is primarily due to the boundary separating locations susceptible and not susceptible being almost horizontal for clean sands for the range of normalised CPT tip resistance obtained in these tests. The curvature of this boundary increases as normalised CPT tip resistance increases and as fines content increases (Robertson & Campanella 1985). Therefore, it is possible that the use of pre and post earthquake CPT data may change the classification of sites with soil properties which differ from those used in the tests presented in this chapter.

6.5 Change in cone resistance

Cone resistance is known to be affected by intrinsic soil properties, parameters describing the current soil stress state, and the test geometry (Bolton et al. 1999). The intrinsic soil properties and the test geometry remained the same during the sequence of earthquakes between the Pre and Post Test CPTs. The soil state will have changed, and will therefore be the cause of changes in cone resistance.

The Post Test CPT profiles conducted after all the earthquakes had been fired, before swing-down, are shown in Figure 6.3(b). It is evident from this figure that there were significant differences in the cone resistance measured at the end of each of the centrifuge tests. The Pre Test CPT profiles were comparable (Figure 6.3(a)), therefore the difference in Post Test CPT profiles were a result of changes during shaking, and not because of differences during model preparation. The change in cone resistance during each of the tests can be clearly seen in Figure 6.6 where the Pre and Post Test CPT profiles are replotted on a separate subplot for each centrifuge test.

Figure 6.6(a) shows that during Test FEH07 there was no change in cone resistance at shallow depths, but an increase occurred at depths greater than approximately 2 m. The same trend was observed during Tests FEH08 and FEH09, shown in Figures 6.6(b,c), however, the depth below which an increase occurred increased to 6 m and 3 m respectively. In contrast, there was a significant reduction in cone resistance during Test FEH10, shown in Figure 6.6(d), particularly in the region of 3 - 7 m below the initial ground surface. A reduction in cone resistance was also observed during Test FEH11, but only at shallow depths (Figure 6.6(e)), with an increase recorded below a depth of 5 m. These observations are in contrast to the progressive increase in cone resistance at all depths observed by Darby et al. (2017) during dynamic centrifuge testing of a saturated level sand bed during a sequence of sinusoidal shaking events of increasing amplitude. Darby et al. (2017) correlated the increase in cone resistance to densification of the initially loose soil layer. The primary difference between the centrifuge tests conducted by Darby et al. (2017) and those presented in this chapter was the presence of a partially buried structure. It is evident that soil-structure interaction must be considered for the tests presented in this chapter.

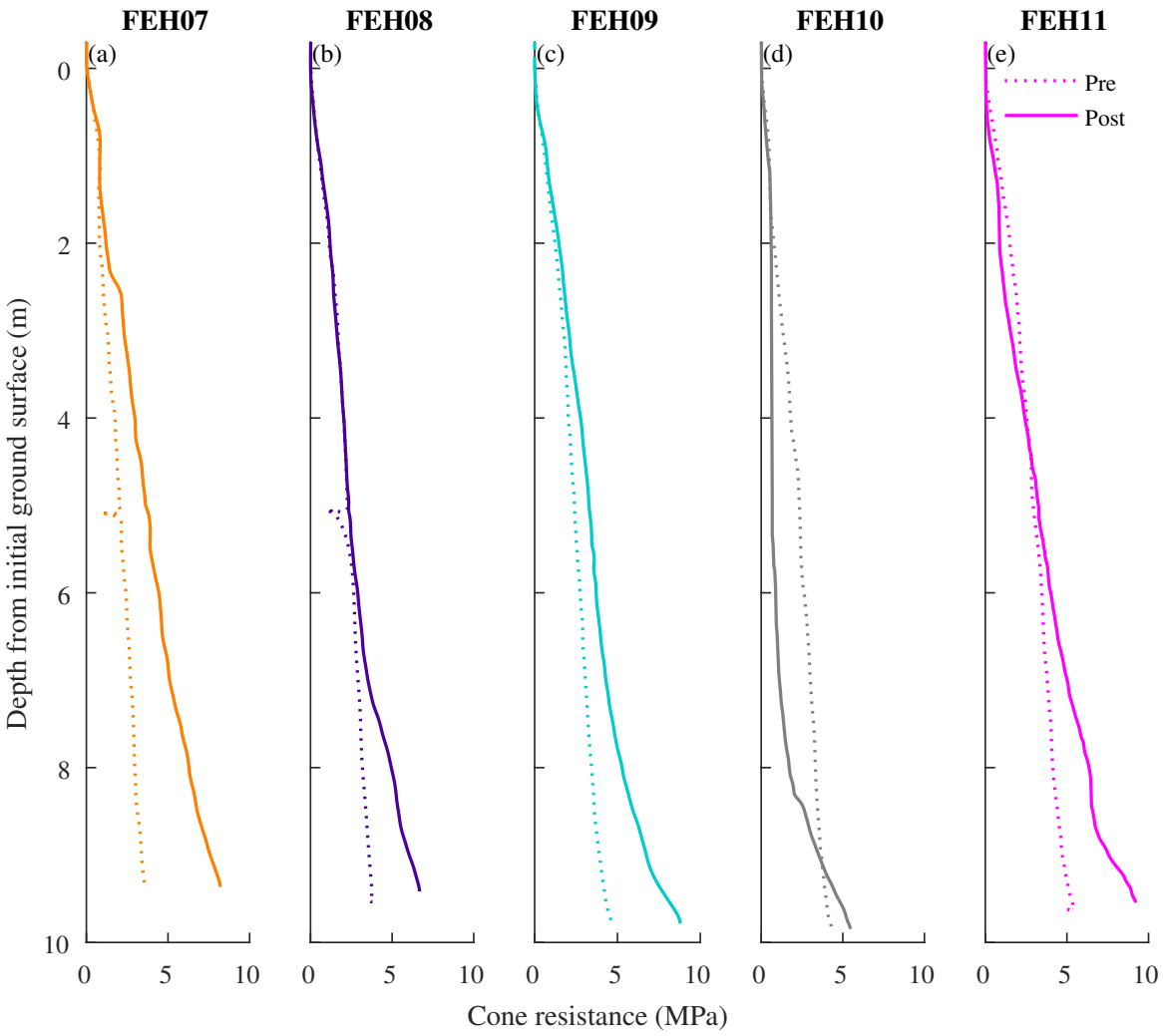

Fig. 6.6 Comparison of cone resistance before and after a sequence of earthquakes: (a) FEH07, (b) FEH08, (c) FEH09, (d) FEH10, (e) FEH11. Dotted lines are Pre Test CPTs, conducted after swing-up, pre earthquakes. Solid lines are Post Test CPTs, conducted post earthquakes, before swing-down.

6.5.1 Change in cone resistance compared to soil displacements

Each of the five centrifuge tests discussed in this chapter included one model structure with a basement. As discussed in Chapters 4 and 5, the behaviour of these structures was comparable during small magnitude shaking events. However, they experienced very different behaviour during the same large sinusoidal base shaking event, EQ3. This earthquake had a peak acceleration of approximately 0.4 g which caused liquefaction to occur in the entire soil layer. For this reason, the change in cone resistance between the Pre and Post Test CPTs will now be compared to the soil and structure behaviour observed during EQ3.

The total co-seismic soil displacements accumulated in each test during EQ3 were calculated using GeoPIV-RG (White et al. 2003, Stanier et al. 2015) and are shown in Figure 6.7 as contours, with the change in cone resistance between the Post and Pre Test CPTs plotted in black. The location where the CPT was driven is shown by the dashed grey line. It can be seen in Figure 6.7 that EQ3 caused very different horizontal and vertical soil displacements in the region where the CPT was driven. The observed displacements can be used to calculate strains in these regions, which can give further insight into the soil behaviour. Interpretation of these strains should be done with care because of the limited resolution of the images taken using the high-speed camera. The derivatives of the displacements are used to calculate strains, which means that any errors in measuring displacement are amplified in strains.

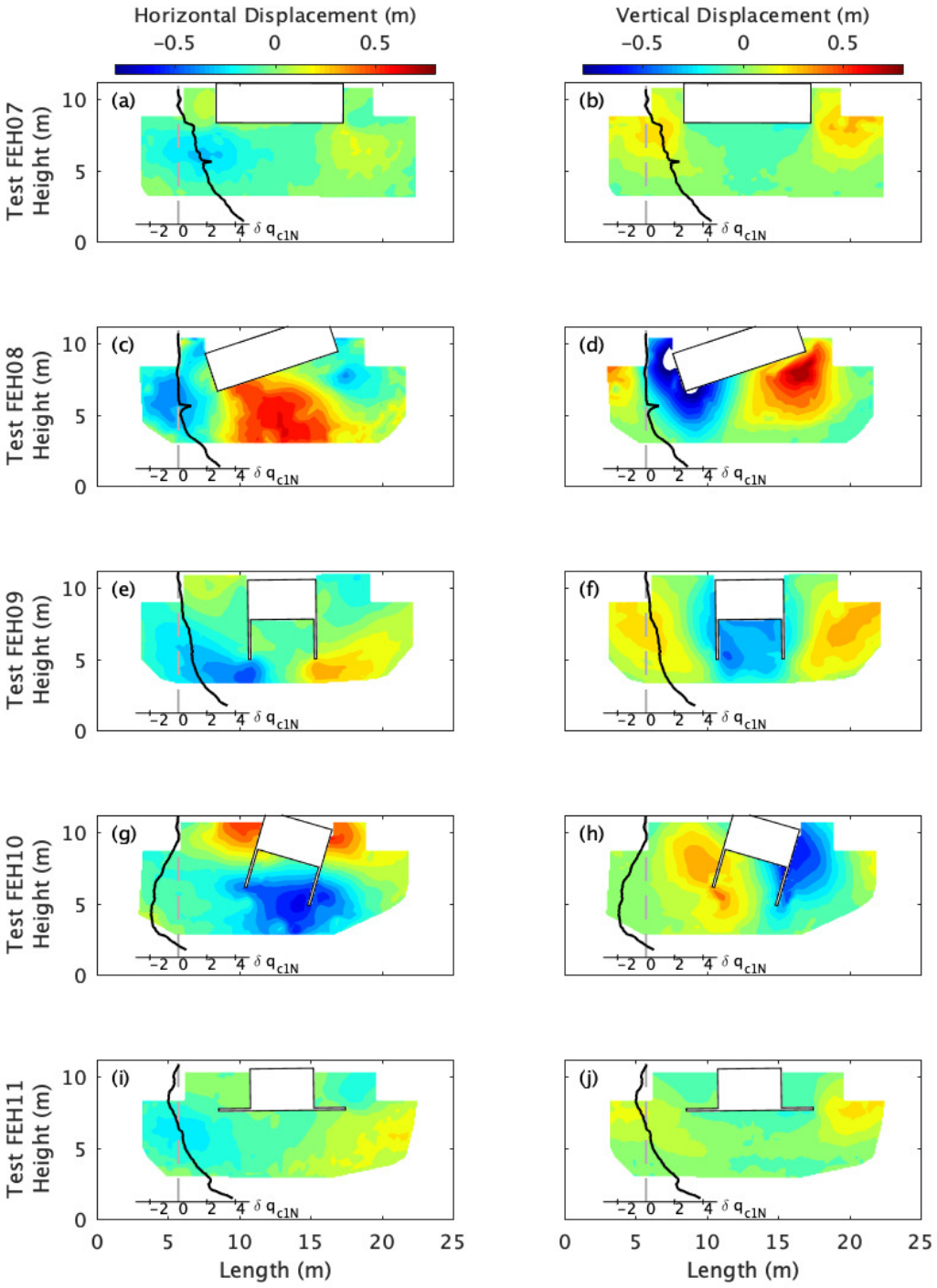

Fig. 6.7 Total co-seismic soil displacements accumulated during EQ3, plotted as contours, compared to the change in cone resistance between the Post and Pre Test CPTs plotted in black. The dashed grey lines show the location where the CPT was driven.

6.5.2 Change in cone resistance compared to soil strains

When looking at the cause of the difference in Post Test CPTs it is worthwhile considering the parameters known to affect cone resistance which may have changed during shaking. These include vertical and horizontal effective stress, and relative density.

The initial vertical effective stress at the location where the CPT was driven can be readily calculated using Terzaghi's effective stress principle (Terzaghi 1943). It is the proportion of the applied stress carried by the structure of the soil particles and increases linearly with depth in the far-field. After shaking, once excess pore pressures have dissipated, the vertical effective stress will no longer be equal to its initial value. However, only a slight change is anticipated to have occurred. The density of the soil layer may have changed, however, the mass of soil above a given depth will not have changed appreciably. It is believed that changes in vertical effective stress during shaking are therefore not the cause of the changes in cone resistance shown in Figure 6.6.

The initial horizontal effective stresses can be estimated by multiplying the corresponding initial vertical effective stress by the earth pressure coefficient at rest, K_0, which in this case it is logical to assume has a value of 0.5. Correlations of lateral earth pressure coefficient, K, with excess pore pressure, u_{ex}, presented by Ishihara (1996) show that K increases as positive excess pore pressure is generated, and reaches a maximum value of one when liquefaction occurs:

$$K = K_0 + \frac{u_{ex}}{\sigma'_{v0}}(1 - K_0) \tag{6.7}$$

Liquefaction occurred in the far-field during EQ3 for all of the centrifuge tests (see Figures 4.11 and 5.2), implying that the lateral earth pressure coefficient reached a value equal to one. In addition, significant co-seismic soil displacement occurred due to soil-structure interaction (Figure 6.7). Lateral displacement and rotation of the basement will have resulted in spatial variation in horizontal effective stress. In addition, following the earthquakes, changes in lateral earth pressure coefficient will have occurred during post liquefaction reconsolidation. Soil stresses were not measured in the centrifuge tests presented in this thesis. Horizontal strains were obtained from the digital image correlation using GeoPIV-RG (White et al. 2003, Stanier et al. 2015). It is assumed that changes in horizontal stress were proportional to the recorded changes in horizontal strain: compressive horizontal strains correspond to an increase in horizontal effective stress.

Cone resistance is dependent on relative density (Villet & Mitchell 1981, Bolton et al. 1993, Gaudin et al. 2005), therefore changes in relative density during shaking must also be considered. Regions of densification and dilation can be identified by looking at volumetric strains, whereby compressive volumetric strains correspond to a decrease in void ratio and

an increase in density, whilst dilative volumetric strains correspond to an increase in void ratio and a decrease in density.

Inferred changes in horizontal stress and relative density will be considered further to investigate their effect on the change in cone resistance during shaking. The left-hand column of Figure 6.8 shows the horizontal strains accumulated during EQ3 and the right-hand column shows the volumetric strains. Both were calculated using GeoPIV-RG (White et al. 2003, Stanier et al. 2015). Compression is positive and dilation is negative. The change in cone resistance between the Post and Pre Test CPTs is plotted in black, with the location the CPT was driven shown by the dashed grey line. Areas of compression and dilation can be more easily identified by replotting Figure 6.8 as a binary image in Figure 6.9, where yellow and blue correspond to compression and dilation respectively. The change in cone resistance is plotted in red for clarity.

The left-hand column of Figure 6.9 shows total horizontal strains. Compressive horizontal strains, shown in yellow, implies an increase in horizontal effective stress, whilst blue corresponds to horizontal extension and implies a decrease in horizontal effective stress. The right-hand column of Figure 6.9 shows total volumetric strains, which use the same colour convention. Compressive volumetric strains, shown in yellow, implies an increase in relative density, whilst blue corresponds to volumetric dilation and implies a decrease in relative density. It is interesting to compare the inferred changes in horizontal effective stress and relative density during EQ3 to the change in cone resistance between the Post and Pre Test CPTs.

During Test FEH07, at shallow depths where the CPT recorded no change in cone resistance there was extension in the horizontal direction (Figure 6.9(a)) which implies a reduction in horizontal effective stress. The opposite was observed at deeper depths, whereby an increase in cone resistance corresponds to the CPT passing through soil which experienced compression in the horizontal direction, implying an increase in horizontal effective stress. The same correlation can be made for Tests FEH08, FEH09 and FEH11 (Figures 6.9(c,e,i) respectively) whereby compression in the horizontal direction and therefore an increase in horizontal effective stress corresponds to an increase in cone resistance.

The correlation between change in cone resistance and change in horizontal strain is less clear for Test FEH10. At the location where the CPT was driven, Figure 6.9(g) shows that the large decrease in cone resistance corresponds to horizontal compression and extension in neighbouring regions of soil. This implies that there were local increases and decreases in horizontal stress. The net change in the region was contractive horizontal strain, implying an increase in horizontal effective stress. Figure 6.8(g) shows that the magnitude of the

horizontal strains in this area were small in comparison to Tests FEH08 and FEH09, which implies that the change in stress will have been smaller.

It should be noted that changes in cone resistance occurred before the device passed through the soil which is believed to have caused that change. This is consistent with the understanding of the failure mechanism surrounding an advancing cone, where it has been shown that the cone tip is sensitive to an interface between 5 and 10 cone diameters before and after passing through it (Schmertmann 1978). This equates to 1.9 to 3.8 m at prototype scale for the tests presented in this chapter.

The trends for volumetric strains are not as clear as for horizontal strains. Figure 6.8 shows that, in general, the volumetric strains were of a smaller magnitude than the horizontal strains. It can be seen in Figure 6.9 that alternating regions of compressive and extensive volumetric strains occurred in all tests, which imply local densification and dilation. However, by considering the overriding change for the location where the CPT was driven it can be seen that the depths at which the cone resistance started to increase in Tests FEH07, FEH08, FEH09, and FEH11 do not correlate to the CPT reaching a region which has increased in relative density (Figure 6.9 (b,d,f,j) respectively), as would intuitively be expected .

These correlations are interesting for a number of reasons. Firstly, there is a difference of opinion on whether cone resistance is more strongly affected by vertical or horizontal effective stress. Numerous correlations for relative density from CPT cone resistance have been proposed which depend on vertical effective stress (Jamiolkowski et al. 1985, Bolton & Gui 1993). However, Houlsby & Hitchman (1988) showed that for a given density of sand, the cone tip resistance depended on the in-situ horizontal effective stress and not on the vertical effective stress. Subsequently, it was proposed that correlations for relative density from CPT cone resistance should depend on horizontal effective stress (Houlsby 1998). However, horizontal effective stress is not an easy parameter to determine outside an element testing laboratory scenario. In addition, Gaudin et al. (2005) proposed that cone resistance is in fact controlled by mean stress, p'. The data presented in Figure 6.9 provides evidence that, in clean sands, the post liquefaction cone resistance is dependent on horizontal strain, which implies a dependency on horizontal stress. The observed changes in cone resistance could not be explained by the volumetric strains, which implies that they were not solely a result of changes in relative density. Changes in vertical effective stress between the Pre and Post CPTs are unlikely to have changed noticeably, and it is improbable that they caused the changes observed.

Secondly, it is interesting to consider the implications that these correlations have on the database of CPT profiles that have been conducted on post earthquake reconnaissance missions at sites which were observed to have suffered liquefaction induced damage. Salgado

et al. (1997) showed that cone resistance should be normalised to an equivalent 1D, normally consolidated K_0 value when conducting liquefaction susceptibility analysis to account for consolidation taking place under conditions differing from 1-D consolidation (i.e. some soil densification field methods) or overconsolidation. The data presented in this chapter shows that changes in horizontal stress due to soil-structure interaction must also be considered. Otherwise, using post-liquefaction CPTs to determine pre-earthquake soil conditions may be misleading. Compression of soil in the horizontal direction due to liquefaction induced settlement or rotation of a structure in the proximity of where a CPT is driven can cause an increase in cone resistance. Likewise, extension of soil in the horizontal direction, say due to lateral spreading, can result in a reduction in cone resistance. The data presented in this chapter shows that the classification of whether the soil layers were susceptible to liquefaction was not affected by using the Pre or Post CPT tip resistance (Figures 6.4 and 6.5). This is primarily due to the boundary separating locations susceptible and not susceptible being almost horizontal for clean sands for the range of normalised CPT tip resistance obtained in these tests. The curvature of this boundary increases as normalised CPT tip resistance increases and as fines content increases. Therefore, it is possible that the use of pre and post earthquake CPT data may change the classification of sites with soil properties which differ from those used in the tests presented in this chapter.

It can be hypothesised that the observations from these tests can be extended to cases where liquefaction induced lateral spreading has occurred. Lateral extension that occurs in regions that have suffered liquefaction induced lateral spreading will result in a reduction in horizontal effective stress which it is anticipated will cause a decrease in cone resistance.

Finally, it is possible that the observations made in this chapter mean that more can be learnt from post earthquake CPT data than is currently realised. Changes in cone resistance that cannot be accounted for by a change in soil stratum may be caused by changes in horizontal effective stress. This may in turn help understand observations of earthquake induced damage. This concept can be extended to the use of miniature CPT devices in the centrifuge, whereby they may be able to provide more insight into co-seismic soil behaviour than is currently realised.

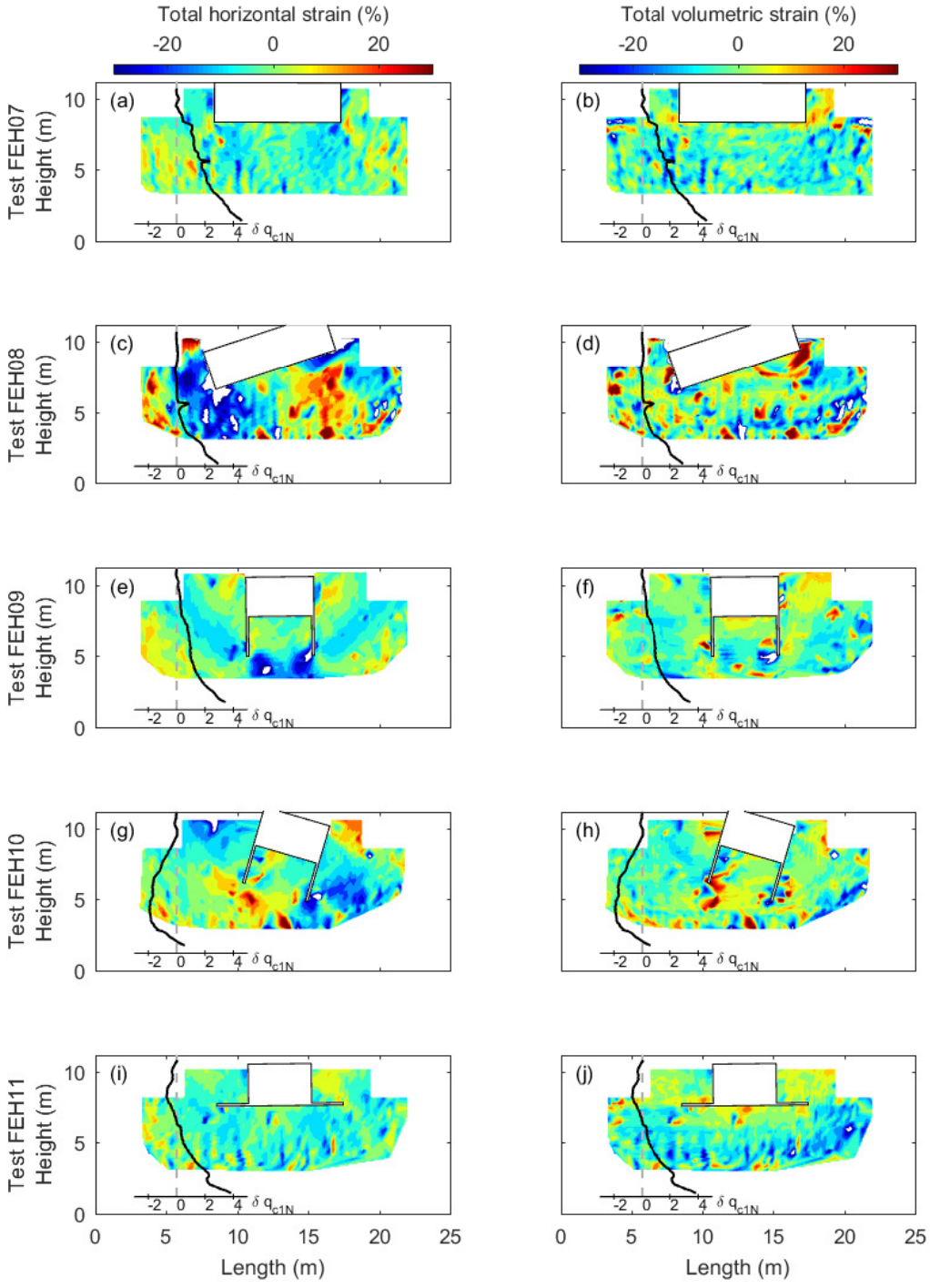

Fig. 6.8 Total co-seismic horizontal (left-hand column) and volumetric (right-hand column) strain accumulated during EQ3, plotted as contours, compared to the change in cone resistance between the Post and Pre Test CPTs plotted in black. Compression is positive and dilation is negative. The dashed grey lines show the location where the CPT was driven.

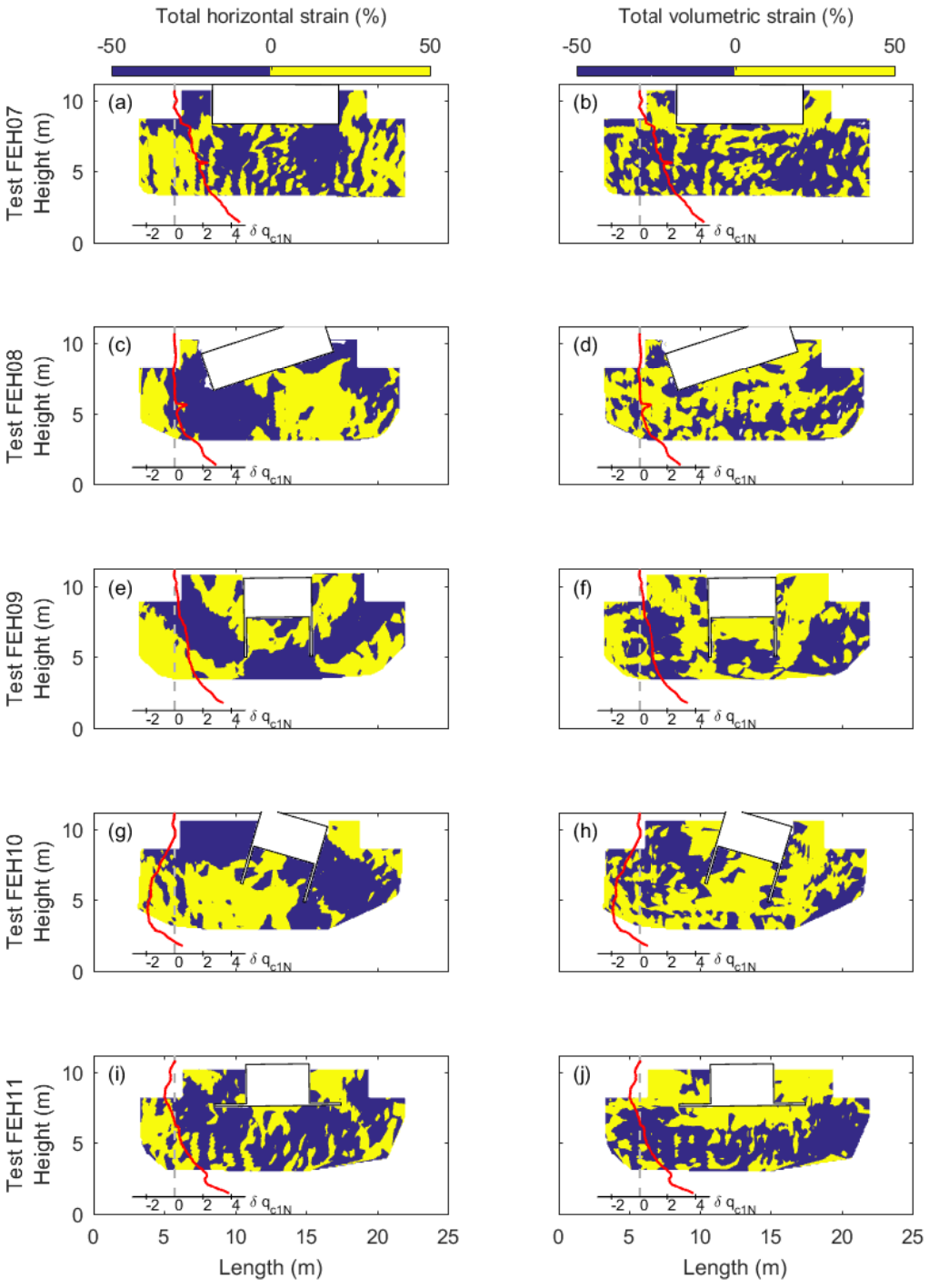

Fig. 6.9 Total co-seismic horizontal (left-hand column) and volumetric (right-hand column) strain accumulated during EQ3, plotted as binary contours, compared to the change in cone resistance between the Post and Pre Test CPTs plotted in red. Compression is positive and dilation is negative. The dashed grey lines show the location where the CPT was driven.

6.6 Limitations

It is necessary to discuss the potential limitations of the data presented in this chapter.

In the centrifuge, careful consideration of the location of the CPT and the size of the cone is required. To avoid data being influenced by the cone size, the cone diameter, B_c, should be at least twenty times greater than the mean particle diameter, d_{50} (Bolton et al. 1999). To avoid boundary effects, it is recommended that CPTs should be performed at least $10B_c$ away from any hard boundary (Bolton et al. 1999). For the data presented in this chapter, the CPT was performed $11.7B_c$ away from the edge of the layer of Duxseal and $8.7B_c$ away from the transparent PMMA window (Figure 6.2). The Pre Test CPT was $10.6B_c$ away from the wide basement, and $16.9B_c$ away from the narrow basement. The guidelines suggested by Bolton et al. (1993) were used to select the location of the CPT, however the location was also governed by the centrifuge model container dimensions and the layout of the instrumentation within the model. The proximity of the CPT location from the transparent PMMA window was slightly closer than the recommended distance, and is not felt to have influenced the data presented in this chapter. Only one miniature cone was available to use in this research project. It had a diameter of 6.35 mm, which equates to 17.8 times the mean particle diameter. This is slightly smaller than the recommended minimum cone size. This is close to the recommended cone size, and is therefore not felt to have influenced the results presented in this chapter.

In each of the centrifuge tests, the Pre and Post Test CPT were driven in the same location. Liquefaction occurred in the far-field between the Pre and Post CPTs for all of the tests (see Figures 4.11 and 5.2) therefore, it is logical to assume that the cavity created by the Pre Test CPT closed during shaking. The soil stress state is reset by shaking and the location was once again representative of the surrounding soil conditions when the Post Test CPT was conducted. As a result, it is not believed that driving the CPT in the same location will have had an impact on the cone resistance obtained. In fact, driving the CPT in the same location was one of the strengths of this testing programme as it enabled a direct comparison to be made between the Pre and Post Test CPTs.

CPTs were only conducted at the start and end of each of the centrifuge tests. Stronger correlations would be possible if CPTs had been conducted between each of the earthquakes that were simulated. For this to be possible and for the data obtained to be meaningful, it would have been necessary to drive the CPTs at different locations. This would have required either multiple CPT assemblies, or a 2-dimensional actuator to move the CPT laterally to a new location between vertical penetrations. Neither of these were available at the time of this research.

A larger data set would strengthen the data presented in this chapter. A total of 10 CPTs were conducted, which consisted of 5 Pre and 5 Post Test measurements. The data obtained from these tests is consistent and coherent, and justifies the discussions made in this chapter. A larger number of CPT data obtained in parallel to digital image correlation would further the conclusions made. An independent measure of lateral pressure would also strengthen the data.

6.7 Conclusions

The focus of this chapter was on the use of a miniature CPT device in-flight in centrifuge tests investigating the seismic behaviour of structures with basements in liquefiable soil. Emphasis was placed on the change in cone resistance between CPTs conducted before and after a sequence of earthquakes.

For clean sands with normalised tip resistances less than 60, the classification of susceptibility to liquefaction using state-of-practice empirical charts was found not to be affected by whether the cone resistance used was obtained before or after a sequence of earthquakes. In some cases, locations which were classified as not being susceptible to liquefaction using the CRR line proposed by Robertson & Wride (1998) were found to generate significant excess pore pressures; a maximum excess pore pressure ratio of 0.6 was recorded in one instance. Liquefaction was not observed for any locations classified as not being susceptible to liquefaction, however, soil softening occurred due to the reduction in vertical effective stress caused by the generation of positive excess pore pressure. The binary nature of liquefaction susceptibility charts is misleading as it incorrectly implies that locations classified as not being susceptible to liquefaction are "safe".

The combination of CPT data with soil displacements obtained from digital image correlation using GeoPIV-RG (White et al. 2003, Stanier et al. 2015) has provided novel insight into the change in cone resistance before and after a sequence of earthquakes. Changes in horizontal strains resulting from the liquefaction induced settlement and rotation of a structure with a basement were found to correlate with the measured changes in cone resistance. It was assumed that changes in horizontal stress were proportional to the observed changes in horizontal strain. Compressive horizontal strain, implying an increase in horizontal stress, was found to correlate with an observed increase in cone resistance. Likewise, extension in the horizontal direction, implying a decrease in horizontal stress, was found to correlate with a decrease in cone resistance. Compressive volumetric strain, implying a decrease in void ratio and an increase in relative density, did not correlate with observed increases in cone resistance. The data presented in this chapter shows that, in clean sands,

the change in cone resistance before and after a sequence of earthquakes is dependent on accumulated horizontal strains, which implies that the post liquefaction cone resistance is dependent on horizontal effective stress. The change in cone resistance was found to be less dependent on changes in volumetric strain, and therefore changes in relative density. A larger data set would strengthen the observations made in this chapter. Additionally, an increase in the resolution of the images obtained from the high-speed camera may enable quantitative correlations to be made.

Chapter 7

Mechanical model for displacement and rotation in liquefiable soil

7.1 Introduction

There are a number of advanced techniques available for detailed investigations into problems encountered in geotechnical earthquake engineering, namely centrifuge modelling, numerical simulations, and shaking table testing. Dynamic centrifuge modelling was used in the preceding chapters to investigate the seismic behaviour of structures with basements in liquefiable soil. Novel information on these types of structures, specifically the soil-structure interaction, was obtained for a finite number of structures during a number of shaking events. It is not feasible to do this for every possible scenario that could be encountered, due to both time and cost considerations. The development of simplified methods are therefore crucial to enable valuable information obtained from novel testing using advanced methods to be applied to a wider number of applications. Dobry (2014) summarises a number of simplified methods and solutions that are currently available for various soil dynamics problems.

Simplified methods are powerful as they enable an overview of the system behaviour and the role of important parameters to be obtained by hand calculation or with minimal computational effort. A number of simplified methods exist relating to earthquake induced liquefaction and the damage it can cause. One of the most well known is the simplified procedure for evaluating soil liquefaction potential presented by Seed & Idriss (1971). The procedure evaluates the liquefaction potential of a soil deposit by comparison of the stress induced by an earthquake against that required to cause liquefaction, both of which are obtained using a simplified procedure. Advances in the understanding of liquefaction over recent years has led to questions on the suitability of this methodology (Cubrinovski et al.

2018). Nevertheless, the procedure proposed by Seed & Idriss (1971) is still being used, albeit with the addition of a number of scaling factors that have been developed to incorporate additional factors such as earthquake magnitude. The unwillingness of the engineering community to incorporate new findings into practice is of concern. However, the continued use of this procedure is also a testimony to the success of simplified methods which can easily be applied in practice.

Simplified methods exist to estimate the post liquefaction volumetric strain accumulated in a level sand bed, including those proposed by Tokimatsu & Seed (1987) and Ishihara & Yoshimine (1992). Subsequently, the liquefaction induced settlement of the ground surface can be calculated by integrating the volumetric changes throughout the depth of the soil layer. These methods are not suitable for estimating liquefaction induced building settlements as they neglect displacements due to deviatoric strains caused by soil-structure interaction. However, they are commonly used for this purpose (Dashti & Bray 2013). Recently, Bray & Macedo (2017) presented a simplified procedure to estimate liquefaction induced settlement of structures with shallow foundations. Displacement due to mechanisms causing shear and volumetric strains, and as a result of soil ejecta are each calculated independently and then summed. This method simplifies the problem, however, it is still lengthy and it states in its requirements that a significant amount of "engineering judgement" is needed.

An alternative approach which is commonly used in simplified methods for soil dynamics problems is to idealise the system as a mass-spring-damper system. The springs are characterised by a modulus of subgrade reaction which relates deflection to the corresponding soil pressure. The dashpot elements are characterised by a viscous damping coefficient, the value of which is chosen to ensure that the energy it dissipates is equivalent to the energy dissipated in the damping mechanisms in the soil, which include material, viscous and radiation damping. Consequently, the force in the springs is proportional to displacement and the force in the dashpots is proportional to velocity. D'Alembert's principle can then be used to solve the equation of motion for the system when subjected to time-varying loading. Complexity can be increased by increasing the number of degrees of freedom being considered. The difficulty in these methods lies in determining the parameters of the spring and dashpot components which replicate the behaviour of the system obtained from more advanced methods. Numerous methods have been developed to estimate these parameters, which are highly dependent on a range of interdependent factors, including the stiffness of the soil, the dimensions of the structure, and frequency of the dynamic loading.

It was evident in Chapter 5, Section 5.4, that the very different liquefaction induced behaviour of the three structures with wide basements can be explained by considering the resultant co-seismic vertical force and moment imposed by the structures on the surrounding

soil. It was proposed that settlement and rotation were accumulated when the loading exceeded the resistance provided by the surrounding soil. In this chapter, this data will be used to develop a mechanical model, the DRILS - "Displacement and Rotation In Liquefiable Soil" - model, that can replicate the behaviour obtained in the dynamic centrifuge test series. Firstly, a model will be developed which can capture the dynamic response of the structures with basements. It will then be modified to include the accumulation of rotation and displacement of the structures. This model will then be used to undertake parametric studies to extend the findings from the centrifuge test series to a wider range of structure properties and input motions.

7.2 Mechanical model to capture the dynamic response

A mechanical model was developed to capture the dynamic response of structures with basements in liquefiable soil, which were presented in Chapters 4 and 5. Henceforth, this model will be referred to as the dynamic DRILS - "dynamic Displacement and Rotation In Liquefiable Soil" - model.

7.2.1 Degrees of freedom

The dynamic centrifuge tests replicated plane strain conditions. The structures therefore had three degrees of freedom - translation in the horizontal and vertical directions and rotation about an axis perpendicular to these aforementioned directions. For these three degrees of freedom, the co-seismic forces and moment imposed by the structures with basements on the surrounding soil had dynamic and static components during horizontal base shaking, which are shown in Figure 7.1.

The purpose of the dynamic DRILS model is to capture the dynamic response of the structures with basements. The dynamic components shown in Figure 7.1 contribute to excitation of the structure during shaking, and are therefore the input for this model. The dynamic horizontal and moment loading had a greater amplitude than the dynamic vertical loading in the centrifuge tests. Therefore, only the dynamic horizontal and moment loading will be considered in the dynamic DRILS model. Later, the vertical loading will be included when the accumulation of displacement and rotation is addressed.

7.2.2 Formulation of dynamic response

When a foundation is subjected to a horizontal force or a moment about its centre of gravity, it will simultaneously translate and rotate. Therefore, the equation of motion used in the

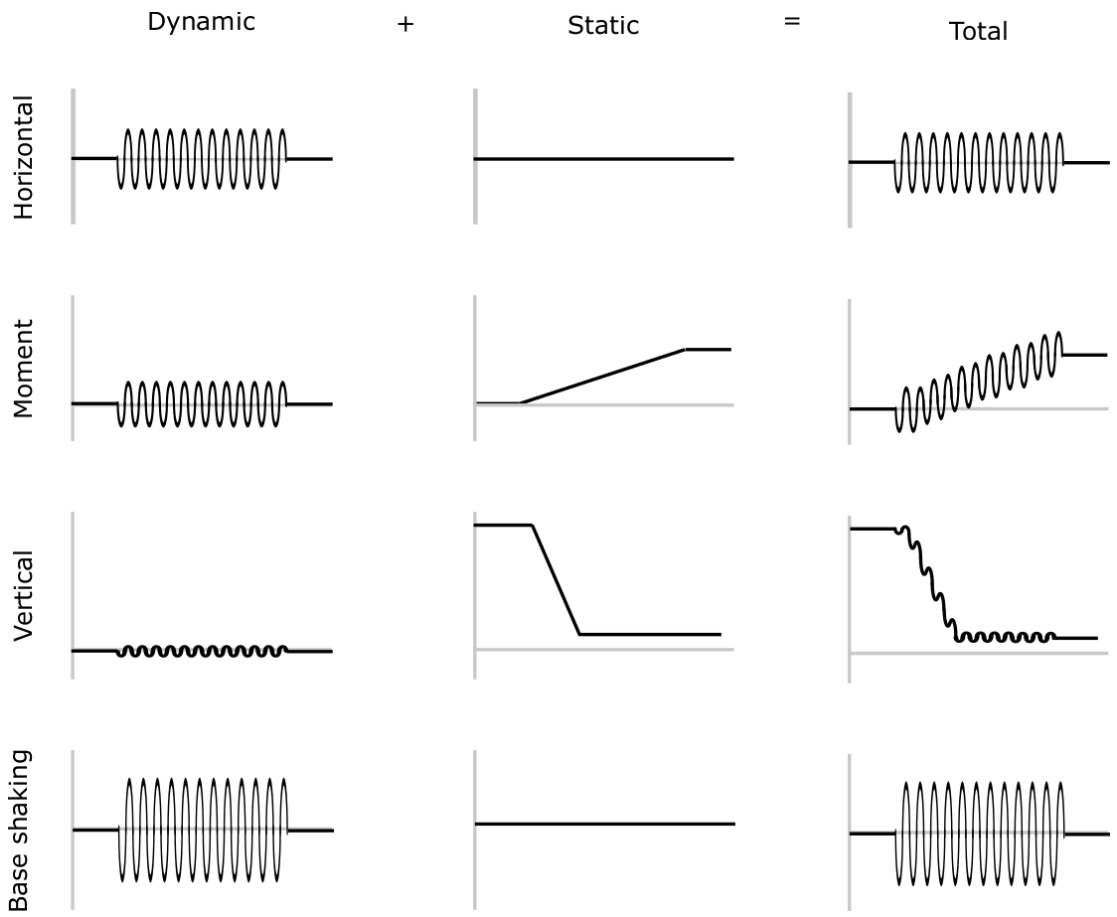

Fig. 7.1 Components of structure excitation during horizontal base shaking for the 3 degrees of freedom of the structures with basements in the centrifuge tests: horizontal and vertical translation, and rotation about the axis perpendicular to these aforementioned directions.

formulation is required to have coupled horizontal translation and rotation. Kumar & Prakash (1995) presented an equation of motion for a rigid block foundation embedded in an elastic half space with a soil side layer, for coupled horizontal and rocking vibration. They assumed that:

- The soil reactions at the base of the foundation were independent of the depth of embedment.
- The soil reactions on the sides were produced by an independent elastic layer lying above the level of the foundation base.
- There was a perfect bond between the sides of the foundation and soil.

In addition, when applying this mathematical formulation to the analysis of the structures with basements in this chapter, it was assumed that:

- No resistance to translation was provided along the bottom of the basement, i.e. no base shear.

The assumption of no base shear is considered to be reasonable as resistance provided by horizontal earth pressures in the soil adjacent to the basement will have been much greater than the resistance due to base shear. The bottom of the model basements were smooth sheet aluminium, meaning shear resistance was limited. In addition, the generation of positive excess pore pressure beneath the basement further reduced the resistance due to base shear.

The translation and rotation can be calculated:

$$\begin{bmatrix} m & 0 \\ 0 & I_o \end{bmatrix} \begin{bmatrix} \ddot{x} \\ \ddot{\theta} \end{bmatrix} + \begin{bmatrix} c_x & -c_{x\theta} \\ -c_{\theta x} & c_\theta \end{bmatrix} \begin{bmatrix} \dot{x} \\ \dot{\theta} \end{bmatrix} + \begin{bmatrix} k_x & -k_{x\theta} \\ -k_{\theta x} & k_\theta \end{bmatrix} \begin{bmatrix} x \\ \theta \end{bmatrix} = \begin{bmatrix} F_{x,dy} \\ M_{z,dy} \end{bmatrix} \tag{7.1}$$

where

$$c_x = c_{xs} \tag{7.2}$$

$$c_{x\theta} = c_{\theta x} = c_{xs} d \tag{7.3}$$

$$c_\theta = c_{\theta b} + c_{xs} d^2 \tag{7.4}$$

$$k_x = k_{xs} \tag{7.5}$$

$$k_{x\theta} = k_{\theta x} = k_{xs} d \tag{7.6}$$

$$k_\theta = k_{\theta b} + k_{xs} d^2 \tag{7.7}$$

where m is mass, I_o is moment of inertia, k is the spring stiffness, c is the damping constant, d is the height of the horizontal spring and dashpot above the bottom of the basement, $F_{x,dy}$ is the dynamic horizontal force, and $M_{z,dy}$ is the dynamic moment. Terms with the subscript s are associated with the soil to the side of the basement, and terms with the subscript b are associated with the soil beneath the bottom of the basement. These parameters are shown in a schematic diagram in Figure 7.2, along with the sign convention. This formulation is consistent with using the right-hand rule to define the positive direction of the axes and corresponding rotations. Equations 7.1 to 7.7 are combined to obtain:

$$m\ddot{x} + c_{xs}(\dot{x} - \dot{\theta} d) + k_{xs}(x - \theta d) = F_{x,dy} \tag{7.8}$$

$$I_0 \ddot{\theta} + c_{\theta b}\dot{\theta} + c_{xs}(\dot{\theta} d - \dot{x})d + k_{\theta b}\theta + k_{xs}(\theta d - x)d = M_{z,dy} \tag{7.9}$$

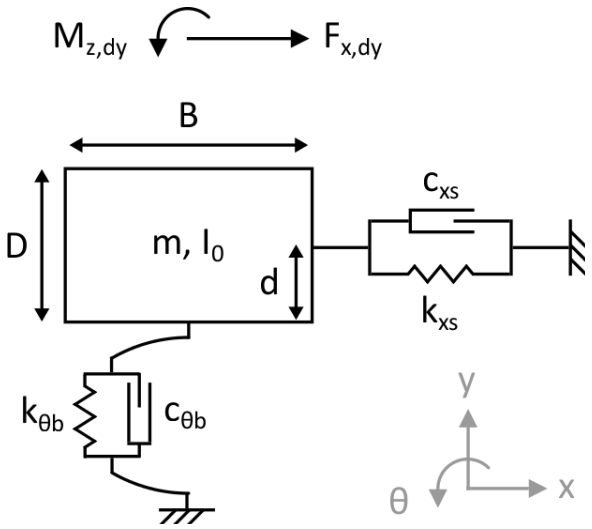

Fig. 7.2 Schematic of mechanical model for the dynamic response of a rigid basement embedded in a soil layer, with coupled horizontal and rotational motion.

7.2.3 Determination of model parameters

The values of the model parameters shown in Figure 7.2 were calculated using data recorded during the dynamic centrifuge tests presented in Chapters 4 and 5. The horizontal spring, $k_{xs}(t)$, and dashpot, $c_{xs}(t)$, were characterised by the behaviour of the soil adjacent to the side of the basement. The rotational spring, $k_{\theta b}(t)$, and dashpot, $c_{\theta b}(t)$, were characterised by the behaviour of the soil below the bottom of the basement.

Structural parameters

The basement was modelled as a rigid, embedded block with a rectangular cross section with dimensions width, B, depth, D, and length, L. The contributions from each of the rigid sections of the superstructure and the basement were summed to calculate the total mass, m, and moment of inertia, I_0. The height of the horizontal spring and dashpot above the bottom of the basement, d, was chosen to be equal to half the depth of the basement, $D/2$.

Structural excitation

The embedded structures were acted upon by a horizontal force, $F_{x,dy}(t)$:

$$F_{x,dy}(t) = ma_h(t) \tag{7.10}$$

where m is the mass of the structure and $a_h(t)$ is the horizontal acceleration of the base shaking applied to the model container, in ms^{-2}, which simulated earthquake shaking.

The moment acting on the structures, $M_{z,dy}(t)$, was about the z-axis shown in Figure 7.2, perpendicular to both the horizontal and vertical axes. It was calculated by splitting the model structures into rigid sections - the eccentric mass (where applicable), the roof, the ground floor and basement which were rigidly connected, and the buoyancy force provided by the basement - and summing the contribution of each section. This methodology was discussed in detail in Chapter 5, Section 5.4. A high-pass filter was used to obtain only the dynamic part of this moment, which consisted primarily of two components. The first was the moment due to the horizontal inertia force of the structure components accelerating due to the transmission of base shaking through the soil layer to the structure. The second was the moment due to the rotational inertia of each of the components of the structure.

Dynamic shear strains

Time histories of horizontal accelerations measured in the soil layer were used to calculated time histories of shear strains, using the methodology presented by Elgamal et al. (1996) and Brennan & Madabhushi (2005). The horizontal accelerations recorded by the piezo accelerometers in L3 and L4 in the column of instruments in the far-field were used to calculate the shear strains characterising the behaviour of the soil adjacent to the side of the basement. The horizontal accelerations recorded by the piezo accelerometers in L2 and L3 in the column of instruments below the centre of the basements were used to calculate the shear strains characterising the behaviour of the soil below the bottom fo the basement. These locations are shown in the schematics in Chapter 3, Section 3.7. Interpolation between peaks of shear strain were used to obtain time histories of shear strain amplitude, $A_\gamma(t)$.

Excess pore pressures

Time histories of pore pressures measured in the soil layer were used to calculate time histories of excess pore pressure ratio, $r_u(t)$:

$$r_u(t) = \frac{u_{ex}(t)}{\sigma'_{v0}} \tag{7.11}$$

where $u_{ex}(t)$ was the instantaneous excess pore pressure and σ'_{v0} was the initial vertical effective stress at the corresponding location, calculated using Plaxis 2D analysis which was detailed in Chapters 4, Section 4.3.1.

In previous studies, conventional $p-y$ curves developed for the lateral response of piles in non-liquefied soils (e.g. soft clay and sand) have been modified for use in liquefaction problems. One approach has been to apply a degradation factor to conventional $p-y$ curves

for non-liquefied sand to account for the reduction in soil resistance due to a reduction in effective stress caused by the generation of positive excess pore pressures. Dynamic centrifuge tests by Liu & Dobry (1995) found this degradation parameter reduced linearly from a maximum of 1 when $r_u(t) = 0$ to a minimum of 0 when $r_u(t) = 1$. An alternative approach has been to use $p - y$ curves for soft clays, but replacing the undrained shear strength of the clay by the residual strength of the liquefied soil (Goh & O'Rourke 1999). In the method presented in this chapter, a reduction factor similar to the one used by Liu & Dobry (1995) was developed.

The excess pore pressure ratio was used to calculate a pore pressure reduction factor, $R(t)$, to account for changes in stiffness due to a reduction in effective stress caused by the generation of positive excess pore pressure:

$$R(t) = 1 - [1 - R_0] r_u(t) \tag{7.12}$$

where R_0 is the pore pressure reduction constant, which is equal to the pore pressure reduction factor, $R(t)$, when the excess pore pressure ratio, $r_u(t)$, is equal to one. Equation 7.12 shows that the pore pressure reduction factor was set to change linearly with excess pore pressure ratio. When $r_u(t) = 0$, $R(t) = 1$. When $r_u(t) = 1$, $R(t) = R_0$. The pore pressure reduction constant, R_0, was not set to zero, as adopted by Liu & Dobry (1995). This allowed R_0 to be set to reflect the observations from the centrifuge tests. The pore pressure reduction factor was subsequently applied to dynamic stiffness values determined from empirical methods developed for non-liquefied sands, which are detailed in the following paragraphs.

Shear modulus

Oztoprak & Bolton (2013) proposed that the small-strain shear modulus, G_{max}, can be estimated using:

$$G_{max} = \frac{5760 p_a}{(1+e)^3} \left(\frac{p'_0}{p_a} \right)^{0.49} \tag{7.13}$$

where e is the void ratio, p_a is atmospheric pressure in kPa, and p'_0 is the initial mean effective confining pressure in kPa. The void ratio was calculated from the mass of sand in the model container and the volume it occupied before shaking commenced. The initial mean effective confining pressure was calculated using the initial vertical effective stresses obtained from the Plaxis 2D analysis, and assuming $K_0 = 0.5$:

$$p'_0 = \sigma'_{v0} \left(\frac{1 + 2K_0}{3} \right) \tag{7.14}$$

The degradation of stiffness with dynamic shear strain was calculated using the hyperbolic curves and equations proposed by Ishibashi & Zhang (1993) for dry sand:

$$\frac{G}{G_{max}} = K(A_\gamma)(p'_0)^{m(A_\gamma)-m_0} \tag{7.15}$$

$$K(A_\gamma) = 0.5\left[1+tanh\left\{ln\left(\frac{0.000102}{A_\gamma}\right)^{0.492}\right\}\right] \tag{7.16}$$

$$m(A_\gamma) - m_0 = 0.272\left[1-tanh\left\{ln\left(\frac{0.000556}{A_\gamma}\right)^{0.4}\right\}\right] \tag{7.17}$$

where p'_0 is the mean effective confining pressure in kPa and A_γ is the peak cyclic shear strain amplitude, which is dimensionless. The value of p'_0 was used, rather than $p'(t)$, as the equations proposed by Ishibashi & Zhang (1993) were formulated to account for the reduction in stiffness with strain, not stress. Figure 7.3 shows the shear modulus degradation with increasing cyclic shear strain amplitude for three different values of mean effective confining pressure, p'_0, using the hyperbolic curves and equations proposed by Ishibashi & Zhang (1993), detailed in Equations 7.15 to 7.17.

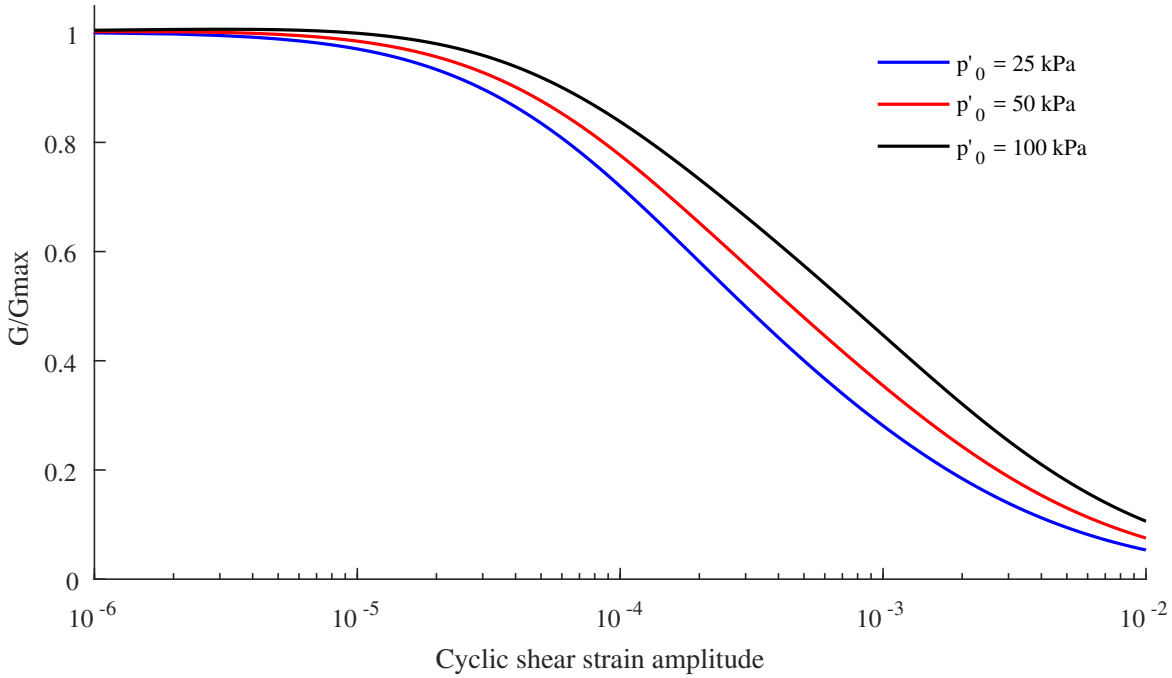

Fig. 7.3 Shear modulus degradation with increasing cyclic shear strain amplitude, using the hyperbolic curves and equations proposed by Ishibashi & Zhang (1993), detailed in Equations 7.15 to 7.17. Curves shown for three different values of mean effective confining pressure, p'_0.

The reduction in stiffness with stress caused by the generation of positive excess pore pressures was accounted for by multiplication by the pore pressure reduction factor, $R(t)$, detailed in Equation 7.12. A time history for stiffness was obtained which accounted for changes due to both dynamic strain and positive excess pore pressure generation:

$$G(t) = G_{max}R(t)K(A_\gamma(t))(p_0')^{m(A_\gamma(t))-m_0} \tag{7.18}$$

The damping ratio, $\zeta(t)$, was assumed to follow the equation proposed by Ishibashi & Zhang (1993):

$$\zeta(t) = 0.333\left\{0.586\left(\frac{G(t)}{G_{max}}\right)^2 - 1.547\left(\frac{G(t)}{G_{max}}\right) + 1\right\} \tag{7.19}$$

Spring stiffness values

Once soil stiffness values had been obtained, they could be used to obtain values for the stiffness of the springs in Figure 7.2. Simple expressions for the static stiffness of rigid embedded strip foundations in a homogeneous stratum over bedrock were proposed by Jakub & Roesset (1977). They were obtained following an extensive parametric study investigating the dynamic response of structures in layered soils, and assumed that the soil could be modelled as a homogenous, isotropic, and linearly visco-elastic stratum and that the embedded foundation was rigid, massless, and with perfect contact between the sidewalls and the soil. The equations for static stiffness of rigid embedded strip foundations "welded" into a homogeneous stratum over bedrock proposed by Jakub & Roesset (1977) were utilised in the formulation presented in this chapter:

$$k_{xs}(t) = \frac{2.1G(t)}{2-\nu}\left(1+\frac{B}{H}\right)\left(1+\frac{2D}{3B}\right)\left(1+\frac{4D}{H}\right) \tag{7.20}$$

$$k_{\theta b}(t) = \frac{\pi G(t)B^2}{8(1-\nu)}\left(1+\frac{B}{10H}\right)\left(1+\frac{2D}{B}\right)\left(1+\frac{2D}{3H}\right) \tag{7.21}$$

where B and D are the foundation width and depth respectively, ν is Poisson's ratio, and H is the depth of the soil stratum overlying bedrock. Poisson's ratio of 0.3 was used to reflect the partially drained conditions observed in the centrifuge tests presented in Chapters 4 and 5.

Due to the range of parameters used in their parametric study, Jakub & Roesset (1977) state that these equations are valid for the conditions where $H/B \geq 1$ and $D/B \leq 1/3$. The ratio of D/B for the narrow basements in Chapter 4 is equal to 0.625 and therefore does not comply with these conditions. However, it is assumed that for the purpose of the work

presented in this chapter that the equations proposed by Jakub & Roesset (1977) were satisfactory for the narrow basements.

Damping constant values

The coupling of the horizontal translation and rotation of the embedded foundation being modelled resulted in a non-diagonal damping matrix in Equation 7.1. The system therefore has non-classical damping. The damping constant of the dashpots in Figure 7.2 were calculated as a function of the damping ratio, and assumed stiffness proportional damping:

$$c(t) = \frac{2k(t)\zeta(t)}{\omega_n(t)} = 2\zeta(t)\sqrt{mk(t)} \tag{7.22}$$

Table 7.1 and the flow diagram in Figure 7.4 summarise the procedure required to calculate the spring and dashpot parameters shown in Figure 7.2. This was required for each degree of freedom.

Table 7.1 Dynamic DRILS model procedure for each degree of freedom

Step	Calculation process	Data required	Reference for method
1.	Shear strain time history $\gamma(t)$	Soil acceleration time histories $a(t)$ Depth of accelerometers	Elgamal et al. (1996)
2.	Shear strain amplitude time history $A_\gamma(t)$	Shear strain time histories $\gamma(t)$	
3.	Excess pore pressure ratio time history $r_u(t)$	Pore pressure time histories $u(t)$ Corresponding initial vertical effective stress σ'_{v0}	
4.	Pore pressure reduction factor $R(t)$	Excess pore pressure ratio time history $r_u(t)$ Maximum reduction factor R_0	
5.	Small-strain shear modulus G_{max}	Initial vertical effective stress σ'_{v0} Lateral earth pressure coefficient at rest K_0 Void ratio e	Oztoprak & Bolton (2013)
6.	Dynamic shear modulus time history $G(t)$	Shear strain amplitude time history $A_\gamma(t)$ Small-strain shear modulus G_{max} Initial vertical effective stress σ'_{v0} Lateral earth pressure coefficient at rest K_0 Pore pressure reduction factor $R(t)$	Ishibashi & Zhang (1993)
7.	Damping ratio time history $\zeta(t)$	Dynamic shear modulus time history $G(t)$ Small-strain shear modulus G_{max}	Ishibashi & Zhang (1993)
8.	Soil spring stiffness time history $k(t)$	Dynamic shear modulus time history $G(t)$ Basement depth D Basement width B Basement length L Soil layer depth H Poisson's ratio ν	Jakub & Roesset (1977)
9.	Soil dashpot damping coefficient time history $c(t)$	Damping ratio time history $\zeta(t)$ Mass of structure m Soil spring stiffness time history $k(t)$	

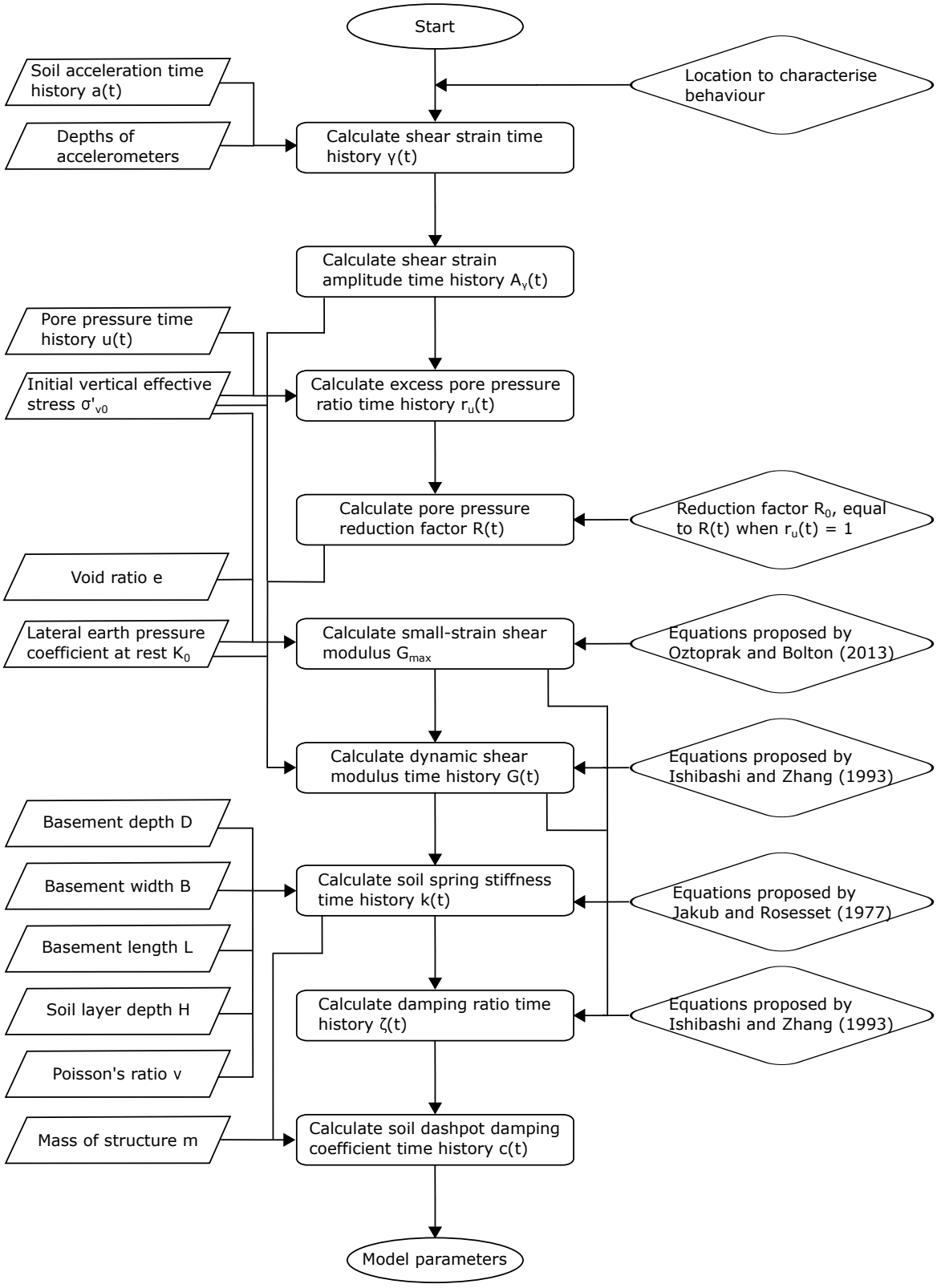

Fig. 7.4 Flow diagram of procedure used in the dynamic DRILS model for each degree of freedom.

Method of solution

The preceding sections show that the stiffness and damping terms vary with time during shaking. Consequently, numerical integration was required to solve the equation of motion. Use of the central difference method allowed the non linearities in stiffness and damping to appear explicitly.

A number of conditions must be considered when using the central difference method. For the conditions listed below, Δt is the time step in the numerical scheme and T_n is the natural period of the system being modelled.

- Stability. This is achieved when:
$$\frac{\Delta t}{T_n} < \frac{1}{\pi} \tag{7.23}$$
where the highest mode of vibration must be considered, even if its contribution to the overall response is minimal. During an earthquake, the stiffness of liquefiable soil decreases due to both the increase in shear strain amplitude and the generation of positive excess pore pressures which reduce the vertical effective stress. A reduction in stiffness increases the natural period of the system, T_n. Therefore the most critical point for stability is at the start of any simulation, and improves as earthquake shaking progresses.

- Computational error. Period elongation is worsened as $\Delta t/T_n$ increases, and is minimised if:
$$\frac{\Delta t}{T_n} < 0.05 \tag{7.24}$$

- Accuracy. For highly irregular earthquake ground acceleration, Chopra (2014) stated that typically:
$$\Delta t < 0.02 \text{ sec} \tag{7.25}$$

Consequently, the time step required when using the central difference method is small. The smaller the time step, the greater the computation time.

Discrete instrumentation within the centrifuge model was sampled at a rate of 6000 Hz which equates to a time step of 0.000167 seconds at model scale. This equates to 100 Hz and 0.01 seconds at prototype scale. If the time step required for the central difference method was smaller than the time step between centrifuge data sampling points, the centrifuge data was re-sampled. The low time step between centrifuge data sampling points compared to the frequency of base shaking means that interpolation was unlikely to add erroneous features to the data, however, it was a possibility that had to be considered.

7.2.4 Determination of user defined parameters

Initial, trial runs of the DRILS model were used to determine the values of a number of user defined parameters.

Pore pressure reduction constant

As previously discussed in Section 7.2.3, the reduction in stiffness with stress and dynamic shear strain were calculated separately, and then multiplied to determine the time history for stiffness given in Equation 7.18. The pore pressure reduction factor, $R(t)$, accounted for the reduction in stiffness with stress caused by generation of positive excess pore pressures and was dependent on the pore pressure reduction constant, R_0, as detailed in Equation 7.12. The smaller the pore pressure reduction factor, the greater the impact that the generation of positive excess pressures had on the soil stiffness. The value of R_0 was determined from the centrifuge test data. A value $R_0 = 0.25$ was found to best fit the data. A higher value resulted in an underestimation of accelerations, and a lower value resulted in an overestimate. This is shown in Figure 7.5, using Test FEH08 EQ3 as an example. This earthquake had a peak horizontal acceleration of 0.4 g and liquefied the entire soil layer (see Figures 5.2 and 5.3).

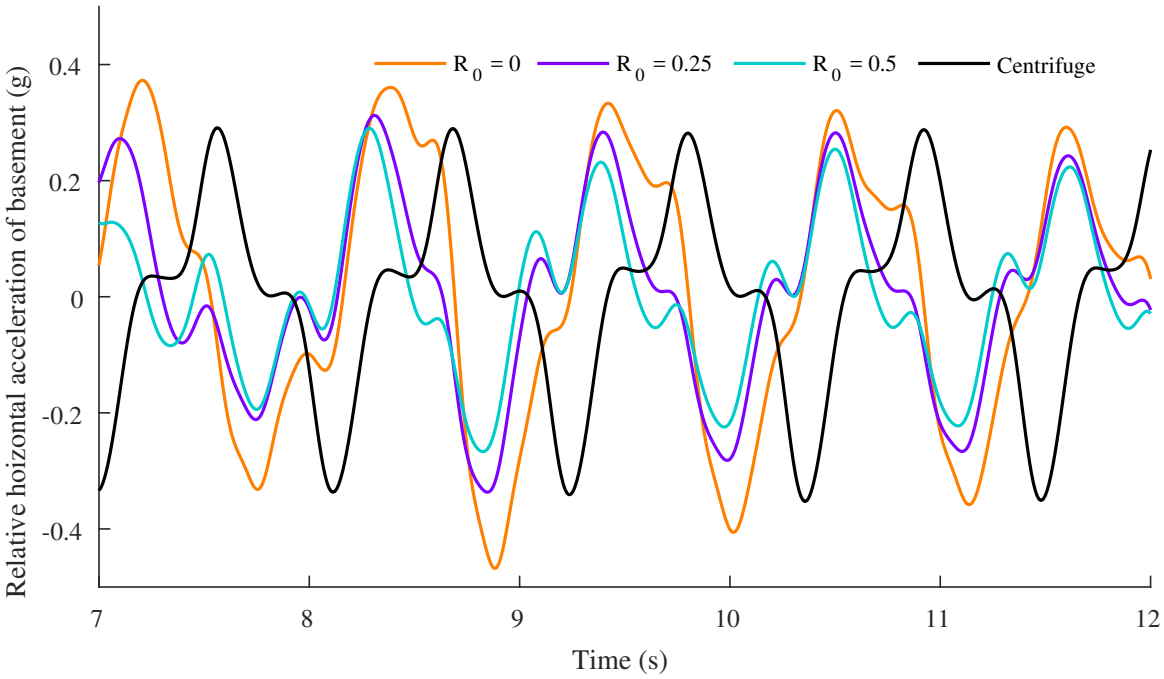

Fig. 7.5 Calculated relative horizontal acceleration of basement for different values of pore pressure reduction constant, R_0, for Test FEH08 EQ3 (shown in colour), compared to measured values in the centrifuge test (shown in black).

Taking centrifuge Test FEH08 EQ3 as an example, the amplitude of cyclic shear strains were of the order of 10^{-2} in the far-field adjacent to the basement. Using the hyperbolic curves and equations proposed by Ishibashi & Zhang (1993), and assuming $p'_0 = 15\ kPa$, the stiffness reduced by a factor of 0.04 due to dynamic shear strain. The value of $R_0 = 0.25$ suggests that the stiffness of the soil reduced by an additional factor of 0.25 due to positive excess pore pressure generation when liquefaction occurred. In the methodology detailed in this chapter, the two factors are multiplied to give an overall reduction in stiffness by a factor of 0.01. This is in reasonable agreement with the liquefaction induced reduction in stiffness obtained from dynamic centrifuge test data by Haigh (2002), whereby the calculated shear wave velocity decreased by an order of magnitude between the start of an earthquake and when liquefaction subsequently occurred. Soil shear stiffness is proportional to shear wave velocity squared, so reduced by two orders of magnitude (Haigh 2002).

Time step

The most critical requirement for the time step, Δt, in the numerical scheme was found to be the condition required for stability of the central difference method. Where possible, the time step in the numerical scheme was set to be equal to the time step of sampling the centrifuge data. This avoided the need to re-sample the centrifuge data. If stability was not achieved with this time step, the time step was halved, which required the centrifuge data to be re-sampled at double the original frequency.

7.2.5 Replication of centrifuge test results

The ability of the dynamic DRILS model to reproduce the dynamic behaviour observed in the centrifuge tests presented in Chapters 4 and 5 was tested. The centrifuge data from three base shaking events were used. The base shaking events differed in duration, peak acceleration, and frequency content. EQ1 was a low amplitude, sinusoidal input motion, consisting of 20 cycles with the same frequency as the fixed base natural frequency of the corresponding superstructure (either 1 Hz or 0.88 Hz). It had a peak acceleration of approximately 0.03 g. EQ2 had the same frequency content as the 1979 Imperial Valley earthquake, which was characterised by its long duration and high frequency content, and was scaled to have a peak acceleration equal to 0.1 g. EQ3 was a high amplitude, sinusoidal input motion with the same frequency as EQ1. EQ3 had a peak acceleration of approximately 0.4 g which resulted in liquefaction within the entire soil layer, as shown in the excess pore pressure time histories in Figures 5.2 and 5.3.

The acceleration and pore pressure time histories recorded in the centrifuge tests were input into the model, and the methodology detailed in the preceding sections, summarised in Table 7.1 and Figure 7.4, was followed. The output from the dynamic DRILS model was the dynamic displacement, velocity and acceleration for the two degrees of freedom being modelled - horizontal translation and rotation. This was compared to the measured and calculated movement of the basement of the structures in the centrifuge tests.

Relative horizontal acceleration

The most informative comparison was between relative horizontal acceleration of the basements. The sensitivity of the accelerometers and the frequency of sampling meant this was reliably measured in the centrifuge tests for the earthquakes of both small (EQ1 and EQ2) and large (EQ3) amplitude. Figure 7.6 shows the time histories for relative horizontal acceleration of the basement calculated using the dynamic DRILS model in black and the corresponding acceleration measured in the centrifuge tests in colour for the wide basements presented in Chapter 5. It is evident from this figure that there is general agreement between the horizontal accelerations calculated by the dynamic DRILS model and the centrifuge test data.

For the earthquakes shown in the nine sub-plots in Figure 7.6, EQ1 for FEH06 and FEH07 were the only cases where liquefaction did not occur at shallow depths in the soil adjacent to the basement. The dynamic DRILS model under-predicted the amplitude of relative horizontal acceleration for these two cases, shown in Figures 7.6(a,d). This implies that the stiffness of the soil adjacent to the basements was over-predicted by the dynamic DRILS model, which resulted in smaller displacement and therefore smaller acceleration. This could have manifested from an overestimation of the maximum shear modulus, G_{max}, calculated using the equations proposed by Oztoprak & Bolton (2013), or underestimating the rate of degradation of stiffness with dynamic shear strain using the equations proposed by Ishibashi & Zhang (1993), or an overestimation of the spring stiffness values using the equations proposed by Jakub & Roesset (1977).

The amplitude of the relative horizontal accelerations measured in the centrifuge tests and calculated using the dynamic DRILS model are closer for the other seven sub-plots shown in Figure 7.6. These correspond to cases where base shaking was stronger and liquefaction occurred adjacent to the basements, as shown in the excess pore pressure time histories in Figures 5.2(a,b,c). The amplitude of the calculated horizontal acceleration closely matches the corresponding measured values during mixed frequency and varying amplitude shaking in EQ2 for all three tests (Figures 7.6(b,e,h)). During EQ3, the model correctly replicates the reduction in horizontal acceleration of the basement during shaking as observed in the centrifuge test data shown in Figures 5.4(d,e,f). However, the magnitude is not correctly

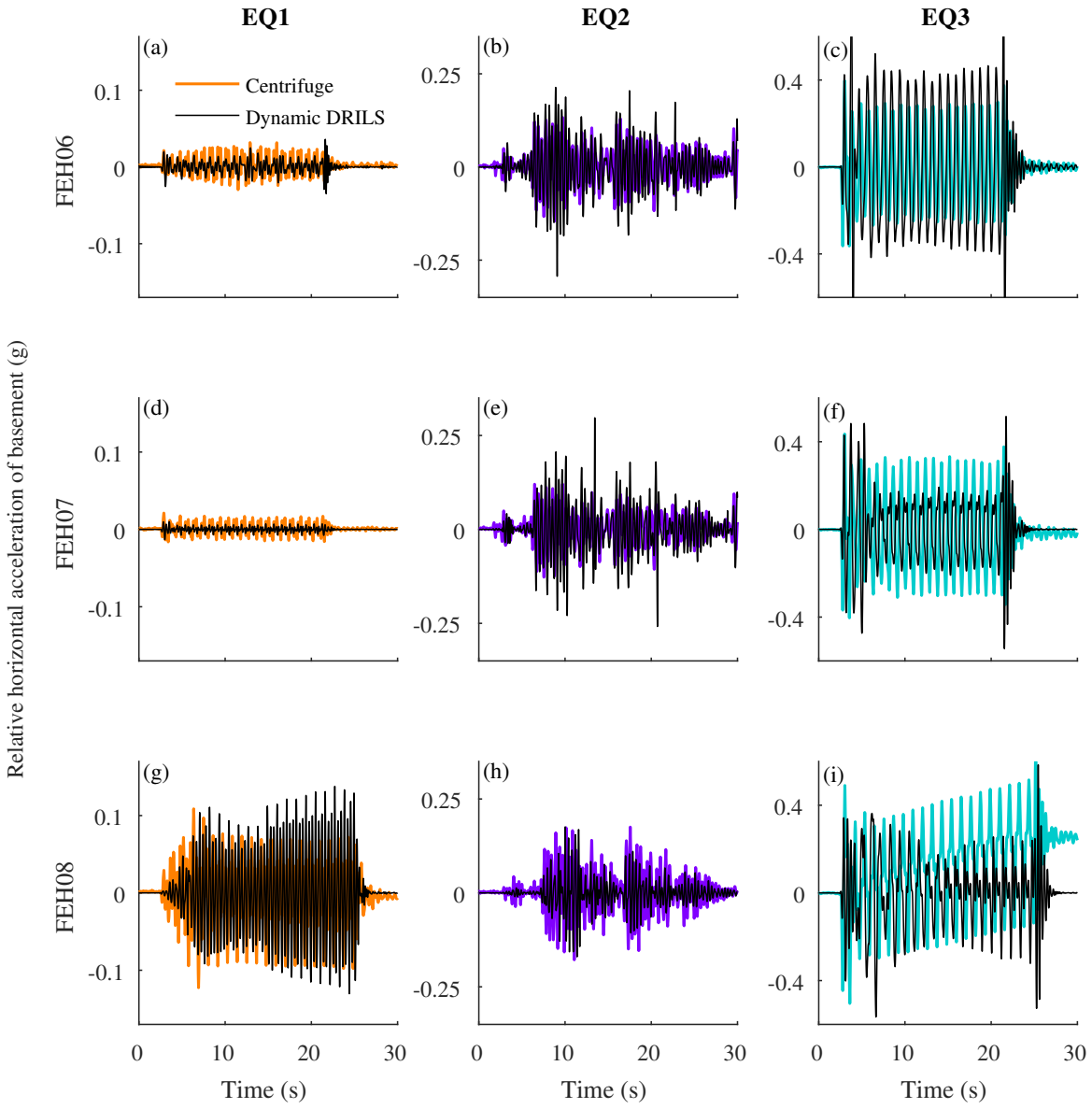

Fig. 7.6 Comparison of time histories of the relative horizontal acceleration of the wide basements. Dynamic DRILS model shown black. Centrifuge test data in colour: EQ1 in orange, EQ2 in purple, and EQ3 in turquoise.

matched in all tests as an over-prediction occurs for Test FEH06 whilst under-prediction occurs for FEH07. The reasonable agreement in these figures means that it is possible to study how the spring stiffnesses in the dynamic DRILS model changed during the simulation and correlate it to the behaviour observed in the centrifuge tests.

Soil spring stiffness

Figure 7.7 shows time histories of horizontal and rotation spring stiffness, per unit length of the basement, for earthquakes EQ1, EQ2 and EQ3 for Test FEH07. During each of these three earthquakes there are three distinct phases in this figure:

1. When time on the x-axis is less than 2 seconds, the stiffnesses correspond to the initial spring stiffness values with no reduction due to either dynamic shear strain or positive excess pore pressure generation.

2. During shaking, when the base shaking horizontal acceleration shown in sub-plot (c) is non-zero, the spring stiffness values are degdraded due to dynamic shear strain, and, where applicable, positive excess pore pressure generation.

3. After base shaking ceases, and the base shaking horizontal acceleration in sub-plot (c) returns to being zero, there is a period of time before excess pore pressures are dissipated from the soil surrounding the basements. Consequently, stiffness is degraded by positive excess pore pressure generation, but less by the dynamic shear strain.

There are a number of interesting features in Figure 7.7. It should be noted that the interpretation of these figures should be done with care, owing to the number of empirical correlations and assumptions used in the dynamic DRILS model, which have been discussed in the preceding sections of this chapter.

During EQ1 close to zero excess pore pressures were generated below and beside the basement, therefore the reduction in stiffness during shaking was only due to dynamic shear strain. The horizontal and rotational spring stiffness reduced to approximately 30 % and 60 % of their respective static values during shaking. This difference in reduction factor is because the dynamic shear strains were greater in the soil adjacent to the basement than below it.

The rotational stiffness during EQ3 was lowest during the initial cycles of shaking, before increasing slightly for the remainder of shaking. The plot of excess pore pressure time history in Figure 5.3(b) shows that excess pore pressure increased during shaking whilst Figures 5.4(h,k) show that horizontal accelerations were greatest during the initial cycles of shaking before being attenuated by the reduction in vertical effective stress due to the generation of positive excess pore pressure. This implies that the rotational spring stiffness is more strongly influenced by dynamic shear strain than positive excess pore pressure generation during large amplitude shaking that resulted in liquefaction below a structure with a basement.

When shaking ceased in EQ3, at approximately 23 seconds in Figure 7.7, the horizontal and rotation spring stiffness values rapidly increased. This increase was due to the sudden

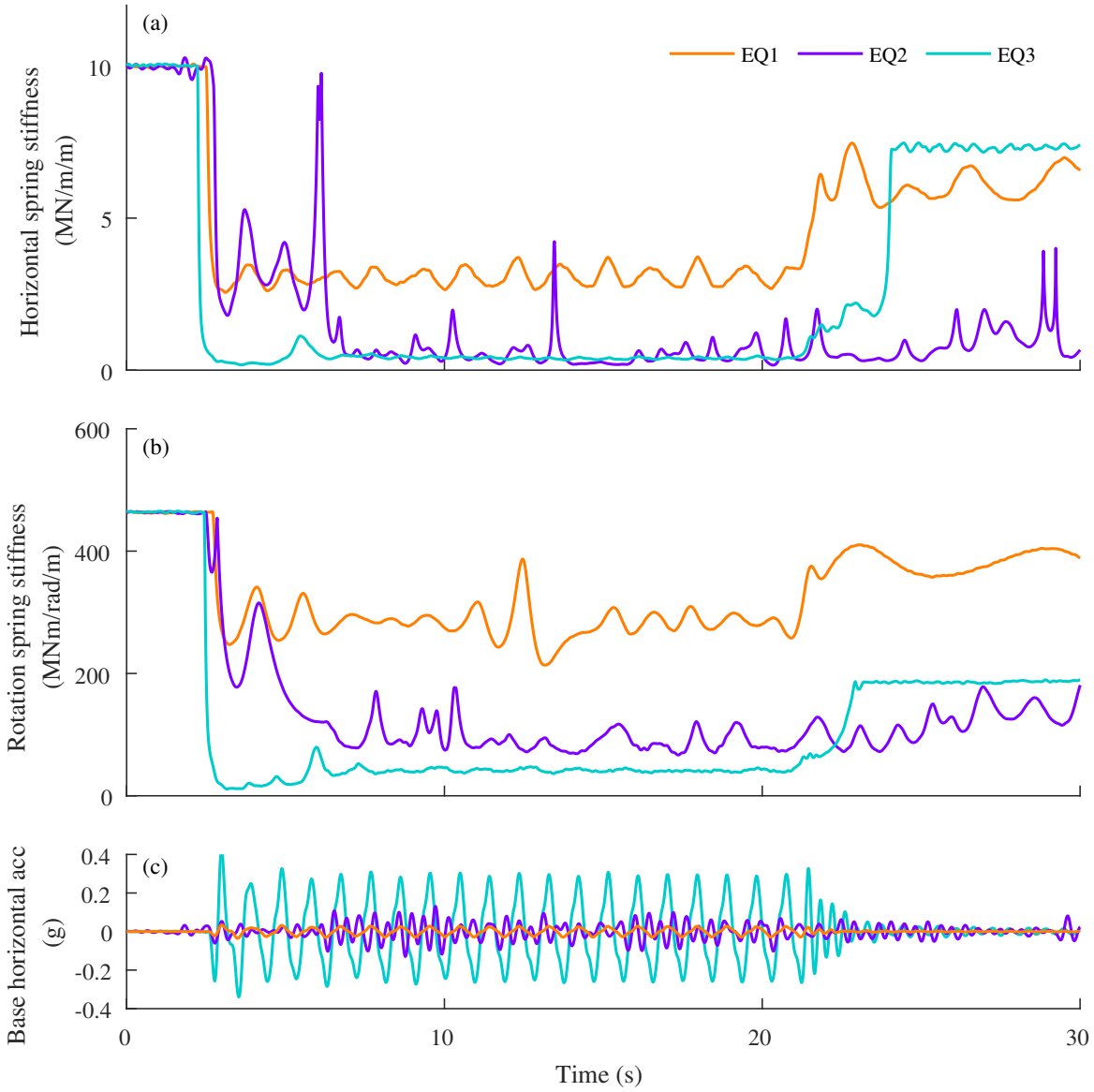

Fig. 7.7 Spring stiffness in the dynamic DRILS model during replication of centrifuge Test FEH07, shown in Figures 7.6(d,e,f). EQ1 in orange, EQ2 in purple, and EQ3 in turquoise.

reduction in dynamic shear strains, whilst the excess pore pressures remain elevated because of the time taken for dissipation to occur. The difference in steady state stiffness at 0 seconds and 25 seconds corresponds to the influence of reduction in vertical effective stress due to positive excess pore pressure generation. The difference in steady state stiffness at 20 seconds and 25 seconds corresponds to the influence of the amplitude of dynamic shear strains.

Horizontal displacement and rotation

The measured and calculated relative horizontal displacement and rotation can also be compared. This is shown in Figure 7.8 for EQ3 only. The smaller amplitude earthquakes, EQ1 and EQ2, were not included due to the difficulties in obtaining accurate horizontal displacement time histories from the centrifuge data. The limited resolution of the images taken using the high-speed camera meant that it was not possible to accurately obtain this from the PIV data, and the small amplitude of acceleration made it difficult to obtain accurate displacements by double integration of the acceleration time histories.

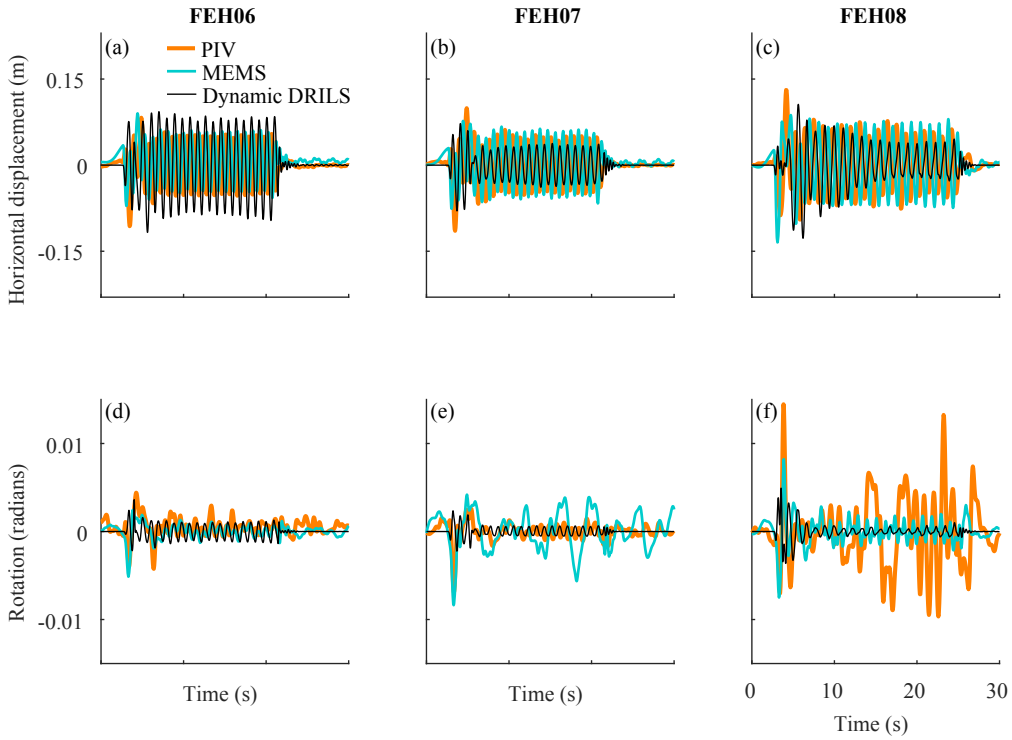

Fig. 7.8 Comparison of time histories of the relative horizontal displacement and rotation of the wide basements during EQ3. Dynamic DRILS model in black. Centrifuge test data in colour: from PIV in orange and from MEMS in turquoise.

As anticipated, the relationship between calculated and measured horizontal displacement in Figure 7.8 was the same as for relative horizontal acceleration shown in Figure 7.6 - overestimation for Test FEH06 and underestimation for Test FEH07. The dynamic component of the rotation of the structures was small. The y-axes for the dynamic rotation plots in Figures 7.8(d,e,f) are $\pm$ 0.01 radians, which is equal to $\pm$ 0.6 $^{\circ}$. The amplitude of dynamic rotation was in good agreement for FEH06, where the rotations were in the order of $\pm$ 0.1 $^{\circ}$. The calculated and measured rotation for FEH07 and FEH08 are of the same

order of magnitude. However, it is difficult to determine whether the differences shown in Figures 7.8(e,f) are a result of errors in the dynamic DRILS model or inaccuracies in the measurements from the centrifuge tests.

Structures with basements with rigid extenders

The dynamic DRILS model detailed in the preceding chapters was developed for basements with a rectangular cross section. It is proposed that it can also be used for the structures with narrow basements with rigid extenders which were presented in Chapter 4, Section 4.4.

The projected area of the rigid extenders must be included in the soil stiffness and dynamic components of the DRILS model to reflect the volume of soil affected by the shaking of the basement. The extenders must therefore be included in the basement dimensions used to calculated the soil spring stiffness values using the expressions presented by Jakub & Roesset (1977), detailed in Equations 7.20 and 7.21.

Figure 7.9 shows the time histories for relative horizontal acceleration of the basements calculated using the dynamic DRILS model in black and the corresponding acceleration measured in the centrifuge tests in colour for the narrow basements with rigid extenders presented in Chapter 4, Section 4.4. Figure 7.9 shows that the dynamic DRILS model under-predicted the amplitude of the horizontal acceleration of the structures during EQ1, and to a greater extent than for the wide basements shown in Figure 7.6. For EQ2 and EQ3, where large positive excess pore pressures were generated (Figures 4.11 and 4.12), there is good agreement between the calculated and measured relative horizontal accelerations shown in Figure 7.9, with the attenuation of horizontal acceleration of the basement correctly captured during EQ3.

It is concluded that the dynamic DRILS model can replicate the dynamic response observed in the centrifuge tests. However, its application is limited as it does not capture the most problematic behaviour observed in the centrifuge tests - accumulation of displacement and rotation.

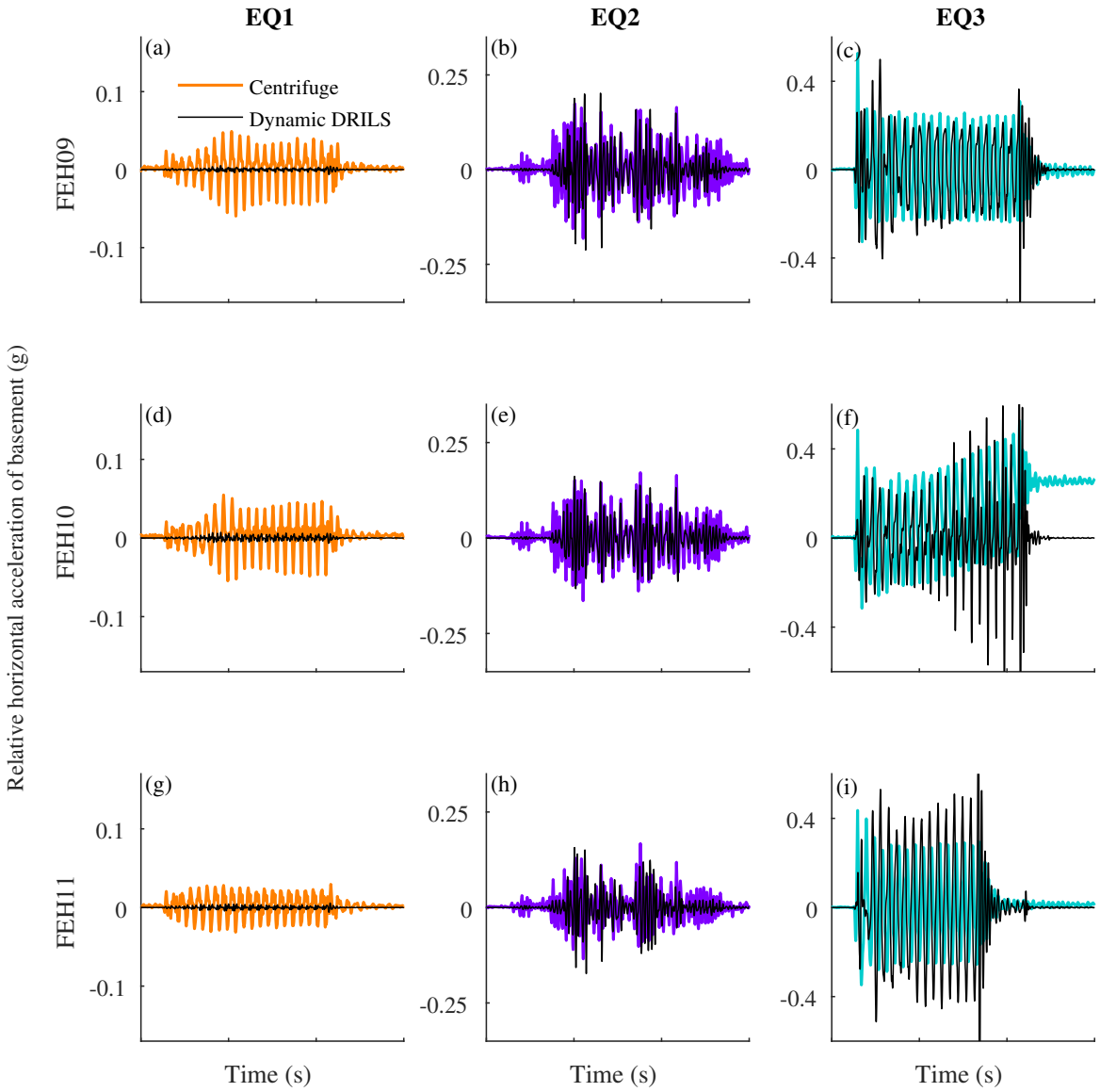

Fig. 7.9 Comparison of time histories of the relative horizontal acceleration of the narrow basements with rigid extenders. Dynamic DRILS model in black. Centrifuge test data in colour: EQ1 in orange, EQ2 in purple, and EQ3 in turquoise.

7.3 Mechanical model to capture the accumulation of rotation and displacement

In Chapters 4 and 5, results from the dynamic centrifuge tests showed that, when liquefaction occurred, accumulation of rotation and displacement were more problematic for structures with basements than the magnitude of accelerations transmitted to the superstructure. For the mechanical model to be of most use it must therefore be able to reliably estimate the accumulation of rotation and displacement. In this section, the methodology detailed in Section 7.2 will be modified to include the accumulation of rotation and displacement of the structures. Henceforth, the model will be referred to as the DRILS - "Displacement and Rotation in Liquefiable Soil" - model, without the prefix "dynamic".

7.3.1 Degrees of freedom

As previously discussed, the dynamic centrifuge tests replicated plane strain conditions. Therefore, the structures had three degrees of freedom - translation in the horizontal and vertical direction and rotation about an axis perpendicular to these aforementioned directions. To be able to replicate the accumulation of rotation and displacement observed in the centrifuge test series, all three degrees of freedom were required to be included in the DRILS model.

7.3.2 Incorporating accumulation of rotation and displacement in the mechanical model

The following sections detail how the DRILS model was modified to include the accumulation of rotation, and both horizontal and vertical displacement.

Horizontal displacement and rotation

A slider was added in series with each of the spring-dashpot elements to allow the model to accumulate rotation and horizontal displacement, as shown in Figure 7.10. It was important to now incorporate the total resultant forces and moment imposed by the structure on the soil, not just the dynamic components that were considered in Section 7.2. The force in the horizontal slider was therefore always equal to the sum of the forces in the corresponding spring and dashpot, plus the static component of the horizontal force. Displacement of the slider was added to the displacement of the spring-dashpot element to determine the total displacement. Progression of the slider occurred when the horizontal velocity and force

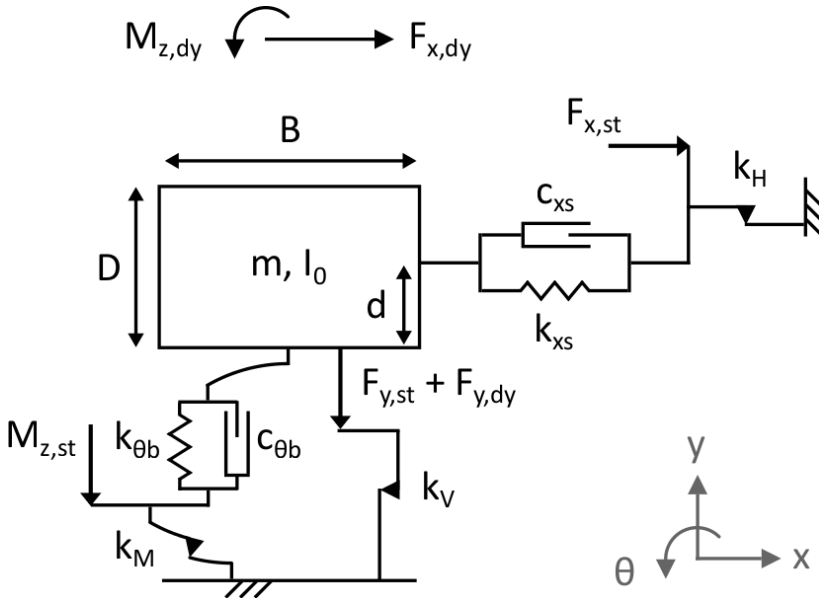

Fig. 7.10 Schematic of mechanical model of a rigid basement embedded in a soil layer, with sliders included to capture accumulation of displacement and rotation.

were acting in the same direction and the force acting on the slider was greater than a given threshold, as shown in Figure 7.11(a). This is akin to friction models that model both viscous and Coulomb friction. The same methodology was used for the moment in, and progression of, the rotation slider, which is shown in Figure 7.11(b).

Vertical displacement

A third slider was included to capture the accumulation of vertical displacement of the structures with basements. The force in this slider was equal to the sum of the static and dynamic component of the vertical force imposed by the structures on the surrounding soil. Progression of this slider occurred when the vertical force exceeded a given threshold, as shown in Figure 7.11(c).

Sliders

The slider constants were determined from the centrifuge test results from Chapters 4 and 5, and will be discussed in more detail in the following sections. The horizontal slider constant, k_H, was set to be the same for horizontal translation of the basement to the right or left. The rotation slider constant, k_M, was set to be the same for clockwise and anticlockwise rotation of the basement. In the vertical direction, a different slider constant was set for uplift, $k_{V,U}$,

and settlement, $k_{V,S}$. For a given exceedence of the threshold value, a smaller slider constant results in a larger accumulation.

The threshold values of the sliders, Q_H, Q_M, and Q_V shown in Figure 7.11, were the co-seismic resistance provided by the soil surrounding the basements to horizontal translation, rotation and settlement respectively. They were calculated using established soil mechanics principles, which will be discussed in Section 7.3.3. The threshold force for uplift was set to zero. This was considered to be a reasonable assumption because, for the structures with basements being considered in this thesis, liquefaction must occur for the resultant vertical force to become upward. In the event of liquefaction, the shear resistance of the soil reduces significantly so the shear resistance along the soil-structure interface can be assumed to be negligible (Koseki et al. 1997).

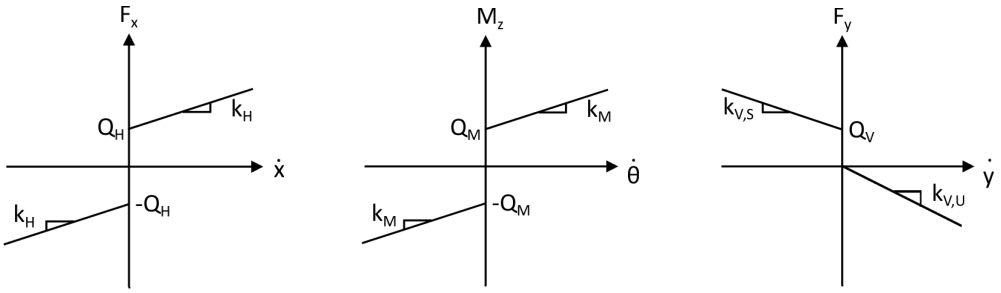

(a) (b) (c)

Fig. 7.11 Schematic of slider properties, showing the force-velocity relationship. (a) Horizontal slider, (b) Rotation slider, (c) Vertical slider.

The horizontal slider shown in Figure 7.11(a) has the following relationship between force and velocity:

$$\dot{x} = \begin{cases} 0 & \text{for } \mid F_x \mid \leq \mid Q_H \mid \\ \frac{[F_x - Q_H]\ sgn(\dot{x})}{k_H} & \text{for } \mid F_x \mid > \mid Q_H \mid \end{cases} \tag{7.26}$$

The distance travelled by the slider, δx, during a small increment of time, δt, can be approximated:

$$\delta x = \begin{cases} 0 & \text{for } \mid F_x \mid \leq \mid Q_H \mid \\ \frac{\delta t[F_x - Q_H]\ sgn(\dot{x})}{k_H} & \text{for } \mid F_x \mid > \mid Q_H \mid \end{cases} \tag{7.27}$$

The same approach was used for the rotation and vertical sliders.

7.3.3 Methodology to calculate seismic resistance of soil

It is widely known that during seismic loading, the resistance provided by soil can reduce whilst the loading on it can increase. A number of studies have been conducted to investigate

the impact of these two concurrent effects on the seismic performance of geotechnical structures.

For soils that do not experience a significant loss of strength during seismic loading, a pseudo-static approach is often used, whereby the inertia forces due to earthquake loading are represented by permanent horizontal and vertical loads related to the peak ground acceleration. This approach has been used to obtain analytical solutions for the seismic bearing capacity of shallow foundations using, for example, limit equilibrium analysis (Budhu & Al-Karni 1993, Richards Jr et al. 1993), upper-bound kinematic analysis (Paolucci & Pecker 1997) and lower-bound analysis by the method of stress characteristics (Kumar & Rao 2002). The most common method used to determine seismically induced lateral earth pressures is also a pseudo-static approach. It is known as the Mononobe-Okabe method and is based on the work of Okabe (1924) and Mononobe & Matsuo (1929).

For the centrifuge test series presented in Chapters 4 and 5, significant strength loss occurred in the soil during seismic loading. A method was therefore developed whereby the data obtained from the accelerometer and pore pressure transducers in the soil layer were used to estimate the co-seismic resistance provided by the soil surrounding the basements to simultaneous translation in the horizontal and vertical direction, and rotation about an axis perpendicular to these aforementioned directions. This will be detailed in the following sections.

Horizontal resistance

It was assumed that the total lateral pressure distribution in the soil to the side of the basement is always triangular. This assumption required the excess pore pressure ratio, $r_u(t)$, to be the same for the whole depth of the basement. Given the shallow depth of the basements, this is considered a reasonable approximation. In reality, the earth pressures will be mobilised based on the soil strains, particularly on the passive side. In addition $r_u(t)$ may vary with depth.

Pore pressure measurements in the soil layer were used to calculate the hydrostatic and excess pore water pressure generated, u_h and $u_{ex}(t)$ respectively, and subsequently the instantaneous vertical effective stress at the corresponding location, $\sigma'_v(t)$:

$$\sigma'_v(t) = \sigma'_{v0} - u_{ex}(t) \tag{7.28}$$

where σ'_{v0} is the initial vertical effective stress obtained from Plaxis 2D analysis detailed in Section 4.3.1. The total lateral pressure acting against the basement, $p(t)$, can be calculated:

$$p(t) = u_h + u_{ex}(t) + K_p \sigma'_v(t) \tag{7.29}$$

where K_p is the passive earth pressure coefficient and can be calculated using:

$$K_p = \frac{1 + sin\phi_{crit}}{1 - sin\phi_{crit}} \tag{7.30}$$

when ϕ_{crit} is the critical state friction angle of the soil adjacent to the basement. The total lateral force acting to resist the horizontal translation of the basement, $Q_h(t)$, can then be calculated:

$$Q_h(t) = 0.5 p(t) DL \tag{7.31}$$

where D and L are the depth and length of the basement respectively.

A similar methodology was used by Dewoolkar et al. (1999) to calculate the effect of liquefaction on the post-shaking thrust acting on a retaining wall, and was found to be in good agreement with their dynamic centrifuge test data. In contrast to the approach used in this chapter, the methodology of Dewoolkar et al. (1999) allowed the excess pore pressure ratio profile with depth to be bi-linear. This allowed liquefaction to occur only for a limited depth of the retaining wall, which in total was 10 m deep. This was not deemed necessary in the DRILS model presented in this chapter given the shallow depth of the basements. However, it could be implemented in this methodology if deeper basements were investigated in the future.

The contribution of active resistance adjacent to the basement was not included. This decision was made in light of observations in the centrifuge tests, where lateral extension of the soil to the side of the basement caused localised piping, as shown in Figure 4.22. This shows that contact was lost between the basement and soil adjacent to it, therefore potential resistance provided by this region of soil will not have been transferred to the structure. For cases where contact was not lost, omission of active resistance provided by the soil will result in a conservative estimate of soil resistance.

The Mononobe-Okabe method was not applied. The earth pressures calculated using the Mononobe-Okabe method are due to inertia of a rigid block of soil. In contrast, the soil adjacent to the basements in the centrifuge tests presented in this thesis did not behave as a rigid block. This is evident in the soil displacement vectors shown in Figures 5.11 and 5.13. In addition, generation of positive excess pore pressures significantly reduced the lateral earth pressures adjacent to the basements. Also, recent research using highly

instrumented dynamic centrifuge model testing has shown that co-seismic horizontal stresses can be calculated using conventional static earth pressure coefficients, if variations in vertical stress during shaking are accounted for, without needing to use dynamic earth pressure coefficients (Madabhushi 2018).

Vertical resistance

A number of methodologies exist to calculate the static vertical bearing capacity, q_f, of a shallow foundation. Eurocode 7 provides the following method to calculate the bearing resistance of cohesionless soils in drained conditions (CEN 2014):

$$q_f = s_q N_q \sigma'_{v0} + s_\gamma N_\gamma \frac{\gamma'_s B}{2} \tag{7.32}$$

where B is the foundation width, σ'_{v0} is the vertical effective stress acting at the level of the foundation base, γ'_s is the effective weight of the soil beneath the foundation, N_q and N_γ are the bearing capacity factors to account for the resistance arising from surcharge and self-weight of the foundation soil respectively, and s_q and s_γ are shape correction factors. For a strip footing on weightless soil, the exact solution for N_q is:

$$N_q = tan^2\left(\frac{\pi}{4} + \frac{\phi}{2}\right) e^{\pi tan\phi} \tag{7.33}$$

An empirical relationship to estimate N_γ from N_q given in Eurocode 7 is:

$$N_\gamma = 2(N_q - 1)tan\phi \tag{7.34}$$

Shape correction factors for a rectangular footing of length L and breadth B are given in Eurocode 7 to be:

$$s_q = 1 + \frac{Bsin\phi}{L} \tag{7.35}$$

$$s_\gamma = 1 - \frac{0.3B}{L} \tag{7.36}$$

A simplified method to make this methodology applicable for soils which experience a significant strength loss during shaking due to positive excess pore pressure generation was proposed by Cascone & Bouckovalas (1998), whereby the critical state friction angle of the sand, ϕ_{crit}, was set to degrade to $\phi_{equivalent}$ with increasing excess pore pressure ratio, r_u:

$$\phi_{equivalent} = tan^{-1}([1 - r_u]tan\phi_{crit}) \tag{7.37}$$

However, this is not a logical approach to take since the critical state friction angle is a material parameter which governs the mechanical behaviour of soil, and it does not change when excess pore pressures are generated. An alternative approach was therefore taken in the DRILS model, and the critical state friction angle was kept constant.

The influence of positive excess pore pressures on the contributions to bearing capacity arising from the surcharge and self weight were considered separately. Firstly, when positive excess pore pressures were generated in the soil adjacent to the basement, the component due to surcharge reduced. The effective weight of this layer of soil decreased which consequently reduced the vertical effective stress acting at the level of the foundation base, σ'_{v0} in Equation 7.32. Secondly, the generation of positive excess pore pressures beneath the basement reduced the component due to self-weight because the self-weight of the foundation soil reduced, γ'_s in Equation 7.32. Both of these components decreased linearly with an increase in excess pore pressure ratio. These changes can be incorporated into the standard bearing capacity equation to calculate a degraded bearing resistance, $q_{ult}(t)$:

$$q_{ult}(t) = s_q N_q \sigma'_{v0}[1 - r_{u,s}(t)] + s_\gamma N_\gamma \frac{\gamma'_s[1 - r_{u,b}(t)]B}{2} \tag{7.38}$$

where $r_{u,s}(t)$ is the excess pore pressure ratio in the soil adjacent to the basement and $r_{u,b}(t)$ is the excess pore pressure ratio in the soil below the bottom of the basement. The degraded vertical capacity, taking into account positive excess pore pressure generation, $V_{ult}(t)$, is therefore given by:

$$V_{ult}(t) = q_{ult}(t)BL \tag{7.39}$$

where B and L are the width and length of the basement respectively.

Moment resistance

During shaking, the structures with basements were subject to simultaneous vertical, horizontal and moment loading. Soil resistance during concurrent V-H-M loading must therefore be considered.

A yield surface for the general case of V-H-M loading on drained soil was presented by Butterfield & Gottardi (1994):

$$\left(\frac{H}{t_h}\right)^2 + \left(\frac{M}{Bt_m}\right)^2 - \frac{2CMH}{Bt_h t_m} = \left[\frac{V}{V_{max}}(V_{max} - V)\right]^2 \tag{7.40}$$

where V, H and M are the vertical, horizontal and moment load that will cause a bearing capacity failure of a shallow footing of width B. The best-fit values of the parameters of the surface to model footings on the surface of sand were found to be $t_h = 0.52$, $t_m = 0.35$,

and $C = 0.22$ (Butterfield & Gottardi 1994). When using this surface, the direction of the moment and horizontal loading must be considered. A greater moment capacity is obtained if they are acting in opposition, compared to when they are acting in conjunction.

Data obtained from the centrifuge tests were used to calculate the resultant vertical, horizontal and moment load transmitted from the structures with basements to the surrounding soil. The resultant co-seismic vertical force, $F_y(t)$, transmitted from the structure to the surrounding soil was calculated by subtracting the uplift force provided by the basement during shaking from the combined weight of the superstructure and basement, as detailed in Sections 4.4.8 and 5.4. The resultant horizontal force, $F_x(t)$, was calculated by multiplying the horizontal acceleration by the mass of the structure. The resultant moment transmitted from the structure to the surrounding soil, $M(t)$, was calculated by summing the components due to the $P-\delta$ effect, and horizontal and rotational inertia of the components of the structure, as detailed in Section 5.4.

The surface presented by Butterfield & Gottardi (1994) was then used to calculate the maximum moment the soil below the basements could resist, $Q_M(t)$, for a given vertical load, $F_y(t)$, horizontal load, $F_x(t)$, and degraded central vertical load capacity of the footing, $V_{ult}(t)$:

$$\left(\frac{F_x(t)}{t_h}\right)^2 + \left(\frac{Q_M(t)}{Bt_m}\right)^2 - \frac{2CQ_M(t)F_x(t)}{Bt_ht_m} = \left[\frac{F_y(t)}{V_{ult}(t)}(V_{ult}(t) - F_y(t))\right]^2 \tag{7.41}$$

This is shown schematically in Figure 7.12(a). Likewise, it can be used to calculate the range of vertical loads that the soil can resist, $Q_{V,min}(t) < F_y(t) < Q_{V,max}(t)$, for a given moment load, $M_z(t)$, horizontal load, $F_x(t)$, and degraded central vertical load capacity of the footing, $V_{ult}(t)$:

$$\left(\frac{F_x(t)}{t_h}\right)^2 + \left(\frac{M_z(t)}{Bt_m}\right)^2 - \frac{2CM_z(t)F_x(t)}{Bt_ht_m} = \left[\frac{Q_V(t)}{V_{ult}(t)}(V_{ult}(t) - Q_V(t))\right]^2 \tag{7.42}$$

This is shown schematically in Figure 7.12(b). The upper limit, $Q_{V,max}(t)$, corresponds to the maximum vertical load that can be sustained for the given moment, $M_z(t)$, and horizontal, $F_x(t)$, loading to avoid bearing failure. The lower limit, $Q_{V,min}(t)$, corresponds to the minimum vertical load needed to avoid lift off. It is assumed that if the vertical loading is less than this value, settlement of the basement occurs due to ratcheting.

This failure surface assumes that lift-off occurs. In the dynamic centrifuge tests presented in Chapter 4 and 5 the liquefied soil was observed to move with the rotating basements (Figures 5.11(e,f) and 5.13(c)). Lift-off did not occur. It is possible that the failure surface proposed by Butterfield & Gottardi (1994) may underestimate the moment capacity of the soil

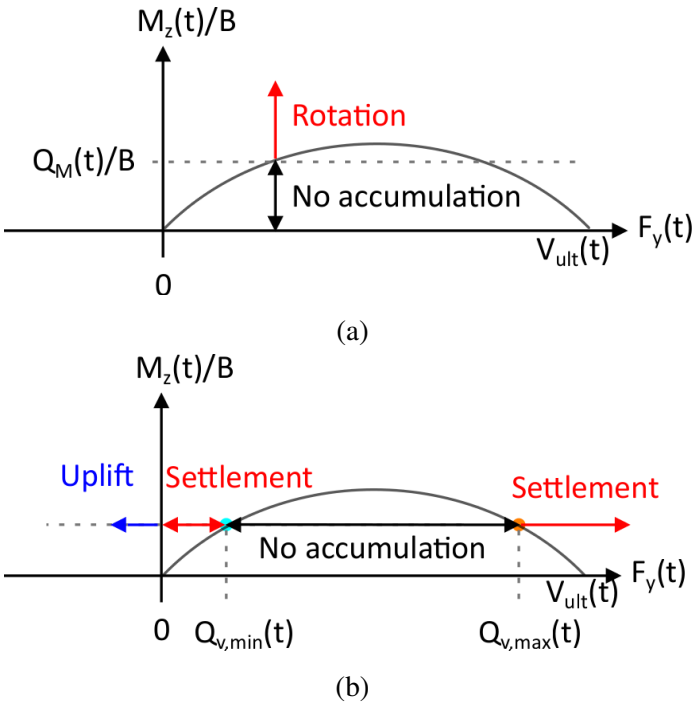

Fig. 7.12 Schematic of failure surface for simultaneous V-H-M loading, with type of structure failure shown by coloured text. (a) Calculating the maximum moment, $Q_M(t)$, for a given vertical load, $F_y(t)$, and degraded central vertical load capacity, $V_{ult}(t)$, (b) Calculating the range of vertical loads the soil can resist, $Q_{V,min}(t) < F_y(t) < Q_{V,max}(t)$, for a given moment load, $M_z(t)$, and degraded central vertical load capacity, $V_{ult}(t)$.

below the basements for a given loading combination. However, the excess pore pressures measured beneath the basements remained positive (Figures 5.12(a,b,c)), implying that net tension did not occur. Any underestimation is therefore likely to be small.

The total moment capacity of the soil surrounding the basements was found by adding together the moment capacity of the soil below the basements and the resistance to moment loading provided by the passive resistance in soil adjacent to the basement. The latter component was calculated using the triangular stress distribution detailed in Equation 7.29.

7.3.4 Shaking switch

In Chapter 5 it was observed that the rotation of the eccentrically loaded structure with a basement ceased at the end of shaking. This was despite the static component of the moment exerted on the soil being large and high excess pore pressures indicating that a near zero effective stress state still remained. Likewise, settlement of the heavier structures with basements in Tests FEH06 and FEH09 ceased at the end of shaking despite high excess pore pressures remaining. This is consistent with the current understanding of liquefaction

induced damage to structures - a near zero effective stress state is on its own insufficient, and must be accompanied by soil particle disturbance created by the earthquake motion (Madabhushi & Haigh 2012). Earthquake shaking is required to maintain the soil particles in a near suspended state, resulting in very low contact stresses between particles and an increase in permeability which allows rapid settlement to occur (Madabhushi & Haigh 2012).

Once shaking ceased, the horizontal and rotational velocity of the basement did not instantaneously become zero because of free vibration of the system. Using only the slider properties shown in Figure 7.11, the structures with basements would continue to accumulate displacement and rotation during this period, which is not in agreement with the observations in the centrifuge tests. A clause was therefore added to the methodology in the DRILS model to only allow accumulation of rotation and displacement to occur during shaking.

It has been observed in dynamic centrifuge tests that during earthquake induced liquefaction the settlement - time history for a structure with a shallow foundation follows the shape of the Arias intensity - time history for the earthquake motion (Dashti et al. 2010*a*, Adamidis & Madabhushi 2018*a*). As a result, Dashti et al. (2010*a*) proposed a new measure of intensity called the shaking intensity rate (SIR):

$$SIR = \frac{I_{a5-75}}{t_{5-75}} \tag{7.43}$$

where I_{a5-75} is the change in Arias intensity from 5 to 75 % of its total value (equal to 0.7 I_a) and t_{5-75} is the corresponding time duration. This measure of intensity is therefore equal to the average rate of Arias intensity build up during this time duration. Dashti et al. (2010*a*) argued that this measure captures the rate of soil particle disturbance, positive excess pore pressure generation and seismic demand on structures, and therefore should correlate with the initiation, rate and amount of liquefaction induced settlement.

Progression of the sliders used to model accumulation of displacement and rotation in the DRILS model was therefore restricted to when the amplitude of the time history of the rate of Arias intensity build up was greater than a specified threshold, $\dot{I}_{a,min}$.

7.3.5 Determination of user defined parameters

The mechanical model to capture the accumulation of rotation and displacement, detailed in the preceding sections, required a number of user defined parameters. Initial trial runs of the DRILS model, and sensible engineering judgement, were used to determine the values of these parameters.

Soil properties

To calculate the resistance provided by the soil surrounding the basement, the DRILS model required the void ratio and effective unit weight of the soil. For simplicity, these parameters were assumed to be equal to the values calculated using the mass of sand poured and the volume occupied post-swing up, before any earthquakes were fired.

Slider constants

To ensure that the methodology was applicable for basements of different lengths, the slider constants shown in Figures 7.10 and 7.11 were set per unit length of the basement. This is in accordance with the spring stiffness values proposed by Jakub & Roesset (1977), used in the dynamic analyses, which were specified per unit length of the basement (see Equations 7.20 and 7.21). It is logical that resistance is increased when the length of the basement increases, therefore, for example, less rotation is accumulated for a given moment loading. The slider constants therefore increased with increasing basement length.

The centrifuge tests where significant displacement and rotation were accumulated were used to determine the most suitable values for the four slider constants, k_H, k_M, $k_{V,U}$, and $k_{V,S}$:

- Test FEH06 EQ3 was used to set the vertical slider constant for settlement, $k_{V,S}$.
- Test FEH07 EQ3 was used to set the vertical slider constant for uplift, $k_{V,U}$.
- Tests FEH05 EQ1 and FEH08 EQ3 were used to set the rotation slider constant, k_M.
- Tests FEH08 EQ3 was used to set the horizontal slider constant, k_H.

Extra consideration was required when setting the rotation slider constant, k_M. In Test FEH05 EQ1 a 4.8 m wide basement rotated about the edge of the bottom of the basement, whilst in Test FEH08 EQ3 a 9.6 m wide basement rotated about the centre of the bottom of the basement. For a given basement width, in comparison to rotation about the edge, rotation about the centre requires both a smaller volume of soil to be displaced and shearing along a shallower plane with a smaller cross sectional area, as discussed previously in Chapter 5, Section 5.3.2. This suggests that the rotation slider constant should be smaller for rotation about the centre of the bottom of the basement than about the edge, as less resistance to rotation is provided by the soil. In addition, the width of the basement must also be considered. For a given point of rotation, an increase in basement width will increase both the volume of soil to be displaced, and the depth and cross sectional area of the plane of shearing. This implies that resistance to rotation about any axis of rotation increases

with an increase in basement width, which suggests that the rotation slider constant should increase with an increase in basement width. The data obtained from the centrifuge test series presented in this thesis did not enable these effects to be decoupled. The rotation slider constant was therefore set to be proportional to basement width, and did not depend on the point of rotation.

Point of rotation

The DRILS model required the point of rotation to be specified in the input. This determined where the moment loading imposed by the structure was calculated about.

Peak excess pore pressure ratio

In this model, the maximum excess pore pressure ratio was set to one. At instances in the centrifuge tests, the measured excess pore pressure in the far-field exceeded the initial vertical effective stress, as shown in Figures 4.11(a,b,c) and 5.2(a,b,c). When this occurred, the model reduced the excess pore pressure ratio to be equal to one. This was to ensure that the values of instantaneous vertical effective stress, $\sigma'_v(t)$, in the model were always greater than or equal to zero.

Shaking switch threshold

The centrifuge test data presented in Chapters 4 and 5 was used to set the minimum amplitude of the rate of Arias intensity build up, $\dot{I}_{a,min}$, to be 0.02 m/s/s for displacement and rotation to be accumulated. This value is slightly greater than, but in close agreement with, the shaking intensity rate corresponding to a zero rate of settlement presented by Dashti et al. (2010*a*), shown in Figure 7.13, for structures with shallow foundations located on a shallow layer of liquefiable soil with an initial relative density of 40 - 60 %. An exact match of the numerical value was not anticipated because the dominant mechanisms causing settlement are different for structures with and without shallow basements.

7.3.6 Replication of centrifuge test results

The ability of the DRILS model to reproduce the accumulation of horizontal and vertical displacement, and rotation observed in the centrifuge tests presented in Chapters 4 and 5 was tested. The centrifuge test data was used to calculate the dynamic and static components of the resultant vertical, horizontal and moment load transmitted from the structure to the surrounding soil, after which the methodology detailed in the preceding sections was followed.

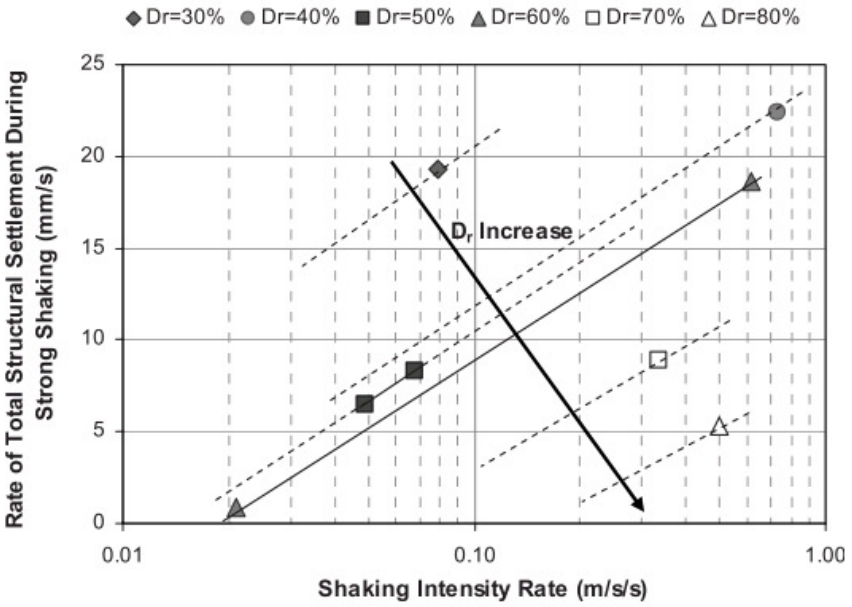

Fig. 7.13 Trends in settlement rate of structures with shallow foundations in experiments with 3 m thick liquefiable soil layer, where D_R = pre-event relative density of the liquefiable layer (Dashti et al. 2010*a*).

The output from the model was horizontal and vertical displacement, and rotation about an axis perpendicular to these aforementioned directions. This was compared to the measured movement of the basement of the structures in the centrifuge tests.

Replication of displacement and rotation during liquefaction

Figure 7.14 shows the time histories for the three degrees of freedom for the centrifuge tests with structures with basements that were rectangular in cross section (ie without rigid extenders), where liquefaction occurred both adjacent to and below the basement of the structure being tested. This corresponds to EQ1 for Test FEH05, which was discussed in Chapter 4, Section 4.3, and EQ3 for Tests FEH06, FEH07 and FEH08, which were discussed in Chapter 5. The first impression from this figure is that the DRILS model is able to replicate the general behaviour observed in each of these shaking events. This is very pleasing considering the very different behaviour observed across these centrifuge tests. The ability of the model to replicate the accumulation of displacement and rotation in each of the centrifuge tests presented in this figure will now be discussed separately.

During EQ1 for Test FEH05, the magnitude of the accumulated rotation was accurately predicted by the DRILS model, which was expected as this test was one of two used to

calculate the rotation slider constant, k_M. The model correctly matched the time at which accumulation of rotation began, however it calculated vertical displacement of the structure to begin slightly before it did in the centrifuge test. Vertical displacement of the structure was correctly replicated for only the first half of shaking, after which settlement was over-estimated. This is likely to be a result of the rotation of the structure in the centrifuge test causing redistribution of total vertical stress which was not accounted for in the DRILS model. This means that changes in vertical effective stress at the instrumented locations will not have been equal to the measured changes in excess pore pressure. In addition, the DRILS model did not account for the change in plan area of the basement due to rotation. The reduction in resistance provided by the soil surrounding the basement may therefore have been smaller than calculated in the model.

In Test FEH06, during EQ3, the time at which settlement of the structure began was correctly replicated in the DRILS model, shown in Figure 7.14(j). The magnitude of accumulated vertical displacement was replicated, which was expected because this test was used to calculate the vertical slider constant corresponding to settlement, $k_{V,S}$. The DRILS model correctly replicated that this structure did not accumulate rotation (Figure 7.14(f)).

For Test FEH07 EQ3, as for Test FEH06, the time at which settlement of the structure began was correctly replicated in the DRILS model and the rate of the initial settlement of the structure was reproduced, as shown in Figure 7.14(k). However, the DRILS model estimated settlement to cease sooner than was observed in the centrifuge test. The model correctly replicated the time at which uplift of the structure began, and matched the residual vertical displacement of the structure. The residual vertical displacement was replicated because this centrifuge test was used to set the vertical slider constant for uplift, $k_{V,U}$.

For Test FEH08 EQ3, the DRILS model replicated the centrifuge test data for the first half of the earthquake only, after which accumulation of displacement and rotation was over-predicted for all three degrees of freedom, as shown in Figures 7.14(d,h,l). This is likely to be a result of the large rotation of the structure in the centrifuge test. Redistribution of total vertical stress and change in plan area of the basement were not accounted for in the DRILS model, as discussed for Test FEH05. In addition, rotation of the structure may have displaced instruments positioned close to the structure. The change in pre and post earthquake hydrostatic pore pressure was used to estimate the vertical displacement of the pore pressure transducers during shaking, and this was accounted for in the DRILS model. However, it was not possible to accurately incorporate the possible change in displacement with time for every instrument. This may have resulted in inaccuracies in the calculated resistance provided by the surrounding soil.

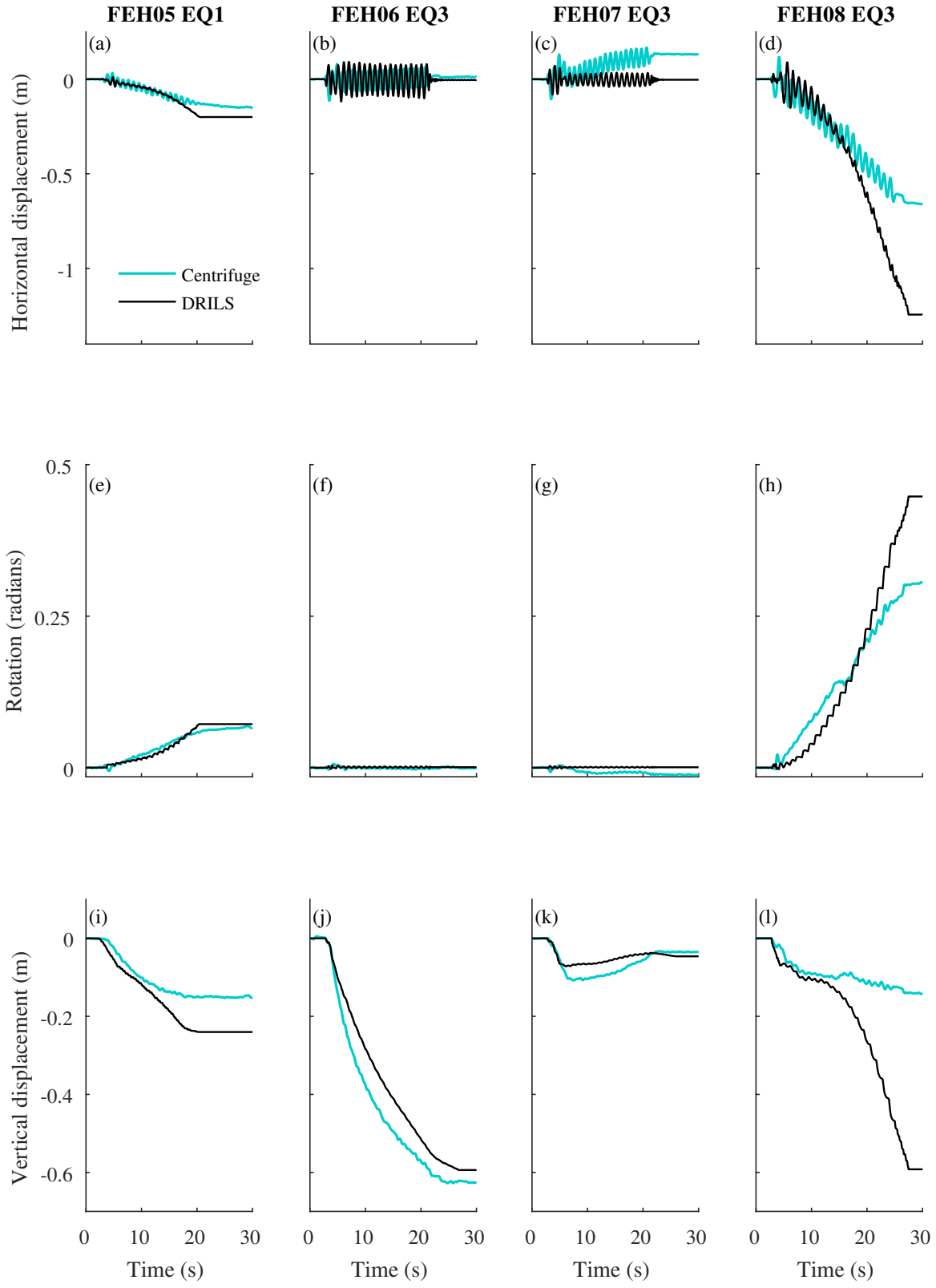

Fig. 7.14 Comparison between centrifuge test data (in turquoise) and output from the DRILS model (in black) for centrifuge tests where liquefaction occurred throughout the soil layer. Accumulation of horizontal displacement (top row), rotation (middle row), and vertical displacement (bottom row). Rightward horizontal displacement is positive, anticlockwise rotation is positive, and settlement is negative vertical displacement.

Structural loading compared to soil resistance during liquefaction

The reasonable agreement in the time at which accumulation of displacement and rotation occurred in the centrifuge tests and in the output of the DRILS model means that it is possible to use the DRILS model to study how the resistance provided by the soil changed during the simulation, and correlate it to the observed behaviour of the structures with basements during the centrifuge tests. Figure 7.15 shows time histories of loading imposed by the structures with basements, in black, and the corresponding resistance provided by the surrounding soil, in colour, for the same earthquakes shown in Figure 7.14. When the loading imposed by the structure, shown in black, was between the corresponding values of the soil resistance, no accumulation occurred. The general trends in loading and resistance can be obtained from this figure.

In Figure 7.15, the y-axis intercepts correspond to the resistance provided by the soil in static conditions, with no reduction due to concurrent V-H-M loading. Once shaking commenced, the resistance provided by the soil reduced due to both the generation of positive excess pore pressures (Equations 7.29 and 7.38) and simultaneous V-H-M loading (Equations 7.41 and 7.42).

It is clear from Figures 7.15(a,b,c,d) that the horizontal loading imposed by the structures with basements on the soil was symmetric. This was expected given that the base shaking horizontal acceleration was sinusoidal and therefore symmetric. The horizontal resistance provided by the soil was roughly the same magnitude in both the right and left direction, with the exception of Test FEH08, shown in Figure 7.15(d), where the smaller magnitude of horizontal resistance to the left compared to the right is likely to have been caused by the rotation of the structure displacing the pore pressure transducer which was used to calculate the horizontal resistance.

Likewise, Figures 7.15(e,f,g,h) show that the resistance to both clockwise (turquoise) and anticlockwise (orange) moment loading were approximately the same magnitude for each of the structures. As expected, rotation was accumulated due to a bias in the loading imposed by the structures rather than a bias in the resistance provide by the soil surrounding the basements.

The reduction in vertical resistance provided by the soil is of particular interest. At a time of zero seconds on the x-axis, the orange lines in Figures 7.15 (i,j,k,l) correspond to the ultimate vertical load in static conditions, with no reduction due to horizontal or moment loading. Once shaking commenced, the vertical resistance provided by the soil reduced due to both the generation of positive excess pore pressures (Equation 7.38) and simultaneous V-H-M loading (Equation 7.42). For a given moment and horizontal load, the vertical load must remain between an upper (orange) and lower (turquoise) limit to avoid failure, as shown

in the schematic in Figure 7.12(b). The upper limit corresponds to the maximum vertical load, $Q_{V,max}(t)$, that can be sustained for the given moment and horizontal loading to avoid bearing failure. The lower limit corresponds to the minimum vertical load, $Q_{V,min}(t)$, needed to avoid lift off. It is assumed that when the vertical loading was less than $Q_{V,min}(t)$ settlement occurred due to ratcheting.

Concurrently, the loading imposed by the structures reduced during shaking due to the increase in uplift provided by the basement. It is clear from Figures 7.15(i,j,k,l) that the vertical loading imposed by the structures with basements (in black) was always far less than the vertical load required for bearing failure (in orange). Initially, this may seem surprising. However, it makes logical sense given the high initial factor of safety for vertical loading for the structures with basements, which was equal to 48, 67, 99 and 99 for Test FEH05, FEH06, FEH07 and FEH08 respectively. An excess pore pressure ratio of 0.979, 0.985, 0.99 and 0.99 would therefore be required for Test FEH05, FEH06, FEH07 and FEH08 respectively, to reduce the vertical load at which bearing failure occurs to below the static load imposed by the structures with basements. This is before the increase in uplift and reduction in vertical load due to the generation of positive excess pore pressure is considered. Time histories of excess pore pressures obtained from the centrifuge tests, shown in Figures 4.3 and 5.3, show that this did not occur below the basements in the centrifuge tests.

Further insight can be attained by re-plotting Figure 7.15 and decreasing the range on the y-axes to focus on the loading imposed by the structures. This is shown in Figure 7.16, using the same line colours as the previous figure. It is evident in Figure 7.16 that the vertical loading imposed by the structures with basements did reduce to less than the minimum vertical load required to prevent lift-off for the given moment loading. Ratcheting was therefore the likely cause of the liquefaction induced settlement of the structures with basements. This corroborates with the soil displacements observed in the centrifuge tests. The vertical load of the structures in Tests FEH07 and FEH08 reduced to less than zero, shown in Figures 7.16(k,l). This explains why uplift occurred in Test FEH07 EQ3.

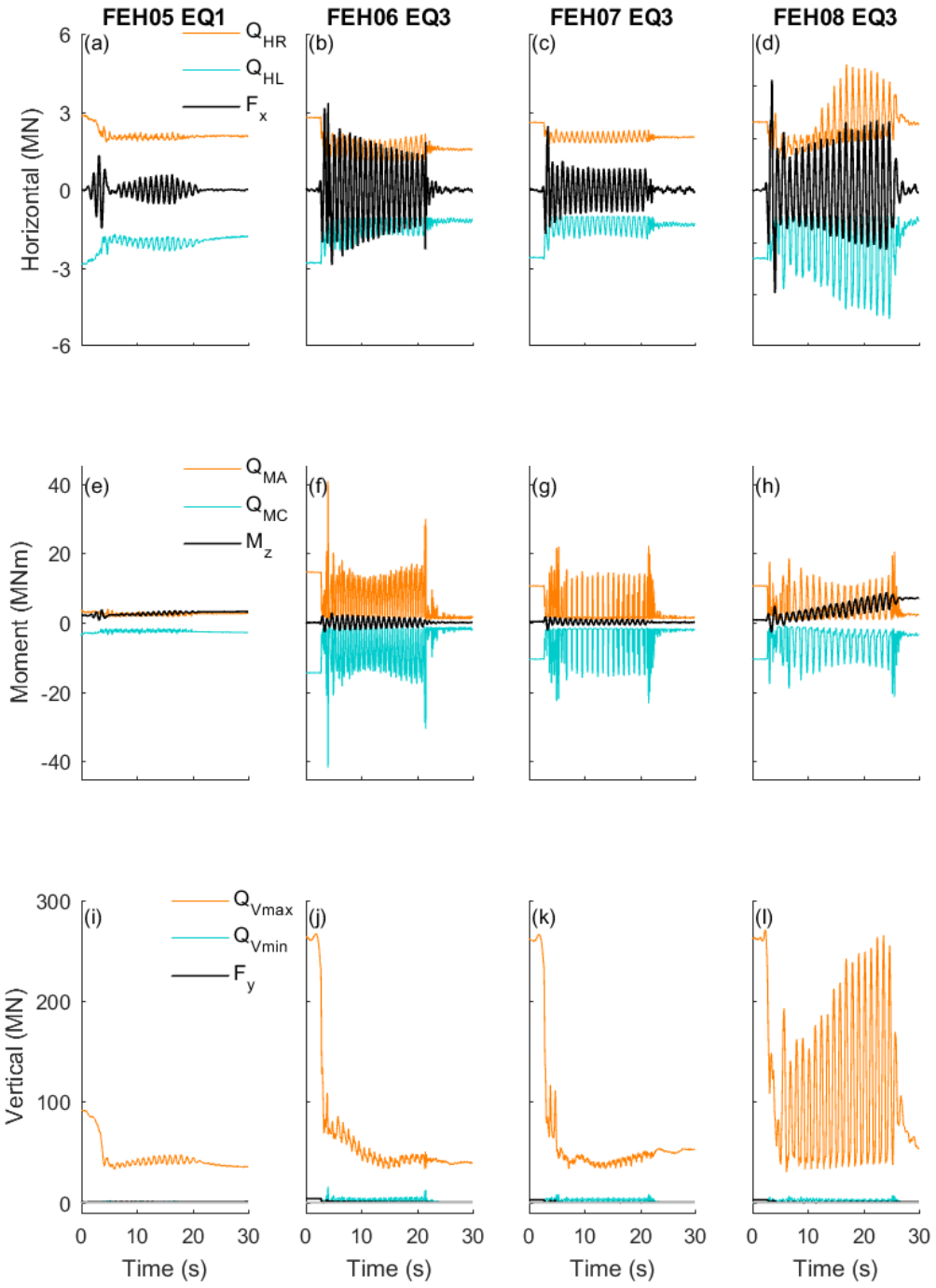

Fig. 7.15 Using the DRILS model to compare the loading imposed by the structures with basements (in black) and the resistance provided by the soil during shaking (in colour). Legend subscripts: *R* is right, *L* is left, *A* is anticlockwise, *C* is clockwise.

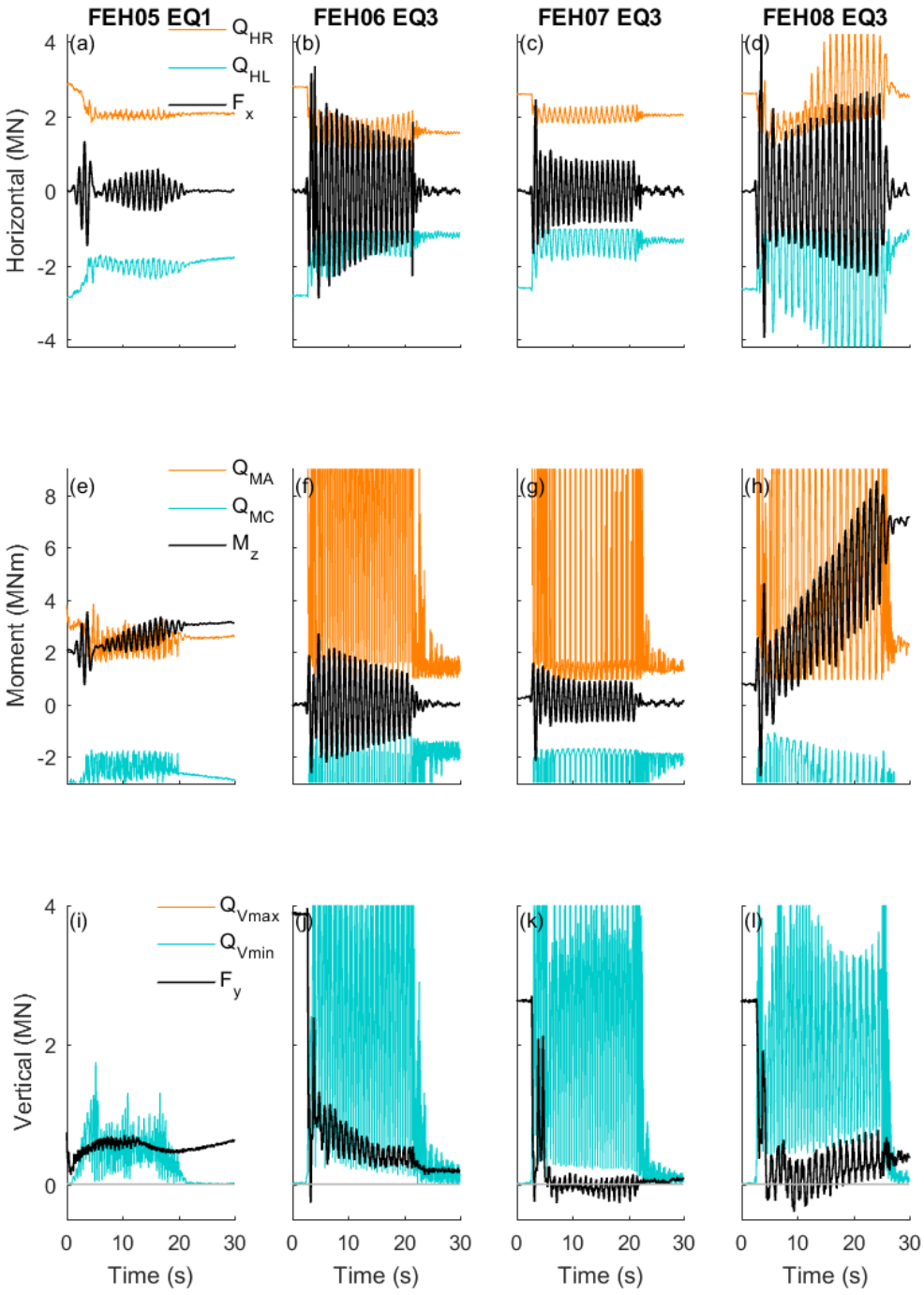

Fig. 7.16 Using the DRILS model to compare the loading imposed by the structures with basements (in black) and the resistance provided by the soil during shaking (in colour). Legend subscripts: *R* is right, *L* is left, *A* is anticlockwise, *C* is clockwise. Replot of Figure 7.15, y-axes range decreased to focus on structure loading.

Replication of displacement and rotation during small amplitude shaking

In the preceding sections, the ability of the DRILS model to replicate the behaviour observed during large amplitude shaking which caused liquefaction to occur throughout the entire soil layer has been presented. It is also important to confirm that the model can replicate the behaviour during small amplitude shaking.

Figures 7.17 and 7.18 show the time histories for the three degrees of freedom for Tests FEH06, FEH07 and FEH08 for EQ1 and EQ2 respectively. Unfortunately, the resolution of the images taken with the high-speed camera was not high enough to accurately measure the small magnitude of displacement and rotation of the structures in these tests using PIV. For the centrifuge data shown in Figures 7.17 and 7.18, which is plotted in colour, accumulated horizontal displacement was omitted as it was only measured using PIV. The accumulated rotation plotted is the sum of the static component obtained from PIV and the dynamic component obtained through double integration of the vertically orientated MEMS, and the accumulated vertical displacement presented was measured using LVDTs. For a given degree of freedom, the scale of the y-axes is the same in Figures 7.17 and 7.18, with the range on the y-axes for horizontal displacement and rotation being approximately 2 orders of magnitude smaller than in Figure 7.14.

It is evident from Figures 7.17 and 7.18 that the DRILS model was able to correctly reproduce the negligible accumulation of rotation that was observed in the centrifuge tests. Unfortunately, the centrifuge test data is very noisy for these small angles of rotation. The DRILS model correctly reproduced zero accumulation of vertical displacement observed in the centrifuge during EQ1 for Test FEH06 and FEH07. However, vertical displacement was over-estimated for all the other cases in Figures 7.17 and 7.18. For FEH06 EQ2, FEH07 EQ2 and FEH08 EQ1, the DRILS model calculated uplift which was not observed in the centrifuge tests, and for FEH08 EQ2 it calculated greater settlement than was observed in the centrifuge test. For these four tests, liquefaction occurred at shallow depths adjacent to and directly below the bottom of the basement, but not for the entire soil layer, as shown in the excess pore pressure time histories in Figures 5.2 and 5.3.

Settlement calculated by the DRILS model which was not observed in the centrifuge test for FEH08 EQ2 is likely to be because the vertical resistance provided by the soil beneath the basement was not correctly captured by the model, which only considered one location at a shallow depth below the centre of the bottom of the basement. Uplift calculated by the DRILS model which was not observed in the centrifuge tests for FEH06 EQ2, FEH07 EQ2 and FEH08 EQ1 may be because the zero threshold force for uplift is incorrect when liquefaction only occurs at shallow depths. This assumption was based on the shear resistance being negligible along the entire depth of the soil-structure interface. Alternatively, the uplift

force provided by the basement may have been overestimated using the excess pore pressure measurements from the centrifuge tests.

To correctly capture the vertical displacement of structures with basements during shaking events which liquefy only a fraction of the full depth of the liquefiable soil layer, the number of locations used in the model to characterise the soil behaviour below and adjacent to the basement would need to be increased. The number and location of instrumentation in the centrifuge tests would need to be changed for this purpose. A method to account for side friction on the basement walls would need to be added. In addition, an increase in the resolution of the images obtained from the high-speed camera would be needed to calibrate the model for small amplitude shaking events. This was beyond the scope of the present study.

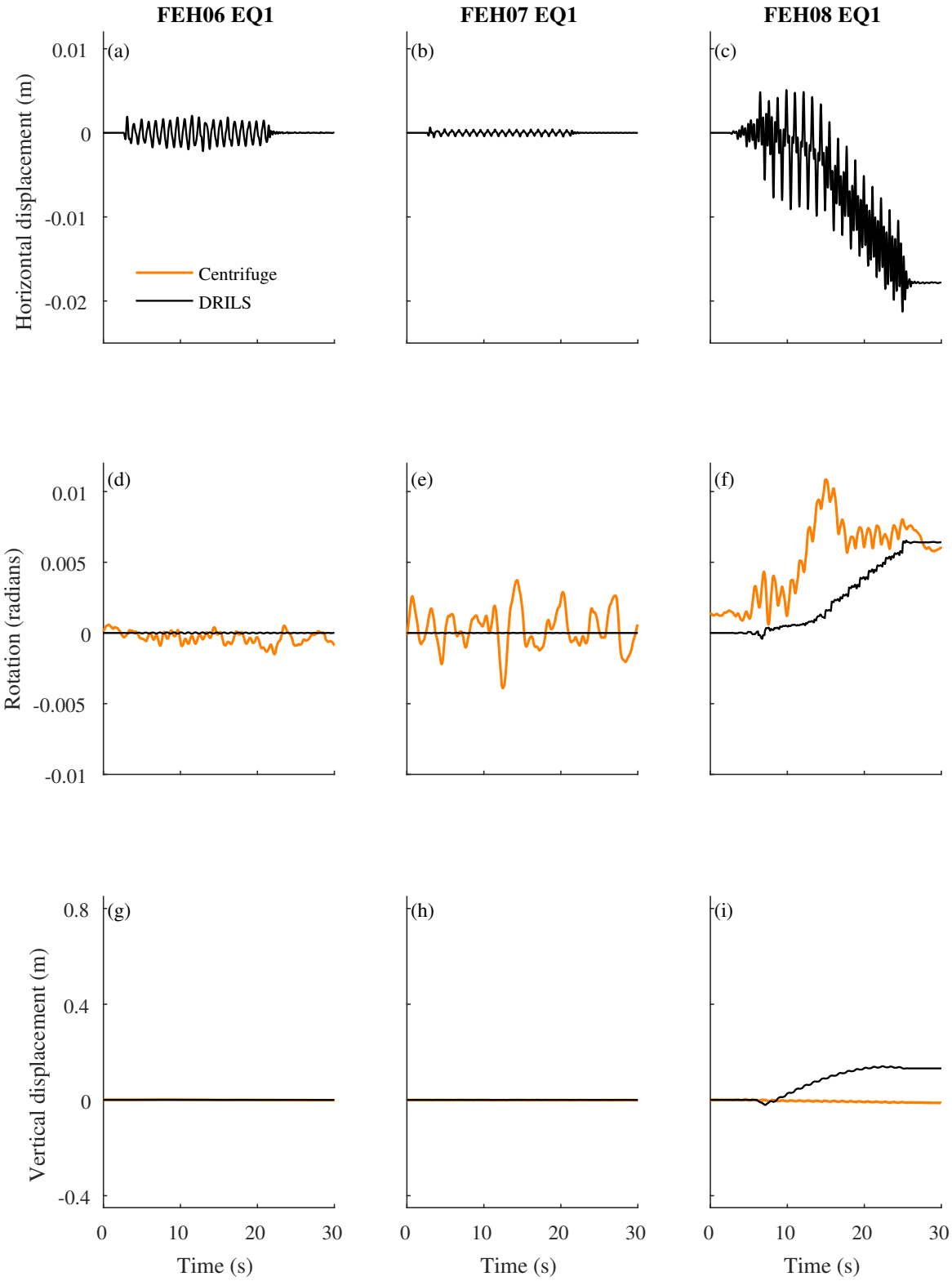

Fig. 7.17 Comparison between centrifuge test data (in orange) and output from the DRILS model (in black) for centrifuge tests with wide basements during EQ1. Accumulation of horizontal displacement (top row), rotation (middle row), and vertical displacement (bottom row). Rightward horizontal displacement is positive, anticlockwise rotation is positive, and settlement is negative vertical displacement.

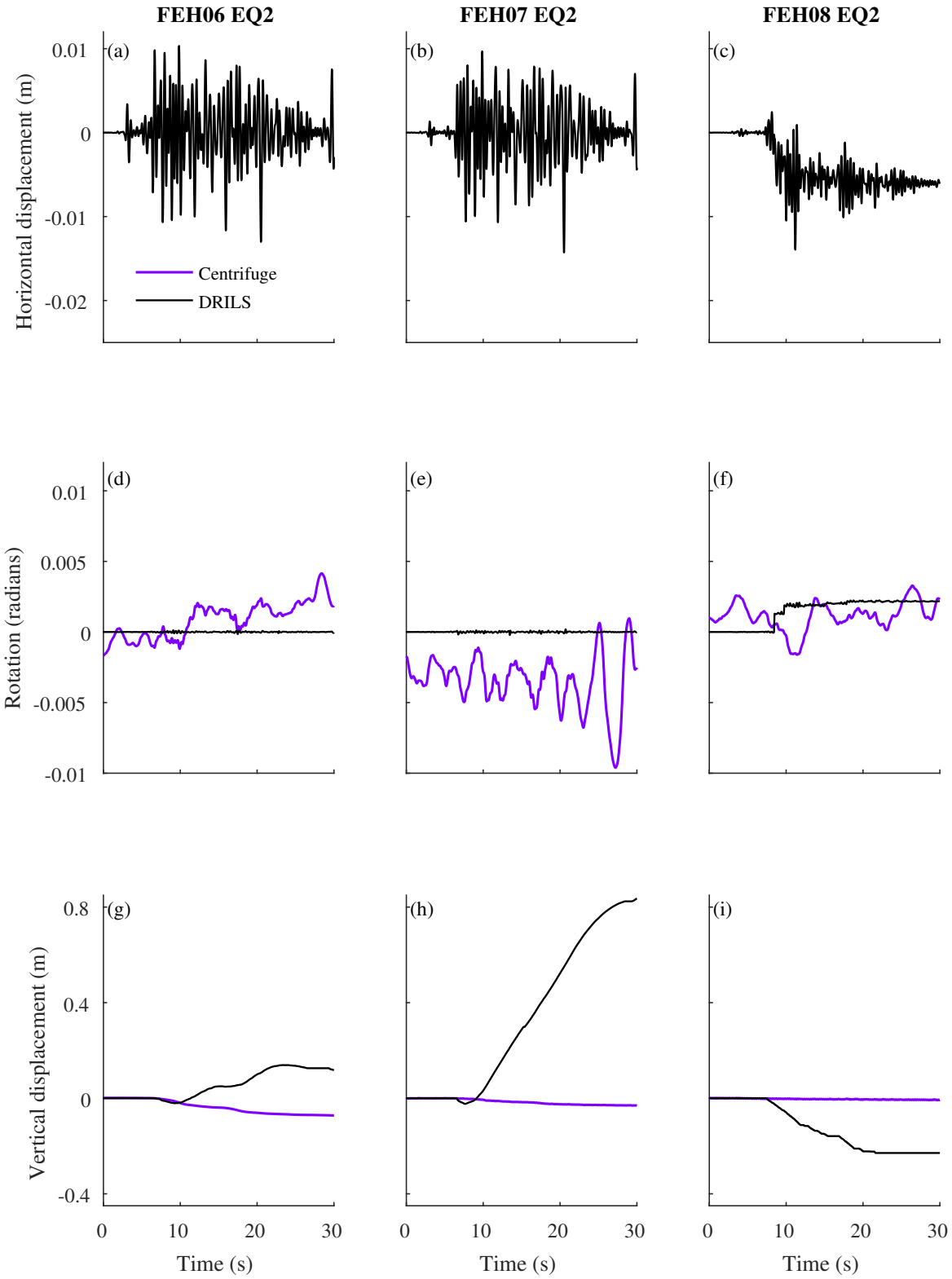

Fig. 7.18 Comparison between centrifuge test data (in purple) and output from the DRILS model (in black) for centrifuge tests with wide basements during EQ2. Accumulation of horizontal displacement (top row), rotation (middle row), and vertical displacement (bottom row). Rightward horizontal displacement is positive, anticlockwise rotation is positive, and settlement is negative vertical displacement.

7.3.7 Structures with basements with rigid extenders

It is desirable that the DRILS model can be used to model the accumulation of rotation and displacement of the structures with narrow basements which have both vertical and horizontal rigid extenders, which were presented in Chapter 4, Section 4.4.

For the dynamic DRILS model in Section 7.2, the projected area of the extenders was used to reflect the volume of soil affected by the shaking of the basement. Inclusion of the extenders in the methodology developed to calculate accumulation of displacement and rotation was more complicated and required further consideration.

Structures with vertical extenders

The effect of the vertical extenders on the vertical resistance was first considered. The soil displacement vectors in Figures 4.18(a,b) and 4.20(a) and the excess pore pressure time histories shown in Figure 4.19(a) showed that the soil constrained between the vertical extenders behaved as an almost rigid block and moved with the basement. For this reason, when considering the vertical capacity, the depth of the bottom of the vertical extenders was considered and the weight of soil constrained within the extenders was added to the total weight of the structure. The methodology detailed in Section 7.3.3 was then followed.

The effect of the vertical extenders on resistance provided by the adjacent soil to both horizontal translation and rotation was then considered. The basement, vertical extenders and the soil constrained between the extenders was considered as a rigid body, which meant that lateral resistance provided by the soil between the extenders was not included. Figure 7.19(a) shows regions of active (A) and passive (P) lateral earth pressures in the soil adjacent to the basement and vertical extenders for clockwise rotation about the depth of the bottom of the enclosed basement, which was observed for Test FEH10 (Figure 4.20(b)). Figure 7.19(b) shows the same for rotation about the bottom of the extenders. In the calculation procedure in the DRILS model, active pressure was ignored, which corresponds to regions which the basement rotated away from. This was justified by the observation of localised piping along the side of the upper half of the basement in Test FEH10, shown in Figure 4.22, due to lateral extension of the soil in this region.

The geometry in Figure 7.19 corresponds to the centrifuge tests conducted with basements with vertical extenders (see Chapter 4), where the vertical extenders doubled the depth of the underground structure. For this geometry, the schematics in Figure 7.19 show that the total lateral force contributing to resistance to rotation due to passive lateral earth pressure was the same for the two axes of rotation shown. However, the difference in lever arm of these forces resulted in less resistance to rotation about an axis at the depth of the bottom of

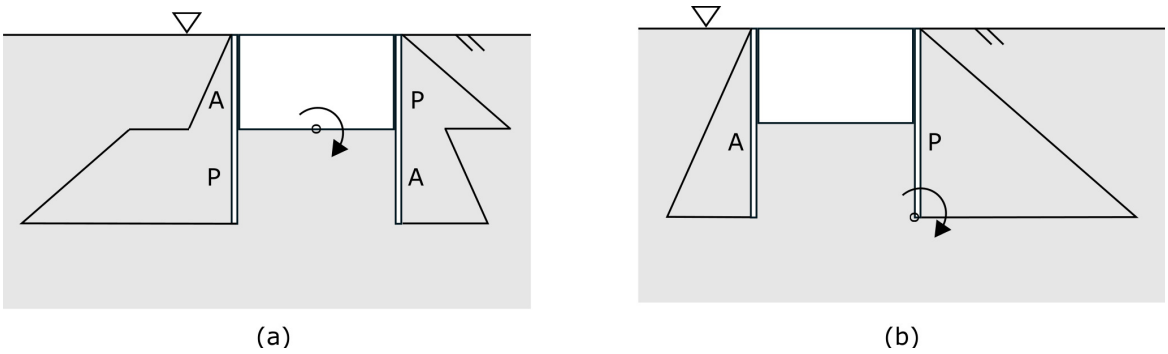

Fig. 7.19 Lateral earth pressure adjacent to a basement with rigid vertical extenders, for clockwise rotation about (a) the bottom of the enclosed basement and (b) about the bottom of the extenders, showing regions of both active (A) and passive (P) pressure.

the basement (Figure 7.19(a)) compared to the depth of the bottom of the vertical extender (Figure 7.19(b)). This corroborates with the behaviour observed in the centrifuge tests, where rotation occurred about the bottom of the enclosed basement for Test FEH10, as shown in Figure 4.20(b).

The resistance to rotation provided by the passive resistance shown in Figure 7.19 was added to the resistance to rotation provided by the soil below the bottom of the basement, which was calculated using the methodology detailed in Section 7.3.3.

Structures with horizontal extenders

The weight of the soil overlying the horizontal extenders increased the weight being supported by the basement, and was therefore added to the total weight of the structure. The projected area of the horizontal extenders was used when calculating the uplift force due to positive excess pore pressures below the basement, and the vertical capacity and the moment resistance provided by the soil

When considering the horizontal resistance provided by the soil adjacent to the basement with a horizontal extender, the projected area did not change which meant that the horizontal resistance did not change.

Replication of centrifuge test results

Figure 7.20 shows time histories for the three degrees of freedom for the structures with basements with rigid extenders during centrifuge tests where liquefaction occurred both adjacent to and below the basement of the structure being tested. This corresponds to EQ3 for Tests FEH09, FEH10 and FEH11, which were discussed in Chapter 4, Section 4.4. The values of the slider constants determined in Section 7.3.5 were unchanged.

Figures 7.20(d,e,f) show that the model was able to replicate the magnitude of accumulation of rotation of the structures with basements with rigid extenders, however the rate of rotation was not correctly matched. Likewise, Figures 7.20(a,b,c) show that the model was able to replicate the accumulation of horizontal displacement, the majority of which was due to rigid body rotation of the basements.

In contrast, Figures 7.20(g,h,i) show that the model was not able to replicate the magnitude of the vertical displacement of these structures. The model over-predicted the magnitude of settlement for all the structures with basements with rigid extenders. The initial rate of settlement of the structures was correct, however, the model accumulated settlement at a constant rate for the duration of shaking whilst the centrifuge tests data shows that the rate of settlement slowed during shaking. This discrepancy is likely to be due to inaccuracies in the simple assumptions regarding the weight of soil constrained by the rigid extenders which was assumed to move with the structures. Ability of the model to replicate the initial rate of settlement suggests that the assumptions were correct at the start of shaking, but that the mass of soil moving rigidly with the structures reduced during shaking.

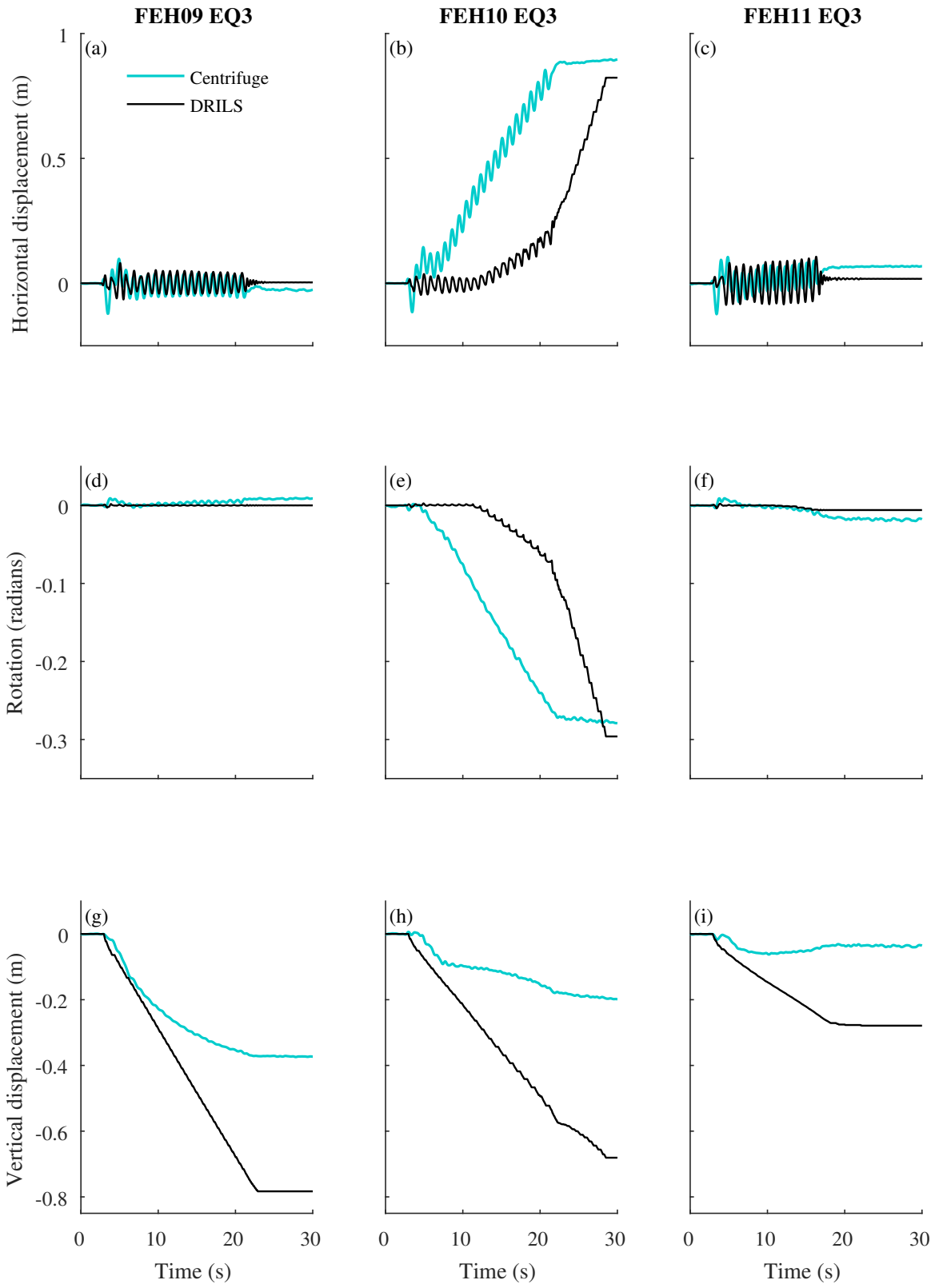

Fig. 7.20 Comparison between centrifuge test data (in turquoise) and output from the DRILS model (in black) for centrifuge tests with structures with basements with rigid extenders where liquefaction occurred throughout the soil layer. Accumulation of horizontal displacement (top row), rotation (middle row), and vertical displacement (bottom row). Rightward horizontal displacement is positive, anticlockwise rotation is positive, and settlement is negative vertical displacement.

7.4 Predicting accumulation of displacement and rotation

In Section 7.3, a mechanical model was developed that was able to closely replicate the liquefaction induced accumulation of displacement and rotation of the structures with basements observed in the centrifuge tests presented in Chapters 4 and 5. It was desirable to use this model to predict the accumulation of settlement and rotation of structures with basements with intermediate properties to those tested in the centrifuge.

7.4.1 Input data

The centrifuge tests were highly instrumented. A large volume of data was collected from these centrifuge tests, which was subsequently used to set up the DRILS model. It is not realistic, or desirable, to require this volume of data to be input into a model which would be of use to practitioners interested in estimating the settlement and rotation of a structure. The number of user specified input parameters required by the model were therefore reduced. The centrifuge test data was used to inform procedures to generate any additional data required to be input into the DRILS model. These procedures will be detailed in the following sections.

Input structure properties

Details of the structure properties were required:

- Superstructure mass, moment of inertia, and location of centre of gravity
- Basement mass, moment of inertia, and location of centre of gravity
- Basement geometry

Replicating earthquake input motion

Any realistic earthquake input motion time history can be used in the model. Alternatively, a sinusoidal input motion can be specified, with a prescribed amplitude, frequency and number of cycles.

Replicating soil behaviour

It was necessary to replicate the co-seismic soil behaviour, as it was required as an input to the model. The soil behaviour was characterised in two locations: 1) adjacent to the basement, at half the depth of the basement, 2) below the bottom of the centre of the basement, at a depth of half the basement width. At each location, the maximum, steady-state excess

pore pressure ratio, the number of cycles of shaking required for it to be reached, and the amplitude of the oscillations in excess pore pressure ratio during shaking were required, as shown in the schematic in Figure 7.21. The peak excess pore pressure ratio was not allowed to exceed the value of one. The model required each of these values to be specified by the user, to allow these parameters to be studied in isolation. In future iterations of the model, it would be possible to make them a function of the input motion and the initial soil properties by incorporating liquefaction susceptibility analyses into the model. This was beyond the scope of the present study.

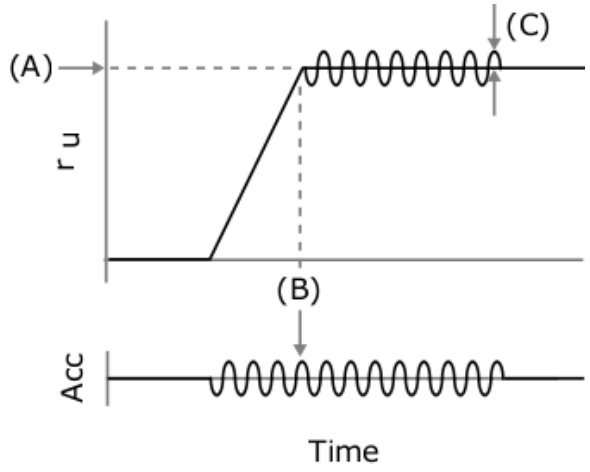

Fig. 7.21 Model excess pore pressure ratio values, r_u, specified by the user for sinusoidal input motion: the maximum, steady-state excess pore pressure ratio (A), the number of cycles of shaking required for it to be reached (B), and the amplitude of the oscillations in excess pore pressure ratio during shaking (C).

Analysis of shear strain time histories from the centrifuge test data were used to formulate simple expressions to estimate shear strain at the two locations detailed in the preceding paragraph. Centrifuge test data presented in Chapters 4 and 5 showed that shear strain increased with increasing input acceleration and decreased with increase in excess pore pressure ratio. The observation of smaller shear strain underneath the structure than adjacent to the basement was also noted. Using this data, an expression to estimate shear strain time history, $\gamma(t)$, was formulated and the constants were set to best fit the experimental data:

$$\gamma(t) = \frac{a_h(t)}{g}[C - (0.013 r_u(t))] \tag{7.44}$$

where a_h is the input horizontal acceleration in ms^{-2}, g is Earth's gravity, $r_u(t)$ is the excess pore pressure ratio, and C is a constant and was set to be 0.03 adjacent to the basement and 0.02 beneath the centre of the basement.

Replicating co-seismic structure loading

The mean of the artificially generated excess pore pressure ratio time history at the location beneath the basement and the location adjacent to the basement was used to calculate the uplift force provided by the basement, $F_U(t)$. This was subtracted from the specified total weight of the structure to obtain the time history of effective weight of the structure.

Modelling the moment loading imposed by the structure on the soil surrounding the basement required more consideration. The dynamic, $M_{z,dy}(t)$, and static, $M_{z,st}(t)$, components of the moment loading were calculated separately. The centrifuge test data showed that the dynamic component of the moment loading, $M_{z,dy}(t)$, could be best approximated from the input horizontal acceleration by multiplying the mass of the superstructure, the height of the centre of gravity of the superstructure above the soil surface, and the horizontal base acceleration. The static component, $M_{z,st}(t)$, was calculated following a methodology which was similar to that which was detailed in Section 5.4 for the centrifuge test data, and was calculated incrementally at each time step in the model. When rotation occurred about the centre of the bottom of the basement, the static component of the moment loading, $M_{z,st}(t)$, was calculated using:

$$M_{z,st}(t) = mg\left[y_{CoG}sin\theta(t) - x_{CoG}cos\theta(t)\right] - F_U(t)\left[\frac{D}{2}sin\theta(t)\right] \tag{7.45}$$

where m is the total mass of the structure, $\theta(t)$ is the accumulated rotation at time t, x_{CoG} and y_{CoG} are the co-ordinates of the centre of gravity of the structure in relation to the centre of the bottom of the basement, $F_U(t)$ is the uplift force provided by the basement, and D is the depth of the basement. When rotation occurs about the edge of the basement, the static component of the moment loading increases, and can be calculated using:

$$M_{z,st}(t) = mg\left[y_{CoG}sin\theta(t) + \left(\frac{B}{2} - x_{CoG}\right)cos\theta(t)\right] - F_U(t)\left[\frac{D}{2}sin\theta(t) + \frac{B}{2}cos\theta(t)\right] \tag{7.46}$$

where B is the width of the basement.

Seismic resistance of soil

The seismic resistance of the soil surrounding the basement was calculated as detailed in the Sections 7.3.3.

Summary of input data required

In summary, the following input data was required:

- Superstructure mass, moment of inertia, and location of centre of gravity
- Basement mass, moment of inertia, and location of centre of gravity
- Basement geometry
- Axis of rotation: centre or edge of bottom of basement
- Earthquake input motion characteristics
- Maximum, steady-state excess pore pressure ratio, the number of cycles of shaking required for it to be reached, and the amplitude of the oscillations in excess pore pressure ratio during shaking
- Soil properties: critical state friction angle, buoyant unit weight of soil, depth of layer

Replication of centrifuge test data

These simplifications and approximations can be justified by comparing the output from the DRILS model when the centrifuge test data and artificially generated data are used as input. Figure 7.22 compares the output from the DRILS model when the centrifuge test data and artificially generated data are input, and compares them with the centrifuge test data for the structures with wide basements presented in Figure 5.9.

Figure 7.22 shows that the output from the DRILS model when the artificially generated data is used as input is comparable to when the centrifuge test data is used as input. The most notable omission is that the DRILS model did not calculate the structure in Test FEH07 EQ3 to uplift when artificially generated input data was used. However, it did calculate the rate of settlement to reduce during shaking, as shown in Figure 7.22(h). This is likely to be a consequence of the sensitivity of the DRILS model to the vertical load imposed by the structure on the soil. In the DRILS model, the structure changes from accumulating settlement due to ratcheting to uplifting with only a very small increase in uplift provided by the basement. Figure 7.22(h) shows that the artificially generated input data underestimated this uplift force.

The simplifications and assumptions detailed in Section 7.4.1 mean that an exact fit was not expected. However, the ability of the model to capture the trends in behaviour observed in the centrifuge test series means that it is suitable to use for parametric studies.

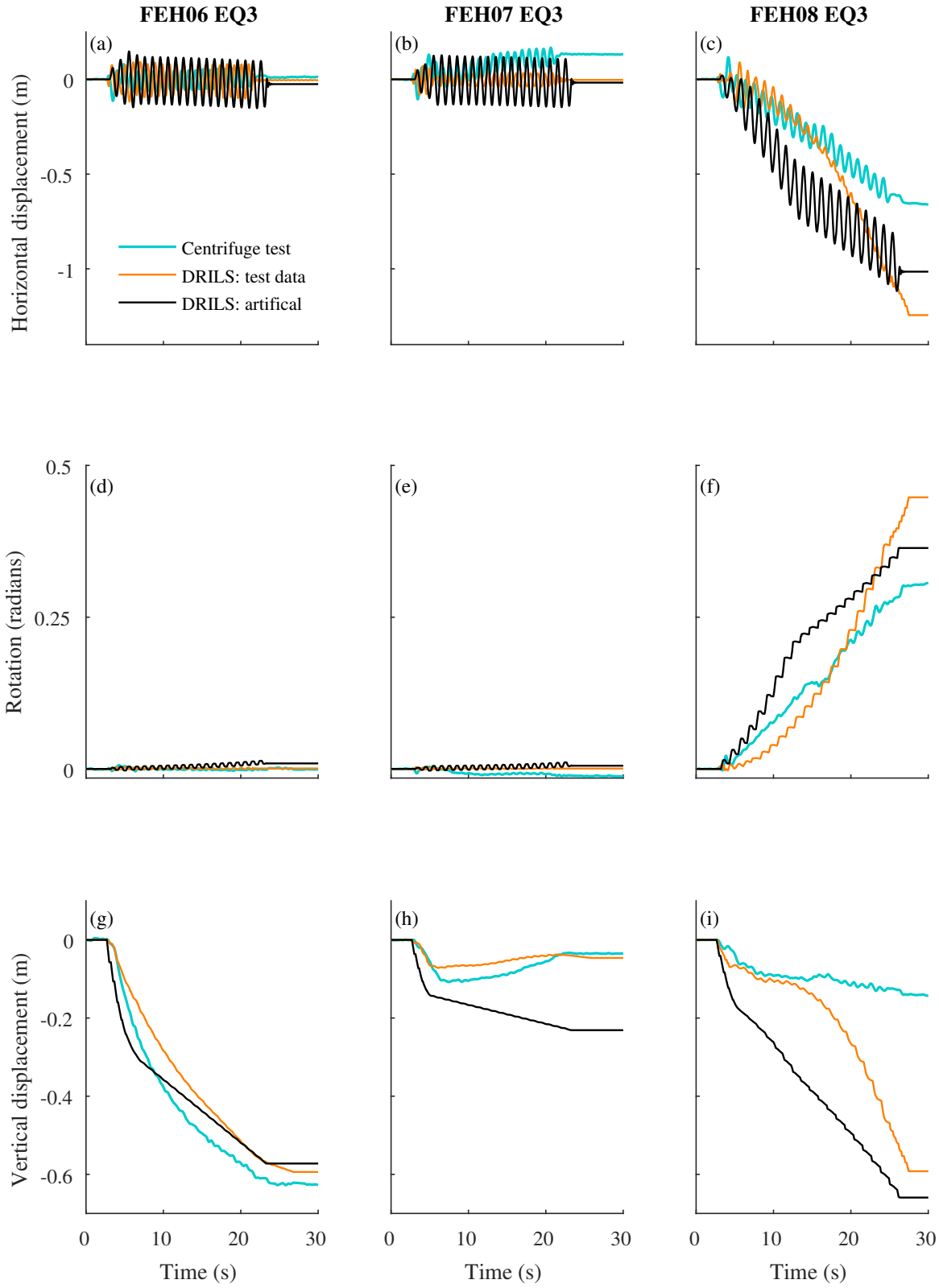

Fig. 7.22 Comparison between the centrifuge test data (turquoise) and the output from the DRILS model when the centrifuge test data (orange) and artificially generated data (black) are input.

7.4.2 Parametric studies

The development of a simplified method can allow information obtained from novel testing using advanced methods to be applied to a wider number of applications. The DRILS model developed in this chapter has been used to extend the findings from the centrifuge test series to a wider range of structure properties and base shaking characteristics. In each of the parametric studies detailed below, the behaviour of a structure in one of the centrifuge tests conducted and presented in Chapter 5 was used as a starting point. One parameter was changed and the effect on the liquefaction induced accumulation of displacement and rotation was investigated. These parametric studies were restricted to structures with basement without extenders and base shaking which was sufficiently strong to cause liquefaction.

Simultaneous settlement and rotation

In Section 5.4, it was noted that the three structures with wide basements tested in the centrifuge either settled, rotated or did neither when liquefaction occurred, as shown in Figure 5.19(d). None of the structures accumulated both large settlement and rotation. This was anticipated given the sequential structure parameter selection process between the centrifuge tests conducted, which aimed at eliminating displacement and rotation. However, from an academic curiosity point of view, this posed the question as to whether large accumulation of both rotation and settlement could occur simultaneously.

The DRILS model was used to interpolate between the properties of structures tested in the centrifuges tests, and predict the behaviour of a structure with a combination of the mass and eccentricity of the structures tested in FEH06, which settled and did not rotate, and FEH08, which rotated and did not accumulate notable vertical displacement except due to rigid body rotation. A summary of the structure properties in the parametric study are given in Table 7.2. Figure 7.23 shows the time histories for accumulated horizontal displacement, rotation and settlement during 20 cycles of 0.33 g amplitude sinusoidal shaking, which caused liquefaction to occur. Figure 7.24 shows the same data, with vertical displacement plotted against rotation. Caution must be taken when considering the magnitude of the vertical displacement of these structures, as the DRILS model has previously been found to over-estimate settlement when large rotation occurs, as seen in Figure 7.14.

Figures 7.23 and 7.24 show that for structures with basements, large accumulation of both rotation and settlement can occur simultaneously when liquefaction occurs. Simulation Q1, which had the same U/W and y_{CoG} as FEH06, and the x_{CoG} of FEH08, settled a comparable amount to FEH06 and rotated less than FEH08. This makes logical sense as, when the

Table 7.2 Properties of structures in parametric study to investigate the simultaneous liquefaction induced settlement and rotation of structures with wide basements

Simulation ID	U/W	x_{CoG}	y_{CoG}	Note
M06	0.8	0	-0.44	Replica of Test FEH06
M08	0.9	-0.184	1.37	Replica of Test FEH08
Q1	0.8	-0.184	-0.44	U/W and y_{CoG} of FEH06, x_{CoG} of FEH08
Q2	0.8	-0.092	-0.44	U/W and y_{CoG} of FEH06, half x_{CoG} of FEH08
Q3	0.9	0	1.37	U/W and y_{CoG} of FEH08, x_{CoG} of FEH06
Q4	0.9	-0.092	1.37	U/W and y_{CoG} of FEH08, half x_{CoG} of FEH08

vertical load in less than half the degraded vertical capacity of the soil, an increase in vertical loading increases the resistance to rotation (Figure 7.12(a)).

It is also interesting to note from Figures 7.23 and 7.24 that reducing the x_{CoG} by a factor of 0.5 from Test FEH08 whilst keeping U/W and y_{CoG} constant, corresponding to simulation Q4, had a negligible effect on accumulated rotation. It can be concluded that the height of the centre of gravity of the structure tested in FEH08 was the primary factor which governed whether rotation of the structure occurred and the eccentricity worsened the situation further. Simulation Q3 corroborates this finding, as rotation was accumulated for a structure with the same U/W and y_{CoG} as Test FEH08, but with no eccentricity. These findings are valuable additions to the conclusions drawn from the centrifuge tests presented in Chapter 5.

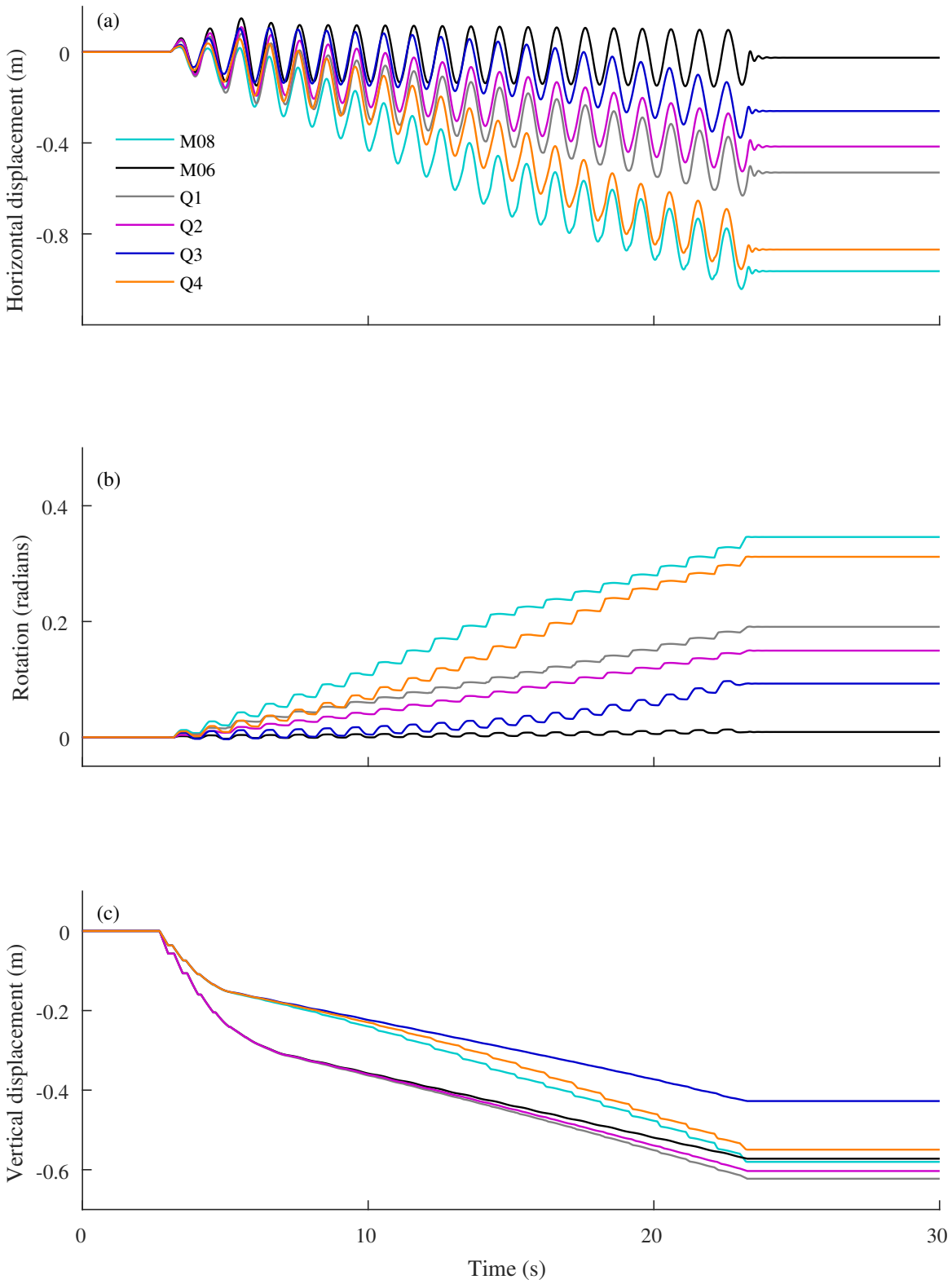

Fig. 7.23 Parametric study to investigate the simultaneous liquefaction induced settlement and rotation of structures with wide basements. Reference test: FEH06, which settled and did not rotate, and FEH08, which rotated and did not accumulate notable vertical displacement except due to rigid body rotation.

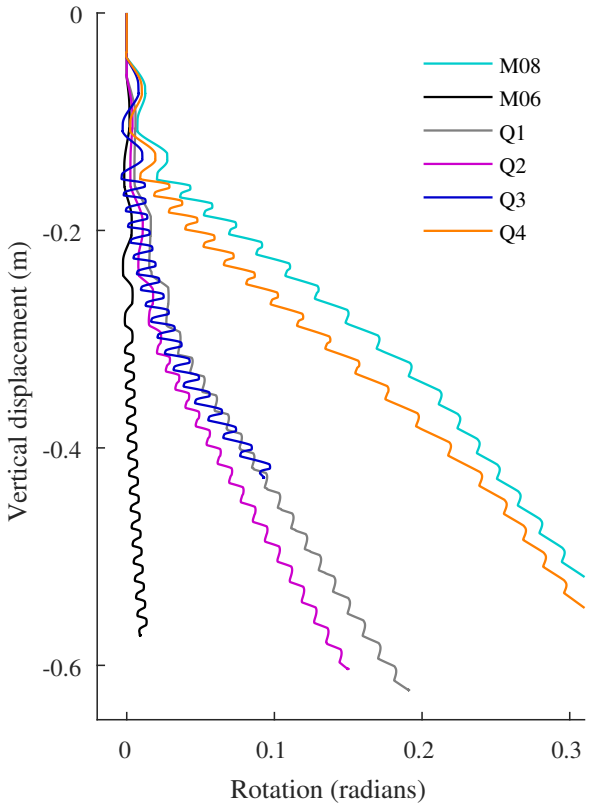

Fig. 7.24 Interaction between vertical displacement and rotation for the parametric study investigating the simultaneous liquefaction induced settlement and rotation of structures with wide basements. Reference test: FEH06, which settled and did not rotate, and FEH08, which rotated and did not accumulate notable vertical displacement except due to rigid body rotation.

Height of centre of gravity

The DRILS model enabled the effect of the height of the centre of gravity of a structure with a basement to be further investigated. The symmetric structure with a wide basement tested in Test FEH07, which neither settled nor rotated, was used as the starting point, and the height of the centre of gravity was gradually increased in increments of 0.25 m, whilst keeping all other parameters constant.

Figure 7.25(b) shows that as the height of the centre of gravity was gradually increased, the accumulated rotation of the structure increased. The increase in accumulated rotation for each 0.25 m increment increased as the height of the centre of gravity rose. Small changes in the height of the centre of gravity are therefore more detrimental for structures with an initially high centre of gravity. The change in the height of the centre of gravity did not have an effect on the settlement of the structures, as shown in Figure 7.25(c).

This parametric study shows that the centre of gravity of a symmetric structure with a wide basement must be kept below a certain height to ensure that negligible rotation is accumulated. For the structure tested in FEH07 and shown in Figure 7.25, this corresponds to the centre of gravity remaining below approximately 1 m above the soil surface. This agrees with the finding from the parametric study investigating simultaneous settlement and rotation of structures with basements, which showed that the height of the centre of gravity of the structure tested in FEH08, which was 1.37 m above the soil surface, governed whether rotation of the structure occurred, rather than the eccentricity.

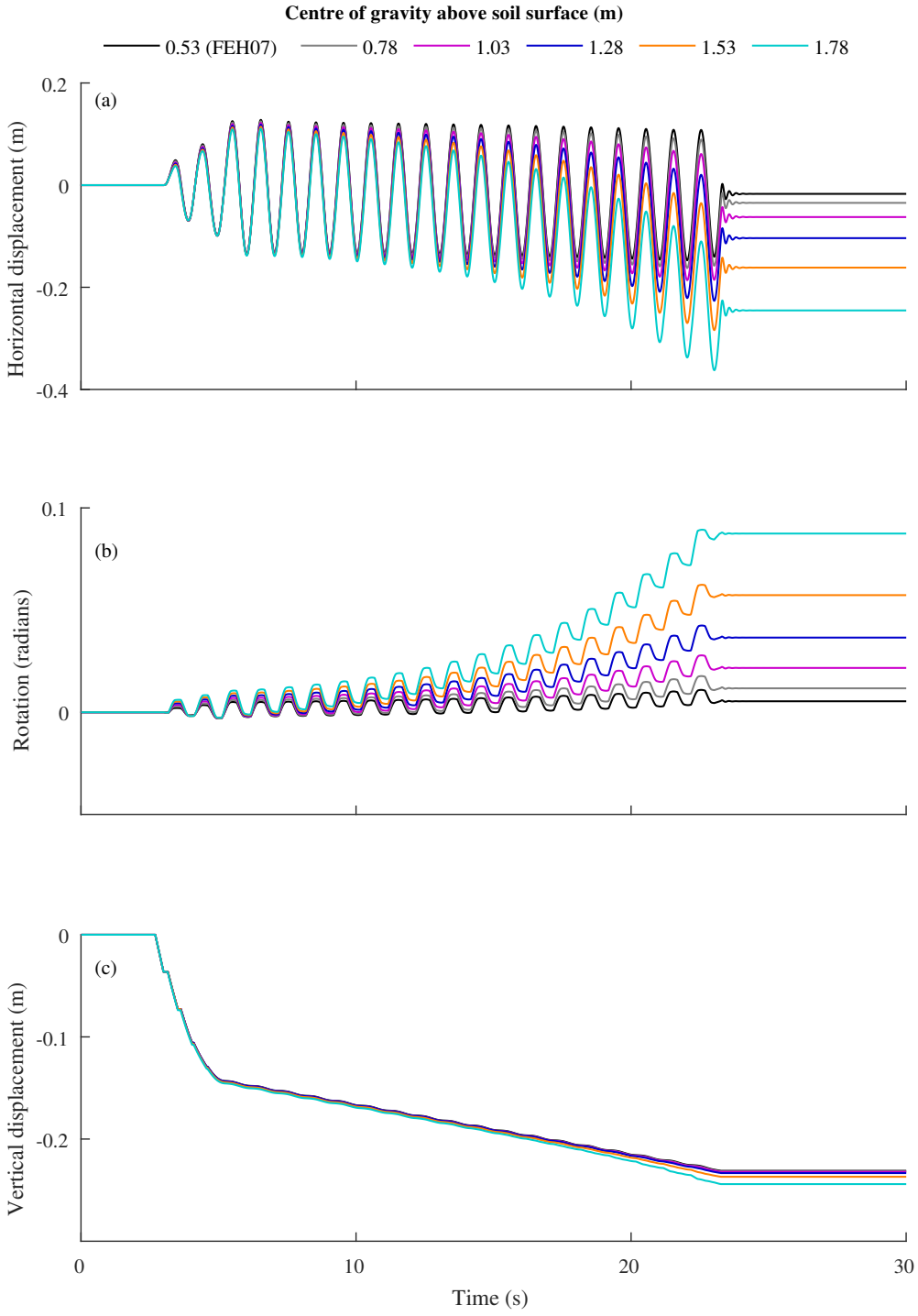

Fig. 7.25 Parametric study to investigate the effect of the height of the centre of gravity on the liquefaction induced accumulation of displacement and rotation of a symmetric structure with a wide basement. Reference test: the structure tested in FEH07 with centre of gravity located 0.53 m above the soil surface.

Basement width

Two different basement widths were used in the centrifuge tests presented in Chapters 4 and 5, 4.8 m and 9.6 m. It is of interest to investigate the behaviour of structures with basements with intermediate widths.

The symmetric structure with a wide basement tested in FEH07, which neither settled nor rotated, was used as the starting point and the width of the basement was reduced in increments of 1 m. The mass of the structure was concurrently reduced in order to keep the ratio of U/W constant. All other properties were kept constant, including the location of the centre of gravity and the axis of rotation being the centre of the bottom of the basement.

Figure 7.26(b) shows that as the width of the basement was reduced from 5 m to 4 m, the limit of stability was surpassed and the structure went from accumulating minimal to significant rotation. The DRILS model calculated the settlement of the structure to reduce as the width of the structure reduced, up to the point at which significant rotation was accumulated, as shown in Figure 7.26(c). This is likely to be a consequence of the difference in mass between the structures. As the width of the basement was reduced the structure mass was concurrently reduced in order to keep the ratio of U/W constant. A smaller mass resulted in a smaller moment loading imposed by the structure on the soil surrounding the basement. This reduced the vertical load needed to avoid lift off so settlement due to ratcheting decreased.

The results of this parametric study show that the stability of a structure with a basement during earthquake induced liquefaction is highly sensitive to the width of the basement. It is important for the design of structures with basements in liquefiable soils to take this into consideration, as a small change in basement width has been shown to have a significant effect on the residual rotation of the structure.

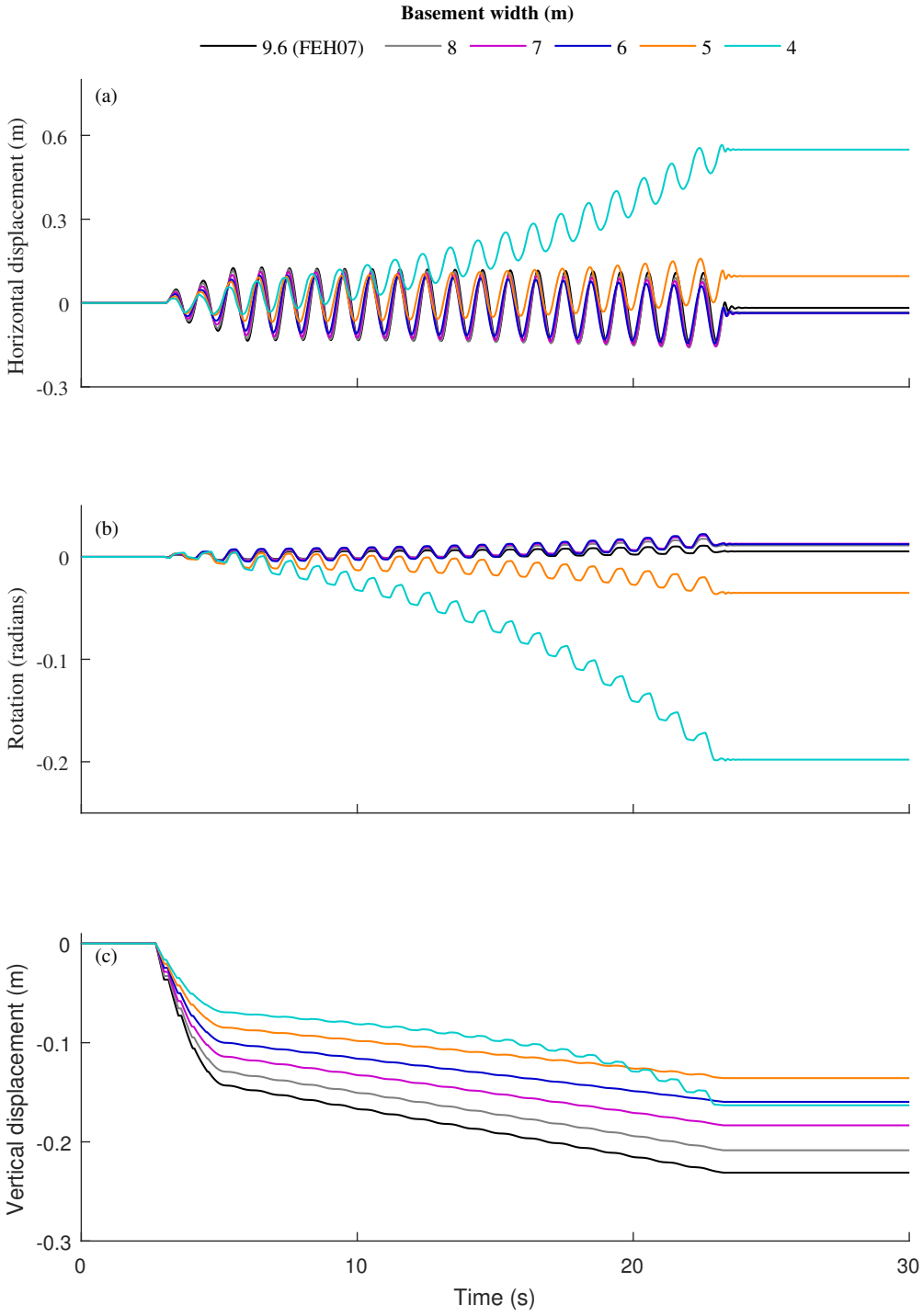

Fig. 7.26 Parametric study to investigate the effect of the width of the basement on the liquefaction induced accumulation of displacement and rotation of a symmetric structure with the centre of gravity located 0.53 m above the soil surface. Reference point: the structure tested in FEH07 with a 9.6 m wide basement.

Amplitude of sinusoidal input motion

The moment loading imposed by the structures with basements on the soil is highly depended on the amplitude of the base shaking, as shown by Equations 5.9 to 5.12. It is therefore of interest to investigate the change in behaviour of the structures for different amplitude base shaking, when the base shaking is of sufficient amplitude to liquefy the soil surrounding the basements.

The asymmetric structure with a wide basement tested in FEH08, which accumulated significant rotation, was used as the starting point and the ampltidue of the sinusoidal base shaking was incrementally reduced. All other properties, including the excess pore pressure ratios, were kept constant. Figure 7.27(b) shows that as the amplitude of the sinusoidal base shaking was incrementally decreased, the accumulation of rotation decreased. The non-zero accumulation of rotation indicates that the moment loading imposed by the structures exceeded the resistance provided by the soil. However, the amount in which it was exceeded reduced, therefore smaller rotation was accumulated per cycle of shaking.

In practice, the number of cycles required to reach the maximum excess pore pressure ratio will increase with the reduction in amplitude of base shaking. This effect was not included in the simulations shown in Figure 7.27 to allow for the effect of shaking amplitude on moment loading to be isolated. It is expected that inclusion of the change in number of cycles to reach the maximum excess pore pressure ratio would further reduce the accumulation of rotation as base shaking acceleration is reduced.

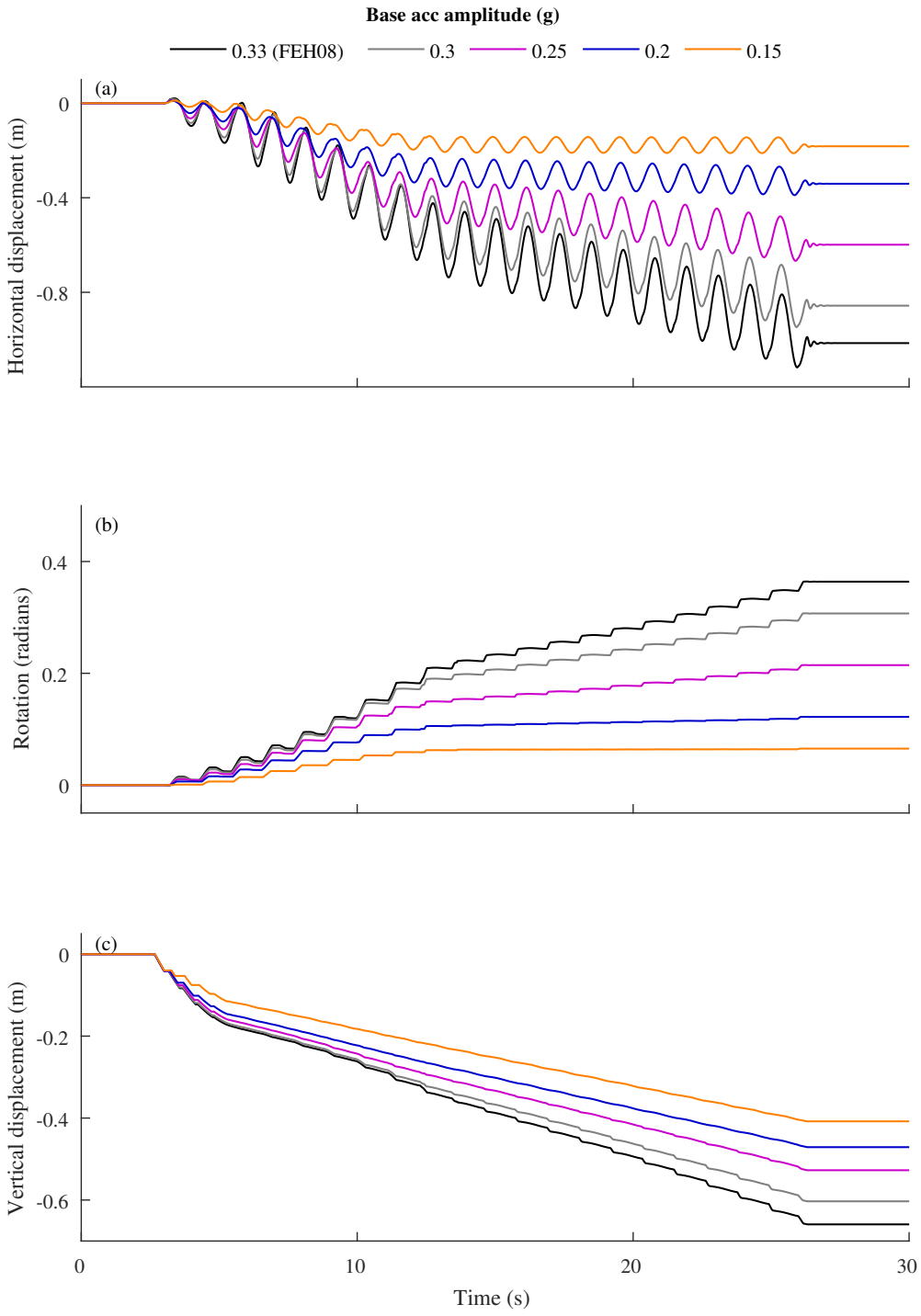

Fig. 7.27 Parametric study to investigate the effect of the amplitude of sinusoidal base shaking on the liquefaction induced accumulation of displacement and rotation of the asymmetric structure with a wide basement tested in FEH08 with a centre of gravity located 1.4 m above the soil surface and 0.18 m from the centreline of the basement. Reference point: the amplitude of the base shaking during EQ3 in the centrifuge test series.

Realistic input motion

The behaviour of the structures with basements during realistic earthquake input motions is of particular interest to practising engineers. During the centrifuge test series, a number of realistic earthquake input motions were replicated using the servo-hydraulic earthquake actuator. However, in each centrifuge test, the first large earthquake to cause liquefaction of the entire soil layer was chosen to be sinusoidal to allow the soil-structure interaction effects to be more easily decoupled. The centrifuge test series therefore provided limited data on the liquefaction induced behaviour of structures with basements during realistic earthquake input motions. For this reason, the DRILS model was used to investigate how the accumulation of displacement and rotation differs between sinusoidal and realistic earthquake input motions.

Artificially generated input data for the DRILS model was produced using data obtained from the centrifuge test FEH07, where earthquakes were fired with both the Imperial Valley and Kobe earthquake waveforms, which had a peak base acceleration of 0.131 g and 0.284 g respectively. Base shaking acceleration and excess pore pressure time histories were utilised. They were scaled to allow a comparison to be made between base shaking time histories with different characteristics but the same peak amplitude or the same Arias intensity.

Figure 7.28 shows the difference in behaviour of the structures with wide basements tested in centrifuge tests FEH06, FEH07 and FEH08 when subjected to base shaking with difference characteristics with a peak amplitude of 0.33 g. In each case, the base shaking acceleration was scaled to have the same peak amplitude, and the excess pore pressure ratio was scaled to have the same maximum that was recorded during EQ3 of the centrifuge test series presented in Chapter 5. From Figure 7.28(j) it can be seen that the sinusoidal input motion consisted of 20 cycles of shaking with an amplitude equal to the specified peak amplitude of 0.33 g, whilst the realistic earthquake motions only had one cycle of shaking with this amplitude.

It is evident from Figure 7.28 that the most destructive of the three base shaking input motions was the sinusoidal wave form shown in turquoise. This resulted in the greatest settlement of the structure with properties the same as that tested in FEH06 (Figure 7.28(g)), and the greatest rotation of the structure with properties the same as that tested in FEH08 (Figure 7.28(f)). This is likely to be because of the greater number of cycles at the peak amplitude which was set for all three input motions, as shown in Figure 7.28(j). Despite the asymmetry in the input motion, the symmetric structures did not accumulate notable rotation when subjected to the non symmetric, realistic earthquake input motions, as shown in Figures 7.28(d,e).

An alternative way to investigate the influence of base shaking characteristics is to normalise with respect to Arias intensity, which is a measure which roughly corresponds to

the energy of the base shaking input motion (Arias 1970). Figure 7.29 shows the difference in behaviour of the structures tested with wide basements in Tests FEH06, FEH07 and FEH08 when subjected to base shaking of difference characteristics with the same Arias intensity as the sinusoidal base shaking in EQ3 in the centrifuge test series. From Figure 7.29(j) it can be seen that matching the Arias intensity results in the realistic earthquake input motions having a greater peak amplitude than the constant amplitude sinusoidal input motion.

The accumulation of settlement and rotation of the structures with basements during base shaking of different characteristics is more closely matched when the input motions have the same Arias intensity, shown in Figure 7.29, than when the input motions have the same peak amplitude, shown in Figure 7.28. However, the sinusoidal wave form, shown in turquoise, remains the most destructive of the three base shaking input motions. This is most notable for the asymmetric structure tested in FEH08 which accumulated significant rotation during sinusoidal base shaking, which was observed in the centrifuge tests presented in Chapter 5.

It can therefore be concluded that sinusoidal input motion is more destructive to structures with wide basements during earthquake induced liquefaction than realistic earthquake input motions with the same peak amplitude or the same Arias intensity. The centrifuge test data presented in Chapter 5 therefore is a cautious and possibly pessimistic view on how structures with wide basements would behave during earthquake induced liquefaction.

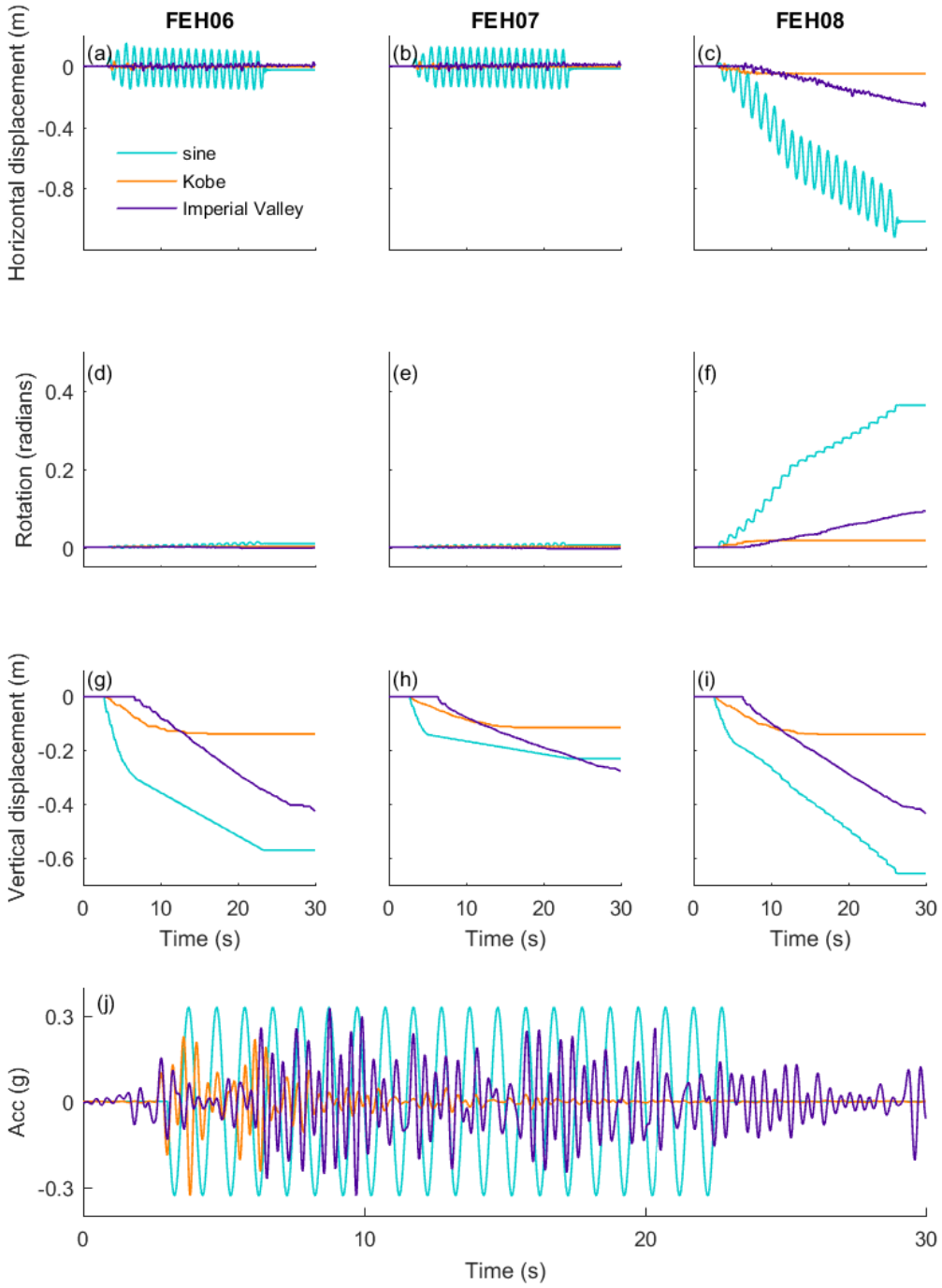

Fig. 7.28 Parametric study to investigate the effect of base shaking characteristics with the same peak amplitude on the liquefaction induced accumulation of displacement and rotation of structures with wide basements. Input motions have the same peak amplitude of 0.33 g.

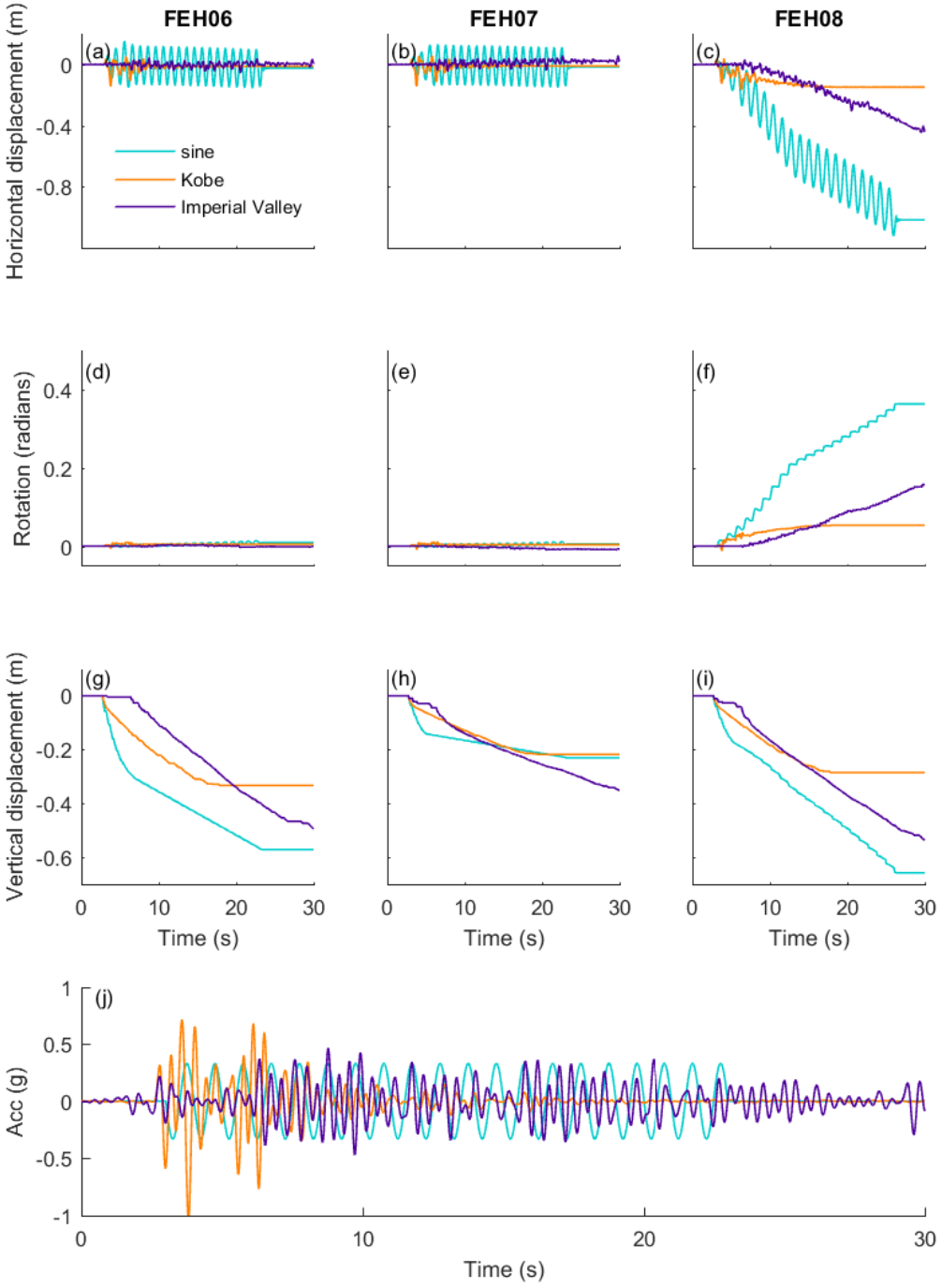

Fig. 7.29 Parametric study to investigate the effect of base shaking characteristics with the same Arias Intensity on the liquefaction induced accumulation of displacement and rotation of structures with wide basements. Input motions have the same total Arias Intensity as EQ3 in the centrifuge test series.

7.5 Limitations and possible extensions

As with all simplified methods, there are a number of limitations that must be noted.

The mechanical model developed in this chapter relies heavily on the data obtained from the discrete instrumentation in the centrifuge model measuring horizontal acceleration and pore pressure. Specifically, both the loading imposed by the structures with basements and the resistance provided by the surrounding soil are highly dependent on the excess pore pressure measurements. During earthquake induced liquefaction, it is possible that these instruments can displace, particularly when they are positioned close to a structure that accumulates rotation or displacement. The change in pre and post earthquake hydrostatic pore pressure was used to estimate the vertical displacement of the pore pressure transducers during shaking, and this was accounted for in the DRILS model. However, it was not possible to accurately incorporate the possible change in displacement with time for every instrument. This may have resulted in inaccuracies in the calculated loading imposed by the structures with basements and the resistance provided by the surrounding soil.

The slider constants used in the DRILS model to calculate the accumulation of rotation and displacement were derived from the centrifuge tests where significant displacement and rotation were accumulated. As a result, their values were heavily dependent on the outcome of a small number of centrifuge tests. In addition, the basements in the tests used for this purpose had a very limited range of dimensions. It is important, therefore, to avoid using the DRILS model to extrapolate outside of the range of input parameters which were used to develop it. For this reason, the parameteric studies conducted in this chapter used structure properties and base shaking characteristics which were intermediate to the ones used in the centrifuge tests. Calibration of the model using an increased number of centrifuge tests, with a wider range of structure properties, would widen the parameter range over which the model could be used with confidence. In addition, it would enable the effect of basement width and point of rotation on the rotation slider constant to be decoupled.

The dynamic response of the superstructure was not included in the DRILS model developed in this chapter. A single degree of freedom sway frame was used in the centrifuge tests, and was idealised as a rigid body in the DRILS model, characterised by its mass, centre of gravity and moment of inertia. Not including the effect of damping within the superstructure may have resulted in the DRILS model overestimating the displacement and rotation of the basement.

This model has been developed for structures with basements which almost compensate for the weight of the structure when liquefaction occurs. The co-seismic behaviour in the soil directly beneath the basement of these structures is representative of the entire column of soil beneath the basements, as shown in excess pore pressure time histories obtained from

the centrifuge tests which are shown in Figures 4.12 and 5.3. As a result, the soil behaviour beneath the basement was characterised by only one location and that was used to estimate the resistance provided by the soil beneath the basements. The DRILS model developed in this chapter is therefore not suitable for structures without basements, or for structures with basements which result in a much smaller ratio of U/W than those tested in the centrifuge tests presented in this thesis. Its use is also limited in cases where small amplitude base shaking only liquefies a fraction of the full depth of the soil layer, as shown in Figures 7.17 and 7.18. In these cases, the soil directly beneath the the structure is not representative of the entire column of soil below the structure.

As a consequence, the model will under-predict the magnitude of settlement of structures with shallow foundations without basements on deep layers of liquefiable soils if the excess pore pressure ratio at shallow depths below the structure is used. The model could be manipulated to be applicable for these scenarios by effectively modelling the structure with a shallow foundation to have rigid vertical extenders that extend to the depth of the non-liquefied bulb beneath it. However, the coupling of the V-H-M loading is unlikely to be modelled correctly given that the structure is not actually attached to this column of soil. Extending the DRILS model to replicate the settlement of structures with shallow foundations would make a worthwhile extension to what has been presented in this chapter, however it is beyond the scope of this research project.

Finally, the model has been developed for one type and density of loose, saturated sand, which corresponds to what was used in the centrifuge test series. It would be desirable to extend the application of the model to a wider range of densities. Furthermore, inclusion of a method to predict the excess pore pressure response around the basement of a structure for a given base shaking input motion would be of particular use to practising engineers. A large number more centrifuge tests, using a range of soil properties and input motions, would be required to calibrate the the model and provide useful output to this end.

7.6 Conclusions

In this chapter, a mechanical model was developed to model the displacement and rotation of a structure with a basement during earthquake induced liquefaction. It was called the DRILS - "Displacement and Rotation in Liquefiable Soil" - model. This model enabled further insight to be obtained on the behaviour of the structures with basements observed in the centrifuge tests. It also allowed the findings from the centrifuge tests to be applied to a wider number of structure properties and input motions, intermediate to those used in the centrifuge test series.

The DRILS model developed in this chapter was able to closely replicate the dynamic response of the structures with basements observed in the centrifuge tests presented in Chapters 4 and 5. The addition of sliders to this traditional mass-spring-damper model enabled liquefaction induced accumulation of displacement and rotation to be included. This substantially increased the functionality of this model, because it was then able to replicate the most problematic behaviour observed in the centrifuge tests.

Within the DRILS model, a methodology was proposed to calculate the reduction in vertical resistance provided by the soil due to positive excess pore pressure generation and simultaneous V-H-M loading, and it was compared to the concurrent reduction in vertical load imposed by the structures due to the increase in uplift force provided by the basements due to positive excess pore pressure generation. It was found that the vertical load imposed by the structures remained below the vertical load required for bearing failure. However, the loading did reduce to less than the vertical load required to prevent lift-off for the given moment loading. Ratcheting was therefore the likely cause of the liquefaction induced settlement of the structures with basements seen in the centrifuge tests.

The DRILS model was used to conduct parametric studies to investigate the effect of the basement width, height of centre of gravity and base shaking characteristics on the behaviour of structures with basements during earthquake induced liquefaction. A number of findings were made which are valuable additions to the conclusions drawn from the centrifuge tests presented in Chapters 4 and 5.

Firstly, the accumulation of rotation of a structure with a basement was found to be more significantly affected by the height of the centre of gravity than the eccentricity, for the range of locations of centre of gravity presented in this thesis. The parametric studies showed that the eccentric structure in Test FEH08 would have suffered significant rotation during EQ3 in the centrifuge test series if its centre of gravity was moved in the horizontal direction to make it symmetric about the centreline of the basement, whilst all other properties remained unchanged. The height of the centre of gravity was the primary factor which governed whether rotation of the structure occurred, and the eccentricity worsened the situation further.

The parametric studies also showed that the magnitude of accumulated rotation gradually decreased as the amplitude of the base acceleration was incrementally reduced. In contrast, when the width of the basement was incrementally reduced, an abrupt reduction in stability occurred. The structure with a basement went from accumulating minimal to significant rotation when a width corresponding to the limit of stability was surpassed.

The DRILS model developed in this chapter was used to show that sinusoidal input motion is more destructive to structures with wide basements during earthquake induced liquefaction than realistic earthquake input motions with the same peak amplitude or the

same Arias intensity. The centrifuge test data presented in Chapter 4 and 5 are therefore a cautious and possibly pessimistic view on how structures with basements would behave during earthquake induced liquefaction.

Chapter 8

Conclusions

This research project was the first of its kind to conduct a detailed investigation into the seismic behaviour of structures with basements in liquefiable soil. In this chapter, the main conclusions will be summarised, their implications to practice will be considered, and recommendations for future research will be made.

8.1 Main conclusions

8.1.1 Seismic behaviour of structures with basements in liquefiable soil

The series of highly instrumented dynamic centrifuge tests presented in this thesis have provided a plethora of novel data on the seismic behaviour of structures with basements in liquefiable soil. In particular, digital image correlation has provided invaluable insight into the soil-structure interaction between the basement and the surrounding soil.

The behaviour of structures with basements in liquefiable soil can be best understood by considering the vertical forces acting on the structure. In static conditions, an upward buoyancy force is present due to hydrostatic water pressure. This uplift force increases when positive excess pore pressures are generated, for example during shaking of a loose, saturated soil layer. Consequently, the effective weight of a structure with a basement reduces. The dynamic centrifuge tests showed that this had the positive desired effect of reducing liquefaction induced settlement of the structure, compared to structures with shallow foundations without basements. This was in spite of the positive excess pore pressures concurrently reducing the stiffness and strength of the soil, which degraded its vertical capacity. These tests identified a number of key design parameters for structures with basements that must be controlled for minimal liquefaction induced settlement and rotation

to be accumulated, which include the total weight of the structure, location of the centre of gravity, and basement geometry.

The liquefaction induced vertical displacement of a structure with a basement was found to be highly sensitive to the ratio of uplift to total weight when the surrounding soil liquefies, U/W. For the geometry of the structures tested in this series of centrifuge tests, structures with a ratio of U/W less than approximately 0.8 were observed to settle. Soil displacements obtained from digital image correlation using GeoPIV-RG (White et al. 2003, Stanier et al. 2015) showed that settlement was primarily due to ratcheting when the structures with basements rocked from side to side. For structures with U/W less than approximately 0.8, increased ratcheting, compared to structures with shallow foundations without basements (Adamidis 2017), was found to have a greater effect on the settlement than the reduction in effective bearing pressure due to the buoyancy force provided by the basement. Structures with a ratio of U/W approximately equal to 0.9 were found to result in the structure accumulating minimal liquefaction induced vertical displacement. Soil-structure interaction results in this ratio being less than unity.

Structures with basements were found to be susceptible to suffer large accumulation of rotation during earthquake induced liquefaction. A reduction in vertical confinement reduced both the vertical and horizontal stresses below the basements, which in turn resulted in decreased resistance to rotation provided by the soil. This was found to be exacerbated by an increase in the moment loading imposed by the structure due to the presence of a basement. In comparison to structures with shallow foundations without basements located on dry sand (Gajan et al. 2005, Gajan & Kutter 2008, Heron et al. 2015) or on liquefiable layers (Adamidis & Madabhushi 2018*c*), the structures with basements presented in this thesis were found to transmit a greater moment to the surrounding soil. This was primarily due to the increased lever arm of all inertia forces because rotation occurred about a point below the soil surface, as opposed to at the soil surface. In addition, the couple due to the non-co-linear weight and buoyancy force did not re-right the structure, and instead worsened the rotation. Oscillations in excess pore pressure under the edges of a basement indicate that strength was regained during shaking due to dilation of the soil. The liquefied soil only momentarily behaved as a dense fluid, before it dilated and returned to behaving like a soil. This resulted in an increase in resistance which restricted the rate of rotation and prevented the structures with basements from toppling uncontrollably. However, in some cases, the resistance was insufficient to keep the rotation of the structure within tolerable limits.

Rigid, vertical extenders, which were attached to the sides of the basement and extended for half the depth of the liquefiable layer, were found to be ineffective at improving the stability of structures with narrow basements. This was surprising as this geometry is

analogous to use of a bilge keel in naval engineering to reduce a ship's tendency to roll (Biran 2003). The vertical extenders resulted in the mobilisation of a bigger failure mechanism compared to the case with no vertical extenders. They changed the point of rotation, however rotation still occurred because the liquefied soil could offer insufficient resistance as it had close to zero strength. Localised piping was observed adjacent to the rotating basement. An opening occurred, and contact was lost between the basement and soil adjacent to it. The gain in resistance implied by lateral extension of the soil and suction spikes in the pore pressure measurements was not transferred to the structure. The worsened behaviour for this basement configuration is concerning as this is the likely geometry of structures with basements when the construction process is considered; diaphragm walls extending below the bottom of a basement are commonly used for construction and then left in place (Tomlinson 2001).

Residual rotation was found to be reduced by increasing the plan area of the basement, either by increasing the width of the basement or using rigid, horizontal extenders protruding horizontally from the sides of a narrower basement. For simplicity, this can be be considered by assuming that a semi-cylinder of soil rotates with the structure, which is an approximation of what was observed in the centrifuge tests. Increasing the basement width requires shearing along a plane with an increased cross sectional area and displacing a larger volume of soil, both which provide increased resistance to rotation, including when the soil is liquefied.

An additional benefit of the reduction in effective bearing pressure due to the presence of a basement is that it allowed the positive excess pore pressures in the column of soil below the structure to approach the corresponding values of initial vertical effective stress. This was found to have the beneficial effect of naturally isolating the structure from the base shaking. It is interesting to compare this behaviour to conventional mitigation methods used to reduce liquefaction induced settlement of structures. Ground improvement methods are commonly used to remove or reduce the tendency for soil to liquefy, for example soil improvement, reducing the degree of saturation of the soil, and improving drainage using vertical drains. However, these methods have the negative result of increasing the seismic demand of the structure (Zeybek & Madabhushi 2016, Olarte, Dashti & Liel 2018, Paramasivam et al. 2018). By reducing the extent of soil liquefaction they remove the natural isolation provided by attenuation of horizontal accelerations in liquefied soil.

The centrifuge test results presented in this thesis show that basements can be used to reduce the liquefaction induced settlement of structures whilst maintaining the natural isolation provided by liquefied soil. The width of the widest section of the basement and the net weight of the structure during liquefaction were found to be the key design parameters to ensure minimal settlement and rotation were accumulated. In addition, the height and eccentricity of the centre of gravity were found to be important parameters to consider, as

rotation was found to be problematic once more when the height or eccentricity of the centre of gravity were increased above a threshold (specific to the weight and geometry of the specific structure), as this increased the moment transferred from the structure to the soil.

Finally, it should be noted that the structures with basements located in liquefiable soil performed advantageously during small magnitude shaking events that did not liquefy the entire soil layer. They accumulated minimal settlement, despite shaking being strong enough to cause the adjacent soil surface to settle. Negligible rotation was accumulated, regardless of whether the mass distribution in the structure was symmetric or asymmetric.

8.1.2 Predicting the seismic behaviour of structures with basements in liquefiable soil

A mechanical model for displacement and rotation in liquefiable soil was developed in Chapter 7 using data from the centrifuge test series. The DRILS - "Displacement and Rotation In Liquefiable Soil" - model was able to closely replicate the dynamic response of the structures with basements observed in the centrifuge tests. The addition of sliders to the traditional mass-spring-damper model enabled accumulation of liquefaction induced displacement and rotation to be included. This substantially increased the functionality of the model, because it was then able to replicate the most problematic behaviour observed in the centrifuge tests.

Within the DRILS model, a methodology was proposed to calculate the reduction in vertical resistance provided by the soil due to positive excess pore pressure generation and simultaneous V-H-M loading. This was compared to the concurrent reduction in vertical load imposed by the structures due to the increase in uplift force provided by the basements due to positive excess pore pressure generation. It was found that the vertical load imposed by the structures remained below the vertical load required for bearing failure. However, the loading did reduce to less than the vertical load required to prevent lift-off for the given moment loading. Ratcheting was therefore the likely cause of the liquefaction induced settlement of the structures with basements observed in the centrifuge tests. This corroborates with the soil displacements observed in the centrifuge tests.

Parametric studies were conducted using the DRILS model to extend the findings from the centrifuge test series to a wider range of structure properties and input motions. The effect of the basement width, height of centre of gravity, and base shaking characteristics on the behaviour of structures with basements during earthquake induced liquefaction were investigated. The parametric studies showed that the magnitude of accumulated rotation gradually increased when either the amplitude of the base acceleration or the height of the

centre of gravity above the soil surface were incrementally increased. In contrast, when the width of the basement was incrementally reduced, an abrupt reduction in stability occurred. The structure with a basement went from accumulating minimal to significant rotation when a width corresponding to the limit of stability was surpassed.

The parametric studies also show that sinusoidal input motion is more destructive to structures with wide basements during earthquake induced liquefaction than realistic earthquake input motions with the same peak amplitude or the same Arias intensity. The centrifuge test data presented in Chapters 4 and 5 is therefore a cautious and possibly pessimistic view on how structures with basements would behave during earthquake induced liquefaction.

8.1.3 Cone Penetration Tests in liquefiable soil adjacent to structures with basements

The combination of Cone Penetration Test (CPT) data with soil displacements obtained from digital image correlation using GeoPIV-RG (White et al. 2003, Stanier et al. 2015) has provided novel insight into the change in cone resistance before and after a sequence of earthquakes.

Changes in horizontal strains resulting from the liquefaction induced settlement and rotation of a structure with a basement were found to correlate with the measured changes in cone resistance. It was assumed that changes in horizontal stress were proportional to the observed changes in horizontal strain. Compressive horizontal strain, implying an increase in horizontal stress, was found to correlate with an observed increase in cone resistance. Likewise, extension in the horizontal direction, implying a decrease in horizontal stress, was found to correlate with a decrease in cone resistance. In contrast, compressive volumetric strain, implying a decrease in void ratio and an increase in relative density, did not correlate with observed increases in cone resistance.

The data presented in this thesis shows that, in clean sands, the change in cone resistance before and after a sequence of earthquakes is dependent on accumulated horizontal strains. This implies that the post liquefaction cone resistance is dependent on horizontal effective stress. The change in cone resistance was found to be less dependent on changes in volumetric strain, and therefore changes in relative density. A larger data set and an increase in the resolution of the images obtained from the high-speed camera may enable quantitative correlations to be made.

8.2 Implications to practice

The findings from this research project have a number of implications to practice.

Firstly, it has been shown that structures with basements in liquefiable soil can perform advantageously during large amplitude earthquakes which liquefy the soil layer. This is in contrast to the behaviour of structures with shallow foundations in the same conditions, which can suffer large settlement and rotation (Adachi et al. 1992, Tokimatsu et al. 1994, Hwang et al. 2003, Gazetas et al. 2004, Cubrinovski et al. 2011, Bertalot et al. 2013, Bray & Dashti 2014). By including a basement, and controlling the basement geometry, mass distribution, and total weight of the structure, the accumulated settlement and rotation, and seismic demand of the structure can be minimised. Stability can be achieved by constructing wide basements, or constructing horizontal grouted anchors or a continuous wider base slab. The increase in usable space that a basement provides in a building is anticipated to make this mitigation method an attractive option compared to conventional mitigation methods such as soil improvement. Further research is required to enable building codes to be developed for this purpose.

The centrifuge tests showed that the method of construction of basements in liquefiable soils must be carefully considered. Rigid, vertical extenders attached to the sides of a basement were found to adversely affect the behaviour of structures with basements during liquefaction. This is concerning as this is the likely geometry of structures with basements when the construction process is considered; diaphragm walls extending below the bottom of a basement are commonly used for construction and then left in place (Tomlinson 2001).

Finally, the combination of CPT data with soil displacements obtained from digital image correlation using GeoPIV-RG (White et al. 2003, Stanier et al. 2015) has potential implications to the current state-of-practice for liquefaction susceptibility analysis. The empirical charts that are used to determine whether regions are "safe" or "not safe" from liquefaction have been developed using post earthquake SPT and CPT data. The data presented in this thesis show that using post liquefaction CPTs to determine pre-earthquake soil conditions may be misleading if changes in horizontal stress due to soil-structure interaction are not considered. Compression of soil in the horizontal direction due to liquefaction induced settlement or rotation of a structure in the proximity of where a CPT is driven can cause an increase in cone resistance. Likewise, extension of soil in the horizontal direction can result in a reduction in cone resistance. For the soil used in the centrifuge tests presented in this thesis (clean sands with normalised tip resistances less than 60), the classification of susceptibility to liquefaction was found not to be affected by whether the cone resistance used was obtained before or after a sequence of earthquakes. However, it

is possible that the use of pre or post earthquake CPT data may change the classification of sites with soil with increased normalised CPT tip resistance or which include fines.

8.3 Recommendations for future research

This research project was the first of its kind to conduct a detailed investigation into the seismic behaviour of structures with basements in liquefiable soil. This thesis has presented many interesting and useful conclusions which were obtained from a series of highly instrumented dynamic centrifuge tests. This project has also identified a number of areas where further research is required to enable the findings of this research project to be applied in industry with confidence.

The ideal outcome of future research on this topic would be a reliable, simplified methodology to predict the settlement and rotation of structures with basements, of different weights and geometries, in liquefiable soil following earthquakes of varying magnitude. This would enable building codes to be developed for structures with basements in liquefiable soils in seismic areas. For this purpose, further centrifuge tests are invaluable. Specifically, tests to isolate the effects of aspect ratio and mass eccentricity would be important. Changes in structure height and basement depth would be informative. Tests investigating the behaviour in different soil types and densities, thickness of the liquefiable layer, and layered stratigraphy would provide a truer replication of soil conditions in the field. It would also be desirable to incorporate liquefaction susceptibility analyses into the methodology, as the centrifuge tests presented in this thesis have shown that the presence of a basement has a significant impact on the seismic behaviour of the soil surrounding it.

An increase in detailed documented cases from post earthquake reconnaissance missions on the behaviour of structures with basements following large earthquakes would be invaluable. Both positive and negative observations would greatly improve the understanding of these type of structures. They would also enable proposed building codes to be validated.

In addition, it would be worthwhile to establish the capacity of different numerical tools to capture the results of the centrifuge experiments presented in this thesis. Numerical simulations can be useful as they can facilitate large parametric studies with relative ease. However, this is only productive if the soil behaviour is captured by the constitutive model and soil-structure interaction is incorporated in the analyses.

This research project has identified an opportunity for further research into the combination of CPT data with soil displacements obtained from digital image correlation to obtain insight into the change in cone resistance before and after a sequence of earthquakes. A key development would be to increase the number of data entries and the resolution of the

images obtained from the high-speed camera to enable quantitative correlations to be made. The observations presented in this thesis could also be extended to different mechanisms of failure in geotechnics.

8.3.1 Example case studies

The recommendations for future research can be better understood by considering a couple of example case studies.

Let us suppose we have a two storey residential building located on liquefiable soil, which imposes a bearing pressure of 35 kPa when no basement is present. This research project has shown that liquefaction induced settlement can be reduced by including a basement with a depth of approximately 1.8 m. The centre of gravity of the structure is likely to be approximately 1 - 1.5 m above the soil surface. The data presented in this thesis has shown that if the structure is approximately 10 m wide it is unlikely to suffer problematic residual rotation during horizontal shaking with a maximum amplitude of 0.3 g. If the residential building is narrower or has an eccentric mass distribution, further research is required to understand the critical aspect ratio to ensure that residual rotation is not problematic.

Instead, let us suppose we have a five storey building on liquefiable soil, which imposes a bearing pressure of 80 kPa when no basement is present. This research project has shown that liquefaction induced settlement should be reduced by including a basement with a depth of approximately 4 m. The centre of gravity of the structure is likely to be approximately 5 m above the soil surface. Further research is required to understand the critical aspect ratio, and consequently width of the building, to ensure that residual rotation is not problematic. The importance of this issue increases when the number of storeys increases, as the height of the centre of gravity and the moment loading imposed by the structure both increase.

Finally, let us consider a 12 storey building on liquefiable soil, which imposes a bearing pressure of 190 kPa when no basement is present. This research project has shown that liquefaction induced settlement should be reduced by including a basement with a depth of approximately 10 m. It is anticipated that the critical aspect ratio to prevent problematic residual rotation may make the required plan size of the structure infeasible. A three storey basement would be required to limit liquefaction induced settlement. Further research is required to understand the behaviour if only a one or two storey basement was included, during horizontal base shaking of different amplitudes.

References

Acacio, A. A., Kobayashi, Y., Yowhata, I., Bautista, R. T. & Ishihara, K. (2001), 'Subsidence of building foundation resting upon liquefied subsoil: case studies and assessment', *Soils and Foundations* **41**(6), 111–128.

Adachi, T., Iwai, S., Yasui, M. & Sato, Y. (1992), Settlement and inclination of reinforced concrete buildings in Dagupan City due to liquefaction during the 1990 Philippine earthquake, *in* 'Earthquake Engineering, 10th World Conference', pp. 147–152.

Adamidis, O. (2017), Earthquake-induced liquefaction of sand and response of structures with shallow foundations, Phd, University of Cambridge.

Adamidis, O. & Madabhushi, S. P. G. (2015), Deformation Mechanisms Under Shallow Foundations During Earthquake-Induced Liquefaction, *in* '6th International Conference on Earthquake Goetechnical Engineering', Christchurch, New Zealand.

Adamidis, O. & Madabhushi, S. P. G. (2018*a*), 'Deformation mechanisms under shallow foundations on liquefiable layers of varying thickness', *Géotechnique* **68**(7), 602–613.

Adamidis, O. & Madabhushi, S. P. G. (2018*b*), 'Experimental investigation of drainage during earthquake-induced liquefaction', *Géotechnique* **68**(8), 655–665.

Adamidis, O. & Madabhushi, S. P. G. (2018*c*), Rotatonal response of shallow foundations on liquefiable sand, *in* K. Pitilakis, ed., '16th European Conference on Earthquake Engineering', Thessaloniki, Greece.

Arias, A. (1970), *A measure of earthquake intensity*, MIT Press, Cambridge, Massachusetts.

Beber, R., Madabhushi, S. S. C., Dobrisan, D., Haigh, S. K. & Madabhushi, S. P. G. (2018), LEAP GWU 2017 : Investigating different methods for verifying the relative density of a centrifuge model, *in* A. McNamara, S. Divall, R. Goodey, R. N. Taylor, S. Stallebrass & J. Panchal, eds, '9th International Conference on Physical Modelling in Geotechnics', Taylor and Francis Group, London, United Kingdom, pp. 125–130.

Been, K. & Jefferies, M. G. (1985), 'A state parameter for sands', *Géotechnique* **35**(2), 99–112.

Bertalot, D. & Brennan, A. J. (2015), 'Influence of initial stress distribution on liquefaction-induced settlement of shallow foundations', *Géotechnique* **65**(5), 418–428.

Bertalot, D., Brennan, A. J. & Villalobos, F. A. (2013), 'Influence of bearing pressure on liquefaction-induced settlement of shallow foundations', *Géotechnique* **63**(5), 391–399.

Bhattacharya, S., Hyodo, M., Goda, K., Tazoh, T. & Taylor, C. A. (2011), 'Liquefaction of soil in the Tokyo Bay area from the 2011 Tohoku (Japan) earthquake', *Soil Dynamics and Earthquake Engineering* **31**(11), 1618–1628.

Biran, A. B. (2003), *Ship Hydrostatics and Stability*, Butterworth-Heinemann.

Bolton, M. D. (1986), 'The strength and dilatancy of sands', *Géotechnique* **36**(1), 65–78.

Bolton, M. D. & Gui, M. W. (1993), CUED/D-SOILS/TR256: The Study of Relative Density and Boundary Effects for Cone Penetration Tests in Centrifuge, Technical report, Department of Engineering, University of Cambridge.
URL: *http://www-civ.eng.cam.ac.uk/geotech_new/publications/TR/TR256.pdf*

Bolton, M. D., Gui, M. W., Garnier, J., Corte, J. F., Bagge, G., Laue, J. & Renzi, R. (1999), 'Centrifuge cone penetration tests in sand', *Géotechnique* **49**(4), 543–552.

Bolton, M. D., Gui, M. W. & Phillips, R. (1993), Review of Miniature Soil Probes For Model Tests, *in* 'Eleventh Southeast Asian Geotechnical Conference', Singapore, pp. 85–91.

Boulanger, R. W. (2003), 'High Overburden Stress Effects in Liquefaction Analyses', *Journal of Geotechnical and Geoenvironmental Engineering* **129**(12), 1071–1082.

Bray, J. D. & Dashti, S. (2014), 'Liquefaction-induced building movements', *Bulletin of Earthquake Engineering* **12**(3), 1129–1156.

Bray, J. D. & Luque, R. (2017), 'Seismic performance of a building affected by moderate liquefaction during the Christchurch earthquake', *Soil Dynamics and Earthquake Engineering* **102**, 99–111.

Bray, J. & Macedo, J. (2017), '6th Ishihara lecture: Simplified procedure for estimating liquefaction-induced building settlement', *Soil Dynamics and Earthquake Engineering* **102**, 215–231.

Brennan, A. J. & Madabhushi, S. P. G. (2002), 'Effectiveness of vertical drains in mitigation of liquefaction', *Soil Dynamics and Earthquake Engineering* **22**(9), 1059–1065.

Brennan, A. J. & Madabhushi, S. P. G. (2005), 'Liquefaction and Drainage in Stratified Soil', *Journal of Geotechnical and Geoenvironmental Engineering* **131**(7), 876–885.

Brennan, A. J., Madabhushi, S. P. G. & Houghton, N. E. (2006), Comparing laminar and equivalent shear beam (ESB) containers for dynamic centrifuge modelling, *in* '6th International Conference on Physical Modelling in Geotechnics', Hong Kong, pp. 171–176.

Budhu, M. & Al-Karni, A. (1993), 'Seismic bearing capacity of soils', *Géotechnique* **1**(43), 181–187.

Bullock, Z., Karimi, Z., Dashti, S., Porter, K., Liel, A. B. & Franke, K. W. (2019), 'A physics-informed semi-empirical probabilistic model for the settlement of shallow-founded structures on liquefiable ground', *Géotechnique* **69**(5), 406–419.

Butterfield, R. & Gottardi, G. (1994), 'A complete three-dimensional failure envelope for shallow footings on sand', *Géotechnique* **44**(1), 181–184.

Carey, T., Gavras, A., Kutter, B. L., Haigh, S. K., Madabhushi, S. P. G., Okamura, M., Kim, D. S., Ueda, K., Hung, W. Y., Zhou, Y. G., Liu, K., M., C. Y., Zeghal, M., Abdoun, T., Escoffier, S. & Manazri, M. (2018), A new shared miniature cone penetrometer for centrifuge testing, *in* A. McNamara, S. Divall, R. Goodey, R. N. Taylor, S. Stallebrass & J. Panchal, eds, '9th International Conference on Physical Modelling in Geotechnics', Taylor and Francis Group, London, United Kingdom, pp. 293–298.

Casagrande, A. (1936), 'Characteristics of cohesionless soils affecting the stability of slopes and earth fills', *Journal of the Boston Society of Civil Engineers* **23**(1), 13–23.

Casagrande, A. (1971), 'On Liquefaction Phenomena, by Professor A. Casagrande: Report of Lecture', *Géotechnique* **21**(3), 197–202.

Cascone, E. & Bouckovalas, G. D. (1998), Seismic bearing capacity of footings on saturated sand with a clay cap, *in* '11th European Conference on Earthquake Engineering', Paris, France.

Castro, G. (1975), 'Liquefaction and Cyclic Mobility of Saturated Sands', *Journal of the Geotechnical Engineering Division* **101**(6), 551–569.

CEN (2004), EN 1998-5, Eurocode 8, Technical report.

CEN (2014), EN 1997-1:2004+A1. Eurocode 7: Geotechnical design - Part 1: General rules, Technical report.

Chian, S. C. (2012), Floatation of Underground Structures in Liquefiable Soils, Phd thesis, University of Cambridge.

Chian, S. C. & Madabhushi, S. P. G. (2012), 'Effect of buried depth and diameter on uplift of underground structures in liquefied soils', *Soil Dynamics and Earthquake Engineering* **41**(1), 181–190.

Chian, S. C. & Tokimatsu, K. (2011), Floatation of Underground Structures during the M w 9 . 0 Tōhoku Earthquake of 11 th March 2011, *in* 'Proceedings of the 15th World Conference on Earthquake Engineering', Lisbon, Portugal.

Chian, S. C., Tokimatsu, K. & Madabhushi, S. P. G. (2014), 'Soil Liquefaction – Induced Uplift of Underground Structures : Physical and Numerical Modeling', *Journal of Geotechnical and Geoenvironmental Engineering* **140**(10), 1–18.

Chopra, A. K. (2014), *Dynamics of Structures: Theory and Applications to Earthquake Engineering*, fourth edi edn, Prentice Hall.

Chou, J. C., Kutter, B. L., Travasarou, T. & Chacko, J. M. (2010), 'Centrifuge Modeling of Seismically Induced Uplift for the BART Transbay Tube', *Journal of Geotechnical and Geoenvironmental Engineering* **137**(8), 754–765.

Coelho, P. A. L. F., Haigh, S. K., Madabhushi, S. P. G. & O'Brien, T. S. (2007), 'Post-earthquake behaviour of footings employing densification to mitigate liquefaction', *Proceedings of the ICE - Ground Improvement* **11**(1), 45–53.

Cubrinovski, M., Bray, J., Taylor, M., Giorgini, S., Bradley, B., Wotherspoon, L. & Zupan, J. (2011), 'Soil Liquefaction Effects in the Central Business District during the February 2011 Christchurch Earthquake', *Seismological Research Letters* **82**(6), 893–904.

Cubrinovski, M., Rhodes, A., Ntritsos, N. & Van Ballegooy, S. (2018), 'System response of liquefiable deposits', *Soil Dynamics and Earthquake Engineering* (Article in press).

Darby, K. M., Boulanger, R. W. & DeJong, J. T. (2017), Effect of multiple shaking events on cone penetration resistances in saturated sand, *in* 'Proceedings of the 3rd International Conference on Performance-based Design in Earthquake Geotechnical Engineering', Vancouver, Canada.

Dashti, S. & Bray, J. D. (2013), 'Numerical Simulation of Building Response on Liquefiable Sand', *Journal of Geotechnical and Geoenvironmental Engineering* **139**(8), 1235–1249.

Dashti, S., Bray, J. D., Pestana, J. M., Riemer, M. & Wilson, D. (2010*a*), 'Centrifuge Testing to Evaluate and Mitigate Liquefaction-Induced Building Settlement Mechanisms', *Journal of Geotechnical and Geoenvironmental Engineering* **136**(7), 918–929.

Dashti, S., Bray, J. D., Pestana, J. M., Riemer, M. & Wilson, D. (2010*b*), 'Mechanisms of Seismically Induced Settlement of Buildings with Shallow Foundations on Liquefiable Soil', *Journal of Geotechnical and Geoenvironmental Engineering* **136**(1), 151–164.

Dewoolkar, M. M., Pak, R. Y. S. & Ko, H.-Y. (1999), 'Centrifuge modelling of models of seismic effects on saturated earth structures', *Géotechnique* **49**(2), 247–266.

Dobry, R. (2014), 'Simplified methods in Soil Dynamics', *Soil Dynamics and Earthquake Engineering* **61-62**, 246–268.

Elgamal, A.-W., Zeghal, M. & Parra, E. (1996), 'Liquefaction of reclaimed island in Kobe, Japan', *Journal of Geotechnical Engineering* **122**(1), 39–49.

Elghazouli, A. Y., ed. (2017), *Seismic design of buildings to Eurocode 8*, 2nd edn, CRC Press, Boca Raton, Florida.

Florin, V. A. & Ivanov, P. L. (1961), Liquefaction of Saturated Sandy Soils, *in* 'The 5th International Conference on Soil Mechanics and Foundation Engineering', Paris, France, pp. 107–111.

Franco, G., Stone, H., Ahmed, B., Chian, S. C., Hughes, F. E., Jirouskova, N., Kaminski, S., Lopez, J., Van Drunen, N. G., Molina Hutt, C. & Querembas, M. (2018), The Muisne, Ecuador Earthquake of 16 April 2016. A field report by EEFIT, Technical report, The Institution of Structural Engineers.
URL: *https://www.istructe.org/resources/report/eefit-mission-muisne-ecuador-earthquake/*

Franco, G., Stone, H., Ahmed, B., Chian, S. C., Hughes, F. E., Jirouskova, N., Kaminski, S., Lopez, J., Van Drunen, N. G. & Querembas, M. (2017), The April 16 2016 MW 7.8 Muisne Earthquake in Ecuador - Preliminary Oberservation from the EEFIT Reconnaissance Mission of May 24 - June 7, *in* '16th World Conference on Earthquake Engineering', Santiago, Chile.

Gajan, S. & Kutter, B. L. (2008), 'Capacity, Settlement, and Energy Dissipation of Shallow Footings Subjected to Rocking', *Journal of Geotechnical and Geoenvironmental Engineering* **134**(8), 1129–1141.

Gajan, S., Kutter, B. L., Phalen, J. D., Hutchinson, T. C. & Martin, G. R. (2005), 'Centrifuge modeling of load-deformation behavior of rocking shallow foundations', *Soil Dynamics and Earthquake Engineering* **25**, 773–783.

Gaudin, C., Schnaid, F. & Garnier, J. (2005), 'Sand characterization by combined centrifuge and laboratory tests', *International Journal of Physical Modelling in Geotechnics* **5**(1), 42–56.

Gay, O., Boutonnier, L., Foray, P. & Flavigny, F. (2003), Laboratory characterization of Hostun RF sand at very low confining stresses, *in* 'Proceedings of the international Conference on Deformation Characteristics of Geomaterials', Lyon, France, pp. 423–430.

Gazetas, G., Apostolou, M. & Anastasopoulos, J. (2004), Seismic Bearing Capacity Failure And Overturning Of ' Terveler ' Building In Adapazari , 1999, *in* 'Fifth International Conference on Case Histories in Geotechnical Engineering', New York, US.

Ghosh, B. & Madabhushi, S. P. G. (2007), 'Centrifuge modelling of seismic soil structure interaction effects', *Nuclear Engineering and Design* **237**(8), 887–896.

Goh, S. & O'Rourke, T. D. (1999), Limit state model for soil–pile interaction during lateral spread, *in* '7th US–Japan workshop on earthquake resistant design of lifeline facilities and countermeasures against soil liquefaction', Seattle, United States.

Gui, M. W. & Bolton, M. D. (1998), Geometry and scale effects in CPT and pile design., *in* '1st International Conference on Site Characterization', Atlanta, United States, pp. 1063–1068.

Guilbert, K. (2017), 'Timeline: World's 14 deadliest earthquakes of last decade'.
URL: *https://www.reuters.com/article/us-iran-quake-global/timeline-worlds-14-deadliest-earthquakes-of-last-decade-idUSKBN1DD257*

Haigh, S. K. (2002), Effects of Earthquake-induced Liquefaction on Pile Foundations in Sloping Ground, PhD thesis, University of Cambridge.

Haigh, S. K., Eadington, J. & Madabhushi, S. P. G. (2011), 'Permeability and stiffness of sands at very low effective stresses', *Géotechnique* **62**(1), 69–75.

Hausler, E. A. & Sitar, N. (2001), Performance of Soil Improvement Techniques in Earthquakes, *in* '4th International Conference on Recent Advances in Geotechnical Earthquake Engineering and Soil Dynamics', San Diego, California.

Hazen, A. (1920), 'Hydraulic fill dams', *Transactions of the American Society of Civil Engineers* **83**(1), 1713–1745.

Heron, C. M. (2013), The dynamic soil structure interaction of shallow foundations on dry sand beds, Phd thesis, University of Cambridge.

Heron, C. M., Haigh, S. K. & Madabhushi, S. P. G. (2015), 'A new macro-element model encapsulating the dynamic moment–rotation behaviour of raft foundations', *Géotechnique* **65**(5), 442–451.

Houlsby, G. T. (1998), Advanced interpretation of field tests, *in* '1st International Conference on Site Characterization', Atlanta, United States, pp. 99–112.

Houlsby, G. T. & Hitchman, R. (1988), 'Calibration chamber tests on a cone penetrometer in sand', *Géotechnique* **38**(1), 39–44.

Hsu, S., Chu, B. & Chang, Y.-M. (2002), 'Liquefaction damage and related remediation in Wufeng after the Chi-Chi earthquake', *Journal of the Chinese Institute of Engineers* **25**(5), 521–532.

Hughes, F. E. & Madabhushi, S. P. G. (2017), Control of liquefaction induced settlement of buildings using basement structures, *in* 'Proceedings of the 3rd International Conference on Performance-based Design in Earthquake Geotechnical Engineering', Vancouver, Canada.

Hughes, F. E. & Madabhushi, S. P. G. (2018*a*), Dynamic Response of a Structure with a Basement Sited on Liquefiable Soil, *in* K. Pitilakis, ed., '16th European Conference on Earthquake Engineering', Springer, Thessaloniki, Greece.

Hughes, F. E. & Madabhushi, S. P. G. (2018*b*), The importance of vertical accelerations in liquefied soils, *in* A. McNamara, S. Divall, R. Goodey, R. N. Taylor, S. Stallebrass & J. Panchal, eds, '9th International Conference on Physical Modelling in Geotechnics', Taylor and Francis Group, London, United Kingdom, pp. 967–973.

Hughes, F. E. & Madabhushi, S. P. G. (2019*a*), Co-seismic rotation and displacement of a structure with a basement sited in liquefiable soil, *in* Silvestri & Moraci, eds, '7th International Conference on Earthquake Geotechnical Engineering', Associazione Geotecnica Italiana, Rome, Italy, pp. 2898–2905.

Hughes, F. E. & Madabhushi, S. P. G. (2019*b*), 'Liquefaction Induced Displacement and Rotation of Structures with Wide Basements', *Soil Dynamics and Earthquake Engineering* **120**, 75–84.

Hwang, J.-H., Yang, C.-W. & Chen, C.-H. (2003), 'Investigations On Soil Liquefaction During The Chi-Chi Earthquake', *Soils and Foundations* **43**(6), 107–123.

Hwang, J.-I., Kim, C.-Y., Chung, C.-K. & Kim, M.-M. (2006), 'Viscous fluid characteristics of liquefied soils and behavior of piles subjected to flow of liquefied soils', *Soil Dynamics and Earthquake Engineering* **26**(2), 313–323.

Ishibashi, I. & Zhang, X. (1993), 'Unified dynamic shear moduli and damping ratios of sand and clay', *Soils and Foundations* **33**(1), 182–191.

Ishihara, K. (1985), Stability of natural deposits during earthquakes, *in* '11th Conference on Soil Mechanics and Foundation Engineering', A. A. Balkema, Rotterdam, The Netherlands, pp. 321–376.

Ishihara, K. (1993), 'Liquefaction and flow failure during earthquakes', *Géotechnique* **43**(3), 351–451.

Ishihara, K. (1996), *Soil Behaviour in Earthquake Geotechnics*, Oxford University Press, New York.

Ishihara, K., Tatsuoka, F. & Yasuda, S. (1975), 'Undrained deformation and liquefaction of sand under cyclic stresses', *Soils and Foundations* **15**(1), 29–44.

Ishihara, K. & Yoshimine, M. (1992), 'Evaluation of Settlements in Sand Deposits Following Liquefaction During Earthquakes', *Soils and Foundations* **32**(1), 173–188.

Isoda, S., Nakai, N., Orense, R. & Towhata, I. (2001), Mitigation of liquefaction-induced uplift of underground strcutures by using sheet pile walls, *in* 'Proceedings of the soil improvement conference', Singapore, pp. 70–77.

Jakub, M. & Roesset, J. M. (1977), Dynamic Stiffness of Foundation: 2-D vs. 3-D Solutions, Technical Report Research Report R77.36, Department of Civil Engineering, Massachusetts Institute of Technology.

Jamiolkowski, M., Ladd, C. C., Germaine, J. T. & Lancellotta, R. (1985), New developments in field and laboratory testing of soils, *in* '11th. Int. Conf. on Soil Mechanics and Foundation Engineering', San Francisco, United States of America, pp. 57–153.

Kang, G. C. (2010), Assessing uplift displacement of buried geotechnical structures in liquefied ground during earthquakes, Phd thesis, Kyoto University.

Karimi, Z. & Dashti, S. (2016), 'Numerical and Centrifuge Modeling of Seismic Soil–Foundation–Structure Interaction on Liquefiable Ground', *Journal of Geotechnical and Geoenvironmental Engineering* **142**(1), 04015061.

Karimi, Z., Dashti, S., Bullock, Z., Porter, K. & Liel, A. (2018), 'Key predictors of structure settlement on liquefiable ground: a numerical parametric study', *Soil Dynamics and Earthquake Engineering* **113**, 286–308.

Kawashima, K. (1999), Seismic design of underground structures in soft ground: A review, *in* 'Geotechnical Aspects of Underground Construction in Soft Ground', Tokyo, Japan, pp. 3–20.

Kirkwood, P. & Dashti, S. (2018), 'Considerations for the Mitigation of Earthquake-Induced Soil Liquefaction in Urban Environments', *Journal of Geotechnical and Geoenvironmental Engineering* **144**(10), 04018069.

Kirkwood, P. & Dashti, S. (2019), 'Influence of prefabricated vertical drains on the seismic performance of similar neighbouring structures founded on liquefiable deposits', *Géotechnique* (Ahead of print).

Kishida, H. (1966), 'Damage to reinforced concrete buildings in Niigata city with special reference to foundation engineering', *Soils and Foundations* **6**(1), 71–88.

Koseki, J., Matsuo, O. & Koga, Y. (1997), 'Uplift behaviour of underground structures caused by liquefaction of surrounding soil during earthquake', *Soils and Foundations* **37**(1), 97–108.

Kumar, J. & Rao, V. B. K. M. (2002), 'Seismic bearing capacity factors for spread foundations', *Géotechnique* **52**(2), 79–88.

Kumar, S. & Prakash, S. (1995), Coupled Horizontal and Rocking Vibration of Block Foundations, *in* 'Third International Conference on Recent Advances in Geotechnical Earthquake Engineering and Soil Dynamics', St. Louis, Missouri, US, pp. 1369–1373.

Lancelot, L., Shahrour, I. & Al Mahmoud, M. (2006), 'Failure and Dilatancy Properties of Sand at Relatively Low Stresses', *Journal of Engineering Mechanics* **132**(12), 1396–1399.

Little, A. L. (1961), *Foundations*, Edward Arnold (Publishers) LTD, London.

Liu, G., Ishikura, R., Yasufuku, N., Kasama, K. & Matsuo, N. (2014), Investigating the Function of Basement for Preventing Liquefaction of Sandy Soil, *in* 'Second European conference on earthquake engineering and seismology', Istanbul, Turkey.

Liu, L. & Dobry, R. (1995), 'Effect of Liquefaction on Lateral Response of Piles by Centrifuge Model Tests', *NCEER Bulletin* (January), 7–11.

Liu, L. & Dobry, R. (1997), 'Seismic Response of Shallow Foundation on Liquefiable Sand', *Journal of Geotechnical and Geoenvironmental Engineering* **123**(6), 557–567.

Luong, M. & Sidaner, J. (1981), Undrained Behaviour of Cohesionless Soils under Cyclic and Transient Loading, *in* 'Proceedings of the First International Conference on Recent Advances in Geotechnical Earthquake Engineering and Soil Dynamics', St. Louis, Missouri, US, pp. 215–220.

Luxford, N. S. (2014), Hydraulic uplift forces on basements subject to liquefaction, *in* '2014 New Zealand Society for Earthquake Engineering Conference', Auckland, New Zealand.

Madabhushi, S. P. G. (2015), *Centrifuge Modelling for Civil Engineers*, CRC Press.

Madabhushi, S. P. G. & Haigh, S. K. (2012), 'How Well Do We Understand Earthquake Induced Liquefaction?', *Indian Geotechnical Journal* **42**(3), 150–160.

Madabhushi, S. P. G., Haigh, S. K., Houghton, N. E. & Gould, E. (2012), 'Development of a servo-hydraulic earthquake actuator for the Cambridge Turner beam centrifuge', *International Journal of Physical Modelling in Geotechnics* **12**(2), 77–88.

Madabhushi, S. P. G., Houghton, N. E. & Haigh, S. K. (2006), A new automatic sand pourer for model preparation at University of Cambridge, *in* 'Proceedings of the Sixth International Conference on Physical Modelling in Geotechnics', CRC Press, Hong Kong, pp. 217–222.

Madabhushi, S. P. G., Schofield, A. N. & Lesley, S. (1998), A new stored angular momentum (SAM) based earthquake actuator, *in* 'Proceedings of the International Conference Centrifuge 98', pp. 111–116.

Madabhushi, S. S. C. (2018), Multi-Hazard Modelling of Dual Row Retaining Walls, Phd, University of Cambridge.

Madabhushi, S. S. C. & Madabhushi, S. P. G. (2015), 'Finite Element Analysis of Floatation of Rectangular Tunnels Following Earthquake Induced Liquefaction', *Indian Geotechnical Journal* **45**(3), 233–242.

Marques, A. S., Coelho, P. A. L. F., Cilingir, U., Haigh, S. K. & Madabhushi, S. P. G. (2012), Centrifuge modelling of liquefaction - induced effects on shallow foundations with different bearing pressures, *in* 'Eurofuge 2012', Delft, The Netherlands.

Mitrani, H. (2006), Liquefaction Remediation Techniques for Existing Buildings, PhD thesis, University of Cambridge.

Mitrani, H. & Madabhushi, S. P. G. (2010), 'Cementation liquefaction remediation for existing buildings', *Proceedings of the ICE - Ground Improvement* **163**(2), 81–94.

Mitrani, H. & Madabhushi, S. P. G. (2012), 'Rigid Containment Walls for Liquefaction Remediation', *Journal of Earthquake and Tsunami* **6**(4).

Mononobe, N. & Matsuo, M. (1929), On determination of earth pressures during earthquakes, *in* 'World Engineering Congress, Engineering Society of Japan', Tokyo, Japan, pp. 179–187.

Muhunthan, B. & Schofield, A. N. (2000), Liquefaction and dam failures, *in* D. V. Griffiths, G. A. Fenton & T. R. Martin, eds, 'Slope Stability 2000', ASCE, Denver, Colorado, USA, pp. 266–280.

Newmark, N. M. (1965), 'Effects of Earthquakes on Dams and Embankments', *Géotechnique* **15**(2), 139–160.

Ohsaki, Y. (1966), 'Niigata earthquake, 1964 building damage and soil conditions', *Soils and Foundations* **6**(2), 14–37.

Okabe, S. (1924), 'General theory of earth pressure and seismic stability of retaining wall and dam', *Journal of Japan Society of Civil Engineers* **10**(6), 1277–1323.

Okamura, M., Takebayashi, M., Nishida, K., Fujii, N., Jinguji, M., Imasato, T., Yasuhara, H. & Nakagawa, E. (2011), 'In-Situ Desaturation Test by Air Injection and Its Evaluation through Field Monitoring and Multiphase Flow Simulation', *Journal of Geotechnical and Geoenvironmental Engineering* **137**(7), 643–652.

Olarte, J. C., Dashti, S., Liel, A. B. & Paramasivam, B. (2018), 'Effects of drainage control on densification as a liquefaction mitigation technique', *Soil Dynamics and Earthquake Engineering* **110**, 212–231.

Olarte, J., Dashti, S. & Liel, A. B. (2018), 'Can ground densification improve seismic performance of the soil-foundation-structure system on liquefiable soils?', *Earthquake Engineering and Structural Dynamics* **47**(5), 1193–1211.

Oztoprak, S. & Bolton, M. D. (2013), 'Stiffness of sands through a laboratory test database', *Géotechnique* **63**(1), 54–70.

Paolucci, P. & Pecker, A. (1997), 'Seismic bearing capacity of shallow strip foundations on dry soils', *Soils and Foundations* **37**(3), 95–105.

Paramasivam, B., Dashti, S. & Liel, A. (2018), 'Influence of Prefabricated Vertical Drains on the Seismic Performance of Structures Founded on Liquefiable Soils', *Journal of Geotechnical and Geoenvironmental Engineering* **144**(10), 04018070.

Paramasivam, B., Dashti, S., Liel, A. & Olarte, J. (2017), Effects of Drains on the Performance and Damage Potential of Shallow-Founded Structures, *in* '3rd International Conference on Performance-based Design in Earthquake Geotechnical Engineering', Vancouver, Canada.

Plaxis (2000), 'Plaxis Version 8.2'.

Renzi, R., Corte, J. F., Bagge, G., Gui, M. & Laue, J. (1994), Cone penetration tests in the centrifuge: Experience of five laboratories, *in* 'International conference centrifuge', pp. 77–82.

Richards Jr, R., Elms, D. G. & Budhu, M. (1993), 'Seismic bearing capacity and settlements of foundations', *Journal of Geotechnieal Engineering* **119**(4), 662–674.

Robertson, P. K. & Campanella, R. G. (1985), 'Liquefaction potential of sands using the CPT', *Journal of Geotechnical Engineering* **111**(3), 384–403.

Robertson, P. K. & Wride, C. E. (1998), 'Evaluating cyclic liquefaction potential using the cone penetration test', *Canadian Geotechnical Journal* **35**(3), 442–459.

Rollins, K. M. & Seed, H. B. (1990), 'Influence of buildings on potential liquefaction damage', *Journal of Geotechnical Engineering* **116**(2), 165–185.

Salgado, R., Boulanger, R. W. & Mitchell, J. K. (1997), 'Lateral Stress Effects on CPT Liquefaction Resistance Correlations', *Journal of Geotechnical and Geoenvironmental Engineering* **123**(8), 726–735.

Sasaki, T. & Tamura, K. (2004), Prediction of Liquefaction-Induced Uplift Displacement of Underground Structures, *in* '36th Joint Meeting US-Japan Panel on Wind and Seismic Effects', pp. 191–198.

Schmertmann, J. H. (1978), Guidelines for cone penetration test (performance and design). Report FHWA-TS-78-209, Technical report, Federal Highway Administration, Washington, United States.
URL: *https://rosap.ntl.bts.gov/view/dot/958*

Schofield, A. (1981), Dynamic and Earthquake Geotechnical Centrifuge Modelling, *in* 'Proceedings of the First International Conference on Recent Advances in Geotechnical Earthquake Engineering and Soil Dynamics', St. Louis, Missouri, US, pp. 1081–1100.

Schofield, A. N. (1980), 'Cambridge Geotechnical Centrifuge Operations', *Géotechnique* **30**(3), 227–268.

Schofield, A. & Wroth, P. (1968), *Critical State Soil Mechanics*, McGraw-Hil, London.

Seed, H. B. (1979), 'Soil Liquefaction and Cyclic Mobility Evaluation for Level Ground During Earthquakes', *Journal of the Geotechnical Engineering Division* **105**(2), 201–255.

Seed, H. B. & Idriss, I. M. (1971), 'Simplified procedure for evaluating soil liquefaction potential', *Journal of the Soil Mechanics and Foundations Division* **97**(9), 1249–1273.

Seed, H. B., Idriss, I. M. & Arango, I. (1983), 'Evaluation of liquefaction potential using field performance data', *Journal of Geotechnical Engineering* **109**(3), 458–482.

Seed, H. B. & Lee, K. L. (1966), 'Liquefaction of Saturated Sands During Cyclic Loading', *Journal of the Soil Mechanics and Foundations Division* **92**(6), 105–134.

Seed, H. B., Tokimatsu, K., Harder, L. & Chung, R. (1985), 'Influence of SPT Procedures in Soil Liquefaction Resistance Evaluations', *Journal of Geotechnical Engineering* **111**(12), 1425–1445.

Sharp, M. K., Dobry, R. & Phillips, R. (2010), 'CPT-Based Evaluation of Liquefaction and Lateral Spreading in Centrifuge', *Journal of Geotechnical and Geoenvironmental Engineering* **136**, 1334–1346.

Silva, T. (2018), Centrifuge modelling of the behaviour of geosynthetic-reinforced soils above voids, PhD thesis, Unviersity of Cambridge.

Stanier, S. A., Blaber, J., Take, W. A. & White, D. J. (2015), 'Improved image-based deformation measurement for geotechnical applications', *Canadian Geotechnical Journal* **53**(5), 727–739.

Stanier, S. A. & White, D. J. (2013), 'Improved image-based deformation measurement in the centrifuge environment', *Geotechnical Testing Journal* **36**(6), 915–928.

Stanier, S., Dijkstra, J., Leśniewska, D., Hambleton, J., White, D. & Muir Wood, D. (2016), 'Vermiculate artefacts in image analysis of granular materials', *Computers and Geotechnics* **72**, 100–113.

Steedman, R. S. & Madabhushi, S. P. G. (1991), Wave propagation in sand medium, *in* 'Proceedings of the 4th International Conference on Seismic Zonation', Stanford, California.

Stringer, M. E. & Madabhushi, S. P. G. (2010), Improving model quality through computer controlled saturation, *in* '7th International Conference on Physical Modelling in Geotechnics', Zurich, Switzerland, pp. 171–176.

Tanaka, Y. (2003), Liquefaction and other geotechnical damages at Chi-Chi earthquake, a departmental bulletin paper, Technical report, Kobe University, Japan, Kobe University, Japan.
URL: *http://www.lib.kobe-u.ac.jp/handle_kernel/80020014*

Taylor, R. N. (1995), Centrifuges in modelling: principles and scale effects, *in* R. N. Taylor, ed., 'Geotechnical centrifuge technology', Chapman & Hall, chapter 2, pp. 19–33.

Terzaghi, K. (1943), *Theoretical Soil Mechanics*, John Wiley and Sons., New York.

Tokimatsu, K., Kojima, H., Kuwayama, S., Abe, A. & Midorikawa, S. (1994), 'Liquefaction-induced damage to buildings in 1990 Luzon earthquake', *Journal of Geotechnical Engineering* **120**(2), 290–307.

Tokimatsu, K. & Seed, H. B. (1987), 'Evaluation of Settlements in Sands Due to Earthquake Shaking', *Journal of Geotechnical Engineering* **113**(8), 861–878.

Tokimatsu, K., Tamura, S., Suzuki, H. & Katsumata, K. (2012), 'Building damage associated with geotechnical problems in the 2011 Tohoku Pacific Earthquake', *Soils and Foundations* **52**(5), 956–974.

Tomlinson, M. J. (2001), *Foundation design and construction*, 7th edn, Prentice Hall.

Towhata, I. (2008), *Geotechnical Earthquake Engineering*, Springer Science in Business Media.

Tsuchida, H. (1970), 'Prediction and countermeasure against the liquefaction in sand deposits', *Abstract of Seminars in the Port and Harbour Research Institute* pp. 3.1 – 3.33 (in Japanese).

Unutmaz, B. (2018), 'Effects of basements and adjacent structures on liquefaction-triggering potential of foundation soils', *Bulletin of Earthquake Engineering* **16**(7), 2757–2773.

Vaid, Y. P. & Chern, J. C. (1983), 'Effect of static shear on resistance to liquefaction', *Soils and Foundations* **23**(1), 47–60.

Vaid, Y. P., Chern, J. C. & Tumi, H. (1985), 'Confining pressure, grain angularity and liquefaction', *Journal of Geotechnical Engineering* **111**(10), 1229–1235.

Vaid, Y. P. & Finn, L. W. D. (1979), 'Static shear and liquefaction potential', *Journal of Geotechnical Engineering* **105**(10), 1233–1246.

Vesic, A. S. (1963), 'Bearing Capacity of Deep Foundations in Sand', *Highway Research Record* **39**, 112–153.

Villet, M. C. B. & Mitchell, J. K. (1981), Cone resistance, relative density and friction angle, *in* G. M. Norris & R. D. Holtz, eds, 'Symposium on Cone Penetration Testing and Experience, Geotechnical Engineering Division, ASCE', St. Louis, Missouri, US, pp. 178–208.

White, D. J., Take, W. A. & Bolton, M. D. (2003), 'Soil deformation measurement using particle image velocimetry (PIV) and photogrammetry', *Géotechnique* **53**(7), 619–631.

Wilkinson, S., Grant, D., Williams, E., Paganoni, S., Fraser, S., Boon, D., Mason, A. & Free, M. (2012), 'Observations and implications of damage from the magnitude Mw 6.3 Christchurch, New Zealand earthquake of 22 February 2011', *Bulletin of Earthquake Engineering* **11**(1), 107–140.

Yang, D., Naesgaard, E., Byrne, P. M., Adalier, K. & Abdoun, T. (2004), 'Numerical Model Verification and Calibration of George Massey Tunnel using Centrifuge Models', *Canadian Geotechnical Journal* **41**(5), 921–942.

Yang, J. & Sato, T. (2000), 'Interpretation of seismic vertical amplification observed at an array site', *Bulletin of the Seismological Society of America* **90**(2), 275–285.

Yasuda, S. & Kiku, H. (2006), 'Uplift of sewage manholes and pipes during the 2004 Niigataken-Chuetsu Earthquake', *Soils and Foundations* **46**(6), 885–894.

Yoshimi, Y., Tanaka, K. & Tokimatsu, K. (1989), 'Liquefaction Resistance of a Partially Saturated Sand', *Soils and Foundations* **29**(3), 157–162.

Yoshimi, Y. & Tokimatsu, K. (1977), 'Settlement of buildings on saturated sand during earthquakes', *Soils and Foundations* **17**(1), 23–38.

Youd, T. L., Idriss, I. M., Andrus, R., Arango, I., Castro, G., Christian, J., Dobry, R., Finn, W., Harder, L. J., Hynes, M., Ishihara, K., Koester, J., Liao, S., Marcuson, W., Martin, G., Mitchell, J., Moriwaki, Y., Power, M., Robertson, P., Seed, R. & Stokoe, K. (2001), 'Liquefaction Resistance of Soils: Summary Report from the 1996 NCEER and 1998 NCEER/NSF Workshops on Evaluation of Liquefaction Resistance of Soils', *Journal of Geotechnical and Geoenvironmental Engineering* **127**(10), 817–833.

Zeghal, M. & Elgamal, A. (1994), 'Analysis of site liquefaction using earthquake records', *Journal of Geotechnical Engineering* **120**(6), 996–1017.

Zeybek, A. & Madabhushi, S. P. G. (2016), 'Centrifuge testing to evaluate the liquefaction response of air-injected partially saturated soils beneath shallow foundations', *Bulletin of Earthquake Engineering* **15**(1), 339–356.

Zhang, G., Robertson, P. K. & Brachman, R. W. (2002), 'Estimating liquefaction-induced ground settlements from CPT for level ground', *Canadian Geotechnical Journal* **39**(5), 1168–1180.

Zhang, Z. & Chian, S. C. (2019), 'Importance of sidewall friction on manhole uplift during soil liquefaction', *Soil Dynamics and Earthquake Engineering* **119**, 51–61.